Switching in Emerging Memories and their Response to Heavy Ion Irradiation

zur Erlangung des akademischen Grades Doktor-Ingenieur (Dr.-Ing.)

genehmigte Dissertation von Tobias Vogel aus Erbach im Odenwald

Fachbereich Material- und Geowissenschaften der Technischen Universität Darmstadt

Tag der Einreichung: 10. Januar 2023, Tag der Prüfung: 6. März 2023

Darmstadt 2023

1. Gutachten: Prof. Dr. Lambert Alff

2. Gutachten: Prof. Dr. Christina Trautmann

“Switching in Emerging Memories and their Response to Heavy Ion Irradiation”

Vom Fachbereich Material- und Geowissenschaften

der Technischen Universität Darmstadt

zur Erlangung des Grades Doktor-Ingenieur (Dr.-Ing.)

genehmigte Dissertation von Tobias Vogel (M.Sc.) aus Erbach im Odenwald, Deutschland

1. Gutachten: Prof. Dr. Lambert Alff

2. Gutachten: Prof. Dr. Christina Trautmann

Tag der Einreichung: 10. Januar 2023

Tag der Prüfung: 6. März 2023

Darmstadt 2023 - D17

Bitte zitieren Sie dieses Dokument als/Please cite this document as:
URN: urn:nbn:de:tuda-tuprints-232636
URI: https://tuprints.ulb.tu-darmstadt.de/id/eprint/23263

Thesis Statement - Erklärung zur Dissertation

Thesis Statement pursuant to § 22 paragraph 7 of APB TU Darmstadt

I herewith formally declare that I, Tobias Vogel, have written the submitted thesis independently pursuant to § 22 paragraph 7 of APB TU Darmstadt. I did not use any outside support except for the quoted literature and other sources mentioned. I clearly marked and separately listed all of the literature and all of the other sources which I employed when producing this academic work, either literally or in content. I state that all passages which have been taken from publications of all means or unpublished material either whole or in part, in words or ideas, have been marked as quotations. This thesis has not been handed in or published before in the same or similar form.

In the submitted thesis the written copies and the electronic version for archiving are pursuant to § 23 paragraph 7 APB identical in content.

Darmstadt, _____________

____

(Tobias Vogel, M.Sc.)

Abstract

Memory technologies are ubiquitous in our everyday life and the number of electronic devices relying on them keeps increasing rapidly. In established memories such as static random-access memory (SRAM), dynamic random-access memory (DRAM) and flash memory, further downscaling of transistors has slowed down leading to deviations from Moore's law. However, this was so far considered a fundamental step towards ever increasing data storage, reduced energy consumption and lowered fabrication cost for decades. Furthermore, new applications such as image recognition or autonomous driving, which implement artificial neural networks, represent a challenge for the classic computer architecture. These challenges are the driving force for the development of new technologies such as emerging memories, including phase-change-based resistive, redox-based resistive and ferroelectric memories. Those memory types store information using different physical concepts than the established, mainly directly charge-based technologies. One important concept can be summarized under the term "memristor" or "memristive system". It is based on a resistance change of a memory cell triggered by electric stimuli, which is dependent on the history of the memory material.[1, 2] The resistance in phase-change memories relies on the reversible transition of a phase-change material such as $Ge_2Sb_2Te_5$ from an amorphous to a crystalline state. In contrast, the resistance in filamentary redox-based systems dependents on ion-migration and the formation/control of a conductive filament in a thin dielectric layer such as HfO_2. This allows the achievement of at least two distinguishable memory states, which are repeatably accessible by applying voltage/current stimuli in a switching process. In ferroelectric memories, the data storage is based on the control of the electric polarization of a ferroelectric material such as doped HfO_2. Due to their good scalability, non-volatility and fast as well as energy-efficient operation, these memories are currently discussed as promising candidates to replace or complement established memory concepts. Additionally, they have been demonstrated to show e.g., interesting synaptic-like properties usable for neuromorphic applications and prospective artificial intelligence.[3-8]

Furthermore, since the information storage principle of these emerging memory types is not directly based on charges, they are promising candidates for utilization in radiation-harsh environments, including e.g., aerospace applications. In general, all types of ionizing radiation of natural or artificial origin are a threat for microelectronics, as they can affect the functionality of electronic components.[9, 10] An extreme case is represented by high-energy heavy ions due to their large ionization potential and high penetration depth. This type of radiation can induce defects and phase transitions in materials relevant for memory technologies such as HfO_2.[11] This could adversely affect the functionality of emerging memories.

Currently, all emerging memories are still in their infancy and not yet fully competitive with established technologies, especially in relation to a detailed understanding of the working principles of the memories, the fabrication of integrated circuits in complementary metal-oxide-semiconductor (CMOS)-compatible processes and production costs. In order to unveil the full potential of the emerging memories and to enable their use for different applications, a deeper understanding of the material properties and the basic physical switching processes is required. This also includes a better understanding of radiation-induced effects such as phase transitions in the materials and related switching properties of emerging memories. In this regard, research needs to be further advanced.

In this context, this work addresses relevant influences on the switching characteristics of three selected emerging memory types, in particular HfO_2-based resistive and ferroelectric memories as well as Germanium-Antimony-Tellurium (Ge-Sb-Te)-based phase-change memories and their response to heavy ion irradiation.

For studies on non-irradiated HfO_2-based memristive devices, specific model systems consisting of single metal-insulator-metal (MIM) capacitor stacks were prepared. This includes doping of HfO_2 films with Zr to potentially induce ferroelectric properties in $Hf_{0.5}Zr_{0.5}O_2$-based memory, which represent one of the most-promising candidates for ferroelectric memory applications. Additional studies were designed to investigate the influence of Zr-doping, the choice of the electrode materials and the oxide layer thickness on the resistive switching behavior of HfO_2-based devices relevant for resistive memory applications ($Pt/Hf_{0.5}Zr_{0.5}O_2/Pt$, $Pt/HfO_2/Pt$ and $Cu/HfO_2/Pt$). For the preparation of Zr-doped HfO_2 films, a growth routine was successfully established. It includes a co-evaporation process of Hf and Zr in a reactive molecular beam epitaxy setup allowing a precise control of the composition. The resistive switching studies have revealed functioning devices with no significant influence of the Zr-doping. Furthermore, a strong dependence of the choice of the electrode materials and the switching types on the dominating switching mechanism was found in $Pt/HfO_2/Pt$ and $Cu/HfO_2/Pt$ devices. While the switching in $Pt/HfO_2/Pt$ devices is based on a thermochemical mechanism, the obtained switching in $Cu/HfO_2/Pt$ devices yielding the best switching performance is based on an electrochemical mechanism. As a reduction of the layer thicknesses of electronic components is of huge interest, studying the related influences on the switching characteristics is essential. In a specifically designed study, the switching mechanism in $Cu/HfO_2/Pt$ devices under bipolar resistive switching was found to be dependent on the oxide layer thickness. A qualitative model based on a strongly Joule heating-assisted electrochemical mechanism was developed.

Furthermore, to investigate the impact of ionizing radiation in the electronic energy loss regime on different memory materials, HfO_2- and Ge-Sb-Te-based films containing different compositions and phases/crystallinity, respectively, were exposed to high-energy Au ions. These studies were conducted in close collaboration with project partners from CEA-Leti and LTM CNRS (Grenoble, France) as well as from Fraunhofer IPMS CNT (Dresden, Germany). Irradiation experiments were performed at the Helmholtzzentrum für Schwerionenforschung (Darmstadt, Germany) in close collaboration with the materials research group of Prof. Dr. C. Trautmann. By combining different characterization methods such as X-ray diffraction, X-ray photoelectron spectroscopy and different scanning transmission electron microscopy methodologies, an improved understanding of the basic mechanisms of the occurring phase transitions was achieved. This was supported by a direct comparison of irradiated with as grown HfO_{2-x} films of different stoichiometry and crystal structure. Those films were prepared using a reactive molecular beam epitaxy setup, which allows a precise control of the oxygen content. In monoclinic HfO_2 films, crystalline-to-crystalline phase transition based on induced oxygen vacancies to a rhombohedral phase of hafnium oxide was observed. This phase transition was found to be accompanied by a significant grain fragmentation at high fluences. In this context, a pattern matching routine was developed in cooperation with the electron microscopy research group of Prof. Dr. L. Molina-Luna for the analysis of a recorded, complex scanning precession electron diffraction dataset. This allowed the investigation of the phase transition at high spacial resolution.

The irradiation of Zr- and Si-doped ferroelectric HfO_2 as well as in $Ge_2Sb_2Te_5$ (GST) and Ge-rich GST (GGST) phase-change layers showed similar irradiation-induced phase transitions. In ferroelectric HfO_2-based layers, the transition from a polar to a non-polar phase occurred, whereas the phase transitions found in Ge-Sb-Te-based layers were related to beam-induced breaking and formation of chemical bonds. Structural characterization revealed that for all tested memory materials the irradiation effects strongly depend on the initial crystallinity and crystal structure as well as on the composition and microstructure of the layers. Moreover, the occurring phase transitions could be directly correlated to switching properties obtained from electrical measurements performed on memory devices. For oxide-based and phase-change random access memories (OxRAM and PCRAM), detrimental beam-induced effects on the access transistors of the one transistor-one memory cell (1T1R) arrays are found to be dominating the failure mechanism at ion fluences exceeding 5×10^{10} ions/cm^2, while it is indicated that the memory cells are radiation-hard as long as no phase transitions occur in the layers. In ferroelectric capacitors, the induced phase transition from the polar orthorhombic to a non-polar phase could even be reversed by electric field cycling after irradiation. Hence, all tested memory types were found to be extremely radiation-resilient. It was shown that a combination of different characterization techniques is needed to achieve a full understanding on occurring structural and compositional changes and related electrical properties. This can also be recommended as general guidelines for the characterization and interpretation of complex irradiation-induced effects in emerging memories.

Overall, this work provides an improved understanding of resistive switching phenomena and of basic mechanisms of irradiation effects in HfO_2- and Ge-Sb-Te-based memories. This is important since these emerging memories are promising candidates for future memory applications replacing or supplementing existing memory technologies. In this context, this work provides useful knowledge for the development of new strategies for the fabrication and characterization of emerging memories.

Zusammenfassung

Speichertechnologien sind in unserem Alltag allgegenwärtig und die Anzahl elektronischer Geräte, die darauf angewiesen sind, nimmt weiter zu. Hinzu kommt die Limitierung der bisher einfach zu erzielenden Reduzierung der Strukturgröße von Transistoren sowie der Dicke der verwendeten isolierenden Schicht in etablierten Speichern wie statischen (SRAM) und dynamischen Direktzugriffsspeichern (DRAM) sowie Flash-Speichern. Eine Reduzierung der Strukturgröße wurde bisher als eine Art grundlegende Möglichkeit angesehen, auf recht einfachem Weg immer größere Datenspeicherung, einem immer weiter reduzierten Energieverbrauch und niedrigere Herstellungskosten zu erzielen. Darüber hinaus stellen neue Anwendungen wie Bilderkennung oder autonomes Fahren eine Herausforderung für die klassische Computerarchitektur dar. Diese Herausforderungen sind die treibende Kraft für die Entwicklung neuer Technologien wie neuartige Speicher (emerging memories) in der Form von phasenwechselbasierten resistiven, redoxbasierten resistiven und ferroelektrischen Speichern. Diese Speichertypen speichern Informationen basierend auf anderen physikalischen Konzepten als die etablierten, meist direkt ladungsbasierten Technologien. In sogenannten memristiven Systemen oder auch Memristoren hängt der gespeicherte Zustand der Speicherzelle, welcher durch elektrische Stimuli geändert werden kann von der Historie des Speichermaterials ab.[1, 2] Während der Widerstand in Phasenwechselspeichern auf dem reversiblen Übergang eines Phasenwechselmaterials (wie z.B. $Ge_2Sb_2Te_5$) von einem amorphen in einen kristallinen Zustand beruht, ist der Widerstand in (filamentbasierten) redoxbasierten Systemen von der Migration von Anionen bzw. Kationen und der Bildung/Kontrolle eines leitfähigen Filaments in einer dünnen dielektrischen Schicht (wie z.B. HfO_2) abhängig. Dadurch lassen sich mindestens zwei unterscheidbare Speicherzustände erreichen, die durch einen wiederholbaren Umschaltvorgang zugänglich sind. Bei ferroelektrischen Speichern basiert die Datenspeicherung auf der Steuerung der elektrischen Polarisation eines ferroelektrischen Materials (z.B. dotiertes HfO_2). Diese Speicher werden derzeit aufgrund ihrer guten Skalierbarkeit, Nichtflüchtigkeit und ihres schnellen sowie energieeffizienten Betriebs als vielversprechende Kandidaten gehandelt, welche etablierte Speicherkonzepte ersetzen oder ergänzen könnten. Darüber hinaus wurde gezeigt, dass diese Speicherklassen z.B. interessante synaptische Eigenschaften aufweisen, welche für neuromorphe Anwendungen und zukünftige künstliche Intelligenz verwendet werden könnten.[3-8]

Da das Informationsspeicherprinzip dieser neuen Speichertypen nicht direkt auf Ladungen basiert, sind sie außerdem vielversprechende Kandidaten für die Nutzung als strahlungsresistente Speicher. Dies könnten Anwendung in strahlungsintensiven Umgebungen wie im Bereich der Luft- und Raumfahrt finden. Generell sind alle Arten ionisierender Strahlung natürlichen oder künstlichen Ursprungs eine Gefahr für die Mikroelektronik, da sie die Funktionalität von elektrischen Bauteilen beeinträchtigen können.[9, 10] Einen Extremfall stellen hierbei hochenergetische Schwerionen dar, welche sich durch ein hohes Ionisationspotential und hohe Eindringtiefen in Materie auszeichnen. So wurde zum Beispiel von induzierten Defekten und Phasenübergängen in HfO_2 berichtet[11], was die Funktionsfähigkeit der neuartigen Speicher negativ beeinflussen könnte.

Aktuell stecken alle neuen Speichertechnologien noch in den Kinderschuhen und sind noch nicht vollständig konkurrenzfähig mit etablierten Technologien, insbesondere in Bezug auf ein

detailliertes Verständnis der Funktionsweise der neuartigen Speicher, der Herstellung in komplementären Metall-Oxid-Halbleiter (CMOS)-kompatiblen Prozessen und der Herstellungskosten. Um jedoch das volle Potenzial der neuartigen Speicher zu enthüllen und diese für verschiedene Anwendungen nutzbar zu machen, ist ein tieferes Verständnis der Materialeigenschaften sowie der grundlegenden physikalischen Schaltprozesse erforderlich. Dazu gehört auch ein besseres Verständnis der strahlungsinduzierten Phasenübergänge in den Materialien und der damit zusammenhängenden elektrischen Eigenschaften der neuartigen Speicher. Diesbezüglich muss die Forschung noch weiter vorangetrieben werden.

In dieser Arbeit wurden deshalb unterschiedliche Einflüsse auf das Schaltverhalten verschiedener neuartiger Speichertechnologien, insbesondere HfO_2-basierter resistiver und ferroelektrischer Speicher sowie Germanium-Antimon-Tellur (Ge-Sb-Te)-basierter Phasenwechselspeichern untersucht. Dabei wurden diese neuartigen Speicher auch mit Schwerionen bestrahlt, um den Einfluss der ionisierenden Strahlung auf das Material- und Schaltverhalten zu untersuchen.

Für Studien an unbestrahlten HfO_2-basierten Bauteilen wurden spezifische Modellsysteme hergestellt, die aus einzelnen Metall-Isolator-Metall (MIM)-Kondensatorstapeln bestehen. Dazu gehört auch das Dotieren von HfO_2 Filmen mit Zr, um $Hf_{0.5}Zr_{0.5}O_2$-basierte ferroelektrische Stapel zu erzielen, die einen der vielversprechendsten Kandidaten für ferroelektrische Speicheranwendungen darstellen. Weitere Studien wurden entwickelt, um den Einfluss der Zr-Dotierung, der Wahl des Elektrodenmaterials sowie der Oxidschichtdicke auf das Schaltverhalten von HfO_2-basierten Zellen zu untersuchen (Pt/$Hf_{0.5}Zr_{0.5}O_2$/Pt, Pt/HfO_2/Pt and Cu/HfO_2/Pt). Zur Herstellung Zr-dotierter Schichten wurde eine Wachstumsroutine erfolgreich etabliert, bei dem eine simultane Verdampfung von Hf und Zr in einem Molekularstrahlepitaxiesystem genutzt wurde, was die präzise Kontrolle der Filmzusammensetzung erlaubt. Die Studien zum resistiven Schalten haben keinen signifikanten Einfluss der Zr-Dotierung auf das Schaltverhalten der Memristoren gezeigt. Weiterhin wurde in Versuchen an Pt/HfO_2/Pt und Cu/HfO_2/Pt Zellen gezeigt, dass die resistiven Schaltprozesse eine starke Abhängigkeit von der Wahl des Elektrodenmaterials sowie der Schaltarten haben und dass diese den dominierenden Schaltmechanismus direkt beeinflussen. Während das Schalten in Pt/HfO_2/Pt Zellen von einem thermochemischen Mechanismus dominiert wird, basiert das resistive Schalten in Cu/HfO_2/Pt Bauteilen, welches die besten Schalteigenschaften aufwies, hauptsächlich auf einem elektrochemischen Mechanismus. Da eine zusätzliche Reduzierung der Dicke in elektrischen Bauteilen von großem Interesse ist, erweist sich eine Untersuchung der damit verbundenen Einflüsse auf die Schalteigenschaften als unerlässlich. In einer speziell angelegten Studie wurde festgestellt, dass der Schaltmechanismus in Cu/HfO_2/Pt Speicherzellen unter bipolarem Widerstandsschalten von der Oxidschichtdicke abhängt. Zur Erklärung dieses Verhaltens wurde ein qualitatives Modell basierend auf einem von Joulescher Wärme unterstützten elektrochemischen Mechanismus entwickelt.

Um den Einfluss ionisierender Strahlung auf verschiedene Speichermaterialien zu untersuchen, wurden HfO_2- und Ge-Sb-Te-basierten Filme mit unterschiedlichen Zusammensetzungen und Kristallinitäten bzw. Kristallstrukturen hochenergetischen Au-Ionen ausgesetzt. Diese Studien wurden in enger Zusammenarbeit mit Projektpartnern von CEA-Leti und LTM CNRS (Grenoble, Frankreich) sowie vom Fraunhofer IPMS CNT (Dresden, Deutschland) durchgeführt. Die

Bestrahlungsexperimente wurden am Helmholtzzentrum für Schwerionenforschung (Darmstadt, Deutschland) durchgeführt. Dies geschah in enger Kooperation mit der Materialforschungsgruppe von Prof. Dr. C. Trautmann. Durch die Kombination verschiedener Charakterisierungsmethoden wie Röntgenbeugung, Röntgenphotoelektronenspektroskopie und verschiedener Methoden der Rastertransmissionselektronenmikroskopie, konnte ein verbessertes Verständnis der grundlegenden Mechanismen der auftretenden Phasenübergänge erzielt werden. Unterstützt wurde dies durch den direkten Vergleich von bestrahlten mit defizitär gewachsenen (unbestrahlten) HfO_{2-x}-Filmen unterschiedlicher Stöchiometrie und kristallinen Struktur. Diese Filme wurden unter Verwendung einer reaktiven Molekularstrahl-Epitaxie-Anlage gewachsen, welche die präzise Steuerung des Sauerstoffgehalts ermöglicht. In monoklinen HfO_2-Filmen wurde ein Phasenübergang (von kristallin zu kristallin) basierend auf induzierten Sauerstoffvakanzen zu einer rhomboedrischen Phase von Hafniumoxid gefunden. Es wurde festgestellt, dass dieser Phasenübergang von einer deutlichen Kornfragmentierung bei hohen Fluenzen begleitet wird. In diesem Zusammenhang wurde in Zusammenarbeit mit der Elektronenmikroskopie-Forschungsgruppe von Prof. Dr. L. Molina-Luna eine spezielle Routine zu Verarbeitung und Analyse (pattern matching) zur Analyse eines aufgenommenen, komplexen Rasterpräzessionselektronenbeugungs-Datensatzes entwickelt. Dies erlaubte die Untersuchung des Phasenübergangs mit hoher räumlicher Auflösung.

Die Bestrahlung von Zr- und Si-dotiertem ferroelektrischem HfO_2 sowie in $Ge_2Sb_2Te_5$ (GST) und Ge-reichen GST (GGST)-Phasenwechselschichten zeigten ähnliche strahlungsinduzierte Phasenübergänge. Während in ferroelektrischen HfO_2-basierten Schichten der aufgezeigte Übergang von einer polaren zu einer unpolaren Phase stattfand, konnten unterschiedliche Phasenübergänge, die in Ge-Sb-Te-basierten Schichten gefunden wurden, mit strahlinduzierten Brüchen der chemischen Bindung sowie deren Bildung in Zusammenhang gebracht werden. Die strukturellen Untersuchungen haben gezeigt, dass bei allen getesteten Speichermaterialien die Bestrahlungseffekte stark von der anfänglichen Kristallinität bzw. Kristallstruktur, der Zusammensetzung und der Mikrostruktur der Schichten abhängen. Darüber hinaus konnten die auftretenden Phasenübergänge direkt mit den Ergebnissen aus elektrischen Messungen an Speicherbauteilen in Verbindung gebracht werden. Bei der Untersuchung der Oxid- sowie Phasenwechselmaterial-basierten Direktzugriffsspeicher (OxRAM und PCRAM) wurde festgestellt, dass strahlinduzierte Effekte auf die Zugriffstransistoren der 1T1R-Arrays den Ausfallmechanismus bei Fluenzen über 5×10^{10} Ionen/cm^2 dominieren, wobei sich die neuartigen Speicherzellen als sehr strahlungshart herausgestellt haben, solange keine Phasenübergänge in den Schichten auftreten. In ferroelektrischen Kondensatoren konnte der induzierte Phasenübergang von einer polaren zu einer unpolaren Phase sogar durch Zyklieren des elektrischen Feldes umgekehrt werden. Somit erwiesen sich alle getesteten Speichertypen als äußerst strahlungsresistent. Es wurde gezeigt, dass eine Kombination verschiedener Charakterisierungsmethoden zur Untersuchung der Kristallstruktur und Materialzusammensetzung mit elektrischen Untersuchungen an Bauteilen erforderlich ist, um ein umfassendes Verständnis der auftretenden Änderungen zu erzielen. Dies kann auch als Richtlinie für die Charakterisierung und Interpretation komplexer strahlungsinduzierter Effekte in neuartigen nichtflüchtigen Speichern empfohlen werden.

Insgesamt liefert diese Arbeit ein verbessertes Verständnis der resistiven Schaltphänomene und der grundlegenden Mechanismen von Bestrahlungseffekten in den getesteten HfO_2- und

Ge-Sb-Te-basierten neuartigen Speichertypen. Dies ist wichtig, da diese Speichertechnologien vielversprechende Kandidaten für zukünftige Speicheranwendungen sind, die bestehende Speichertechnologien ersetzen oder ergänzen können. In diesem Zusammenhang liefert diese Arbeit nützliches Wissen für die Entwicklung neuer Strategien zur Herstellung und Charakterisierung neuartiger Speicher.

List of Abbreviations

ACOM	automated crystal orientation mapping
ADF	annular dark-field
AI	artificial intelligence
ALD	atomic layer deposition
BE	bottom electrode
BEOL	back-end-of-line
BF	bright-field
BTO	barium titanate
BRS	bipolar resistive switching
CBRAM	conductive-bridging random-access memory
CC	current compliance
CIF	crystallographic information file
CMOS	complementary metal-oxide semiconductor
CPU	central processing unit
CRS	complementary resistive switching
DC	direct current
DD	displacement damage
DF	dark-field
DFT	density functional theory
DRAM	dynamic random-access memory
E_C	coercive field
ECM	electrochemical metallization memory (sometimes also: mechanism)
EDX	energy-dispersive X-ray spectroscopy
EELS	electron energy-loss spectroscopy
FeFET	ferroelectric field-effect transistors
FIB	focused ion beam
FPGA	field-programmable gate array
FTJ	ferroelectric tunnel junction
GGST	Ge-rich GST
HRTEM	high-resolution transmission electron microscopy
Ge-Sb-Te	Germanium-antimony-tellurium
GST	$Ge_2Sb_2Te_5$
hcp	hexagonal close-packed
HfO_x	hafnium oxide
HRS	high resistance state
HSO	hafnium-silicon-oxide (3 at% Si)
HZO	$Hf_{0.5}Zr_{0.5}O_2$
IBE	ion beam etching
IoT	internet of things
ICDD	International Center for Diffraction Data
LET	linear energy transfer
LRS	low resistance state
MBE	molecular beam epitaxy
MCU	microcontroller unit
MIM	metal-insulator-metal
MOSFET	metal-oxide-semiconductor field-effect transistor
MRAM	magnetic random-access memory
NBED	nanobeam electron diffraction
OTS	ovonic threshold switch
OxRAM	oxide-based random-access memory
PANBED	position averaged nanobeam electron diffraction
PCM	phase-change memory
PCRAM	phase-change random-access memory
PDF	powder diffraction file
PMU	pulse measure unit
PUND	positive-up-negative-down
P_r	remanent polarization
P_S	saturation polarization
PVD	physical vapor deposition
PZT	lead zirconate titanate
r,c,t,o	rhombohedral, cubic, tetragonal, orthorhombic structure, respectively
RAM	random-access memory
RF	radio frequency
RT	room temperature
RHEED	reflection high-energy diffraction
RRAM	resistive random-access memory
SCLC	space-charge-limited conduction
SCM	storage-class memory
SEE	single event effects
SEGR	single event gate ruptures
SEL	single event latchups
SEU	single event upset
SHI	swift heavy ions
SMU	source measure unit
SPED	scanning precession electron diffraction
SRAM	static random-access memory
SSD	solid-state drive
(S)TEM	(scanning) transmission electron microscopy
TAT	trap-assisted tunneling
TCM	thermochemical memory (sometimes also: mechanism)
TE	top electrode
TID	total ionization dose
TiN	titanium nitride
TMO	transition metal oxide
TRIM	transport of ions in matter
TRS	threshold resistive switching
UHV	ultra-high vacuum
URS	unipolar resistive switching
UV	ultraviolet
VCM	valence change memory (sometimes also: mechanism)
VESTA	Visualization for Electronic and Structural Analysis
QCM	quartz-crystal-microbalance
XPS	X-ray photoelectron spectroscopy
XRD	X-ray diffraction
XRR	X-ray reflectivity
1S1R	1 selector – 1 resistive memory cell
1T1R	1 transistor – 1 resistive memory cell

Table of Contents

Thesis Statement - Erklärung zur Dissertation III

Abstract V

Zusammenfassung IX

List of Abbreviations XIII

Table of Contents XV

1 Introduction 1

1.1 Established memory technologies and challenges 1

1.2 Emerging memory technologies and potential applications 3

1.3 Scope of the work and thesis structure 9

2 Fundamentals on emerging memory materials and memory functionality 11

2.1 Oxide-based resistive switching memories 11
2.1.1 Dielectrics and electrodes 12
2.1.2 Switching mechanisms (VCM, TCM, ECM) 13
2.1.3 Switching modes (URS, BRS, CRS, TRS) 15
2.1.4 Conduction mechanisms 16
2.1.5 Hafnium oxide and parameters influencing resistive switching in HfO_x-based devices 17

2.2 Hafnium oxide-based ferroelectric memory 23

2.3 Germanium-antimony-tellurium-based phase-change memory 28

2.4 Selectors for 1S1R arrays 30

3 Fundamentals on radiation effects in solids 33

3.1 Swift heavy ions 33
3.1.1 Formation of ion tracks 35
3.1.2 Coulomb explosion model and thermal spike model 36

3.2 Heavy ion irradiation-induced phase transitions in hafnium oxide- and Ge-Sb-Te-based powders and films 37

3.3 Memories exposed to heavy ion radiation 39

4 Thin film growth, device preparation and characterization techniques 41

4.1 Thin film growth utilizing reactive MBE 41
4.1.1 Growth process and growth modes 43
4.1.2 Growth monitoring with RHEED 44
4.1.3 MBE growth parameters used for HfO_2, $Hf_xZr_{1-x}O_2$, TiN, Pt and Cu film growth 45

4.2 Electrode Sputtering 49

4.3 Post-deposition annealing and sample structuring 50

4.4 Heavy ion irradiation experiments 54

4.5 Characterisation of film structure and composition 56
4.5.1 X-ray diffraction 56
4.5.2 X-ray reflectivity 61
4.5.3 X-ray photoelectron spectroscopy 62
4.5.4 (Scanning) transmission electron microscopy and related techniques 65

- 4.6 Characterisation of the electrical properties ... 68
  - 4.6.1 Electric polarization measurements of potentially ferroelectric stacks ... 68
  - 4.6.2 Resistive switching in HfO_2-based single memory devices ... 69
- 4.7 External sample preparation and characterisation ... 71

5 Properties of hafnium oxide-based films and switching characteristics of resistive memory devices ... 75

- 5.1 Mixing HfO_2 with ZrO_2 ... 75
- 5.2 Towards a polar crystalline phase for ferroelectric stacks ... 78
- 5.3 Resistive switching characteristics of Pt/HZO/Pt- and Pt/HfO_2/Pt-based devices ... 86
- 5.4 Resistive switching characteristics of Pt/HfO_2/Pt devices and Cu/HfO_2/Pt devices ... 90
  - 5.4.1 Current compliance-dependent switching and potential threshold switching ... 94
- 5.5 Thickness-dependent resistive switching in Cu/HfO_2/Pt-based ECM devices ... 96
  - 5.5.1 Bipolar resistive switching characteristics, filament formation and rupture in Cu/HfO_2/Pt ECM devices with varying oxide layer thickness ... 97
  - 5.5.2 Conduction mechanisms in Cu/HfO_2/Pt ECM devices with varied oxide layer thickness. 101
- 5.6 Impact of the preparation workflow on electrical properties of devices ... 103
- 5.7 Summary and Outlook – Mixed $Hf_xZr_{1-x}O_2$ films and resistive switching of hafnium oxide-based memory devices ... 108

6 Heavy ion irradiation of HfO_x- and Ge-Sb-Te-based materials and emerging memories 110

- 6.1 Phase transitions in HfO_x films exposed to Au swift heavy ions ... 110
  - 6.1.1 Crystalline-to-crystalline phase transition in textured, stoichiometric HfO_2 and oxygen-deficient HfO_x films exposed to heavy ions ... 111
  - 6.1.2 Irradiation-induced phase transition in polycrystalline stoichiometric HfO_2 films grown on SiO_x/Si and TiN/SiO_2/Si ... 119
  - 6.1.3 Irradiation-induced phase transition in polycrystalline oxygen-deficient HfO_x films grown on SiO_x/Si and TiN/SiO_x/Si ... 127
- 6.2 Correlation of induced structural changes in HfO_2 with electrical properties of OxRAM ... 130
  - 6.2.1 Resistive switching behavior of 1T1R arrays with HfO_2-based OxRAM cells exposed to heavy ion radiation ... 130
  - 6.2.2 Resistive switching behavior of an irradiated single 1R memory cell containing 10 nm *m*-HfO_2 films grown in the MBE system ... 133
- 6.3 Heavy ion irradiation induced phase transitions in doped hafnium-oxide ferroelectric layers and electrical properties of ferroelectric capacitors ... 133
- 6.4 Heavy ion irradiation induced phase transitions in $Ge_2Sb_2Te_5$ and Ge-rich GST layers and electrical properties of phase-change memory ... 145
- 6.5 Investigations of emerging memories exposed to heavy ions ... 152

7 Conclusion and Outlook ... 154

- 7.1 Summary of the conducted studies ... 154
- 7.2 Future studies ... 158

Appendix ... XIX

List of Figures ... XXIV

List of Tables ... XXXVI

References.......... XXXVIII
Acknowledgements LIX
Curriculum Vitae.......... LXI
Dissemination LXII

1 Introduction

In our current world, where living seems to be dependent on electronic devices more than ever, the demand for memory technologies keeps increasing. In 2017, *The Guardian* published an article phrasing that a "tsunami of data" is approaching[12], which can be seen as an appropriate and quite impressive metaphor for the exponential increase in stored and transferred electronic data occurring all around the world. This accounts for a significant proportion of the global electricity consumption which becomes increasingly problematic.[13] This trend is further driven by additional potential and already partially available applications summarized under topics such as "Internet of Things (IoT)", "In-memory Computing", and "Machine Learning" or "Artificial Intelligence (AI).[4, 7, 14, 15] These applications represent additionally a challenge for the classic von Neumann computer architecture. So far, a reduced energy consumption could be obtained via downscaling of transistors following Moore's law[16, 17], however, this trend cannot be continued indefinitely in established memory technologies. These challenges are a driving force for the development of new memory technologies summarized under the term "emerging memories". Promising candidates are e.g., hafnium oxide (HfO_x)-based resistive and ferroelectric memories as well as germanium-antimony-tellurium (Ge-Sb-Te)-based phase-change memories.

To introduce the underlying aspects in more detail, established memory concepts and challenges are described in this chapter. Additionally, different emerging memory technologies and potential applications are outlined.

1.1 Established memory technologies and challenges

Since many decades, computing is based on a concept suggested by John von Neumann[18], which is adapted in nearly every computational application created until now. In the corresponding computer architecture, computing is carried out in the central processing unit (CPU) and processed data have to be moved from the CPU to the memory units and back. These steps can consume up to 90 % of the overall required energy[16] and computing time. The necessary permanent data transfer is strongly limiting the performance of the overall system, especially for large amount of transferred data. This limitation is called von Neumann bottleneck. A schematic of the von Neumann architecture (working principle) is shown in Figure 1-1 (a) and a representation of the von Neumann bottleneck in (b). The currently established memory hierarchy of a computer can be schematically depicted as a pyramid (c).

On top the memory hierarchy pyramid, next to the CPU or processor core, flip-flop registers are found, which are a fast accessible (below 1 ns) logic component and on-chip memory. It interacts directly with the different levels of cache (summarized as one single cache for simplification). This is usually a static random-access memory (SRAM) based on 6 transistor cells (6T) with storage capacities in the Kbyte-range (KB) and access times in the ns-range. Random-access memory (RAM) is a memory type used to store data, which is (as implicated by its name) readable and changeable in any order and irrespective of the physical location of the individual data. Below the SRAM in the memory hierarchy, the main memory is located (off-chip), which is a dynamic random-access memory (DRAM) based on an access transistor (1T) and a storage capacitor (1C) in 1T1C configuration. It has a smaller cell size and consequently comparably larger storage capacities in the Gbyte-range (GB) than SRAM. However, both SRAM and DRAM are volatile memory, where data can be stored only for a short time without refreshing.

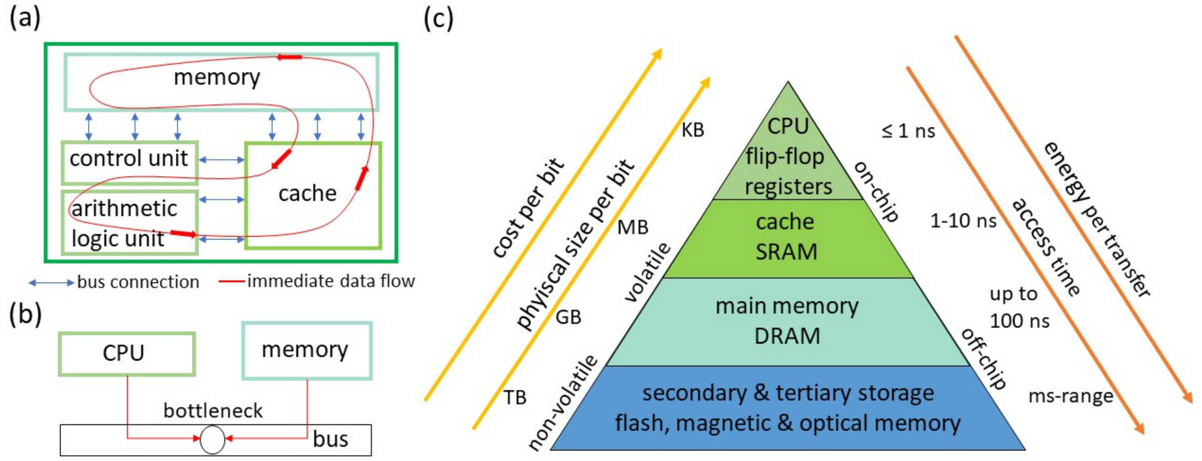

Figure 1-1: (a) Schematic representation of the common von Neumann architecture. Blue arrows indicate the bus connections, while the red path shows the immediate data flow. (b) Representation of the von Neumann bottleneck. (c) Schematic of the currently established memory hierarchy. The width of the schematic pyramid indicates the storage capacity of the different memory (on each level). Increasing property trends are represented by arrows. Created using information from [7, 16, 19, 20].

In contrast, the additional local storage types (also named secondary and tertiary storage) for long-term data purposes located at the bottom of the hierarchy are non-volatile memory, like flash-based storages (solid-state drives (SSD)) or magnetic-based hard disk drives (HDD). Those memories are comparably cheap per bit with high storage capacities in the TB-range. In modern computers, SSDs are often used to replace magnetic drives for faster access, however, the access times in the millisecond-range are comparably low when compared to SRAM performance. SSDs are based on (mostly NAND) flash technology relying on a transistor structure, where information is stored in memory cell arrays of floating-gate transistors. The charges on the gate influence the charge carriers in the underlying channel between source and drain and therefore the electrical conductivity of the transistor. Additionally, long-term storage options such as magnetic tapes as well as (optical) compact discs (CDs) are still present on the market. From top to bottom, the access time of the used memories increases (CPU ≤ 1 ns, cache 1 – 10 ns, main memory 10 – 100 ns and ms-range for secondary and tertiary storage). The difference between processor and memory speed results in a performance gap, which is referred to as the memory gap or memory wall. This is a bandwidth bottleneck. A larger latency of the information transfer occurs from top to bottom of the hierarchy, which is a result of the increasing distance of the memories from the core(s). Additionally, the energy per transfer increases from top to bottom, while the physical size and cost per bit decrease (increasing from bottom to top). The approach of reducing device sizes and additionally aiming for 3D-integration has been considered a good solution. Especially, the commonly used concept of further downscaling of transistors has been considered as the fundamental step towards ever increasing data storage, reduced energy consumption and lowered fabrication cost for decades. However, it became obvious that this path can no longer successfully be followed, which is referred to as the end of Moore's law[16, 17] (number of transistors in an integrated circuit doubling every two years) for the current complementary metal-oxide-semiconductor (CMOS)-based technology. Additionally, 3D-integration leads to new challenges, like facing leakage-current problems, dealing with new and even more complex lithography steps and therefore increasing production cost.[7, 16, 19, 20]

Thus, sticking to the von Neumann architecture concept seems to only limit the achievement of the desired technology applications in demand. There are several alternative concepts proposed which ultimately depend on the desired application and have specific advantages and disadvantages. In this context, emerging memories can be introduced. These are a new kind of memory class comprising different (mostly non-volatile) memory types such as phase-change memory (PCM) or metal oxide resistive memory which are based on other concepts than the established memories. Details will be introduced in the following chapters. Emerging memories are often discussed as contenders to replace the established memories or additions for specific applications next to established memories in a "race for future computing"[21], selectively addressing their respective limitations. To give an application example, emerging memories can be used as a so-called storage-class memory (SCM), a kind of intermediate memory located between the volatile working memory (DRAM) and the non-volatile (mostly NAND flash-based) storage to surmount the memory gap. A commercially available example for a storage class memory is the 32 GB Intel Optane 3D XPoint™.[22] The 3D XPoint™ technology was introduced by Intel and Micron in 2015 and is a resistive memory based on phase-change. Furthermore, ST Microelectronics is producing, selling but also further developing phase-change memory-based microcontroller units (MCUs) for example for automotive applications on the market.[23, 24] Microcontroller units can also be based on magnetic memory technology, where for example a non-volatile MCU based on spin-transfer-torque magnetic random-access memory (STT-MRAM) with ultra-low power consumption and high-speed operation is reported[25]. Traditional ferroelectric memory-based systems, commonly based on perovskite materials as the memory material are established and also available on the market. Those are provided for example by Futjitu[26], Texas Instruments[27] and Infineon/Cypress Semiconductor[28, 29]. However, these memories are facing crucial scaling limitations. Further, technologies like metal oxide-based resistive memory or hafnium oxide-based ferroelectric memory are partially available, as developed by Panasonic[30], Weebit Nano in cooperation with CEA-Leti[31, 32] and Ferroelectric Memory GmbH[33], to name a few examples. However, further development is necessary as these promising technologies are still in their infancy. Emerging memory technologies and potential applications are discussed in the following section 1.2 and chapter 2.

1.2 Emerging memory technologies and potential applications

Emerging memory technologies consist of a multitude of different memory classes storing information using different physical concepts than the established charge-based SRAM, DRAM and flash technologies. A prominent class is called memristive systems which are based on the memristor concept introduced by Leon Chua.[1, 2] A memristor is an electronic component that can change its resistance by electric stimuli applied based on the history of the material. It can retain memory even when no power is applied. In the last decades, various memory types showing different memristive behavior have been introduced, such as magnetic, resistive and ferroelectric memories.[3, 7, 20, 34-36] A variety of different emerging memory technologies are under investigation. An exemplary emerging memory classification is given in Figure 1-2.

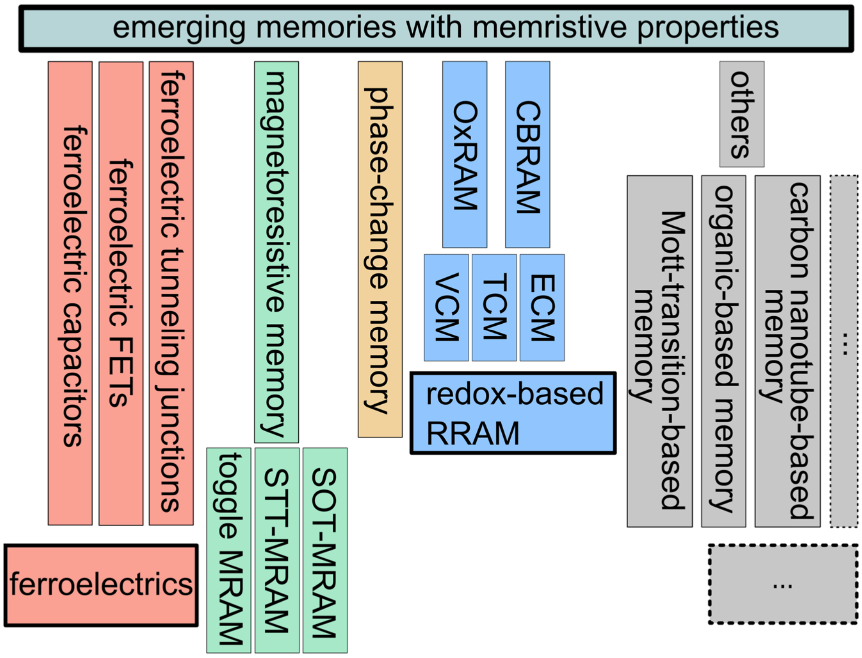

Figure 1-2: Emerging memory classification scheme including ferroelectric (red), magnetic (green) and phase change memories (yellow) as well as redox-based resistive memories (blue) as memory types. While this displays an overview of some important examples, a multiplicity of additional concepts exist which are here summarized as others (grey boxes). Additionally, the operation principle among different memory types can overlap (e.g., ferroelectric tunneling junctions are based on the resistance change but also using a ferroelectric layer). Created using information from [7, 20, 34, 37].

Selected memories with memristive properties are introduced in the following paragraphs. A schematic representation of the basic operation principles of FeRAM, MRAM, PCRAM and redox-based RRAM is given in Figure 1-3.

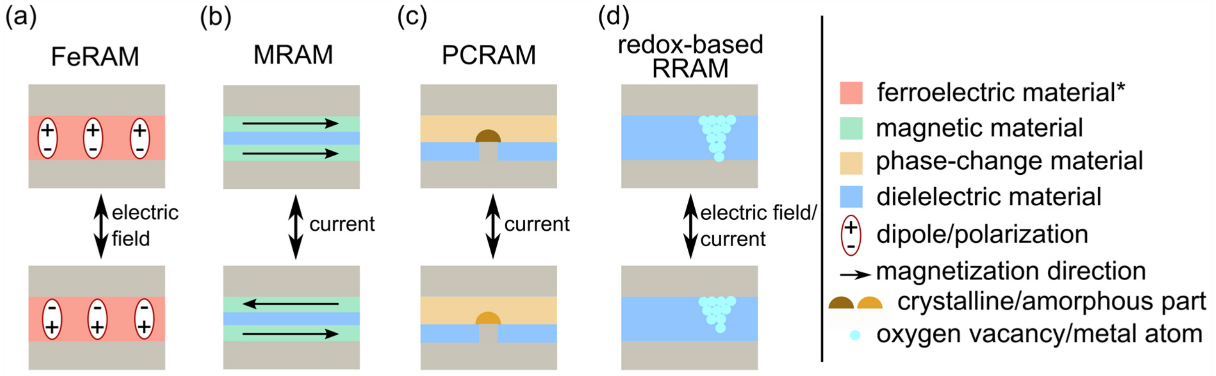

Figure 1-3: Schematic representation of switching mechanisms in FeRAM, MRAM, PCRAM and redox-based RRAM. (a) Ferroelectric switching relies of dipole moments (remanent electric polarization) in a ferroelectric material switched by an electric field. (b) In a magnetic tunnel junction (MTJ), the magnetization (direction) of a free layer can be switched by applying a magnetic field, leading to either a parallel or an anti-parallel orientation. (c) In phase-change memories, a chalcogenide material is switched between a crystalline and an amorphous phase by Joule heating induced by a current. (d) In redox-based resistive memories (filamentary) which are based on the movement of ions, a conductive filament composed of oxygen vacancies (oxygen-deficient/metal-rich region) or metal atoms is reversibly (re)formed and ruptured. Redrawn after[38].
* Ferroelectrics are also dielectrics/insulators.

FeRAM

Ferroelectric random-access memories (FeRAM or FRAM) are based on the storage of data by controlling the electric polarization of a polar, ferroelectric material by an applied electric field. This concept is known since the 1960s[39] and chips were mostly based on perovskite materials[26] showing high polarization values at low electric fields. Unfortunately, the downscaling of these materials is very limited. This limitation seems to be overruled since the discovery of ferroelectric properties in hafnium oxide-based thin films.[40] In the last decade, the development of ferroelectric memory cells therefore rapidly increased. In principle, there are three different major concepts for ferroelectric memory which are ferroelectric tunnel junctions (FTJs), ferroelectric capacitors (mostly in 1T1C configuration) and ferroelectric field-effect transistors (FeFETs). The cell design of ferroelectric 1T1C stacks is similar to DRAM, while FeFETs, where the ferroelectric material replaces the gate dielectric is comparable to flash technology cells.[3]

MRAM

The functionality of magnetic memory or magnetoresistive random-access memory (MRAM) is based on the changeable resistance in dependence of the magnetization of magnetic materials. Since the demonstration of the tunneling magnetoresistance (TMR) effect in the 1990s, the technology has strongly advanced. The currently most-promising memory candidates using this effect are spin-transfer torque magnetic random-access memory (STT-MRAM) and spin-orbit torque magnetic random-access memory (SOT-MRAM), which are controlled by a spin-polarized current applied. Dependent on the magnetization of the layers, two different magnetoresistance states can be achieved. Due to the advanced development, short write times and high endurance, MRAM might be the most promising emerging memory candidate for the usage in application as cache. However, especially the complexity of the devices and the corresponding extensive preparation steps as well as the comparatively larger size are disadvantages of this technology.[35]

RRAM

Resistive random-access memory (RRAM or also ReRAM) covers multiple technologies that are based on a change of the electrical resistance which would in principle also cover some magnetoresistive or ferroelectric and other applications. However, the term is often used to describe oxide-based random-access memory (OxRAM), conductive-bridging random-access memory (CBRAM) and phase-change random-access memory (PCRAM, also abbreviated as PCM). PCRAM is often considered as the most-mature technology among the emerging memory types. The switching is based on the reversible transition of a chalcogenide phase-change material (e.g., a compound of the probably most-prominent and mostly-used Ge-Sb-Te-based material system like $Ge_2Sb_2Te_5$ (GST) or Ge-rich GST (GGST)) from an amorphous to a crystalline state and back. The crystalline phase has a lower resistivity than the amorphous phase. The switching process is induced by Joule heating and mostly controlled by current.[24, 34]

In contrast to PCRAM, OxRAM and CBRAM are redox-based memories. For OxRAM, an oxide dielectric material is used as the switching layer, while CBRAM can be based on different materials such as chalcogenides or also oxides. The switching is based on a process of ion migration where redox reactions occur, in which the resistivity of the device composed of the dielectric material sandwiched between two electrically conductive electrodes (called bottom and top electrode) is changed. The redox process only affects a small volume of the dielectric material. Filamentary RRAM relies on the reversible formation and rupturing of a conductive filament under the application of an external electric field/current, leading to two - for digital memory - distinctive resistance states, the high resistance state (HRS) and the low resistance state (LRS). The underlying mechanisms can be divided into “valence change mechanism”, “thermochemical memory mechanism“ and “electrochemical metallization mechanism”, leading to Valence Change Memory (VCM), Thermochemical Memory (TCM) and Electrochemical Metallization Memory (ECM), respectively. The conductive filament can be composed of an oxygen defect-rich or metal ion-rich region (VCM) or metal atoms (ECM) within the dielectric connecting both electrodes. Therefore, VCM is also called OxRAM, while ECM is also called CBRAM. To control the resistance states and overall device conductivity and to decrease sneak path currents, mostly an access transistor (1T) is used in combination with the RRAM cell (1R) in 1T1R configuration. The usage of a diode (1D) in 1D1R configuration or of a selector (1S) in 1S1R configuration is also possible.[34, 37, 41] More details, specifically addressing hafnium oxide-based ferroelectric and resistive memories as well as Ge-Sb-Te-based phase-change memories are given in chapter 2.

As an overview, a comparison of selected characteristic parameters such as the write and read time of different emerging memory types is given in Table 1-1. It should be noted that this is only a rough overview of some relevant parameters to introduce the topic.

Table 1-1: Characteristic parameters of SRAM, DRAM, Flash, FeRAM & FeFET, MRAM, PCRAM and redox-based RRAM, given as examples. Information from [4, 7, 20, 41-46]. * ferroelectric memory including perovskite- and hafnium oxide-based memories; ** DRAM in ms-range; *** redox-based resistive random-access memory, with best properties mainly from VCM; **** more potential applications are discussed in the text. F is the feature size of the technology node.

parameter/memory	SRAM	DRAM	Flash NOR\NAND	FeRAM (FeFET-based)*	MRAM	PCRAM	red.-based RRAM ***
non-volatility	no	no	yes	yes	yes	yes	yes
cell elements	6T	1T1C	1T	1T1C (1T)	1(2)T1R	1T1R or 1D1R	
cell size	$140F^2$	$6F^2$	$6F^2\backslash 4F^2$	$6F^2$	$6\text{-}30F^2$	$4F^2$	$4F^2$
read/write time	≤0.3 ns	<10 ns	$0.1\ \mu s\backslash 100\ \mu s$/ $10\ \mu s\backslash 0.1$ ms	10 ns (100 ns)	<10 ns	10-60 ns/ 50-120 ns	<10 ns – 100 ns
endurance cycles	$>10^{16}$	$>10^{16}$	10^4-10^5	10^{15} (10^5)	$>10^{16}$	10^7-10^{15}	10^6-10^{12}
retention (years)	volatile memory**		>10	>10	>10	>10	>10
energy per bit access	fJ	pJ	pJ-nJ	50 fJ (1 fJ)	2 pJ	10 pJ	10-50 pJ
application	cache	main memory	storage	storage****	storage****	storage****	storage****

The given parameters reveal that all memories have at least one outstanding property giving an advantage over other technologies. Especially the properties of the emerging memories show their suitability for new memory concepts.

As an example, oxide-based resistive memories (e.g., based on hafnium oxide - HfO_x, titanium oxide - TiO_x or tantalum oxide - TaO_x) are promising for emerging memory applications due to their complementary-metal-oxide-semiconductor (CMOS)-compatibility and possible implementation in established back-end-of-line (BEOL) and front-end-of-line (FEOL) processes as well as in 3D-arrays, their small cell sizes ($4F^2$), good scalability below 10 nm, non-volatility, low operation voltages of below 3 V, possible low write and read times below 10 ns-range and at the same time low energy consumption.[4, 37, 47, 48] Therefore, RRAM is a good candidate for application as main memory and used to replace DRAM with no limitations due to refreshing or rewriting after destructive readout. Additionally, multibit-storage is achievable and interesting synaptic-like properties observed in VCM devices can further expand the application possibilities to neuromorphics. Current drawbacks are especially the high device-to-device and intra-device variability as well as the high fabrication cost compared to established memories.

However, the presence of different emerging memory types with promising properties opens the possibility for a variety of potential applications, like the so-called storage-class memory or in-memory computing. These and other applications will now be introduced shortly:

Storage-class memory (SCM)

SCM is a memory class that can be seen as a link between main memory and secondary memory and could, therefore, replace DRAM (and flash memory) to close the memory gap. The advantages of this new class are its non-volatility, combined with fast operation and a large storage capacity, produced at low cost per bit. This can lead to a reduced latency. A lower amount of data needs to be transferred between DRAM and secondary memory, which results in fast operation that is so far limited by the comparably large access times of flash. Due to these mentioned requirements, SCM can be based on memristive devices such as RRAM, with PCRAM representing the most-mature technology at the current state.[22, 49]

In-memory or near-memory computing

Another approach to surmount the von Neumann bottleneck is the usage of in-memory computing or near-memory computing (also called in-/near-memory processing), by moving away from the von Neumann architecture and bringing memory closer to the logic. This can further have a positive impact on other computing systems, where a high bandwidth is required for a proper functionality (databases; 5G/6G and terahertz switches). In-memory computing has the advantage of a large reduction of computing time and energy. Again, resistive memories are promising candidates for such applications. On the way towards in-memory computing, near-memory computing concepts are considered being promising approaches to achieve these goals. Overall, it seems important to bring memory closer to the logic.[4, 7, 14, 50]

Embedded memory

In the last decades, especially downscaling and a reduction of the required space for electronic components has been revealed as helpful to for example improve the performance of microcontrollers. An increased number of different memory classes can be implemented on one single chip (like microprocessor and memory circuits) which can be an advantage not only for microcontrollers in general, but especially for applications that require small device sizes such as smart phones and other portable devices. So far, this is achieved with SRAM and DRAM. In this context, emerging memory can not only represent an opportunity for a non-von Neumann computing concept, but also help to create smaller and possibly simpler and easier manufacturable electronics. As an example, an embedded phase-change material-based memory was introduced for the 28 nm FD-SOI technology by STMicroelectronics. A further reduction of the dimensions as well as an increase of performance could be achieved in 3D-integration.[4, 7, 23, 41]

Universal memory

Similar considerations are valid for universal memory approaches which are considered as a solution to overcome the memory wall. A universal memory can be defined as a memory with the performance of SRAM or DRAM but with non-volatile behavior like flash and being as cheap as possible (probably comparable to NOR flash). It would be designed to execute logic operation including the main memory as well as permanent storage parts all in one. As resistive memory has been shown to successfully execute logic operations[51], it is considered as a potential candidate. Characteristics like the possibility of multibit storage are of great interest as well. Additionally, MRAM has been presented as a promising candidate to replace SRAM[25]. Overall, a commonly accepted prototypical concept is not yet introduced.

The approach to build working universal memory can also include a 3D-integration of devices, used to further shrink the memory and achieve a larger storage capacity. As conventional 3D approaches still suffer from leakage current and sneak path problems of half-selected cells, replacements of the access transistors by selectors in the array are considered. In a possible 1S1R configuration, similar device stackings based on the very same active layers (e.g., HfO_x or GST) could in principle be used, potentially simplifying the manufacturing of the very complex 3D-structures.[7, 41, 52, 53]

Neuromorphic applications and artificial intelligence

The ultimate goal of neuromorphic computing is to perfectly mimic the behavior of a human brain. Thus, human neurons and connecting synapses need to be built from electronic components and are required to communicate properly. A functioning neural network could be used to replace and exceed human brain power in performing extensive computing tasks. Currently, available electronic building blocks are used to create, train, study and improve artificial neural networks for deep and machine learning. Those are used for example for image or speech recognition.[54, 55] Additionally, an enormous effort is made in the field of autonomous driving.[56, 57] However, when compared to the human brain, speed and energy consumption of artificial neural networks are extensive. It seems to be a dream of humanity to achieve an overall perfect human-like artificial intelligence (AI) but maintaining energy efficiency along the way is a monumental task. Concepts for new hardware based on emerging memories are quite promising, especially due to the achievable analog switching as well as synaptic-like behavior observed in e.g., OxRAM[58, 59], FeRAM[60] and PCRAM[61]. This could lead to the creation of authentic artificial synapses and plasticity characteristics with the required potentiation and depression being achieved by changes of the device resistance or polarization.[6]

Radiation-resistant memory

Radiation-resistant or radiation-hard memories are important for applications in radiation-harsh environments such aerospace or nuclear power plant environments. As the mechanism of most of the established memories is based on charges, they are found to be prone to radiation-induced failures, where already single particles can induce crucial failures of electrical devices.[9, 10, 62] Emerging memories with not directly charge-dependent mechanisms, like RRAM[63] or FeRAM[64], are therefore proven to be more resistant to radiation. Hence, companies like ST Microelectronics are targeting the aerospace market with resistive memory-based circuits.[65] This topic will be further discussed in chapter 3. Specifically, induced changes of the crystallinity or crystal structure of the memory materials and the influence of different types of radiation on devices on the macroscopic but also on the atomic scale are still not fully understood and will be therefore addressed.

Additional possibilities

There are additional possibilities for further applications, like the general usage of memory for *persistent storage* (or stand-alone mass storage). This storage is an any kind of non-volatile data storage designed to permanently store data without the need of a permanent power supply or refresh. Furthermore, the mentioned possible volatility of memory devices and their often occurring high variability can be used as an advantage to improve applications like random number generation[66] for cryptography, statistical sampling, computer simulations or gambling[4], among others.

The large number of memory concepts and scenarios for potential applications, including possible solutions for the addressed limitations like the memory wall or energy consumption have revealed that current efforts on shifting computing away from von Neumann architecture towards memristor-based approaches are still gaining traction. Especially emerging memory types as presented (see also chapter 2) are very promising candidates. Other potential emerging memory classes based on organic or inorganic materials fall outside the scope of this work (examples listed in Table 1-1, like organic-based[67] or Mott-transition-based[68] memory).

Besides the single usage of emerging memory, additional interesting approaches like combining different concepts even enlarge the repertory. As an example, field-programmable gate arrays (FPGAs) can be combined with RRAM devices based on Al/N-doped AlO_x/Al[69] or Cu/polymer solid electrolyte/Ru[70]. FPGAs are integrated circuits that are configurable at the hardware level after manufacturing by utilizing a hardware description language. With this, a quite efficient computing can be obtained and a large number of circuits can be implemented application-specifically. By using FPGAs and connecting them to non-volatile memory cells, an even more efficient (space and energy saving) computing is possible.[69, 70]

The arising question of "Which memory or which concept might win the race?" is still open, while it does not seem realistic that all daily-used computers will be quickly replaced completely by any new technology. A possibly more appropriate way to describe future trends could be given in phrasing an additional question like: "Which memory is an appropriate and affordable candidate for which particular application?" Overall, the fast-developing research field reveals a great potential for a multitude of very interesting applications. The vast number of available concepts and their fitness for applications is widely discussed in literature[3, 4, 7, 14, 41, 49, 71].

1.3 Scope of the work and thesis structure

In the given context of established and potential future memory technologies and applications, it is obvious that the memory types such as OxRAM, CBRAM, FeRAM and PCRAM are subject to many different influences on their switching behavior. Currently, all emerging memories are still in their infancy and not yet fully competitive with established technologies. In order to unveil the full potential of these memories and to enable their use for different applications, a deeper understanding of the material properties and the basic physical switching processes is required.

Therefore, the first part of this work (results and discussion part - chapter 5) is designed to address several of these influences observed on specifically designed HfO_x-based resistive switching model systems. In such systems, the description of the switching characteristics is simplified/limited to a lower number of physical effects and the underlying mechanisms can be provided. These studies are focusing on the different switching mechanisms in resistive switching devices based on stoichiometric HfO_2 and the different switching types such as unipolar and bipolar resistive switching, which are dependent on the choice of the electrodes, but also influenced by the oxide layer thickness or dopants such as Zr.

In the second part of this work (results and discussion part - chapter 6), heavy ion irradiation-induced effects on material characteristics such as the crystallinity and crystal structure as well as electric properties are investigated. The objective is to better understand the high-energy heavy ion irradiation-induced phase transitions in stoichiometric and oxygen-deficient HfO_x, (doped) ferroelectric HfO_2 as well as in Ge-Sb-Te-based films. Investigations of such phase changes are scarce or yet missing. However, the phase transitions can be directly connected to changes of the electrical properties of oxide-based, ferroelectric and phase-change memories, where microstructural changes including material composition on the induced macroscopic properties are of interest. The overall study is designed to provide an improved understanding of the basic mechanisms of irradiation effects in emerging memory materials and memories. This can be useful for the development of new strategies for radiation-hard memories for applications in radiation-harsh environments.

Overall, this work is structured as follows:

Details on filamentary-based resistive and ferroelectric switching in hafnium oxide-based memory as well as the switching in chalcogenide-based phase-change memory are discussed in **chapter 2**. In **chapter 3**, radiation effects with a focus on swift heavy ion irradiation and induced phase transitions in HfO_x and GST as well as induced changes in emerging memories are introduced. Relevant methods and used growth and characterization techniques are described in **chapter 4**.

In **chapter 5**, first mixing of ZrO_2 and HfO_2 is established utilizing a reactive molecular beam epitaxy setup. Those films in combination with TiN electrodes are investigated regarding potential ferroelectric properties and additionally characterized with regards to their resistive switching properties using Pt electrodes. These stacks are also compared to stacks containing non-doped HfO_2 with Pt electrodes. An additional stud with HfO_2-containing stacks with different top electrodes (Pt versus Cu) is presented, where the influence of the electrode on the resisistive switching behaviour is described. Finally, the behavior of ECM devices containing a Cu electrode and HfO_2 switching layers of different thickness is investigated.

In **chapter 6**, heavy ion irradiation-induced changes in HfO_x films are investigated with an emphasis on induced phase transitions. Additionally, the observed phase changes are connected to electrical property changes of OxRAM (1T1R arrays – consisting of an access transistor and a HfO_2-based VCM cell). This procedure is then repeated for doped ferroelectric HfO_2-based materials and capacitor stacks (1C) as well as for GST-based PCRAM (1T1R) containing switching layers with different dopants. Both studies have an additional focus on the initial composition of the layers. The work is summarized in **chapter 7** and an outlook is provided.

2 Fundamentals on emerging memory materials and memory functionality

This work focuses on three different non-volatile emerging memories: Oxide-based resistive memories using hafnium oxide as the resistive switching layer, hafnium oxide-based ferroelectric capacitors and Ge-Sb-Te-based phase-change memories. Thus, the following chapter serves as an overview of fundamentals on the memory materials and the functionality of the corresponding emerging memories that are relevant for the understanding of the scientific results presented and discussed later in this work.

As a large part of this work concentrates on HfO_x-based resistive memory, the corresponding fundamentals are introduced in more detail, including different possible switching mechanisms and switching modes, which are both dependent on the choice of the materials used as electrodes and dielectric layers. An additional introduction is given to HfO_x-based ferroelectric memory. Furthermore, phase-change memory- as well as electrochemical metallization memory-based selector functionalities and selector applications are introduced.

Note that the expression "device" is used to describe a stack of layers consisting of a bottom electrode (BE) layer, an oxide or chalcogenide layer and at least one top electrode (TE) layer that can be contacted for electrical characterization. The notation of "$Cu/HfO_2/Pt$" refers to a Cu TE stacked on a HfO_2 layer on top of a Pt BE.

2.1 Oxide-based resistive switching memories

As described in chapter 1.2, redox-based memories rely on the migration of ions in a dielectric material and at the interface region to the electrode(s). In general, resistive switching in oxide-based memory can be divided into non-filamentary and filamentary RRAM. Non-filamentary switching is based on interfacial effects between the dielectric and the electrode(s) where accumulated charged particles lead to a changed barrier for charge carrier introduction into the dielectric, resulting in an increased conductivity (reduced resistivity). This conductivity is device area-dependent, as the whole device area takes part in the switching process. In contrast, filamentary RRAM relies on the formation and rupture of a conductive filament, connecting or not (fully) connecting both electrodes through the dielectric. It is considered a localized switching, which is independent of the device area but dependent on the area of the conductive filament region.

This work focuses on filamentary resistive switching in VCM/OxRAM and ECM/CBRAM. These memories are composed of a (high-k) dielectric material like HfO_x sandwiched between electrically conducting bottom and top electrodes in a metal-insulator-metal (MIM) structure building a capacitor. The dielectric is used as an electrically insulating layer in the pristine state, when no voltage is applied. A reversible soft dielectric breakdown can be achieved in the dielectric, therefore also called switching layer, by applying a forming voltage (electric field). In this electroforming process, a conductive filament is established in the dielectric which can result in a stable low resistance state (LRS) of the device afterwards. This state represents the "on state" or the logic "1". In a subsequent reset process when a voltage is again applied, this conductive filament can be ruptured and partially dissolved which results in the high resistance state (HRS). This state represents the "off state" or the logic "0". A filament can be re-established, reconnecting both electrodes through the conductive path in a subsequent set process which results again in the LRS of the device (compare Figure 1-3 as introduced in chapter 1 and Figure 2-1 in section 2.1.2). Set and reset are repeatable. This basic switching process leads to two distinct, stable resistance states for digital memory applications. To prevent a hard breakdown of the dielectric (leading to a permanent LRS of the device) during formation or set in real devices, a measurement system-internal current compliance (cc) or an access transistor in 1T1R configuration can be used which limits the overall flowing current.[7, 37, 47, 72] The dielectric and electrode materials used for oxide-based resistive memory and their influence on the switching will be discussed in the following in more detail.

2.1.1 Dielectrics and electrodes

A **dielectric** is an electrical insulator, therefore only very small currents can run through it. If an electric field is applied, a displacement of local charges leads to a polarization and as a result an internal electric field of the opposite direction to the applied field generated. A characteristic value herby is the dielectric displacement $\vec{D}$, which is proportional to the applied electric field $\vec{E}$ and dependent on a factor called permittivity ε (see equation (1)).

$$\vec{D} = \varepsilon\vec{E} \text{ with } \varepsilon = \varepsilon_0\varepsilon_r \qquad (1)$$

$\vec{D}$ represents the density of the electric field lines within the dielectric, while ε is a measure for how easy these lines can penetrate the material. ε is composed of the vacuum permittivity ε_0 and a material characteristic relative permittivity ε_r. ε is also called dielectric constant, traditionally abbreviated with a κ or k, which leads to the expression “high-*k* dielectric” for dielectrics with a high relative permittivity.[73, 74]

High-*k* dielectrics are used for example in capacitors or transistors. Intense investigations were performed on the common CMOS-compatible SiO_x or HfO_x, especially for the usage as improved transistor gate dielectrics to mainly reduce the oxide layer thickness.[73, 74] For resistive switching devices, specifically transition metal oxides such as HfO_x[75, 76], TiO_x[77], VO_x[78], TaO_x[79, 80], Y_2O_x[59, 81], ZrO_2[82], but also e.g., $SrTiO_x$[83] and SiO_x[84] are used. In general, resistive switching was found in a multitude of different materials, including non-oxide ceramics such as SiN_x[85], organic materials[67], and $GeSe_x$[36], serving as the switching layers. As it is relevant to this work, the usage of hafnium oxide as the dielectric layer is further described in section 2.1.5.

Typical **electrode materials** for industrial applications are titanium nitride (TiN) or for example a combination of TiN and Ti (TiN/Ti), but in principle also other conductive materials such as metals (Pt, Au, Cu, Ag, Ni, W, indium tin oxide, etc.) are usable to create MIM structures for resistive switching devices.

Titanium nitride (TiN) is a ceramic material with a high electrical conductivity (single crystal films resistivity of about 13 $\mu\Omega$cm[86]), a density of 5.22 g/cm^3 at normal conditions. It crystallizes in the cubic crystal structure (space group $Fm\bar{3}m$, a ≈ 4.24 Å, reference: International Centre for Diffraction Data (ICDD)[87] number 00-038-1420). In contrast to other nitrides, TiN is quite inert in chemical reactions. In electrical devices, TiN is found as an electrode (work function about 4.6 eV[88]) in field-effect transistors due to its CMOS-compatibility. In resistive switching devices, TiN is often described as a chemically inert electrode, however, the formation of TiO_xN_y when being in contact with an oxide was reported. Therefore, TiN can take up oxygen and function as an oxygen reservoir during switching.[89, 90]

Platinum (Pt) is a highly electrically conducting (9.7×10^6 A/Vm or S/m) cubic ($Fm\bar{3}m$, a ≈ 3,92 Å, ICDD 00-004-0802) transition metal with a density of 21.46 g/cm^3, work function of about 5.7 – 6.35 eV.[91] In resistive switching devices, Pt is usually considered as a chemically inert electrode, however, it has been shown that Pt can take up oxygen in its structure and can actively contribute to the switching process[92]. Unfortunately, Pt is not considered as a CMOS-compatible metal. This is a consequence of the noble metal character of Pt with a high resistance against most acids besides aqua regia. Therefore, common lithography routines based on wet etching processes for example with hydrofluoric acid cannot be applied for structuring.[93] The lithography problem can be solved by utilizing e.g., aqua regia for wet or a plasma-based ion beam etching process for dry etching. However, this requires a much larger effort.

Copper (Cu) and **silver (Ag)** represent two additional electrode materials with interesting properties for resistive switching. They are both transition metals with a density of 8.92 g/cm^3 and 10.49 g/cm^3, crystallizing in the cubic structure ($Fm\bar{3}m$; a ≈ 3.62 Å, ICDD 00-004-0836 and a ≈ 4.09 Å, ICDD 00-004-0783, respectively). The work functions of Cu and Ag are about 4.44 eV and 4.3 eV, respectively. Due to their high electrical conductivities (about 58×10^6 S/m and 62×10^6 S/m), they can be used as electrical contacts, wires and electrodes. The huge interest for resistive memory applications stems from the switching properties of devices due to the high mobility of Cu and Ag ions, which not only allows the metallic conductive filament formation in liquids, but also in solids (oxides).[37, 94-96]

2.1.2 Switching mechanisms (VCM, TCM, ECM)

As mentioned in chapter 1.2, switching in **Valence Change Memory (VCM)**, **Thermochemical Memory (TCM)** and **Electrochemical Metallization Memory (ECM)** can be based on different mechanisms, which is determined by the dominating physicochemical process occurring. This is dependent on the device stacking and hence on the choice of the electrode. As visualized in Figure 2-1, all three mechanisms can be found in HfO_x-based memory.

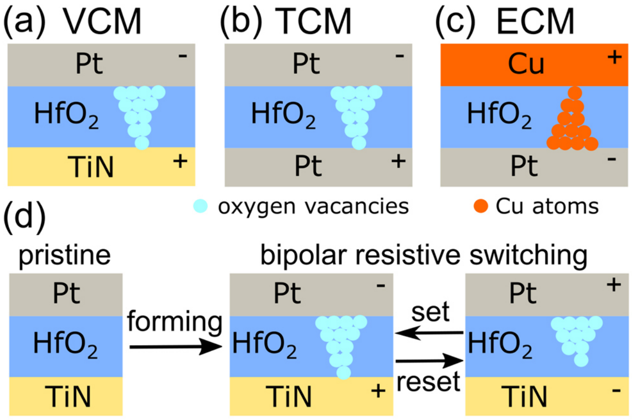

Figure 2-1: Schematic representation of device stackings with an oxygen vacancy filament (bright blue) and a Cu filament (orange) and related changes during forming, reset and subsequent set on the example of bipolar resistive switching in a VCM $Pt/HfO_2/TiN$ device. (a) A $Pt/HfO_2/TiN$ stack with oxygen vacancy filament formed when a negative voltage is applied to the top electrode. This process is dominated by a valence change mechanism (for bipolar resistive switching), thus called VCM. (b) A $Pt/HfO_2/Pt$ stack, where oxygen vacancy filament formation and rupturing is dominated by a thermochemical mechanism, thus called TCM. (c) A Cu conductive filament in a $Cu/HfO_2/Pt$ ECM device. The process is dominated by an electrochemical mechanism. (d) Starting from a pristine state of the insulating HfO_2 layer, a forming step is required where an oxygen vacancy filament is stabilized in VCM. This filament can be ruptured in a reset process and (re-)stabilized in a subsequent set. In real devices, the filament in 3D is considered to have a diameter in the tenth of nanometer-range.[77]

In **Valence Change Memory (VCM)**, the occurring mechanism is called Valence Change Mechanism. It relies on the change of the valence state in the cation sublattice of parts of the switching layer in a redox reaction. The conductive filament is often described to consist of (agglomerated) oxygen vacancies (see Figure 2-1 (a)). It can be therefore also described as a metal-rich conductive region or path (remaining metal ions on regular lattice sites) connecting both electrodes in the LRS. As visualized in Figure 2-1 (d), the set process relies on the oxidation of the metal oxide, in which oxygen ions (the anionic species of the layer) are leaving the arising conductive filament region. In the reset process, resulting in the HRS, a partial reoxidation takes place where oxygen ions partially refill oxygen vacancies. The electrodes used for VCM are often TiN or a combination of Ti and TiN (for one of the electrodes) but also a chemically inert electrode with a high work function as for example Pt combined with a less inert counter electrode with a lower work function such as TiN can be used. Oxygen ions can be incorporated into the structure of the TiN electrode during forming and set process, functioning as an oxygen reservoir for the subsequent reset process[97]. The rupturing of the conductive filament is therefore believed to take place in close vicinity of the electrode interface. The overall mechanism in VCM is dominated by the electric field, which is also causing the movement of the oxygen ions in the dielectric.[5, 36, 37, 98]

For more inert electrodes such as Pt used for both electrodes (see Figure 2-1 (b)), the overall switching is dominated by thermal processes as large Joule heat occurs in the dielectric when a current is passing through a localized region of the dielectric switching layer. This results in a mechanism triggered by strong Soret forces (ionic movement along a temperature gradient) and/or Fick diffusion (movement along a concentration gradient). These memories are called **Thermochemical Memory (TCM)**. The mechanism is called Thermochemical Mechanism. It is believed that the rupturing of the conductive oxygen vacancy filament in TCM occurs less likely directly at the interface between the dielectric and an electrode, but is more likely located closer to the center of the filament. However, as usually a mixture of different processes and underlying forces is likely, a very complex overall mechanism can occur. The true nature of the filament is still subject to further investigations.[99]

In **Electrochemical Metallization Memory (ECM)**, metal ions like Cu or Ag are moving through the dielectric (see Figure 2-1 (c)), forming a metal conductive filament. Electrical devices are also named programmable metallization cells (PMC). Devices usually consist of a so-called active electrode (e.g. Cu or Ag) and an inert electrode (e.g., Pt, W or Pd), however, the usage of two active electrodes is also possible. The underlying mechanism is called Electrochemical Metallization Mechanism. In the switching process, electrode material of the active electrode is ionized (oxidation). Driven by the electric field, the mobile Ag or Cu ions (cations) move towards the counter electrode (ohmic electrode), where a Cu or Ag conductive filament is formed and growing towards the active electrode (reduction/nucleation of a metal filament). If both electrodes are connected by the metal conductive filament building a conductive bridge, the device is in the LRS. A full or partial dissolution (rupturing) of the filament is achieved by applying a reversed bias, which leads to the HRS. [37, 100-103] This reset can be based on a mixture of electric field and heat influences, often being reported to be dominated by Joule heat.[100, 104, 105] Interestingly, a mixed filament also called hybrid filament composed of oxygen vacancies and metal atoms can be found in memristive devices[106]. This could be favored by the use of a less inert electrode than Pt, such as TiN.

2.1.3 Switching modes (URS, BRS, CRS, TRS)

Several different switching modes can be differentiated in resistive switching devices, typically named **unipolar resistive switching (URS)**, **bipolar resistive switching (BRS)**, **complementary resistive switching (CRS)** and **threshold resistive switching (TRS)**. Dependent on the set and reset polarity in BRS, figure-eightwise (f8) and counter figure-eightwise (cf8) switching can be distinguished.[75, 107] Schematic representations of these switching modes are shown in Figure 2-2. A mixture of cf8 and f8 in BRS is also achievable e.g., in oxygen-deficient hafnium oxide[75] (not shown). In contrast to these schematics, the I-V curves presented in the results and discussion part of this work are always plotted using the absolute value of the current to ensure a better overview.

In **URS** (Figure 2-2 (a)), forming/set and reset can be induced by the same bias voltage polarity, which is mostly the case in devices with two inert electrodes and a symmetric stacking using the same bottom and electrode material (e.g., Pt). If the switching is the same in both polarities, it is called non-polar switching. For **BRS** (b) & (c), set and reset are induced by the opposite bias voltage polarity. For the different polarities, this leads to c8 and cf8 BRS, respectively. Both modes are dominated by the applied electric field, which is mostly the case in VCM and ECM devices. For **CRS** (d), the reset occurs in the same polarity as the preceding set, but in contrast to URS in only one voltage sweep (by further increasing the voltage). CRS can be for example achieved by creating a series connection of oppositely oriented c8 and cf8 BRS devices, as demonstrated using VCM devices.[108, 109]

In contrast to the behavior of BRS and CRS, the switching in devices showing URS and **TRS** (e) is dominated by temperature and can therefore be obtained in TCM.[37, 110, 111] Similar to CRS, the LRS in TRS is not stable without an applied electric field. Here, the actual reset to the HRS occurs when lowering the voltage after the device was set to the LRS. As a consequence, devices showing these two modes cannot be used as non-volatile memory, but instead as switches/selectors. Interestingly, TCM can be also found in typical ECM devices.[112, 113]

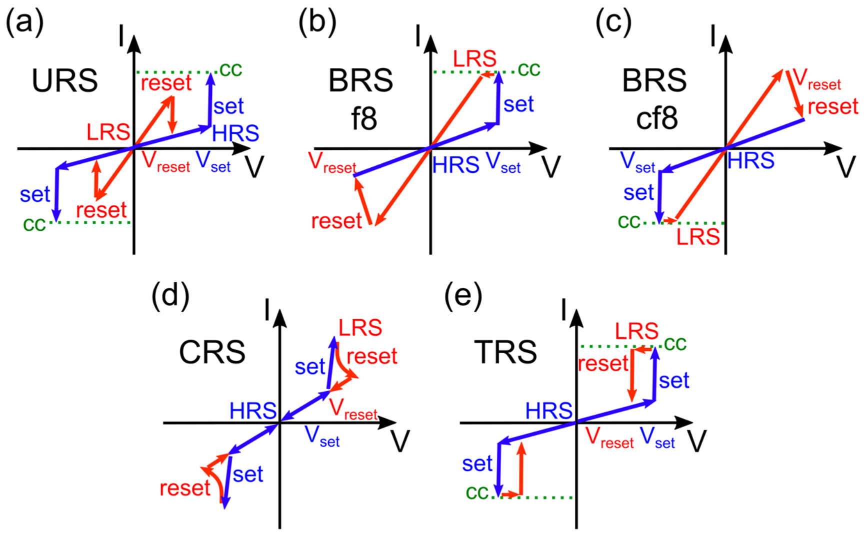

Figure 2-2: Schematic representation of current-voltage (I-V) curves for (a) unipolar resistive switching – URS, (b) f8-bipolar resistive switching (BRS f8), (c) cf8-bipolar resistive switching (BRS cf8), (d) complementary resistive switching (CRS) and (e) threshold resistive switching (TRS). The set starting from the HRS is given in blue, while the reset starting from the LRS is given in red. cc marks the current compliance. Drawn with information from[75, 107].

The exact behavior depends on the choice of the electrodes with a tendency towards the usage of one active and one inert electrode (ECM) or of two inert electrodes (TCM). Additional information on threshold switching in memristive devices is given in chapter 2.4. It should be noted, that this description represents a simplification and model description. In real devices, mixtures of different modes are likely. As an example, all switching modes were found in Pt/HfO_x/TiN devices[75], which could be directly connected to the oxygen content of the switching layer and voltage polarity used for switching.

2.1.4 Conduction mechanisms

In oxide-based RRAM, different conduction mechanisms can be found on which the electron transport and resulting measurable current is based. One group of mechanisms is dependent on the phenomena occurring at the interface between the electrode(s) and the dielectric (electrode-limited conduction mechanisms) like the interface potential barrier height, while another group relies on the properties of the dielectric material (bulk-limited conduction mechanisms) like the carrier drift mobility, trap level/trap spacing/trap density as well as the density of states. Electrode-limited conduction mechanisms include (1) Schottky emission, (2) Fowler-Nordheim tunneling and (3) direct tunneling, while bulk-limited conduction mechanisms can be divided into (a) Poole-Frenkel emission; (b) ohmic conduction; (c) space-charge-limited conduction (SCLC); (d) ionic conduction; (e) hopping conduction and (f) trap-assisted tunneling (TAT). A short description is given in the following. Further details on conduction mechanisms of VCM are summarized in a review paper by E. W. Lim and R. Ismail[114]. This publication also includes the relevant expressions of the current density as well as the field- and temperature-dependencies in mathematical formulae.

(1) Schottky emission: Schottky emission occurs when electrons can pass over the energy barrier into the conduction band of the oxide dielectric. It is therefore dependent on the barrier height. Schottky emission can be found e.g., in Pt/Y_2O_3/TiN devices.[115]

(2) Fowler-Nordheim tunneling and (3) direct tunneling: These effects describe tunneling through the dielectric layer. Fowler-Nordheim tunneling is more likely in thicker films, while direct tunneling is found in thinner films with a thickness below 3 nm.

(a) Poole-Frenkel emission: Trapped electrons can be thermally excited into the conduction band when the Coulomb potential barrier is lowered by the influence of the applied electric field. Poole-Frenkel emission can be found e.g., in HfO_2 films in a Pt/HfO_2/TiN stack configuration.[116]

(b) Ohmic conduction: A small number of mobile electrons can be thermally excited in large band gap oxides. The corresponding current density J_{Ohmic} is proportional to the applied electric field E, which can be described using equation (2).

$$J_{ohmic} = \sigma E = q\mu N_c \, \mathrm{E} * \exp\left[\frac{-(E_c - E_F)}{k_B T}\right] \qquad (2)$$

with the electrical conductivity σ, the electron mobility μ, the effective density of states of the conduction band N_C, the conduction band (minimum) energy level E_C and the Fermi energy level E_F. T represents the temperature, while k_B is the Boltzmann constant. Ohmic conduction is represented by a linear behavior with typically a slope close to 1 in a log(current) versus log(voltage) plot. It is often found for processes occurring at an oxide/Pt-interface like in Pt/TiO_2/Pt devices for both the HRS and LRS[117] and in Pt/Y_2O_3/TiN devices in the LRS[115].

(c) *Space-charge-limited-conduction (SCLC)*: SCLC is characterized by an injection of electrons from the cathode into the oxide layer. A space-charge is created which is limiting the current flow in the dielectric by an occurring recombination of injected electrons and ions of the dielectric. SCLC can consist of different parts: an ohmic-like part at low electric field ($J_{ohmic} \propto E$), a power-law dependent part at higher fields ($J_{SCLC} \propto E^m$), and a subsequent steep increase (current jump). Dependent on the filling of the trap states, the conduction occurring can be either trap-free/trap-unfilled SCLC or trap-filled SCLC ($J_{SCLC} \propto E^m$ with $m = 2$). $J_{SCLC} \propto E^m$ with $m > 2$ represents the trap-filled limit, which is reached at a certain electric field. The occurrence of the individual parts depends on the traps in the insulating dielectric. Conduction in an insulator without traps only relies on the ohmic-like and the trap-free SCLC part. In contrast, charges are filling the trap states in dielectric with traps until a limit is reached. SCLC can be found in different ECM device stackings with inert and active electrodes, like Cu/HfO_2/Pt[118] and Ag/$La_{0.5}Sr_{0.5}CoO_3$/Pt[119] in both the HRS and LRS.

(d) *Ionic conduction*: The movement of ions through a solid driven by the electric field leads to an ionic current.

(e) *Hopping conduction*: Hopping conduction includes nearest neighbor hopping and variable-range hopping of charge-carriers via trap sites.

(f) *Trap-assisted tunneling*: Trap-assisted tunneling (TAT) is a multistep tunneling process, requiring traps relying on defects in an oxide layer, where electrons are located. This mechanism is also found in Pt/HfO_x/TiN devices[120].

In ECM devices based on oxides, similar mechanisms as described for VCM are present. Cu/HfO_2/Pt devices often rely on trap-limited and trap-assisted SCLC, hopping conduction as well as ohmic conduction. The probability for SCLC seems to be increased for electrodes that are highly charge carrier injective.[114, 115, 118, 121, 122]

2.1.5 Hafnium oxide and parameters influencing resistive switching in HfO_x-based devices

In this section, hafnium oxide (HfO_x) is introduced as it is a very promising material for the usage as a resistive switching layer. Resistive switching relies on the electrical properties of the HfO_x layer, which is dependent on its crystal structure and degree of crystallinity. Additionally, other parameters have a direct impact on the switching behavior of HfO_x-based memory devices. Unfortunately, these parameters are interconnected and affecting each other. The most important ones for switching in VCM, TCM and ECM are described in the following and exemplary correlations are discussed.

Crystal structures of HfO_x: Hafnium oxide (HfO_x), also called hafnia, is an insulating dielectric ceramic and a transition metal oxide (TMO) with a melting point of about 2760 °C. At normal conditions, stoichiometric hafnium oxide (HfO_2) is a microcrystalline powder present in the energetically most-favorable monoclinic phase (*m*-HfO_2, space group $P2_1/c$; $a \approx 5.12$ Å; $b \approx 5.17$ Å; $c \approx 5.29$ Å, $\alpha=\gamma=90°$, $\beta \approx 99.25°$) [123, 124]. The density is 9.68 g/cm² [125]. Its bandgap (5.5 – 6.0 eV) and permittivity (16 – 25) made thin film HfO_2 highly interesting for high-*k* dielectric applications and for resistive switching memories.

With increasing temperature, stoichiometric HfO_2 was found to be polymorphous appearing in different crystalline structures such as the high-temperature tetragonal (t-HfO_2, space group $P4_2/nmc$; $a=b\approx 3.58$ Å, $c\approx 5.20$ Å, $\alpha=\beta=\gamma=90°$)[126] or cubic (c-HfO_2, space group $Fm\bar{3}m$; $a=b=c\approx$ 5.06 Å, $\alpha=\beta=\gamma=90°$)[126] phase. Additionally, high-pressure orthorhombic phases (o-HfO_2, oI and oII - space groups *Pbca* and *Pnma*, respectively) are known in powders. These are non-polar phases. However, the observation of ferroelectric properties in hafnium oxide thin films[40] lead to the finding of a polar orthorhombic phase (o-HfO_2, oIII - $Pca2_1$). Recently, additional rhombohedral phases were found in ferroelectric doped hafnium oxide films ($R3$ or $R3m$)[127] and in highly oxygen-deficient undoped HfO_x films ($R3m$)[128]. Representative unit cells of exemplary crystal structures are schematically shown in Figure 2-3. Parameters of the most discussed structures in this work are listed in Table 2-1.

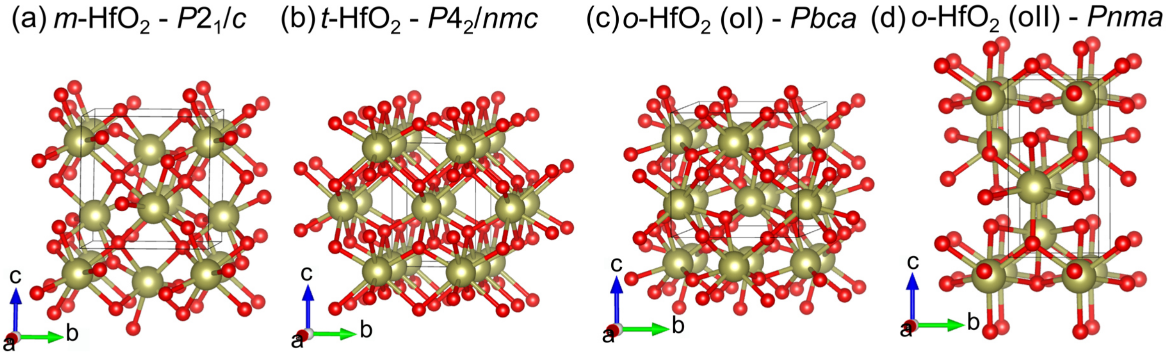
(a) m-HfO_2 - $P2_1/c$ (b) t-HfO_2 - $P4_2/nmc$ (c) o-HfO_2 (oI) - *Pbca* (d) o-HfO_2 (oII) - *Pnma*

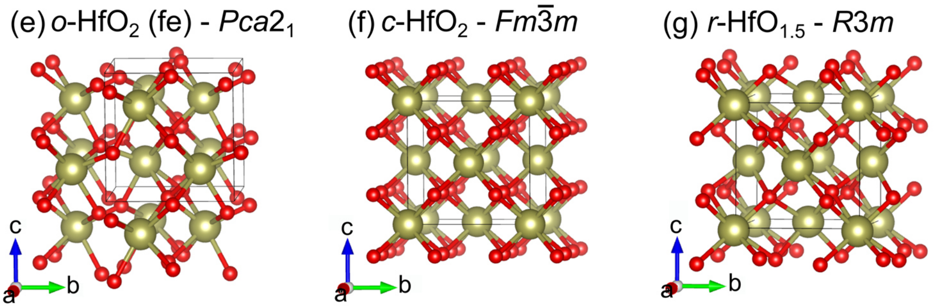
(e) o-HfO_2 (fe) - $Pca2_1$ (f) c-HfO_2 - $Fm\bar{3}m$ (g) r-$HfO_{1.5}$ - $R3m$

Figure 2-3: Exemplary crystal structures of the polymorphous hafnium oxide with Hf ions in gold (larger) and O ions in red (smaller). (a) monoclinic HfO_2, space group $P2_1/c$, (b) tetragonal HfO_2 – $P4_2/nmc$, (c) orthorhombic HfO_2 – *Pbca*, (d) orthorhombic HfO_2 – *Pnma*, (e) orthorhombic HfO_2 – $Pca2_1$ (ferroelectric, mostly doped HfO_2), (f) cubic HfO_2 $Fm\bar{3}m$, (g) oxygen-deficient rhombohedral $HfO_{1.5}$ – $R3m$. Created using VESTA[129], with information from ICDD PDFs ($P2_1/c$, $P4_2/nmc$, *Pbca*, *Pnma*, *Fm*-3*m*) and density functional theory (DFT) calculations ($Pca2_1$[130, 131], $R3m$[128]).

These structures are all closely related to each other (group/subgroup relationship). All structures can be derived from the fluorite-type structure of the cubic HfO_2 with space group $Fm\bar{3}m$. Their lattice parameters are also very similar. However, a small change of the lattice already leads to different properties like dielectric properties of the non-polar cubic phase ($Fm\bar{3}m$) or electrically conducting films of r-$HfO_{1.5}$ ($R3m$) or ferroelectric behavior in the polar ($Pca2_1$) phase. Additionally, small changes of the lattice parameters for the same space group are possible. The distinction of these phases using X-ray diffraction will be discussed in chapter 4.5.1. More details on the ferroelectric phase and related properties are given in chapter 2.2. It becomes evident that the crystal structure of the polymorphous HfO_x plays an important role for the properties of hafnium oxide-based applications.[74] Additionally, several other parameters have a direct impact on the switching behavior of HfO_x-based memory devices, which is discussed in the following.

Table 2-1: Space group and lattice parameters of relevant structures. Information from Powder Diffraction Files (PDF) from the International Center for Diffraction Data (ICDD) database ($P2_1/c$, $P4_2/nmc$, $Pbca$, $Pnma$, $Fm\bar{3}m$) and density functional theory (DFT) calculations ($Pca2_1$ [130, 131], R3m (r-$HfO_{1.5}$)[128]). Additionally, experimental (exp.) values for r-$HfO_{1.7}$ are given. [128]

structure	space group	lattice parameters
m-HfO_2	$P2_1/c$ (monoclinic)	a ≈ 5.12 Å; b ≈ 5.17 Å; c ≈ 5.29 Å; α = γ = 90°, β ≈ 99.25°
t-HfO_2	$P4_2/nmc$ (tetragonal)	a = b ≈ 3.58 Å, c ≈ 5.20 Å; α = β = γ = 90°
o-HfO_2 (oI)	$Pbca$ (orthorhombic)	a ≈ 10.02 Å; b ≈ 5.23 Å; c ≈ 5.06 Å; α = β = γ = 90°
o-HfO_2 (oII)	$Pnma$ (orthorhombic)	a ≈ 5.55 Å; b ≈ 3.30 Å; c ≈ 6.48 Å; α = β = γ = 90°
o-HfO_2 (fe - oIII)	$Pca2_1$ (orthorhombic)	a ≈ 5.27 Å; b ≈ 5.05 Å; c ≈ 5.08 Å; α = β = γ = 90°
c-HfO_2	$Fm\bar{3}m$ (cubic)	a = b = c ≈ 5.06 Å; α = β = γ = 90°
r-$HfO_{1.5}$ (DFT) r-$HfO_{1.7}$ (exp.)	$R3m$ (rhombohedral)	a = b = c ≈ 4.97 Å; α = β = γ ≈ 89.37° a = b = c ≈ 5.03 Å; α = β = γ ≈ 89.56°

Next to the crystal structure, also the degree of crystallinity of the dielectric material itself has a direct influence on the resistive switching properties of RRAM devices. HfO_2 thin film growth at BEOL-compatible temperatures e.g., at 300 °C leads to the formation of the thermodynamically stable monoclinic phase, while room temperature growth or slightly increased temperature (up to about 200 °C) leads to amorphous or poorly crystalline layers. Those are preferred for application of HfO_2 as a gate dielectric due to the simple preparation and a low thermal budget for CMOS-processing, resulting in a high uniformity and surface smoothness of the layer. However, for resistive switching, devices based on amorphous HfO_2 require a forming step with large forming voltages, which stresses the device. This can possibly result in unwanted hard breakdowns, in an uncontrollable redistribution of ions or even in a localized crystallization of the dielectric. The process is often subject to a large variability. This is undesired for a well-controllable device programming. An alternative is to use monoclinic HfO_2 films, however in highly stoichiometric switching layers another disadvantage is seen in the abrupt switching characteristics (large current jumps) occurring during resistive switching.

Influencing the switching in HfO_x-containing VCM:

A lowering of the forming voltage in HfO_x-based devices might be achieved in three different ways: (1) a reduction of the oxide layer thickness, (2) the usage of oxygen scavenging layers or (3) by defect engineering to reduce the breakdown strength. This can also result in lower variabilities and consequently a better control of the switching behavior of the memory devices.

(1) A reduction of the switching layer thickness leads to a reduction of the forming voltage, as the critical electric field required for a successful electroforming is in thinner films already achieved at lower voltages.[132]

(2) Scavenging layers with a high oxygen affinity (e.g., Ti between HfO_2 and TiN) introduce oxygen vacancies in the oxide layer, thus leading to a slightly oxygen-deficient HfO_x film. At the interface between the scavenging and the oxide layer, an oxygen reservoir is created, leading to a reduced breakdown strength in the switching process. Unfortunately, the precise control of the overall stoichiometry or the location of the conductive filament remains challenging. Interfaces can play an important role, as an increased electrode roughness can support the dielectric breakdown due to locally increased electric fields and local heat. Conductive filaments likely form in regions of increased interface roughness or oxygen defect agglomeration.[100, 133]

(3) Defect engineering can be achieved in different ways such as (a) by grain boundary engineering, (b) by oxygen-engineering or (c) by impurity doping of the switching layer.

    (a) Intentional grain boundary engineering can allow the achievement of forming-free switching, where forming and set voltages are in the same range. Instead of an amorphous HfO_2 film acting as the switching layer, the usage of the stable monoclinic HfO_2 phase is possible, which can be obtained by increasing the growth temperature or including a post-deposition annealing step for a layer crystallization. For high-*k* dielectrics, grain boundaries were identified as leakage paths, where electrical breakdowns are likely to occur.[73, 134-136] However, in a polycrystalline structure of the resistive switching layer with grain boundaries connecting both electrodes through the dielectric, the conductive filament can potentially be formed along such grain boundaries, which act as preferential sites for oxygen defect agglomeration.[76, 137]

    (b) The usage of uniform substoichiometric/oxygen-deficient switching layers is possible, as for stable switching in VCM devices oxygen vacancies and oxygen ion diffusion are necessary. This concept requires a precise control of the oxygen content. One approach is the direct growth of homogeneous substoichiometric switching layers, which can be achieved for example by using electron-beam evaporation of Hf and a precise oxidation utilizing an oxygen plasma in a reactive molecular beam epitaxy (MBE) deposition system.[75, 132, 138, 139] Another approach is based on the usage ion bombardment, where oxygen vacancies are created in the oxide layer.[140] A potentially defect-based impact was even reported for HfO_x-based devices exposed to high-energy heavy ions.[141]

    The usage of oxygen-deficient switching layers can lead to a reduced intra- and device-to-device variability, mainly due to the reduction of the forming and operation voltages, down to almost completely forming-free devices[80, 138]. On a local scale, this property is a consequence of the eliminated necessity of creating new oxygen vacancies in a forming step but rather just redistributing already existing oxygen ions/vacancies. In principle, also a material such as Y_2O_3 with an intrinsically oxygen defect-rich structure[59, 81, 115] can be considered as a good alternative to HfO_x. A defect-engineering of these point defects can be used to create oxygen-deficient devices that show a gradual switching behavior and an enhanced accessibility of quantized conductance states (quantum conductance unit $G_0 = 2e^2/h \approx 12.9\ \text{k}\Omega^{-1}$, with e being the elementary charge and h the Planck constant).[59]

Furthermore, the oxygen content of the layer is directly linked to the crystal structures observed, which has an impact on the electrical properties of the layers and resistive switching behavior of devices. During the search for the conductive filament in hafnium oxide, already several possible phases were proposed, including an amorphous phase and crystalline suboxide phases like Hf_2O_3, Hf_6O and metallic Hf.[142-144] Recently, it was shown that the precise control of the oxygen content of HfO_x films in a broad range can be utilized to achieve rhombohedral hafnium oxide[128] (as shown in Figure 2-3 and Table 2-1) with p-type semiconducting properties.[145] This phase ($R3m$) can be seen as a slightly distorted cubic phase, where four oxygen ions are missing in the unit cell (for $HfO_{1.5}$). Therefore, this phase was first assigned to be a low-temperature cubic hafnium oxide phase (LTP c-HfO_x) with a rhombohedral distortion[145] (space group: distorted $Fm\overline{3}m$ close to the structure given in ICDD 04-011-9018). This substoichiometric phase was grown at room temperature by decreasing the oxidation conditions during growth (when compared to the growth of stoichiometric HfO_2 films), thus stabilizing an oxygen vacancy-stabilized structure. A further decrease of the oxygen content in the HfO_x layer lead to a stabilization of an oxygen-rich hexagonal phase (hcp-$HfO_{0.7}$, hexagonal close packed). Both phases are of interest as potential candidates for the conductive filament in VCM. With decreasing oxygen content, the insulating HfO_x becomes electrically more conductive, which is a result of a modified electronic structure. This was already indicated in a previous work, where the surface oxidation (creation of a passivation layer) of substoichiometric hafnium oxide was found and related to the switching properties.[132] These reports show that changes of the oxygen content and resulting structural changes can potentially lead to drastic property changes of the films.

(c) Layer doping was intensively studied to improve high-k dielectric materials[3, 73], but is also important for quite easily engineering the properties of resistive switching layers. This is a consequence of an increased number of oxygen vacancies introduced into the layers for charge neutralization. A few examples for a modification of the switching properties by doping in HfO_x-based devices can be given: For Gd-doped HfO_2, improved uniformity of the resistance states and on/off ratio was found, which was attributed to a suppressed randomness of the conductive filament formation and a reduced oxygen ion migration barrier achieved.[146] Mixing of HfO_2 with ZrO_2 to achieve $Hf_{0.5}Zr_{0.5}O_2$-based RRAM devices, resulted in stable BRS and URS. Doping HfO_2 with 9 at% of Zr additionally lead to an increase of the on/off ratio, lower operation voltages required and overall in a more uniform switching behavior when compared to pure HfO_2-based devices.[147-150]

Doping is also directly linked to the crystal structure of the oxide layers, where e.g., a cubic and a tetragonal phase of HfO_x can be stabilized by La- and Ta- doping, respectively.[151, 152] Additionally, doping of the hafnium oxide layers with various elements (such as Zr, Si, Y, La) supports the creation of the already mentioned polar (ferroelectric) orthorhombic[40] or also a ferroelectric rhombohedral phase ($Hf_{0.5}Zr_{0.5}O_2$)[127], but with a special preparation required (see next chapter 2.2).

Influencing the switching in HfO_x-containing TCM: For TCM, the same parameters discussed for VCM are relevant (oxide layer thickness, oxygen scavenging layers and defect engineering). Additionally, the already mentioned electrode choice plays a role. The usage of Pt top and bottom electrode as inert electrodes strongly promotes the formation and rupturing of an oxygen vacancy filament dominated by thermal effects. In literature, stable BRS and URS was found e.g., in Pt/HfO_2/Pt devices with similar operation voltages regardless of the voltage polarity. The switching is therefore called non-polar switching. On one hand, the switching in HfO_x-based TCM devices is described as being fast (e.g., < 10 ns) with a high off/on ratio (e.g., > 10^6), but on the other hand characterized by a low endurance and high non-uniformity. This is seen by a high device-to-device but especially a high (intra-device) cycle-to-cycle variability. [99, 110, 111, 153-156] Overall, different mechanisms for filament formation and rupturing at Pt/oxide interfaces or in the center of the oxide layer are discussed, leading to quite complex and sometimes contradicting situations obtained for URS versus BRS in one and the same device (configuration). For BRS, a mixture of valence change and thermochemical mechanism can be present. A better control of the switching process(es), like discussed for VCM is also relevant for TCM.

So far, TCM are less reliable as “good” RRAM devices when compared to VCM. A “good“ RRAM device is considered having a low variability, showing low operation voltages and a forming-free behavior. At the same time, a sufficiently high memory window (LRS to HRS resistance ratio), a high endurance (number of I-V cycles where this memory window is maintained and two distinctive memory states are readable) and a large data retention (long-term storage capability) should be achieved. Large leakage currents or in other words unwanted current flows should be avoided. [99]

Influencing the switching in HfO_x-containing ECM: Similar considerations are also valid for hafnium oxide-based ECM with some additional important parameters that need to be considered. First, the conductive filament formation and its dissolution are dependent on the cation movement (ion transport dependent on cation mobility) and redox processes involved, which can be the rate-limiting processes. Additionally, a nucleation step is necessary for the formation of the conductive filament. Overall, nucleation and growth seem to be directly dependent on the cation mobility, while the filament shape and cation supply rely on the redox process rates. The formation of metal cations on defect formation energies, which are reported to be dependent on the oxide material used as a switching layer and on its crystal structure[157]. In orthorhombic HfO_2 for example, a slightly reduced defect formation energy of Ag interstitials is expected theoretically.

For the migration of metal cations, a high ionic conductivity of the dielectric serving as an electrolyte is required. This is a prerequisite for functional ECM, otherwise more likely being a TCM or VCM. Thus, attempts using different chalcogenide materials have been reported in the past (e.g., in Ag/$GeSe_x$/W[36]). However, ECM can be achieved with the very same CMOS-compatible dielectric materials used for VCM such as SiO_x[102] and HfO_x[100]. In different devices with a Ag or Cu electrode such as Ag/HfO_2/Pt and Cu/HfO_2/Pt or also Cu/Ta_2O_5/Pt, switching characteristics as well as important redox reactions are discussed. For ECM devices with a Cu top electrode, stable BRS with positive forming/set and negative reset was found.[96, 103-105, 158-161] Different switching properties further depend on the thickness of the individual layers. For

$Cu/HfO_2/Pt$ devices with varied oxide layer thicknesses, increased forming voltages with increasing HfO_2 film thickness were found[100, 162], which is similar to VCM. However, in contrast to VCM devices, ECM devices are usually characterized by showing lower operation voltages. This can lead to a lower overall power consumption of devices, which is a promising characteristic for real applications as memory. Unfortunately, ECM is often showing a high nonlinearity of the switching, or in other words large current jumps in the set and reset and a high on/off ratio. This can result in a lower endurance when compared to VCM due to the increased stress inflicted to the devices (causing additional heat, etc.).

An improved ionic conductivity or supporting effects can be obtained by additional doping of the electrolyte material, which is often done by introducing the same mobile metal ions used for the already existing active electrode. With this, the ion path length through the solid oxide for each ion might be reduced and additionally created point-defects can support the required ionic conductivity of the dielectric.[74, 157, 163-165] This can support the formation of controlled conduction paths in the dielectric and can further lead to an improvement or a modification of the switching performance, including multilevel resistive switching. Also, the relevant effect of moisture on the switching behavior is described in literature.[166] Combinations and interactions with the described oxygen vacancies as well as grain boundaries are also likely. Additionally, a formation of hybrid filaments is possible, as mentioned earlier in this chapter.[106]

As an additional and very interesting property of ECM devices, threshold resistive switching (compare section 2.1.3) can be obtained, which opens the possibility for applications as selectors. Selectors are switches that are conducting (open) if an applied voltage exceeds a threshold voltage, but insulating (closed) if no voltage is applied.[112, 113, 167, 168] In this case, a high nonlinearity of the switching obtained in ECM, which is accompanied by a highly conducting LRS, is an advantage. In the LRS, a highly-conducting device is obtained, while the HRS is as least conductive as possible. The presence of TRS in ECM devices shows that the dominating mechanism is not only dependent on the choice of the electrodes but also on the voltage polarity and additional factors (e.g. heat). Thermal effects can be also dominating the switching process in ECM stacks in URS mode, which makes them a TCM. The TCM can thus be both cation- and anion-based. More details on threshold switching in memristive devices are provided in chapter 2.4.

The given examples reveal the complex nature of HfO_x and the multitude of influencing parameters relevant for different oxide-based resistive memories. The nature of many of these influences is not yet fully understood. This opens the possibility for further fundamental studies.

2.2 Hafnium oxide-based ferroelectric memory

Ferroelectricity was discovered in the 1920’s in Rochelle salts.[169] Until now, many more ferroelectric materials have been found. A prerequisite for ferroelectricity is the presence of a non-centrosymmetric crystal structure (polar space group) and non-metallic bonding (electrically insulating material), leading to the formation of a polar axis. Therefore, ferroelectrics possess at least two (meta)stable states of different spontaneous polarization, switchable by applying an electric field. This polarization is a temperature-dependent non-zero stable dipole in zero applied electric field, which occurs when negative and positive charge centers within a unit-cell, i.e. position of ions, are not located at the same position (see Figure

2-4 (a)). In general, all ferroelectrics are pyroelectrics (coupling of polarization with temperature), all pyroelectrics are piezoelectrics (coupling of electric polarization and deformation) and all piezoelectrics are dielectrics. Two of the most prominent ferroelectric materials are barium titanate (BTO) and lead zirconate titanate (PZT), both based on the perovskite structure (Figure 2-4 (a)), which are used in multiple applications such as piezoelectric Micro-Electro-Mechanical Systems (MEMS), ferroelectric field-effect transistors (FeFETs), actuators, sensors and to some extent as non-volatile memories in the last four decades.[170] Unfortunately, CMOS-compatibility and further downscaling far below 100 nm without huge effort are limited for recent microelectronic processes.

Especially for the field of microelectronics and non-volatile memory applications, the discovery of unexpected ferroelectricity in doped hafnium oxide, as reported in 2011 by Boeske *et al.*[40] was an important change for the ferroelectric community. Hafnium oxide-based layers were already established in high-*k*-metal-gate CMOS processes and therefore proven to be CMOS compatible without the downscaling limitation for nm-thin films. Since then, research efforts in this field keep rapidly increasing with thousands of scientific publications and patents submitted in the last decade. A brief history of the discovery of ferroelectric hafnium oxide can be found in literature[3]. Switching of the electric polarization by an applied field is exemplarily visualized in Figure 2-4 (b). When the saturation polarization P_S is reached and the field is reduced to zero, a remanent polarization P_r is maintained. A reversal of the field can also reverse the polarization direction. This is a key feature for memory applications, where information is stored in the two distinct polarization states. When the opposite coercive field E_C is reached, the obtained absolute polarization is zero. The observed behavior is a result of the existence of ferroelectric domains in polycrystalline ferroelectrics, which are regions of the same polarization direction separated by domain walls. The obtained domain structure determines the overall polarization. More generally spoken, the overall microstructure including the grain size of ferroelectric materials plays an important role for the properties.[7, 171]

The main difference of perovskite-based ferroelectrics like BST and PZT to hafnium oxide-based ferroelectrics is the presence of a polar phase in a fluorite structure of hafnia, which is achieved mainly in doped oxides. This also benefits the movement of oxygen ions in an applied electric field, which leads to a complex situation. The presence of resistive and ferroelectric switching was even reported in the same hafnium oxide-based ferroelectric system.[172] The switching of the polarization in fluorite-based ferroelectric hafnium oxide (see Figure 2-4 (c)) is based on the off-centering of four oxygen ions (half-cell) in a unit cell from the remaining centrosymmetric Hf-sublattice. This is different to what is described in perovskite-based ferroelectric unit cells, where the central ion is facing a displacement. In contrast to the knowledge about the behavior of perovskite-based ferroelectrics, the nature of ferroelectricity and detailed switching behavior in hafnium oxide-based ferroelectrics is not yet as well understood.

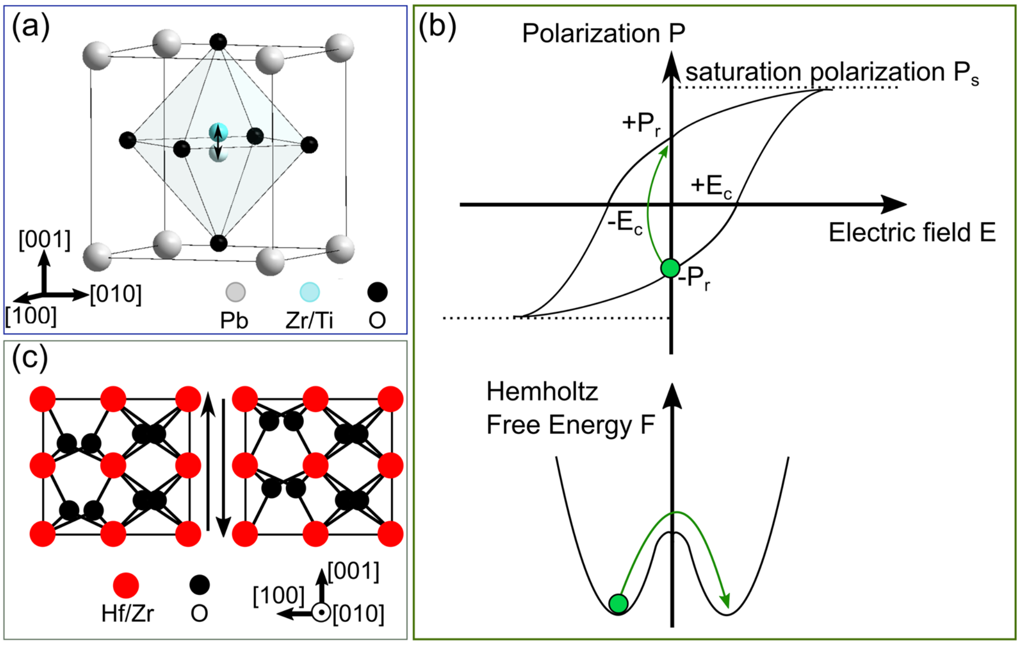

Figure 2-4: (a) PZT cell with two distinct polarization states originating from the displacement of the center ion from the unit cell center. (b) Exemplary electric field-dependent electric polarization loop with remanent polarization P_r, saturation polarization P_s and coercive field E_c. Additionally, the achievable distinct remanent polarization states are represented by the minima of the Helmholtz Free Energy F and the moving green ball. (c) Representation of the *Pca*2_1 orthorhombic crystal structure of ferroelectric hafnium oxide. Created with information from[3, 7].

Typical properties of PZT and ferroelectric hafnium oxide are compared in Table 2-2.

Table 2-2: Comparison of exemplary parameters of PZT and HfO_2-based ferroelectrics. Values taken from[130, 171, 173].

Parameters/Materials	PZT	HfO_2-based ferroelectrics
layer thickness	> 70 nm	1 nm – 1 μm
remanent polarization P_r	20 – 40 $\mu C/cm^2$	1 – 40 $\mu C/cm^2$
coercive field E_c	≈ 0.05 MV/cm	1 – 2 MV/cm
breakdown field E_{BD}	0.5 – 2 MV/cm	4 – 8 MV/cm
relative permittivity ε_r	≈ 1300	≈ 30

Today, the community predominantly agrees on the oIII phase (space group *Pca*2_1) being the polar ferroelectric phase in most hafnium oxide-based ferroelectrics, which is supported by the results from a multitude of subsequent studies[40, 174-183], among others, including X-ray diffraction and (scanning) transmission electron microscopy investigations as well as theoretical calculations. These and further studies were aiming to understand the origin of ferroelectricity and the stabilization of the metastable polar phase. This is still not completely resolved, but it is believed that the stabilization of the ferroelectric phase is based on a combination of thermodynamic (free energy) and kinetic factors, like dopants (species and concentration), oxygen content and oxygen ion movement, surface energy, annealing and quenching speed, mechanical stress and mechanical strain from the substrate/electrodes.

Ferroelectricity in hafnium oxide is mainly obtained in doped thin films, using different doping elements such as Si, Y, La or Al as well as in mixed $Hf_xZr_{1-x}O_2$.[174, 184, 185] The introduction of Zr to HfO_2 is a special case due to the very similar ionic radii of Hf and Zr and can be considered as a mixing of ZrO_2 with HfO_2, leading to a solid solution. In contrast, doping with Al and Y leads to an introduction of oxygen vacancies in the structure, which are also believed to influence the properties to some extent. The oxygen content can also be engineered by utilizing different oxidation setups, like plasma, ozone or molecular oxygen. This leads to very complex systems which are under investigation[184, 186-190], but the true nature of the influences is not yet fully discovered. Additionally, a few studies reported ferroelectricity in undoped HfO_2[191-193] and in bulk Y-doped HfO_2 powder[194], while antiferroelectric behavior was observed e.g., in pure ZrO_2 films[195]. Recently, an additional polar phase of a rhombohedral structure (space group $R3$ or $R3m$) was reported, showing ferroelectric properties in $Hf_{0.5}Zr_{0.5}O_2$ films grown on lanthanum strontium manganite (LSMO) in a very specific process using pulsed laser deposition. In this special case, the present polar phase is believed to be stabilized by epitaxial strain.[127, 196, 197] A comparable case was reported for epitaxial Y-doped HfO_2 grown on indium tin oxide (ITO).[198] This directly points towards another influence, as ferroelectricity is not only affected by the type and amount of dopants but also by the preparation conditions of the layers.[187, 193, 199-201] Here, especially the growth technique, oxidation conditions, substrate choice (strain, etc.) and annealing conditions play a major role.

Most ferroelectric stacks like the very common $TiN/Hf_xZr_{1-x}O_2/TiN$ stacks are prepared by atomic layer deposition (ALD) or sputtering processes, where the hafnium oxide layer is grown at low temperatures and therefore found to be amorphous. Crystallization yielding the polar phase is mainly achieved by a post-metallization annealing process after deposition of the top electrode layer. This is typically a rapid thermal annealing process using temperatures between 400 and 1000 °C and large cooling speed (quenching). Longer annealing at lower temperature is rarely reported, but especially relevant for CMOS BEOL processes.[185] The preparation directly impacts the grain size and distribution, while the success of subsequent annealing is also dependent on annealing speed, temperature, time and cooling speed.[3, 175, 202]

The formation of the $Pca2_1$ phase in annealed stacks can be described in three steps[3, 203]:

(1) Nucleation of a high symmetry phase like the tetragonal phase occurs. This is not possible from the thermodynamically most-stable monoclinic phase.
(2) Crystallites are further growing during the holding time.
(3) It is suggested that the higher symmetry phase is transformed to the polar orthorhombic phase ($Pca2_1$) during quenching. However, additional monoclinic grains can form either during cooling or can grow from monoclinic nuclei created during annealing.

After crystallization, most ferroelectric devices show a strong pinching of the polarization loops, which is reduced upon cycling (opening of the P-E loops). This classical wake-up behavior can be explained by different effects. The most prominent phenomenon is a field-induced transition from the tetragonal to the polar orthorhombic phase[204], but this mechanism requires a supporting phase stabilization mechanism. Here, the presence and diffusion of oxygen-defects such as oxygen vacancies, but also extended defects assigned to dead layers as well as domain wall movement (90°) and stress relaxation are discussed. In contrast, sudden wake-up has been observed in initially amorphous films, which are crystallizing during field-cycling.[130] Similarly, imprint occurring in these ferroelectrics (shift of hysteresis by a voltage bias) is usually related to differences in the work function of the electrodes, and also oxygen vacancy-induced domain wall pinning and internal bias fields, inducing a preferred polarization alignment.[205]

The ferroelectric properties of the stacks can be used in different emerging memory cell concepts, with the most-prominent ones suggested in the 1 transistor (1T) and one-transistor-one-capacitor (1T1C) configuration[3, 130]:

- The usage of a FeFET with the ferroelectric layer integrated into the gate stack. The threshold voltage of the field-effect transistor depends on the polarization of the ferroelectric layer, with an enhanced (on state) or depressed (off state) conduction. This 1T configuration approach is currently useable for FEOL integration.
- The usage of a 1T1C configuration, where the ferroelectric capacitor is connected to the drain of a field-effect transistor. When an electric field above E_c is applied, a large current is flowing through the dielectric, if the cell switches on. When the cell is switched off, the current flow is lower. Unfortunately, the readout of this setup is destructive and as a consequence, a re-write step is required. This configuration is often called FeRAM (concept) and useable for BEOL integration.
- Additionally, it is possible to use a few nanometers thin ferroelectric layer to create a ferroelectric tunnel junction (FTJ). The resistance is dependent on the injection of charge carriers through this very thin layer, where the tunneling current is determined by the direction of its polarization (tunneling electroresistance effect). Together with FeFETs, FTJs are promising candidates for neuromorphic applications.

A schematic overview of the memory cell concepts 1T and 1T1C is given in Figure 2-5. In research, often 1C stacks in a metal/ferroelectric/metal configuration are prepared and investigated as this represents a simple approach of testing and developing memory stacks as needed for FeRAM and FTJs as well as with an additional dielectric layer in FeFETs.

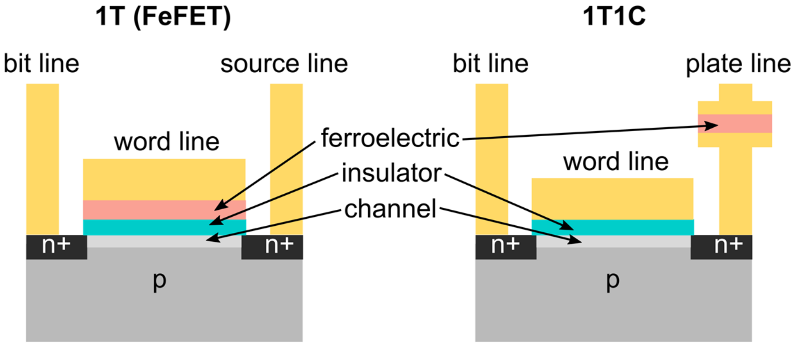

Figure 2-5: A 1T (FeFET) with the ferroelectric capacitor integrated in the gate stack, and a 1T1C memory cell with the ferroelectric capacitor connected to the drain of a FET. Redrawn after[7]. The insulator is a non-ferroelectric dielectric material, like SiO_2. Metal electrodes are presented in yellow. An n-type metal-oxide-semiconductor field-effect transistor (n-type MOSFET or NMOS) is represented in grey and black (n+/p/n+ with a conductive channel).

Currently, companies like the Ferroelectric Memory Company (FMC)[33, 206] together with Globalfoundries Inc., and Merck KGaA/InterMolecular[207] are putting efforts into research and development of hafnium oxide-based memory solutions to better understand their functionality and potentially target the market.

2.3 Germanium-antimony-tellurium-based phase-change memory

Switching in phase-change memory (PCM) relies on the controllable, reversible phase transition between the amorphous (high-resistance) and crystalline (low-resistance) phase of a phase-change material, which gives two distinguishable memory states. This is achieved by passing a current through the memory cell and rapid resistive heating of the phase-change material to change its phase. Crystallization takes place when holding a temperature above the crystallization temperature but below the melting point of the solid material that is sufficiently high and applied long enough (holding time) to create nuclei with radii above the critical radius. This step corresponds to the set of a device. The crystalline state represents the energetically favored state with the lowest free energy. Amorphization is obtained at a temperature around the melting point of the material with a subsequent fast cooling (quenching). This step represents the reset of a device. Schematic temperature profiles are shown in Figure 2-6 (a) together with a scheme of the basic memory cell called “mushroom cell”. It is usually composed of a phase-change material sandwiched between two electrodes. The bottom electrode (usual materials W, TiN or TaN) serves as a heater/heating element, which is confining the high-temperature zone to the bottom electrode interphase. Switching takes place at the whole bottom electrode interface, which is a big difference to the discussed filamentary-based resistive switching. In mushroom cells, a portion of the phase-change material is changing its phase when a heat is applied (leading to a mushroom-shaped transformed volume). A transistor is used to select the memory cell and to avoid disturbance problems when reading the memory state in a matrix. Readout is performed at a much lower current and therefore lower induced temperature than required for set and reset of the cell.[7, 8, 34, 208]

A multitude of different phase-change materials is known, mostly based on glassy chalcogenides, such as $Ag_5In_5Sb_{60}Te_{30}$ and $Ge_2Sb_2Te_5$.[209] Phase-change materials were found to have a characteristic type of bonding called resonant bonding, being present in the crystalline state[210]. $Ge_2Sb_2Te_5$ (abbreviated GST or also GST225), a ternary material system composed of germanium, antimony and tellurium is the most-used and most-studied material systems, due to a fast switching of GST-based memory cells (< 100 ns), its CMOS compatibility and the possibility to engineer the material properties significantly by doping with different elements. An exemplary ternary phase diagram is given in Figure 2-6 (b). The melting point of GST is at about 600 °C. Typical applied temperatures for crystallization and amorphization are about 100 °C – 200 °C and close to 600 °C, respectively. By adding Ge to GST, Ge-rich GST (GGST) alloys can be prepared, showing a high temperature stability especially of the amorphous phase when compared to GST (crystallization temperature > 300 °C). Here, 40 – 45 % of Ge in combination with 60 – 55 % GST225 has been proven to lead to compounds with very promising properties, such as showing a fast phase transition and a high resistance window.[211-213] This temperature stability is connected to the microstructure (Ge grains in GST matrix) of the amorphous material and of particular interest for automotive applications[23, 214, 215] The general usage of phase-change materials for applications was first proposed by S. R. Ovshinsky in 1968[216]. Technological development increased rapidly during the last decades. Currently, phase-change memory is considered as the most-mature emerging memory technology on the market, due to the good scalability, reliability and endurance of the memory cells. Several demonstrators were introduced such as a 1 GB chip in 45 nm technology[217], an 8 GB chip in 20 nm technology[218] and the 32 GB 3D Xpoint™ in 20 nm technology introduced by Intel in 2015[22], which is still further developed to include more layers in the third dimension. At the current stage, STMicroelectronics is developing embedded PCRAM integrated in 28 nm FD-SOI and platform with smaller feature sizes for the memory market[23, 24].

PCRAM currently faces a few limiting challenges, such as the high temperatures required for the amorphization process, which is strongly dependent on the heat capacity and on the thermal as well as electrical conductivity of the cell. Additionally, there is a lacking understanding of the kinetics of the crystallization process (limiting process during switching) for many materials, which can lead to high variabilities and therefore low device reliability. Reliability is also reduced by the drift of the HRS with time (drift), as the amorphous phase is not the thermodynamically stable phase of the phase-change materials. A thermal confinement improvement to reduce the writing current can be obtained by establishing an optimized device architecture[219].

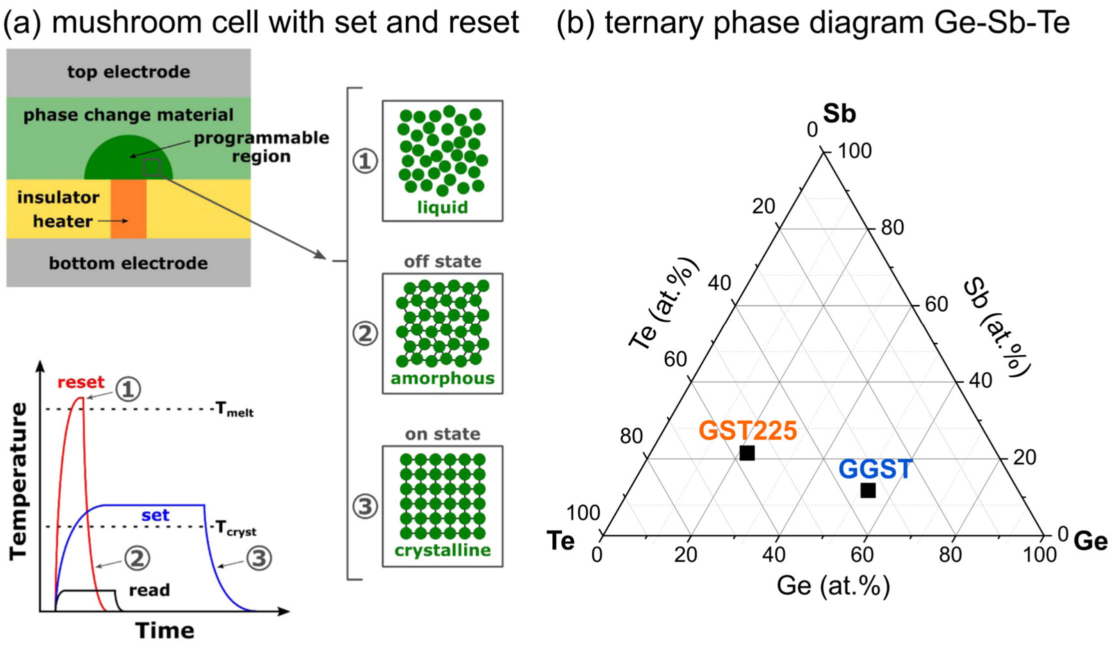
(a) mushroom cell with set and reset (b) ternary phase diagram Ge-Sb-Te

Figure 2-6: (a) Schematic of a mushroom cell, where the programmable region of a phase-change material is changing between the crystalline and amorphous phase, and a schematic time-dependent temperature profile for set, reset and readout operation with corresponding phase changes indicated. T_{melt} = melting temperature, T_{cryst} = crystallization temperature as labeled. Figure reproduced with permission from T. Schenk *et al.*[7], https://doi.org/10.1088/1361-6633/ab8f86; (b) Ternary diagram for Ge-Sb-Te materials for phase-change applications with $Ge_2Sb_2Te_5$ (GST225) and Ge-rich GST (GGST) labeled. Note, that this is an example and not representative for the multitude of different compounds published.

Recent developments further focus on the usage of phase-change materials for neuromorphic computing (applications), as memory cells can show multi-level switching/storage by reaching different crystallization and therefore different resistance levels during the set process. Additionally, threshold switching next to the usual memory behavior was found in phase-change material-based devices, making them suitable for the usage of selectors, as shortly discussed in the next chapter. [7, 8, 34, 208]

2.4 Selectors for 1S1R arrays

Memory cells can be addressed by transistors. In 1T1R configuration, the memory cell is therefore placed on the drain of the transistor, which allows a limitation of the current through the cell. Thus, undesired current overshoots that can lead to device failure can be prevented. However, in (2D & 3D) crossbar-arrays, current sneak paths can occur through half-selected cells (compare Figure 2-7 (a)). This can result in read disturbance.[220] To prevent such undesired current flows, the usage of other selective components such as complementary resistive switching (CRS[109]) devices, threshold switches or pn-diodes is possible, in principle. This chapter focuses on threshold resistive switching (TRS)-based cells (compare chapter 2.1.3), as this behavior can be observed in both Ge-Sb-Te-based and HfO_x-based devices. The threshold selectors can be based on different memory stacks typically used as ECM, TCM and PCM.

In the shown concept, the 1T1R configuration can be replaced by a 1S1R configuration. A schematic drawing of a 1S1R 3D array is given in Figure 2-7 (b). A PCM threshold selector is also called ovonic threshold switch (OTS). An exemplary OTS stack is TiN/Ge-Se-Sb-N/TiN[221], but also the 3D-stacking of the 3D Xpoint™ [22] is composed of an phase-change memory-based OTS cell combined with a non-volatile PCM cell.[222] For oxide-based threshold switching cells, different stacks like Ag/HfO_x/Pd[112], Ag/HfO_x/Pt[53, 223, 224], Cu/HfO_x/Pt[224] or Pt/HfO_x/doped HfO_x/Cu[164] as well as Pt/VO_x/Pt[78] are reported. The switching of these cells relies on the possibility to obtain an electrical resistance that is orders of magnitude lower above a threshold voltage than below this threshold voltage. Only if the threshold voltage is exceeded, the device is in the LRS. When no voltage is applied, the device is in the HRS. In PCM-based OTS, this is based on the freezing of the amorphous phase, where conductive dots of the phase-change material are forming and aligning in the amorphous matrix to form a conductive filament. This filament is not stable without an external electric field. In ECM-based devices with an oxide switching layer, a conductive metal filament, mostly Ag or Cu, is established (LRS) and dissolved (HRS). It is again not stable at zero voltage. A high non-linearity (large current jumps) are desired to achieve a highly conducting LRS, but a highly-insulating HRS in selectors. This instability of the filament is a result of different driving forces like the minimization of the interfacial energy and Joule heat but also dependent on further parameters like the presence of oxygen vacancies and the used current compliance during forming/set.[53] The true nature of this switching effect is still subject to current research. Even crystallization effects potentially occurring in oxides can play a role.[78] An exemplary 1S1R device configuration consisting of a Pd/Ta_2O_5/TaO_x/Pd memristor and a Pd/Ag/HfO_x/Ag/Pd selector can be seen in (c). The current-voltage curves of a Pd/Ag/HfO_x/Pt selector cell are shown in Figure 2-7 (e). In combination with a Pd/Ta_2O_5/TaO_x/Pd RRAM cell (1R) with its characteristic non-volatile behavior (d), a Pd/Ag/HfO_x/Pt selector cell (e) can be used to build a 1S1R crosspoint with the presented switching characteristics (f).

In 3D arrays, the usage of a threshold switching cell gives the opportunity to not only suppress undesired sneak path currents, but can also improve the density of the array when using cells smaller than a whole transistor. This approach can further lead to a reduced power consumption as threshold voltages can be significantly lowered when compared to transistors. Different stack combinations are possible, like combining phase-change material-based ovonic threshold switches with HfO_x-based VCM cells or combining two oxide-based components like the shown

HfO$_x$- and TaO$_x$-based 1S1R stacking. These are only some of many examples published.[22, 53, 112, 164, 167, 220-223] Of particular interest is the possible usage of similar device stackings for both 1R and 1S based on the very same oxide layer (e.g., HfO$_2$), which can simplify the manufacturing of usually very complex structures.

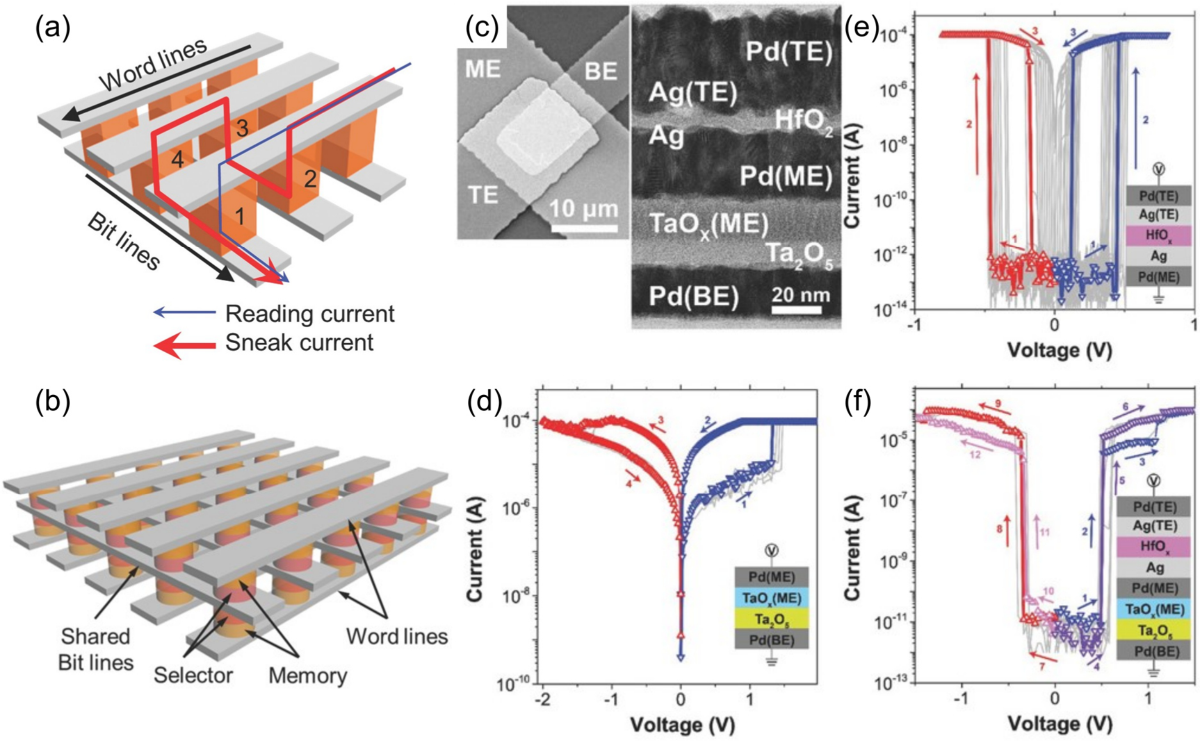

Figure 2-7: (a) Schematic of a typical 2D array with reading current (blue path) and sneak current (red path). (b) Schematic of a 3D 1S1R array (shared bit line). (a) and (b) reproduced with permission from Seok *et al.*[220], https://doi.org/10.1002/adfm.201303520, © 2014 WILEY-VCH. (c)-(f) 1S-1R device configuration consisting of a Pd/Ta$_2$O$_5$/TaO$_x$/Pd memristor and a Pd/Ag/HfO$_x$/Ag/Pd selector with corresponding current-voltage characteristics. (c) Scanning electron microscopy image of the selector and memristor (top view, left) and transmission electron microscopy image of the cross section (right). b) Bidirectional threshold switching (cycling) of a Pd/Ag/HfO$_x$/Ag/Pd selector. c) Repeatable bipolar memristive switching of a Pd/Ta$_2$O$_5$/TaO$_x$/Pd memristor. d) Current-voltage (combined) characteristics of the vertically integrated 1S and 1R cells. Reproduced with permission from Midya *et al.*[112], https://doi.org/10.1002/adma.201604457, © 2017 WILEY-VCH.

3 Fundamentals on radiation effects in solids

In this chapter, radiation effects in solids are shortly introduced with the main focus on swift heavy ion radiation. Especially, the literature describing induced phase transitions in hafnium oxide- and Ge-Sb-Te-based films and irradiation effects in emerging memory (OxRAM, ferroelectric capacitors for the usage in FeFETs/FeRAM and PCRAM) are discussed, as they are specifically relevant to this work.

In general, different types of ionizing radiation are present in all parts of the universe, including photons (gamma-radiation and X-rays), electrons and high-energy protons and alpha particles but also heavy ions, all originating from different sources. Cosmic radiation represents one part of radiation of natural origin, next to e.g., terrestrial radiation. While terrestrial radiation is created when radioactive nuclides decay, cosmic radiation with its high-energy photons and particles originates from different possible sources like the sun in our solar system or other stars' activity, black holes, pulsars and supernovae, therefore being categorized in solar radiation, galactic radiation (energies up to 10^{18} eV) and extragalactic radiation (highest energies). In the high-energy regime (above few 100 MeVs, the spectrum is by far dominated by protons with minor contributions from alphas or other heavy particles. As an example, galactic radiation is composed of about 87 % protons, 12 % alpha particles and 1 % heavy ions. Such heavy ions have energies usually above 1 GeV.[225-228] Artificial sources of radiation are e.g., nuclear power plants, nuclear weapon tests or the synthesis of isotopes (e.g., for medical applications). In the past decades, high-energy ion beam facilities with tailored beam properties were developed for nuclear physics studies and became also of interest for other interdisciplinary fields such as material science or biophysics and are nowadays applied for tumor therapy. Additionally, the interest in ion track technology has increased, where different approaches are used to create defined materials on a nanoscale with specific properties.[229, 230]

3.1 Swift heavy ions

Swift heavy ions (SHI) are ions (usually heavier than carbon) with an energy in the range of MeV – GeV. When propagating through matter, SHI interact with the material in various ways, which results in different kind of effects such as lattice vibrations, structural changes as well as the creation of defects (vacancies and interstitials, defect clusters, etc.). In the MeV-GeV regime, SHI lose energy by the interaction with the electrons of the irradiated material (electronic stopping, $dE/dx_{electronic}$), whereas at lower energies (velocity lower than Bohr velocity of outer target electrons) the interaction is dominated by elastic collisions with the target atoms (nuclear stopping, $dE/dx_{nuclear}$).[231] The overall stopping power S can be expressed by equation (3). This is a property of the target material.

$$S(E) = -\left(\frac{dE}{dx}\right)_{total} = -\left(\frac{dE}{dx}\right)_{nuclear} - \left(\frac{dE}{dx}\right)_{electronic} \qquad (3)$$

with $-(\frac{dE}{dx})$ being the average loss of kinetic energy per path length, also called energy loss or linear energy transfer (LET). As this is a property of the projectile particle, the equation connects particle and target material properties.

Nuclear stopping for SHI dominates when the transferred energy from the projectile to the recoil atom exceeds the displacement energy E_d, which is usually in the range of 10 – 100 eV.

This leads to displacements, where atoms are moved away from their initial lattice sites and the creation of point defects such as vacancies and interstitials. The recoil atom can further collide with other atoms of the lattice in elastic collision (knock-on) processes, which can result in a collision cascade and the creation of extended defects. The process stops as soon as the kinetic energy of the recoil atoms is below E_d. Nuclear stopping is mainly relevant at low energies i.e. towards the end of the ion path.

In contrast, electronic stopping is due to electronic excitation and ionization processes. Because of the high kinetic energy of the released target electrons further ionization events occur leading to a large electron cascade spreading radially around the ion trajectory. The electronic energy loss of a charged particle in a solid depends on the projectile and target properties, which is described by the Bethe-Bloch formula (4).

$$-\left(\frac{dE}{dx}\right)_{electronic} = \frac{4\pi e^4 (Z_{eff,p})^2 Z_t N_t}{m_e v_p^2} \times \left(ln\frac{2m_e v_p^2}{I} - \ln(1-\beta) - \beta^2 \right) \qquad (4)$$

- e = elementary charge
- $Z_{eff,p}$ = effective charge state of projectile
- Z_t = atomic number of target
- N_t = mass density of target
- m_e = electron mass
- v_p = projectile velocity
- I = ionization energy
- β = correction factor

The electronic energy loss increases with atomic mass, density of the target and charge state of the projectile. It is further dependent on the projectile velocity. For the projectiles, a specific energy MeV/nucleon (MeV/u) is usually given. A schematic representation of the electronic and nuclear energy in dependence of the specific energy is given in Figure 3-1.

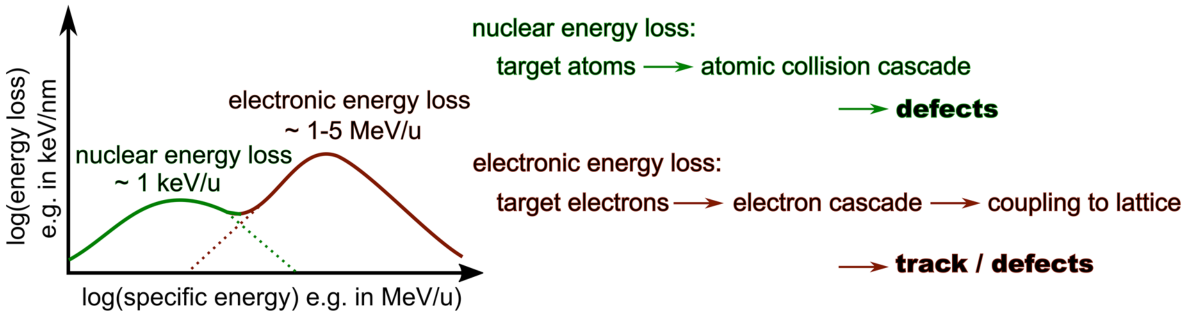

Figure 3-1: Schematic representation of the nuclear and electronic energy loss in dependence of the specific energy of the projectile in a double log presentation (left). Defect formation at low specific energies is dominated by nuclear energy loss, while at higher energies, the electronic energy loss leads to complex defects and track formation. Redrawn after[231].

The electronic energy loss curve shows a maximum, which is called Bragg peak. Here, the velocity of the projectile is close to the average orbital velocity of the target electrons. At higher specific energies (MeV – GeV range), a lower energy transfer between projectile and target atoms occur due to the shorter interaction time. At lower specific energies, the energy loss is lower because the projectile picks up electrons and thus decreases its charge state. At even lower specific energies, nuclear energy loss becomes more and more dominant. At ion velocities above ~ 10^4 MeV/u, relativistic effects occur including the generation of photons (Bremsstrahlung and Cherenkov radiation) is possible. When the kinetic energy of the projectile is large enough to overcome the Coulomb barrier, nuclear reactions occur.[226, 231, 232]

For the description of radiation effects, the following parameters and corresponding units are used. The deposited dose is typically given in Gray (Gy) which corresponds to the absorption of one joule energy by one kilogram of matter (1 Gy is equivalent to 100 rad as former dose unit. The energy loss along the trajectory of ions is given in energy units per path length usually keV/nm or keV/μm (sometimes this unit is converted into MeV/(mg/cm^2)). For irradiation experiments, the accumulated number of ions per area (ions/cm^2) is described by the fluence and the beam intensity by the ion flux in units of ions/cm^{2}s. The beam parameter is usually given as specific energy MeV per nucleon (MeV/u) which can directly be converted to an energy (e.g., for Au ions 8.3 MeV/u corresponds to 8.3 MeV × 197 u = 1.635 GeV). All irradiation experiments were conducted with Au ions of 8.6 MeV/u. Therefore, the electronic energy loss is dominating and the nuclear loss can be neglected (compare chapter 4.4).

3.1.1 Formation of ion tracks

When swift heavy ions enter a solid, ionization of target atoms lead to the production of many highly energetic electrons. If their energy is exceeding the electron binding energy, further ionizations can occur, leading to the creation of a secondary electron cascade. These electronic processes occur on very short timescales. The initial electrons also called δ-electrons are produced within 10^{-17} – 10^{-16} s. The duration of the following secondary electron cascade is in the order of 10^{-15} – 10^{-13} s. These secondary electrons spread the energy radially following a 1/r law, which can affect an overall defective region of up to several tens of nanometers to 1 μm. In a next step, the energy is transferred from the electron to the lattice subsystem within a time scale of 10^{-13} – 10^{-10} s. The energy deposited to the atomic subsystem results in changes of the atomic structure due to bond-breaking and the creation of defects. The final damage along the ion trajectory is denoted as ion track and depends on the deposited energy density and physical properties of the target material.[226, 231, 233-235] Track formation requires that a certain energy loss threshold is exceeded. The value of the threshold depends on the sensitivity of the target material and is low for organic materials and high for metals. First tracks were observed in mica exposed to uranium ions[236]. Track formation is also possible in many oxides[11, 237-240], some metals and in selected semiconductors but not in crystalline pure Si and Ge. In most oxides, track formation and related phase transitions occur for electronic energy losses of a few keV/nm. More information and further studies on the sensitivity of track formation are given in literature (partially summarized e.g., in[226, 231]). Defective tracks are usually stochastically distributed and with increasing radiation fluence the probability to obtain overlapping tracks increases.

The length of the ion path can be several tens of μm depending on the energy of the ions. After entering the target material, the projectile ion is slowed down, transferring its energy until it stops (energy used up – see schematic representation given in Figure 3-2). The penetration depth or ion range in matter is defined as the reciprocal energy loss $(dE/dx)^{-1}$ integrated over the full kinetic energy of the projectile. Heavy ions with the same specific energy also have a similar ion range in the same target material.[226, 231, 233] When irradiating thin films (normal to surface) of tens to hundreds of nanometer thickness, the energy loss can be considered being almost constant over the whole thickness, as the projectile ions move completely through the thin layer and stop deep in the substrate the film is grown on.

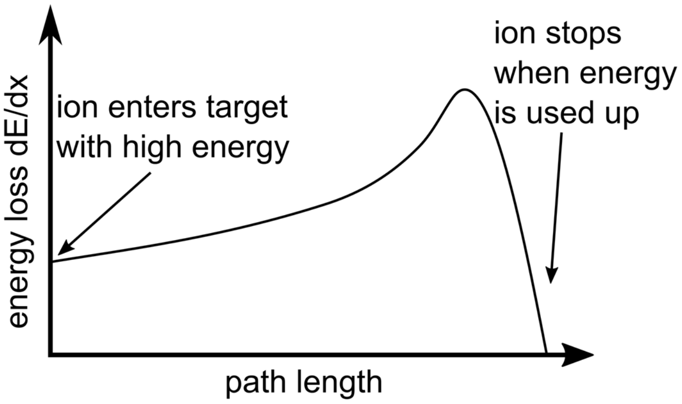

Figure 3-2: Schematic representation of the energy loss dE/dx in dependence of the path length (Bragg curve). Most energy is deposited before the ion stops. The ion range is defined as the integral of the reciprocal energy loss $(dE/dx)^{-1}$ over the full ion energy. Heavy ions with the same specific energy have a similar ion range in the same target material. Redrawn after[241].

3.1.2 Coulomb explosion model and thermal spike model

The precise mechanism(s) of track formation and a universal model are not yet established, but two promising models are often used for description: the Coulomb explosion model and the thermal spike model. Those are described in the following.

The **Coulomb explosion or ionic spike model** is characterized by a burst of ionizations along the ion path (ion explosion spike), which results in an electrostatically unstable lattice due to Coulomb repulsion and subsequently in bond-breaking and defect creation, if the forces are strong enough to overcome binding energies. This model was first proposed by Fleischer *et al.*[242] in 1965. The process happens on a timescale of 10^{-15} – 10^{-13} s. Therefore, the lifetime of the ionized state is the crucial parameter. Track formation requires that the time is sufficiently long for an energy transfer of potential to kinetic energy. A defective track can be created along the ion path, if sufficient time for atomic motion is provided before the electrons return. This is the case for insulators, where the density of free electrons is not high enough for rapid neutralization of the target atoms. In contrast, this is not valid for metals. This concept is mainly a theoretical concept (including calculations), but no convincing proof is yet given.

The **thermal spike model** describes track formation by a localized large temperature increase above the melting temperature of the target material and a subsequent rapid quenching. This is a transient thermal process occurring in a small cylindrical volume around the ion trajectory on a timescale of 10^{-14} – 10^{-10} s. After δ-electrons thermalize as a result of the electron-electron interaction, the energy of the electron gas is transferred to the lattice (atoms). The time-dependent temperature distribution is described by two separate classical heat transport equations (heat flow) for the electrons and lattice subsystem. Both systems are coupled by a constant describing the energy transfer from the electron system to the lattice system. The melted cylindrical volume depends on the deposited energy (projectile velocity) and the target material properties, such as thermal conductivity and specific heat. The thermal spike concept is based on early ideas from the beginning to mid of the 20th century was further developed e.g., by Toulemonde *et al.*[243-245] and adapted to track formation. Nowadays the model can be used to quantitatively describe the evolution of the track radii as a function of the electronic energy loss regime, which fits experimental observations and energy loss threshold values. However, there exist clear limitations and criticism of the thermal spike model. The model uses analytical formulae initially developed for the descriptions of macroscopic phenomena of equilibrium thermodynamic processes. The thermal spike model applies them for microscopic, extremely fast and therefore non-equilibrium processes and a heat transfer that is not considered to be limited in velocity.[231]

3.2 Heavy ion irradiation-induced phase transitions in hafnium oxide- and Ge-Sb-Te-based powders and films

Heavy ion irradiation-induced **phase transitions in HfO_2 powders** (and also the polymorph ZrO_2) were observed and extensively described by A. Benyagoub[11, 238, 239, 246]. Based on X-ray diffraction analysis of ion irradiated m-HfO_2, a phase transition from the monoclinic to the tetragonal phase occurs, if the necessary threshold for the electronic energy loss of about 18 keV/nm is exceeded. Below this threshold, no phase transition was observed. The mechanism for the crystalline-to-crystalline phase transition is ascribed to a double impact mechanism. Oxygen vacancies are considered to be created by a first ion impact, while a second hit of the defective track region initiates the phase transition. Significant track overlap occurs when the material is exposed to fluences above around 1×10^{12} ions/cm².[11] According to Garvie and Nicholson[247], the phase composition of a sample can be quantified from the integrated reflection intensities obtained from XRD patterns. The concentration C of a specific phase is given by the sum of the integrated intensities of this phase divided by the sum of the overall integral intensities of all phases present. For a material composed of the monoclinic and tetragonal phase, the concentration of a tetragonal phase is given by the following equation (5):

$$C = \frac{I(101)_t}{I(\bar{1}11)_m + I(111)_m + I(101)_t} \tag{5}$$

with $I(\bar{1}11)_m$, $(111)_m$ and $(101)_t$ being the peak integrals of the reflections of the monoclinic (m) and tetragonal (t) phase, respectively. Given by the stochastic distribution of the ion impacts, Poisson statistics can be applied providing quantitative values of single and double hit ion impact regions. The transformed phase fraction and damage cross-section σ can be extracted from a fit to experimental data points as described by Gibbons[248] and expressed as equation (6):

$$C(\Phi) = \Delta C(\infty)(1 - \sum_{k=0}^{n-1} \frac{(\sigma\Phi)^k}{k!}\, e^{-(\sigma\Phi)}) \tag{6}$$

with C representing the concentration of the (e.g., tetragonal) phase, Φ the fluence and n = 2 the double impact scenario. $\Delta C(\infty)$ denotes the maximum concentration increase at saturation. With this, a damage cross-section in HfO_2 exposed to 1×10^{13} (250 MeV) I ions/cm² of about $4.8(\pm0.3)\times10^{-13}$ cm² or 48(±3) nm² was deduced[11]. This corresponds to a track radius of 3.9(±0.12) nm. A similar phase transition as described by A. Benyagoub[11] was also reported by B. Schuster[240]. The deduced damage cross-section in m-HfO_2 exposed to 7×10^{12} (2.3 GeV) Pb ions/cm² at ambient conditions is about $1.01(\pm0.08)\times10^{-12}$ cm² or 101 nm² (track radius about

5.67(±0.2) nm).[240] Additionally, transitions from the monoclinic to the orthorhombic (oI and oII) phases were revealed for high-pressure conditions during irradiation[240].

Regarding heavy ion irradiation-induced **phase transitions in HfO_2 thin films**, only few studies have been reported, describing amorphous to crystalline and polycrystalline to polycrystalline transitions.[249-251] Li *et al.*[251] reported a transition from amorphous HfO_2 to a layer consisting of monoclinic crystallites, which was revealed by High-Resolution Transmission Electron Microscopy (HRTEM) investigations. Crystallization occurs, if the ion energy exceeds the electronic energy loss threshold of 10 keV/nm. Further, Suvorova *et al.*[252] published a quite extensive study on structural changes in irradiated La-doped hafnium oxide films using HRTEM, electron diffraction and electron energy-loss spectroscopy. An orthorhombic to tetragonal crystalline-to-crystalline phase transition was observed after the irradiation with 160 MeV Xe ions. For oxygen-deficient hafnium oxide, no heavy ion irradiation studies related to phase transitions exist. This also applies for ferroelectric doped hafnium oxide films (apart from this work and a directly related study[64]). In proton irradiation studies, no evidence for an induced phase transition in ferroelectric hafnium oxide-based films was found[253, 254], not even at a high fluence of 10^{15} protons/cm^2. This indicates that the energy loss of the protons is too low to initiate a phase transition.

Another important point related to induced material changes, track formation and phase transitions is the growth or fragmentation of grains. In HfO_2 films, crystallization is reported to be accompanied by grain growth, while for the transition from monoclinic to potentially tetragonal HfO_x, field emission scanning electron microscopy studies revealed a topological grain fragmentation at high fluence irradiations with 100 and 120 MeV Ag ions above 3×10^{12} ions/cm^2.[249, 255] No amorphization was found in doped films undergoing a transition from orthorhombic to tetragonal phase by HRTEM investigations.[252]

Ion irradiation-induced phase transitions in Ge-Sb-Te-based films were reported e.g., by De Bastiani *et al*. where a crystalline to amorphous transition was introduced by implantation with 90 – 150 keV Ar ions.[256] Such an ion implantation can also affect the crystallization kinetics during the annealing process of amorphous $Ge_2Sb_2Te_5$, with a reduced thermal stability and increased transition time.[257] In Ag-doped GST films exposed to 120 MeV heavy Ag ions, a high stability of the amorphous state was shown, while in undoped films exposed to $1\text{x}10^{13}$ ions/cm^2 crystallization was no longer suppressed.[258] The nature of this (suppressed) transition is related to the introduction of defects, but its true nature is not yet fully clear.

3.3 Memories exposed to heavy ion radiation

All types of ionizing radiation are a threat for microelectronics. Especially advanced conventional memories are at risk, because the information storage is mostly based on charges, like it is the case for all transistor-based technologies such as flash memory.[259, 260] The interaction of energetic charged particles or high-energy photons can lead to a variety of effects causing errors in the electronic devices, which can be categorized in total ionizing dose (TID) effects, displacement damage (DD) effects and single event effects (SEE). TID effects are characterized by property changes accumulating over time (cumulative radiation effect), which are often a result of trapped charges. Single event effects in contrast are characterized by changes originating from a single particle strike (mainly ions), which can lead to the generation of electron-hole pairs and transient currents. They can result in so-called soft (non-destructive, non-permanent damage) or hard (destructive, permanent damage) errors. An example for soft errors is the so-called single event upset (SEU). A high sensitivity to SEU is known for metal-oxide-semiconductor field-effect transistors (MOSFETs). A SEU is characterized by the generation of local charges in the gate through interaction with heavy ions or high-energy protons. This results in an incorrect change of the logic value (often seen as bitflips) and a shift of the transistor (changed threshold voltage). In contrast, so-called single event latchups (SEL) and single event gate ruptures (SEGR) are hard errors. In SEL, a high current is induced resulting in an electrical short and a thermal destruction of the electronic devices. A SEGR is characterized by a hard breakdown of the dielectric, which preferably occurs when an electric field is applied during radiation exposure. Detrimental radiation effects become even more crucial with further downscaling of devices. In transistors, the presence of a smaller gate area is accompanied by a lower number of electrons participating in the switching process.[261, 262] Due to the increasing demand for larger memory storage capacities and advanced computing technologies, also the general interest in radiation hardness for e.g., aerospace applications and corresponding radiation-induced effects in memories keeps increasing. The growing interest is emphasized by two recent publications by M. J. Marinella[263] and D. M. Fleetwood[9].

For applications in radiation-harsh environments, emerging memories can act as promising radiation-hard candidates. Compared to the charge-based flash technology, the underlying mechanisms of HfO_x- and GST-based memories are strongly depending on defects (such as oxygen vacancies in oxides), the movement of ions (like oxygen or metal ions), and the crystal structure (such as an orthorhombic ferroelectric phase or an amorphous/crystalline phase transition occurring in phase-change layers) of the active material. They have been demonstrated to show an improved resilience towards ionizing radiation.

For **filamentary oxide-based resistive memory** this includes a low sensitivity to different types of radiation such as X-rays[264, 265], γ-radiation[266, 267], high-energy protons[163, 260, 264, 265] and heavy ions[268, 269]. For HfO_x-based RRAM stacks, a few studies on the impact of heavy ion radiation on resistive switching are reported[63, 141, 268-273]. For **hafnium oxide-based ferroelectric stacks**, only minor influences on the electrical properties were reported for stacks exposed to protons[253, 254] and heavy ions[64, 274]. Observed changes are mainly related to the creation of oxygen vacancies in the oxide layer or degradation effects in access transistors for 1T1R memory configurations. Overall, studies combining beam-induced electrical changes with potential phase transitions at high energies and fluences, as described in the previous part, are scarce.

Possible phase changes are usually not discussed for electronics, which is mainly related to the very thin layers and small (structured) device sizes (small interaction volume with X-rays when using X-ray diffraction). However, the interaction of heavy ions with emerging memories can be considered being one of the most crucial types due to the large penetration depth and high ionization potential, where phase transitions can occur. The important role of the film thickness and the increasing difficulties of test scenarios when downscaling electronics was recently discussed by D. Fleetwood.[9] As the detailed failure mechanisms of oxide-based resistive and ferroelectric memories are yet unclear and sometimes results appear to be quite inconsistent, especially the mentioned beam-induced phase transitions can be considered to play an important role.

Regarding radiation effects in **phase-change memories**, the knowledge of the phase is also crucial and with further development of this technology, radiation hardness and the understanding of possible failure mechanisms are getting increasingly relevant. This in turn can help to better understand material properties in general. In literature, several irradiation studies discuss the impact of mainly protons and (heavy) ions on the properties of phase-change memories, also in dependence on the structure of devices and arrays.[275-281] However, heavy ion irradiation studies discussing potential phase transitions of Ge-Sb-Te-based films in combination with electrical results of devices are again scarce. Failures are often reported to be a result of the degradation of the CMOS transistors used in the electric circuits (trapped gate charges). Nevertheless, as the information storage of the phase-change memory is based on the crystallinity and strongly influenced by composition and microstructure of the active layer, the evolution and investigation of such properties is essential for the understanding of the memory cell functionality.

4 Thin film growth, device preparation and characterization techniques

In this chapter, the relevant fundamentals and experimental details for thin film growth, device preparation as well as material and device characterization are introduced. The described methods include the hafnium oxide film growth utilizing reactive molecular beam epitaxy (MBE), the preparation of bottom and top electrodes (TiN, Pt, Cu, Au) by MBE and DC (direct current) sputtering, post-deposition treatments such as post-deposition annealing and sample structuring using lithography and ion beam etching processes for electrical device fabrication and the conducted heavy ion irradiation experiments. The individual preparation techniques will be introduced separately, but an overview of the investigated material stackings will also be provided in the corresponding results and discussion parts to simplify the overview and to directly connect the different parts of this thesis.

In all these preparation steps, the knowledge of structure, layer thickness and composition of the individual layers is required. Therefore, relevant characterization techniques, like X-ray diffraction (XRD), X-ray reflectivity (XRR), X-ray photoelectron spectroscopy as well as (scanning) transmission electron microscopy ((S)TEM) and related techniques used in this work are introduced. The electrical characterization techniques including electric polarization measurements, resistive switching measurements on single devices (capacitor stacks) are separately described in the following section.

In the final part of this chapter, the sample preparation of external samples and their characterization are briefly described. External partners are CEA-Leti in Grenoble, France in cooperation with LTM CNRS, Grenoble, France, and the Fraunhofer-Institut für Photonische Mikrosysteme IPMS - Center Nanoelectronic Technologies (CNT) in Dresden, Germany, abbreviated in this work as Fraunhofer IPMS CNT.

Note that for the description of the resistive switching in single memory devices the terms VCM, TCM and ECM are used in relation to the switching mechanism in the respective memory, while for integrated 1T1R arrays containing a HfO_2-based VCM cell the term OxRAM is used.

4.1 Thin film growth utilizing reactive MBE

Molecular beam epitaxy (MBE) is a physical vapor deposition (PVD) technique based on thermal evaporation of material to grow thin films in ultra-high vacuum (UHV) conditions. The basic principle is known since the 1960's. Solid material from a so-called evaporation source located in an evaporation crucible is brought to the gaseous phase in an evaporation process by introducing a large amount of localized heat. This can be achieved by resistive thermal evaporation for lower temperature melting materials or by utilizing high-energy electrons (e.g., 10 kV applied with a current of up to 1 A) from an electron gun (tungsten filament), which are accelerated towards and focused by deflections coils on the material surface by a magnetic field. The process is only possible due to the UHV conditions in the deposition chamber with pressures of 10^{-8} mbar and below, where evaporation temperatures and energies of the materials are reduced. At the same time, the collisions of electrons, atoms and molecules with each other are drastically reduced (increased mean free path), which is necessary for the evaporation process as well as for the successful transfer and deposition of the evaporated materials on a substrate in form of a thin layer. In general, metals (e.g., Hf, Ti, Pt and Cu) can be deposited with this technique, but also films of semiconducting and organic materials as well as oxides (e.g., HfO_x) and nitrides (e.g., TiN) are possible. For the latter cases, additional gases have to be supplied during growth in a reactive MBE setup. In general, MBE is used to achieve highly-ordered layers of epitaxial and single crystalline nature. However, also polycrystalline layers can be grown. A big advantage of MBE film growth is the possibility to precisely control the evaporation and therefore growth rates, which results in a low film roughness, a low defect concentration, the highest structural quality at the atomic layer level and an excellent stoichiometry control when multiple materials are evaporated. This so-called co-evaporation can be done by either using an alternating source shuttering, growing one material after the other, or by permanent co-evaporation by simultaneously evaporating material from multiple evaporation sources. A disadvantage of MBE is the limited scalability to larger deposition areas and the long deposition times, when compared to other techniques like atomic layer deposition and sputtering.[282-285] A schematic of the MBE setup used for film growth in this work can be seen in Figure 4-1.

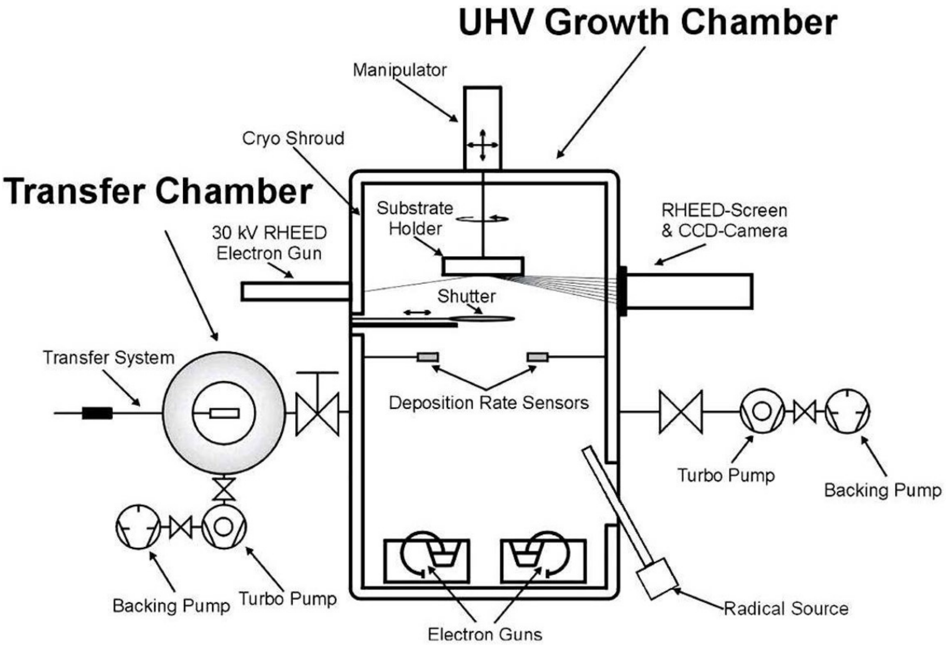

Figure 4-1: Schematic of the reactive molecular beam epitaxy setup used in this work with load lock chamber, UHV growth chamber, corresponding pumping systems (backing and turbo pump), manipulator with substrate and shutter, RHEED system, QCM sensors as well as electron guns, crucibles and radical sources). Figure from Buckow *et al.*[283], http://dx.doi.org/10.1088/0953-2048/26/1/015014. © IOP Publishing. Reproduced with permission. All rights reserved.

The control of the rates is achieved by using a monitoring system of deposition rate sensors based on quartz-crystal-microbalances (QCMs). QCMs show a change of their resonance frequency when the amount of material deposited on the quartz transducer changes. By knowing the molar mass and density of the individual material, a material-specific rate is determined.[286] In this work, a Cygnus controller was used, providing values like deposition rate per time or each source and achieved layer thickness. Calibration of growth rates can be done by comparing the value of the QCM installed close to the substrate position with the value(s) of the QCMs and connected collimators located on top of the source(s). The thickness of the film was calibrated after growth by comparing the achieved thickness value with measurement results obtained e.g., from X-ray reflectivity (XRR) or profilometry. A shutter located between the sources and the substrate manipulator (sample stage) was used to protect the substrate surface or the already grown film from undesired deposition, like too high rates due to fluctuations or during ramping up the rates or temperature before deposition, and to stop the deposition after film growth. The substrate manipulator can be used to heat sample holders from the backside by resistive heating to the desired growth temperature up to about 900 °C. The manipulator stage with the substrate holder was rotated with 10 rounds per minute (rpm) during film growth to achieve a uniform layer over the whole substrate area. Oxidation or nitridation of the evaporated metal was achieved with gas radicals (O* or N*) by creating plasma in radio frequency (RF) plasma guns. Critical parameters are the gas flow, the forward power applied to the plasma tube and the optical output given by the controller from an optical cable as soon as the plasma starts glowing. An introduction of gases into the chamber during metal evaporation also changes the background or so-called growth pressure in the system. This multitude of influencing parameters makes MBE film growth a complex technique, including many calibration and optimization steps, but at the same time opens the rare possibility of precisely controlling thin film growth and achieve e.g., substoichiometric/oxygen-deficient HfO_x films within a broad range of different stoichiometries.[145] Unfortunately, stable conditions can change as soon as the MBE setup is changed (physically or by e.g., heat during summer compared to colder winter months), resulting in additional (re)calibration runs. As a tool for growth monitoring and calibration, a reflection high-energy diffraction (RHEED) system is attached to the chamber. During growth, high-energy electrons (acceleration voltages of 25 kV) are diffracted at the substrate/film surface (incident angle about 1°), giving diffraction spots and patterns due to constructive and destructive interference on a fluorescent screen which is then displayed on a monitor. With this in-situ technique, the growth mode during layer growth can be identified.[287] It should be noted that the nature of the patterns is also dependent on the growth parameters used. Different parameters used for the growth of the same material can result in different growth modes and therefore varied RHEED patterns.[152] This is further described in the following sections 4.1.1 and 4.1.2.

4.1.1 Growth process and growth modes

The film growth is a complex process including sub-processes such as adsorption, desorption and re-evaporation, penetration, interdiffusion and surface diffusion, as well as nucleation, which can occur simultaneously. A simplified schematic representation of growth and related processes is given in Figure 4-2. In general, those are important for all growth techniques. The film growth by MBE is characterized by a comparably slow speed in the (sub-)Angstrom-range. The actual subprocess is determined by the kinetic energy of the incoming atom from the gaseous phase and from parameters such as surface temperature. At low energy, adsorption is more likely, while at higher energies, penetration into the substrate or atom reflection (or re-evaporation) can occur. An adsorbed particle is first bound by van-der-Waals forces (physisorption), but a (stronger) chemical bonding (chemisorption) can be created. Additionally, surface diffusion can occur. These processes are dependent on temperature, where a sufficient temperature increases diffusion, but a large thermal energy can also lead to collisions of particles with others, which can result in desorption (to the gaseous phase) or diffusion into the substrate. An agglomeration of the same particle species is called nucleation. Its driving force is the lowering of the overall energy. Above a critical nucleation radius, the agglomerated volume (growing film) continues to grow further. This complex process is dependent on the interface energies γ. Different growth modes, like Frank-van-der-Merwe growth ($\gamma_{\mathrm{substrate}} \geq \gamma_{\mathrm{film}}+\gamma_{\mathrm{interface}}$ → layer-by-layer growth), Vollmer-Weber growth ($\gamma_{\mathrm{substrate}} < \gamma_{\mathrm{film}}+\gamma_{\mathrm{interface}}$ → 3D island growth) and Stranski-Krastanow growth (first $\gamma_{\mathrm{substrate}} \geq \gamma_{\mathrm{film}}+\gamma_{\mathrm{interface}}$, then changing to $\gamma_{\mathrm{substrate}} < \gamma_{\mathrm{film}}+\gamma_{\mathrm{interface}}$ → first layers, then islands growing on top) can be distinguished, as visualized schematically in Figure 4-2.[288, 289]

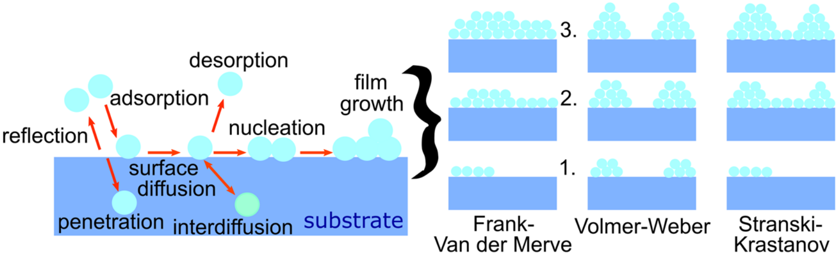

Figure 4-2: Schematic growth and related processes occurring and schematic representation of the Frank-Van der Merwe, Volmer-Weber and Stranski-Krastanov growth modes. Redrawn with information from[288, 289].

4.1.2 Growth monitoring with RHEED

These growth modes can be monitored by RHEED (schematic setup shown in Figure 4-3 (a)), where different patterns are visible on the fluorescence screen. To give a few examples relevant to this work, the patterns of a crystalline TiN film grown on *c*-cut Sapphire ((0001)-oriented Al_2O_3) and a crystalline HfO_2 film grown on TiN (on *c*-cut Sapphire) are shown in Figure 4-3 (b) and (c), respectively. In (d), the pattern of an amorphous HZO layer grown on TiN is seen. Additionally, the pattern of a single crystalline *c*-cut Sapphire substrate is given in (e).

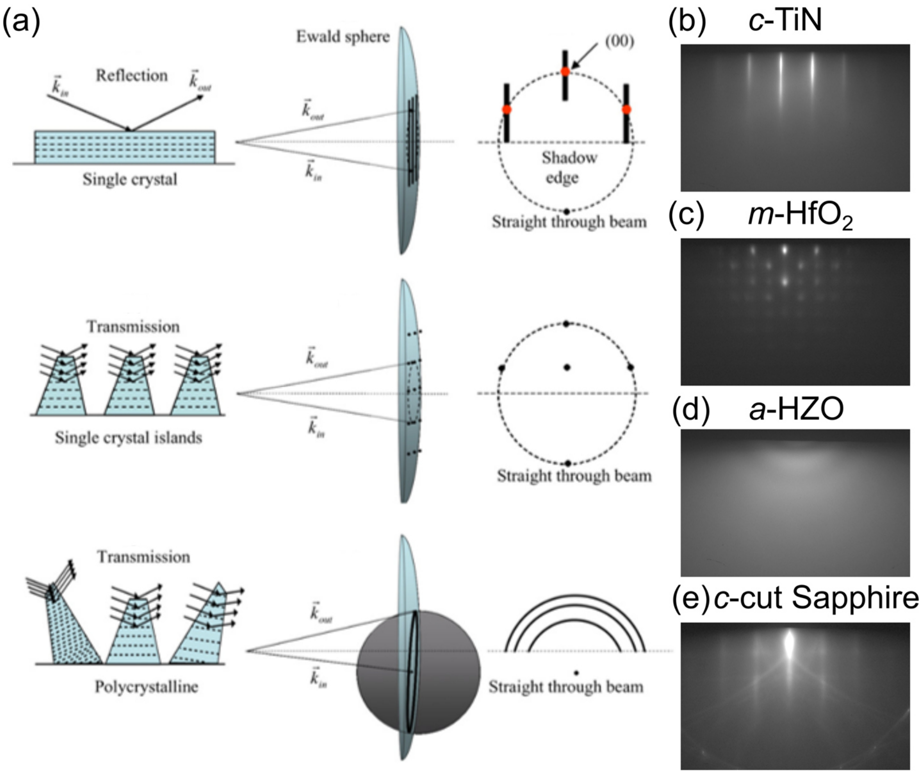

Figure 4-3: (a) Schematic representation of different electron scattering geometries and crystalline structures of films (left) with representation of the Ewald sphere construction (middle) and RHEED diffraction patterns (right). Figure taken from Tang *et al.* [290], http://dx.doi.org/10.1088/0022-3727/40/23/R01; © IOP Publishing. Reproduced with permission. All rights reserved. (b)-(e) Exemplary RHEED patterns of (b) a crystalline (cubic) TiN film with a flat surface grown on *c*-cut Sapphire, (c) a crystalline *m*-HfO_2 film on TiN/*c*-cut Sapphire (island growth), (d) an amorphous HZO film (only blurred rings), (e) a *c*-cut Sapphire single crystalline substrate with an atomically flat surface.

Layers can be textured, which is a result of the created interface between individual (stacked) layers or films on a substrate. Textured films exhibit a characteristic relation to the lattice parameters of the underlying substrate. Epitaxial crystalline films have a near-range order and long-range order with at least one matching crystallographic orientation. A slight deviation of the lattice parameters of substrate and grown film can lead to quasi-epitaxial relations, while an increasing mismatch can result in less but possibly still textured films. On top of *c*-cut Sapphire substrates, TiN can be grown in a quasi-epitaxial way, which is seen as sharp lines in the RHEED patterns (surface rods). Quasi-epitaxial growth of TiN films is also observed on (002)-oriented MgO substrates, due to the low lattice mismatch of the layers (see also chapter 5.2 and Appendix).[291, 292] While a high quality, atomically flat surface is represented by sharp reflections, an increased number of steps or islands present on the film surface is leading to a broadening effect. This is seen for the HfO_2 layer in Figure 4-3 (c). An increased roughness is represented by round dots, which corresponds to an island growth. While for polycrystalline samples, a well-defined ring structure is seen, a diffuse ring-shaped pattern is visible for amorphous *a*-HZO (e). In amorphous films, only a near-range order is present (isotropic).[290]

4.1.3 MBE growth parameters used for HfO_2, $Hf_xZr_{1-x}O_2$, TiN, Pt and Cu film growth

In Figure 4-4, sources and pellets, glued substrates as well as QCMs used in this work are shown exemplarily. Prior to deposition, 5 mm × 5 mm substrates were glued with Ag paste to sample holders using a heating plate (> 100 °C for 15 min). In this work, either only one (centered) sample, two or four 5×5 mm^2 substrates were used (Figure 4-4 (b)). Prior to deposition, the substrate holder and glued substrates were heated up to the desired growth temperature but at minimum to 300 °C for 15 min to remove adsorbates from the surface. The substrate holders were introduced over the load lock into the MBE growth chamber in UHV.

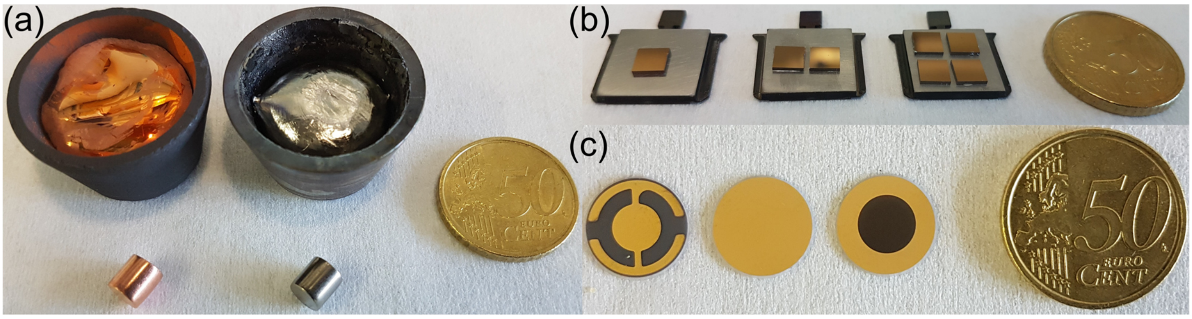

Figure 4-4: (a) Cu (orange) and Hf (grey) source with a Cu and Hf pellet. Those pellets are molten inside the crucible utilizing the electron beam to create the respective source. (b) Glued one, two and four $TiN/SiO_2/Si$ 5x5 mm² pieces as substrates on substrate holders. (c) from left to right: Backside contacts of a gold QCM, clean front side, and front side of a QCM covered with Hf. As a size reference, a 50 Cent coin is shown in images.

The relevant growth parameters of all films grown utilizing the custom-designed MBE system in this work are listed and described in the following. The obtained layer stacks of the finally investigated samples for each series are shown in the respective results and discussion parts.

(1) For the growth of HfO_2, ZrO_2 and their solid solution $Hf_xZr_{1-x}O_2$ films (results presented in chapter 5.1) of different composition on *c*-cut Sapphire substrates from CrysTec GmbH (one-side polished 5 mm × 5 mm × 0.5 mm single crystals of (0001)-orientation with miscut below 0.1°), the following parameters were used (listed in Table 4-1).

Table 4-1: Deposition parameters for $Hf_xZr_{x-1}O_2$ films grown on *c*-cut Sapphire substrates. Additionally, calculated and controlled compositions (QCM thickness ratios) are given. T_{set} is the set temperature of the heat control unit, while T_{pyro} is the temperature at the sample surface prior to deposition measured with a pyrometer, which corresponds to the thermocouple-calibrated temperature. The (system internal) deposition height control was always set to 36.6 and the overall controlled thickness (sum of oxidized Hf and Zr deposited from respective QCMs) was 100 Å.

calculated composition	Hf rate/ Zr rate (rates in Å/s)	controlled composition	oxidation conditions	additional parameters
HfO_2	0.70:0.00	HfO_2	oxygen plasma O*, flow 1 sccm, power 280 W, > 635 mV optical output	rotation speed: 10 rpm; growth pressure: 6.8-7.3 $\times 10^{-5}$ mbar; time ≈ 2:30 min; $T_{set} \approx 120$ °C $T_{pyro} \approx 300$ °C
$Hf_{0.86}Zr_{0.14}O_2$	0.60:0.10	$Hf_{0.86}Zr_{0.14}O_2$		
$Hf_{0.79}Zr_{0.21}O_2$	0.55:0.15	$Hf_{0.81}Zr_{0.19}O_2$		
$Hf_{0.72}Zr_{0.28}O_2$	0.50:0.20	$Hf_{0.72}Zr_{0.28}O_2$		
$Hf_{0.65}Zr_{0.35}O_2$	0.45:0.25	$Hf_{0.64}Zr_{0.36}O_2$		
$Hf_{0.58}Zr_{0.42}O_2$	0.40:0.30	$Hf_{0.58}Zr_{0.42}O_2$		
$Hf_{0.51}Zr_{0.49}O_2$	0.35:0.35	$Hf_{0.51}Zr_{0.49}O_2$		
$Hf_{0.44}Zr_{0.56}O_2$	0.30:0.40	$Hf_{0.45}Zr_{0.55}O_2$		
$Hf_{0.36}Zr_{0.64}O_2$	0.25:0.45	$Hf_{0.38}Zr_{0.62}O_2$		
$Hf_{0.29}Zr_{0.71}O_2$	0.20:0.50	$Hf_{0.28}Zr_{0.72}O_2$		
ZrO_2	0.00:0.70	ZrO_2		

For the film deposition, a Hf (99.9 % purity except Zr, from Kurt J. Lesker Company) and a Zr (Grade 702, from Kurt J. Lesker Company) source were used. Corresponding evaporation rates were calculated using equation (7). An overall rate of 0.7 Å/s (sum of Hf and Zr rate during co-evaporation) was kept constant for all films to reach a broad composition range during mixing/entire phase space from HfO_2 to ZrO_2, also including $Hf_{0.5}Zr_{0.5}O_2$ and to ensure similar oxidation conditions for all films. *In situ* oxidation was achieved by utilizing an oxygen plasma (oxygen radicals O*) created from 1 sccm (oxygen 99.9999 %, from AIR LIQUIDE) oxygen flow using a mass flow controller (from MKS) and a radio frequency power of 280 W applied to the discharge glass tube of the plasma gun (Oxford Applied Research, HD 25). The ionization of oxygen promotes the reaction with the evaporated metal in the chamber.

$$\frac{\rho_{Hf}}{M_{Hf}} \times R_{Hf} = r \times \frac{\rho_{Zr}}{M_{Zr}} \times R_{Zr} \rightarrow R_{Hf} = r \times \frac{\frac{\rho_{Zr}}{M_{Zr}}}{\frac{\rho_{Hf}}{M_{Hf}}} \times R_{Zr} \tag{7}$$

with ρ_{Hf}= density of Hf = 13.09 g/cm³; M_{Hf}= molar mass of Hf = 178.49 g/mol, ρ_{Zr}= density of Zr = 6.49 g/cm³; M_{Zr}= molar mass of Zr = 91.224 g/mol and R_{Hf} as the Hf evaporation rate, R_{Zr} as the Zr evaporation rate and r as the desired ratio. The element-specific parameters are used according to the handbook corresponding to the software of the used Inficon rate control unit. Due to the similar chemical behavior of Hf and Zr, the respective ratios of density to molar mass is similar (≈ 0.07 mol/cm³), which simplifies further calculations and $R_{Hf} = R_{Zr}$ for $r = 1$ is leading to a calculated composition of almost $Hf_{0.5}Zr_{0.5}(O_2)$.

(2) For all stacks with potentially ferroelectric properties, TiN bottom and top electrodes were grown in the MBE chamber by evaporating Ti from an evaporation source (99.995 % purity, from Kurt J. Lesker Company) and *in situ* nitridation utilizing a nitrogen plasma with nitrogen radicals N* (nitrogen 99.9999 %, from AIR LIQUIDE). In advance to all depositions, gas lines are purged to ensure clean gas lines. 30 – 50 nm thick crystalline TiN bottom electrodes were grown on *c*-cut Sapphire substrates at a growth temperature of 750 °C (stabilized prior to deposition for at least 30 min) with a Ti rate of 0.3 Å/s, a gas flow of 0.8 sccm and 350 W power (leading to 900 – 930 mV optical output) applied to the BN discharge tube. This results in a growth pressure of about $7.8 – 8.0 \times 10^{-6}$ mbar. Sample rotation of 10 rpm during growth was started after 20 Å of displayed QCM layer thickness to take RHEED pictures and achieve a smooth layer growth from the start.

Hafnium zirconium oxide films with a composition of $Hf_{0.5}Zr_{0.5}O_2$ (labeled as HZO in the following) and a thickness of 10 – 12 nm were grown on TiN bottom electrodes similar to the conditions as mentioned in (1) – using Hf and Zr evaporation rates of 0.35 Å/s. Amorphous (*a*-)HZO films were grown also at lower temperatures from room temperature to about 120 °C. TiN top electrodes (on top of the HZO layers) were grown at similar conditions, but different growth temperatures were tested ranging from room temperature (RT ≈ 25 °C) up to 300 °C. A low temperature was necessary to prevent crystallization of the HZO films in the monoclinic phase already during TiN top electrode growth (see discussion in chapter 5.2). This leads to TiN/HZO/TiN stacks. As the amorphous TiN was considered being too nitrogen-deficient and the growth conditions changed over time (within one year), the rate was lowered to 0.1 Å/s with 0.8 – 1.1 sccm (8×10^{-6} – 1×10^{-5} mbar) and an increased temperature of 800 – 850 °C had to be used.

Additionally, TiN was grown on (001)-oriented MgO substrates from CrysTec GmbH to achieve a (200)-oriented, quasi-epitaxial TiN bottom electrodes similar to TiN bottom electrodes grown on c-cut Sapphire, were a (111)-oriented, highly-textured electrode can be achieved. From this, *a*-TiN/*a*-HZO/cry-TiN stacks were created. Additionally, HZO/TiN stacks were prepared without a TiN top electrode, but instead with a Pt top electrode achieved by sputtering to investigate the influence of the different top electrodes used. One reference Pt/HfO_2/TiN stack was prepared.

(3) Hafnium oxide-based layers for stacks containing a Pt bottom (on *c*-cut Sapphire) and a Pt top electrode (corresponding to stacks and results presented in chapter 5.3) were grown in the MBE chamber. Pt electrode layers of these stacks were deposited using DC sputtering. 11 – 12 nm thin *m*-HfO_2 and *m*-HZO layers deposited on sputtered Pt bottom electrodes at a temperature of about 300 °C. The growth parameters are listed in (1). Amorphous layers of both types were achieved at room temperature. The four different stackings (Pt/*m*-HfO_2/Pt, Pt/*a*-HfO_2/Pt, Pt/*m*-HZO/Pt and Pt/*a*-HZO/Pt) of the devices are further described and depicted in chapter 5.3.

(4) Pt/*m*-HfO_2/Pt and Cu/*m*-HfO_2/Pt stacks (chapter 5.4) for a direct comparison of the resistive switching characteristics of devices were prepared in a similar way as described in (3). Pt and Cu electrodes were deposited utilizing a DC sputtering unit (results shown in chapter 5.4), while the 10 nm thin *m*-HfO_2 layers were prepared in the MBE system using a Hf evaporation rate of 0.1 Å/s and an O* plasma - oxidation conditions: 0.18 sccm oxygen flow, 200 W plasma power and optical output of about 435 mV. These parameters (reduced rate, flow and power) were chosen based on the results from (1), (2) and (3) to achieve a better growth controllability. The HfO_2 layers for both stacks were grown simultaneously on two glued substrates on the very same holder to have the best possible comparability.

(5) For an oxide layer thickness dependency study (see chapter 5.5), 6 different Cu/x nm HfO_2/Pt stacks were grown using the parameters described in (4). *m*-HfO_2 layers were calibrated to thicknesses of 20 nm, 15 nm, 10 nm (same sample as in 4)), 7 nm, 5 nm and 3 nm by means of XRR investigations in comparison to QCM thickness values. The respective HfO_2 layers were always grown on two Pt/*c*-cut Sapphire samples simultaneously, which results in 12 samples (6 different stacks × 2). One sample (of each thickness) was cut *in vacuo* using a razor blade fixed to the sample garage in the MBE load lock in UHV. The second sample was remaining glued to the sample holder. This sample was transferred back to the MBE growth chamber and covered with about 30 nm of Cu (99.999 % purity, from Kurt J. Lesker Company; rate 0.7 Å/s) and about 5 nm of Pt (rate 0.5 Å/s) by thermal evaporation of the metals utilizing electron beams. This "*in vacuo* capping" preparation method using is relevant especially for stacks with oxygen-deficient switching layers that would otherwise oxidize in contact with air. The performed preparation routine on stacks containing stoichiometric HfO_2 layers was a test run for future works. For the other series of "*in vacuo*-cut" samples, the Cu and Pt top electrode layers were sputtered *ex situ*. These two different preparation methods and more details on the stack and device preparation can be found in chapters 4.2 and 4.3 (experimental), 5.2, 5.3, 5.4, 5.5 and 6.2.2 (results and discussion).

(6) Samples for the first heavy ion irradiation study of this work consisting of about 200 nm thick stoichiometric monoclinic hafnium oxide layers (providing sufficient volume for XRD investigations) grown at about 300 °C on *c*-cut Sapphire substrates were prepared with a Hf evaporation rate of 0.7 Å/s and an oxygen plasma with an oxygen flow of 1 sccm, and 280 W power. The comparably high rates during growth are necessary to achieve a thick layer in a reasonable time (< 40 min). Substoichiometric i.e. oxygen-deficient films of about 200 nm thickness were achieved at 0.5 Å/s, 0.05 sccm flow and 200 W. Calibration was done using XRD to obtain the desired phases.

As a comparison sample series, oxygen-engineered 20 nm thin HfO_x films were grown (non-irradiation samples) on *c*-cut Sapphire substrates using 0.1 Å/s, 0.18 sccm and 200 W for the stoichiometric film, and reducing the oxygen flow steadily (Hf rate for oxygen-deficient films 0.9 Å/s and an oxygen flow of 0.14 sccm/0.10 sccm/0.06 sccm, respectively). Calibration of these films was done using XRD, XRR as well as *in vacuo* XPS. More details can be found in chapters 4.5 & 6.1.1, as well as in literature[145, 293].

(7) Similar films were grown on (001)-oriented Si substrates (from CrysTec GmbH) with a native SiO_2 layer on top. About 200 nm thick *m*-HfO_2 films were achieved using a rate of

0.5 Å/s, a flow of 0.5 sccm and a power of 280 W. Oxygen-deficient 200 nm thick HfO_x and HfO_y (with $x > y$) films were grown using 0.5 Å/s, 0.06 sccm (HfO_x) and 0.05 sccm (HfO_y) and 200 W. It should be mentioned that in this case, similar oxygen flows lead to different oxidation, revealing the outstanding possibility to precisely grow different phases of hafnium oxide by slightly varying the oxidation conditions (see chapter 6.1.3).

Additionally, 10 nm thin stoichiometric and substoichiometric/oxygen-deficient films were grown on top of $TiN/SiO_2/Si$ stacks provided by CEA-Leti to achieve electrical contacting for switching operation (see also chapter 4.7 for details on the external sample preparation; results in chapter 6.1.2 and chapter 6.2.2). These stackings are closer to those of real applications. All stacks are used to study fundamental irradiation-induced changes of the crystal structure. The results can be connected to the obtained switching characteristics of devices.

4.2 Electrode Sputtering

Many electrode layers for the stacks characterized in this work were achieved by sputtering processes, mostly using DC (direct current) magnetron sputtering but also RF (radio frequency) magnetron sputtering. DC magnetron sputtering is a PVD method for growing films based on direct current as the power source. This method is well-suited for metal deposition. A plasma is injected in a vacuum chamber with a pressure in the 10^{-3} mbar-range from an inert process gas like Ar. The target material such as Au, Ag or Cu in form of a sputtering target acts as the anode for discharge. During the high-energetic bombardment of the target surface, target material is atomized, which condenses on a substrate surface (cathode) in form of a coating. In magnetron sputtering, the ions of the plasma are forced in a concentric area near the target surface by an applied magnetic field. Advantages of this sputtering process are the relatively simple and fast deposition of pure films with good coverage and high adhesion at low temperature. RF magnetron sputtering can be used to deposit conducing materials but also non- or less-conducting target materials such as TiN, where a current cannot run through the target or charge accumulation can occur. RF sputtering is based on a high frequency alternating field by changing the bias of anode/cathode in cycles at a high rate. The fluctuating field results in a negatively-charged target material, where ionized gas ions remain at the anode after one cycle, while the reverse polarity leads to positively-charged sputtering gas atoms that are accelerated towards the substrate in the subsequent cycle. This change prevents permanent charge-buildup. In this process, it is possible to use an inert gas such as Ar only or additionally provide a more reactive gas such as N for nitridation.[294, 295]

Sputtering experimental: In this work, electrodes were achieved by sputtering as listed below for the corresponding stacks as listed in chapter 4.1.3. Thin films were directly calibrated using X-ray reflectivity (XRR) investigations, while for the scaling of thick films thinner layers of 20 nm or 50 nm thin films were deposited, their thickness measured and the necessary deposition time calculated to achieve the desired thickness. A control of the finally achieved thickness can be done by utilizing profilometry measurements.

(1) For the $Hf_xZr_{1-x}O_2$ mixing series no electrodes were sputtered.

(2) For all stacks with potentially ferroelectric properties (compare chapter 5.2), about 100 nm Pt (current: 30 mA; target: 99.99 %, from Umicore) and 250 nm Au (30 mA;

99.99 &, from BALTIC präparation) were deposited using DC sputtering from metal targets in a Q150T deposition system by Quorum Technologies on top of the TiN top electrode or the HZO or HfO_2 layer. This results in Au/Pt/TiN/HZO/TiN, Au/Pt/HZO/TiN and Au/Pt/HfO_2/TiN stacks. Additional trials to prepare TiN electrodes on *c*-cut Sapphire substrates were performed by RF magnetron sputtering (in a separate vacuum chamber) from a bonded TiN ceramic target using a power of 50 W, 1.4 sccm N_2/0.6 sccm Ar flow leading to a growth pressure of about 2×10^{-4} mbar and varied substrate temperatures (RT, 100 °C, 200 °C, 320 °C and 480 °C).

(3) About 60 nm thick bottom electrodes were deposited on four *c*-cut Sapphire substrates using DC sputtering. On top of the *m*-HfO_2, *a*-HfO_2, *m*-HZO and *a*-HZO (MBE grown) layers, about 100 nm thick Pt and 250 nm thick top electrodes were sputtered (compare results and discussion part in chapter 5.3).

(4) For the Pt/*m*-HfO_2/Pt and Cu/*m*-HfO_2/Pt stacks, 130 nm Pt plus 250 nm Au and 30 nm Cu (30 mA; 99.9 %, from BALTIC Präparation) plus 100 nm Pt/250 nm Au were sputtered, respectively (chapter 5.4).

(5) For the oxide layer thickness dependency study using Cu/HfO_2/Pt devices of 6 different stacks (chapter 5.5), 60 nm thick Pt serving as the bottom electrode on *c*-cut Sapphire substrates, and 30 nm of Cu, 100 nm of Pt and 250 nm of Au as top electrode layers were sputtered on top of the HfO_2 layers (*in vacuo* “cut” in MBE load lock – compare 4.1.3). For the *in vacuo*-capped layers (with Cu and Pt in MBE), 100 nm of Pt and 250 nm of Au were *ex situ* sputtered afterwards, additionally.

(6) No electrodes were sputtered for the heavy ion irradiation study on 200 nm thick stoichiometric monoclinic hafnium oxide layers grown on *c*-cut Sapphire substrates.

(7) As a protection layer for the focused ion beam lamellae preparation for subsequent STEM analysis, 100 nm of Pt were sputtered on top of 200 nm thick *m*-HfO_2 films grown on SiO_2/Si and on 10 nm thin HfO_2 grown on TiN/SiO_2/Si (provided by CEA-Leti, compare chapter 4.7). For electrical characterization as shown in chapter 6.2.2, 100 nm of Pt and 250 nm of Au serving as top electrode layers were sputtered on top of both, as grown and irradiated (5×10^{12} ions/cm^2) 10 nm HfO_2/TiN/SiO_2/Si stacks.

4.3 Post-deposition annealing and sample structuring

In this chapter, treatments performed after the sample synthesis in MBE as conducted in this work are introduced, namely post-deposition annealing (1) and sample structuring (2). First, annealing experiments of samples with potentially ferroelectric properties as discussed in chapter 5.2 are described. As this annealing procedure is only performed after the TiN or Pt top electrode was deposited on top of the oxide layer and no other annealing steps were included, it is named post-deposition annealing for simplification. Second, the sample structuring necessary to achieve measurable electric devices is described. This includes the top electrode layer sputtering as described in the previous chapter as well as optical lithography and in several cases also ion beam etching (IBE). The preparation of external samples is described in chapter 4.7.

(1) Most **post-deposition annealing experiments** were conducted in a vacuum chamber usually used for pulsed layers deposition utilizing the mounted infrared diode laser system (by Jenoptik) with a wavelength of 938 nm. This laser is used for heating of the sample holder and the attached sample from the backside, while the temperature is monitored using an IR pyrometer (SensorTherm). The aim of the post-deposition annealing was to crystallize the HZO layers (initially amorphous after thin film growth, sandwiched between two TiN electrodes or a TiN BE and a Pt TE) in a polar phase showing ferroelectric properties. As a reference, a stack containing a polycrystalline HZO film was annealed. Annealing parameters were varied from 400 – 800 °C with ramp-rates (up and down – for quenching) ranging from 5 °C/s to 20 °C/s and a holding time of 20 s to 2 min. Individual parameters used are shown with the results in chapter 5.2. All annealing experiments were conducted in 380 Torr N_2 or N_2/Ar atmosphere (maximum possible), by introducing the gases in the vacuum chamber and stopping the flow as soon as the desired background pressure was reached. A few additional post-annealing attempts were conducted in the MBE system directly after TiN top electrode growth at 400 °C – 600 °C for 10 min in vacuum using resistive heating. One additional TiN/HZO/TiN/*c*-cut Sapphire test sample was annealed in a furnace at 400 °C for 1 h in air (ramp-rate 5 K/min).

(2) **Sample structuring** can in general be performed in many different ways, including photolithography like optical lithography, electron lithography, chemical etching, ion beam etching, etc. as used in both (semiconductor) industry and in research laboratories for different purposes such as electrical devices from multilayer structures and integrated circuits. In this work, optical lithography and ion beam etching procedures were used. In optical lithography, the image of a so-called photomask is transferred by applying UV light to a photoresist, i.e. a light-sensitive polymer. Exposed areas are either hardened or dissolved, dependent on the nature of the photoresist, and serve as masks (predefined open parts) for subsequent deposition processes or etching (removal of material to achieve indentations). Ion beam etching (IBE), also called ion beam milling, is a technique to etch profiles in materials by utilizing a direct beam of ions at a sample surface in high vacuum. In this work, depending on the initial stacking after growth of layers in the MBE system, subsequent sample preparation, including structuring was achieved in two different ways, in this work named “with IBE” and “without IBE”. A schematic representation of the different workflows is given in Figure 4-5.

(a) ***<u>“With IBE”:</u>*** For stacks with a closed top electrode layer after growth in the MBE system, further top electrode layers were sputtered before lithography was performed, followed by an ion beam etching step (see chapters 5.2 & 5.5; as an exception, this procedure was also applied for the test sample “annealed Pt/HZO/TiN” as described above in (1). This routine is called “with IBE” in this work. As an example, the preparation steps to obtain (Au/Pt/)Cu/HfO_2/Pt devices is shown in Figure 4-5.

After the HfO_2 layer was grown and a Cu and a Pt layer or a TiN top electrode layer was added in the MBE system, the samples were removed from the vacuum chamber and additional thicker Pt and Au layers were sputtered using DC sputtering. This results in a stacking with closed electrode layers as the top layers. For the subsequent optical photo-lithography routine performed in a clean room environment, the samples were cleaned by rinsing with acetone and isopropanol. Then, a negative photoresist (ma-N 1429, Microresist Technology) was applied on top (Au surface) in a spin coating process (6000 rpm, 40 s), followed by edge-beard removal with a razor blade and a pre-bake step at 105 °C for 2 min to remove residual solvents.

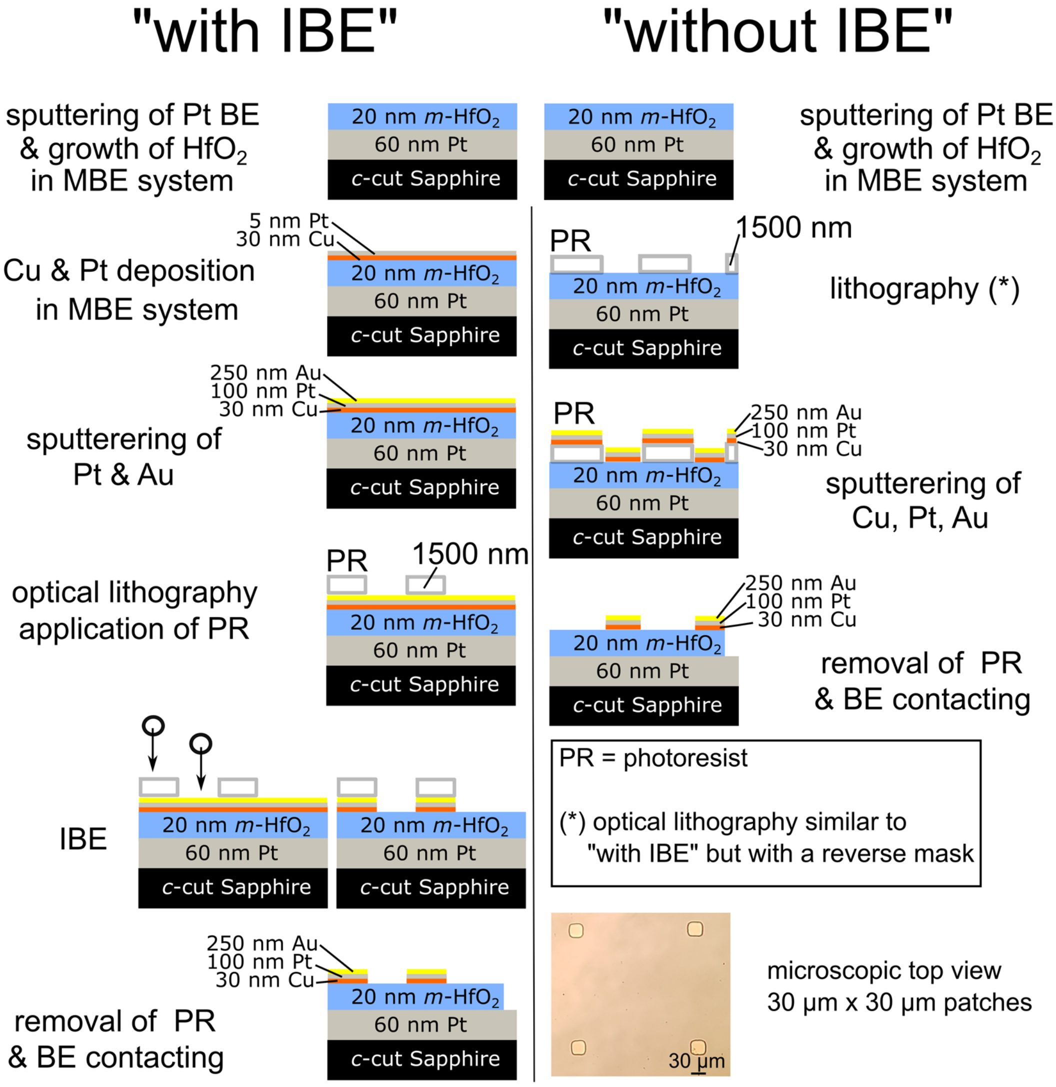

Figure 4-5: Schematic representation of applied stack preparation possibilities used. The two workflows are named “with IBE” and “without IBE”. Both yield the same stacking with 30 µm × 30 µm patches (device area). Additionally, an exemplary microscopic top view of the sample surface with four devices is shown.

Structures are achieved from a lithography mask with the desired predefined structure (chromium mask on a glass plate), which was pressed against the surface of the sample with the photoresist, positioned using a mask aligner (MJB4, SÜSS MicroTec) and radiated with UV light (wavelength 365 nm; required dose ≥ 635 mW*s/cm²). The used masked for this “with IBE” sample preparation has 30 μm × 30 μm patches that are exposed to UV light. Afterwards, a development step is carried out placing the sample in a developer (ma-D533/S, Microresist Technology) for 80 s, where the residual photoresist (the part not hardened by UV light) is removed in a deionized water bath (dried with nitrogen flow). With an optical microscope, the achieved photoresist patches can be checked. Afterwards, the samples need to be ion beam etched to remove the surface layer that are not protected by the photoresist patches, which have an area of $30 \times 30\ \mu m^2$ and a thickness of about 1.5 μm.

For ion beam etching, the samples are glued with Ag paste (above 60 °C but below 100 °C for more than 30 min to affect the heat-sensitive photoresist as less as possible) on sample holders and introduced in the vacuum chamber of the custom-designed IBE system (by Mantis Deposition). The used IBE procedure is a dry etching process, where material is removed from a sample by ion bombardment from a created plasma (RF generator).[296] In this work, IBE is carried out using a 150 W Ar plasma with an acceleration voltage (18 mA current) and cooling of the sample stage with liquid nitrogen to prevent heating, which could otherwise result in undesired diffusion processes in the sample or a hardening (further cross-linking) of the photoresist that cannot be removed anymore afterwards. This IBE procedure was never taking longer than 15 min. After IBE, the photoresist is removed in an acetone bath or in pre-heated remover (ReM 500, Microresist Technology). Afterwards, the sample is cleaned by rinsing with acetone and isopropanol and dried with nitrogen flow. An optical microscope was used to check the success of the process. Finally, the desired structure with 140 devices with a patch size of 30 μm × 30 μm is achieved (in best and cleanest preparation case).

After IBE, two problems occurred, which were part of the subsequent optimization processes:

- Potentially ferroelectric samples (see chapter 5.2 for TiN/HZO/TiN and Pt/HZO/TiN devices) were etched to the TiN bottom electrode surface. Those were found to potentially face an increased leakage current, which could be a result of redeposited conductive material at the edge of a device (stack) or other detrimental effects that can be induced by dry etching[297]. Additionally, an oxidation of the TiN surface is likely for the prepared samples (substoichiometric TiN). This can result in a poor electrical contacting of the bottom electrode. The occurrence of such disadvantages for the specific stack preparation used was not known at the time of the conduction of these studies. An advantage of stopping the process at the TiN surface would be the achievement of a contact area for the bottom electrode tip for electric measurements in a clean process. The established endpoint detection in the IBE system utilizing a quadrupole mass spectrometer to monitor the quantity of Ti, Zr, Hf, Au, Pt and Cu allowed a good control of the point, where etching could be stopped by closing shutter in front of the sample.
- To achieve devices showing lower leakage and a more uniform switching behavior, the Cu/HfO_2/Pt samples presented in chapter 5.5 were only etched to the HfO_2 surface as depicted in Figure 4-5. The bottom electrode is reached by scratching to the bottom electrode at the edge of a sample, applying a small Ag paste dot to connect bottom electrode and Au layer at the edge of the sample, where the bottom electrode tip was placed. The advantage of this procedure is the simple preparation of working devices. A disadvantage is the quite “dirty” use of scratching and Ag paste. Potential influences of the preparation techniques on the device behavior are discussed in the results and discussion part - chapter 5.5.

(b) ***<u>"Without IBE"</u>*:** For stacks with a HfO_2 or HZO film as the top layer after growth in the MBE system (all samples which were not treated as discussed in a., optical lithography was used BEFORE the top electrode layers were deposited by sputtering (compare Figure 4-5). This routine is named "without IBE" in this work and often also called "(normal) lift-off". The corresponding electrical results of the achieved devices are shown in chapter 5.3 (Pt/HfO_2 or HZO/Pt), 5.4 (Pt/HfO_2/Pt and Cu/HfO_2/Pt), chapter 5.5 (Cu/HfO_2/Pt) and chapter 6.2.2 (Pt/HfO_2/TiN). After photoresist was applied on the HfO_2 or HZO films by spin coating, edge-beard removal and 2 min of pre-baking, structures were achieved again by UV exposure through a lithography mask. In contrast to the lithography performed for "with IBE" samples, a negative mask is used for this process ("without IBE"). With this mask, $30\,\mu m \times 30\,\mu m$ squares are photoresist-free after UV exposure and the subsequent development process, while photoresist is hardened on the rest of the sample surface area. Afterwards, top electrode layers (Cu, Pt, Au) are applied by DC sputtering on top of the whole sample. The metal layers then cover the top of the photoresist as well as the HfO_2 layer in the $30\,\mu m \times 30\,\mu m$ holes. The photoresist and all layers on top are removed afterwards by placing the samples in an acetone bath (similar to (a)). With this, the same stacking is achieved.

4.4 Heavy ion irradiation experiments

The irradiation experiments with swift heavy ions were conducted at the GSI Hemholtzzentrum für Schwerionenforschung in Darmstadt at the universal linear accelerator (UNILAC), which is schematically depicted in Figure 4-6.

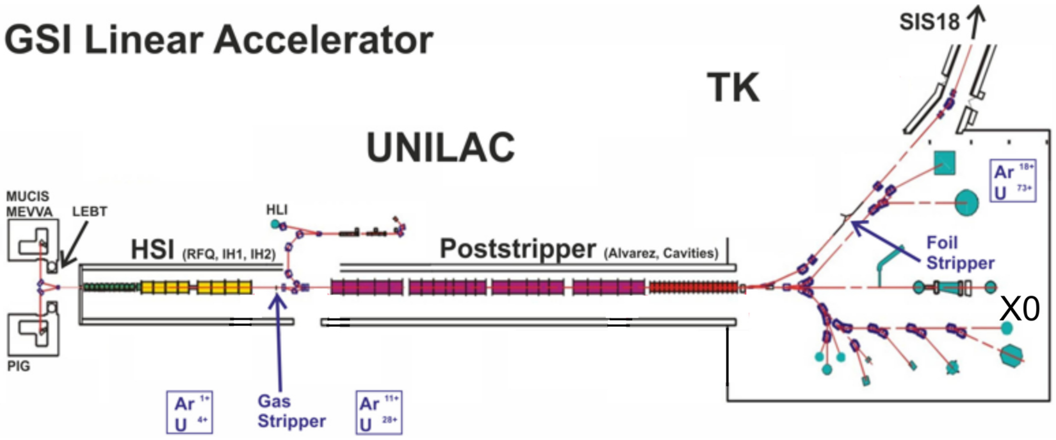

Figure 4-6: Schematic representation of the UNILAC at GSI in Darmstadt. Ions from one of the ion sources are pre-accelerated in the high current injector. At the gas stripper, the charge state of the ions is increased and then the ions are further accelerated in a four-tank Alvarez structure. The beam can be delivered to different experimental stations in the UNILAC hall or injected into the heavy ion synchrotron SIS 18. Figure adjusted from GSI website, where additional information can be found.[298]

The 120 m long UNILAC at GSI can be used to accelerate all elements up to uranium. Specific energies up to 11.4 MeV/nucleon (MeV/u) can be reached, which corresponds to about 16 % of the speed of light. Higher beam energies are obtained by injecting ion pulses into the heavy ion synchrotron SIS18. All experiments for this work were conducted at the X0-beamline at the end of the UNILAC. This beamline is operated by the materials research department and exclusively dedicated to the irradiation of user samples or electronic devices. More information can be found on the webpages of the GSI facility[299-301]. For the irradiations of the samples of this work, 8.6 MeV/u Au ions were used. This initial energy is slightly reduced to 8.3 MeV/u (≈ 1.635 GeV) because the beam passes through a secondary electron transmission monitor consisting of three 1 μm thick Al foils before reaching the samples. All irradiations were performed under normal beam incidence and at room temperature.

Some of the samples were analyzed prior to the ion irradiation by X-ray diffraction or electrical measurements. For the irradiation the samples were fixed to 5×5 cm^2 aluminum plates using double-sided tape. The standardized plates were inserted in vacuum by a remote-control inlet system. By defocusing the beam using quadrupole magnets, a homogeneously irradiated area of 5×5 cm^2 is possible. The ion flux during irradiation was kept below $\sim 5\times10^8$ ions/cm^{2}s to avoid macroscopic heating of the samples. The overall sample temperature is estimated to not exceed 50-60 °C during irradiation. In the actual study, the samples were exposed to different fluence series to investigate ion-induced structural and electrical property changes. For HfO_x-based samples, the fluence values ranged from 5×10^9 to 8×10^{12} ions/cm^2, while for Ge-Sb-Te-based samples, fluences from 5×10^9 to 1×10^{13} ions/cm^2 were used. Details can be easily seen from the results presented in chapter 6. The uncertainty of the fluence as a consequence of inhomogeneous beam defocusing is about 10 – 20 %. During irradiation, samples were "floating", which means that no electrical grounding or electrical contacting of bottom or top electrodes was used. After the irradiation, the samples had to stay in quarantine until deactivated before transport and characterization were possible.

The interaction between the ions and the target matter with characteristic values like the transferred energies was calculated using the TRIM ("Transport of Ions in Matter") code (TRIM-2010).[235, 302] The code allows the simulation of interactions in multi-layer configurations and compounds, like it is the case of HfO_2 grown on TiN and a SiO_2/Si substrate. In this work, the TRIM ("Transport of Ions in Matter") code (TRIM-2010) was used to simulate interactions in multi-layer configurations and compounds, like it is the case of HfO_2 grown on TiN.

For the irradiation of all stoichiometric pure and doped HfO_2 films (density of about 9.68 g/cm^2)[125] with 1.635 GeV Au ions, the electronic energy loss is about 53 keV/nm (chapters 6.1.1, 6.1.2, 6.2.2.) The slowing down process of the ions is dominated by electronic interactions. The nuclear energy loss is only about 69 eV/nm, resulting in only 4.4×10^{-4} displacements per atom (dpa), which was determined by Full Cascade TRIM Calculations. Thus, elastic collisions only play a minor role. The ion range in the stacks is in μm-range and therefore exceeding the overall stack thickness (always below 1 μm). As a consequence, the ions stop in the substrate. The electronic energy loss in oxygen-deficient HfO_x (exact stoichiometry of as grown and irradiated films not known) with an increased density of 10 – 11 g/cm^2[145] is generally expected to exceed the value of 53 keV/nm obtained for HfO_2 (chapters 6.1.1, 6.1.3). In Ge-Sb-Te-based phase-change materials (chapter 6.4), the electronic energy loss is about 34 keV/nm.

4.5 Characterisation of film structure and composition

For the characterization of the crystalline structure X-ray diffraction was used, while thickness, density and roughness of the films was determined using X-ray reflectivity. The film composition (Hf:Zr ratio in $Hf_xZr_{1-x}O_2$ films and oxygen content in HfO_x films) was investigated utilizing X-ray photoelectron spectroscopy. These techniques will be briefly introduced in this chapter together with the experimental method as performed in this work. Additionally, relevant (scanning) transmission electron microscopy techniques from a large pool of advanced techniques will be discussed in the context of this work.

4.5.1 X-ray diffraction

X-ray diffraction (XRD) is a fast, non-destructive and precise characterization technique with a multitude of operation modes that can be used to investigate characteristics like crystal structures, grain sizes, film textures, and strain/stress states of crystalline materials. XRD is based on two principles – (1) Thomson or elastic scattering of photons allows the treatment of atomic planes as (semi-transparent) mirrors and (2) the wavelength of the used electromagnetic radiation called X-rays below 1 nm (10^{-10} – 10^{-12} m) is of the same order of magnitude as the interatomic distances in the investigated crystals (Å-range/10^{-10} m). The X-ray beam is diffracted at the periodically arranged atomic planes, which results in constructive and destructive interference. This phenomenon can be visualized as depicted in Figure 4-7 (a), and described by Bragg's law (equation (8)).

$$\mathrm{n} \times \lambda = 2d_{hkl} \times \sin(\theta) \tag{8}$$

where the plane spacing d_{hkl} (individual planes identified using Miller indices *hkl*) is directly related to the wavelength λ and incident angle θ (Bragg angle) of the X-ray beam. n is an integer starting with 1 that represents the order of the diffraction maxima. For each group of lattice planes of a crystal, diffraction conditions are fulfilled for specific Bragg angles. Constructive interference occurs when the path difference Δ between scattered waves is an integer multiple of λ ($\Delta = \mathrm{n} \times \lambda$), which results in a measurable intensity of diffracted X-rays. The constructive and destructive interference is dependent on the crystal structure under investigation, following cancellation rules.[303]

An X-ray diffractometer consists of different components: An X-ray source including a shutter, primary beam or incident optics, a goniometer (and sample holder/stage), receiving or diffracted beam optics, and a detector. This setup is usually situated in a radiation enclosure. It is closed during running experiments, which are therefore controlled externally using a computer software. X-rays are generated in an X-ray source (X-ray tube), where a cathode material is heated and emits electrons, which are accelerated towards an anode material like Cu by an electric field. The high-energy electrons collide with the anode material, creating continuous radiation (Bremsstrahlung) and characteristic for the allowed transitions in the material of the anode (e.g., Cu $K_{\alpha1}$, $K_{\alpha2}$ and K_β). The beam is then guided by incident optics such as Soller slits, incident slits, divergent and axial slits towards the sample, where it is diffracted at the periodically arranged atoms in the crystal structure. Afterwards it passes secondary or receiving optics such as parallel slit analyzers, Soller slits, scattering and receiving slits before reaching the detector. To achieve a monochromatic X-ray beam, different monochromators can be used such as a primary 2-bounce monochromator (2×Ge(200)) mounted on the incident optics side, as well as a graphite secondary monochromator mounted directly in front of the detector. Both were (separately) used in this work. The detector used in this work is a 1D detector (scintillation counter). An attenuator should be used to reduce the intensity of the X-ray beam reaching the detector, preventing damaging of the detector.[303]

In general, different geometries can be utilized, like the Bragg-Brentano or parallel beam geometry. In this work, a parallel beam setup in a 4-circle goniometer as commonly used for thin film characterization, was utilized. The setup is schematically shown in Figure 4-7 (b).

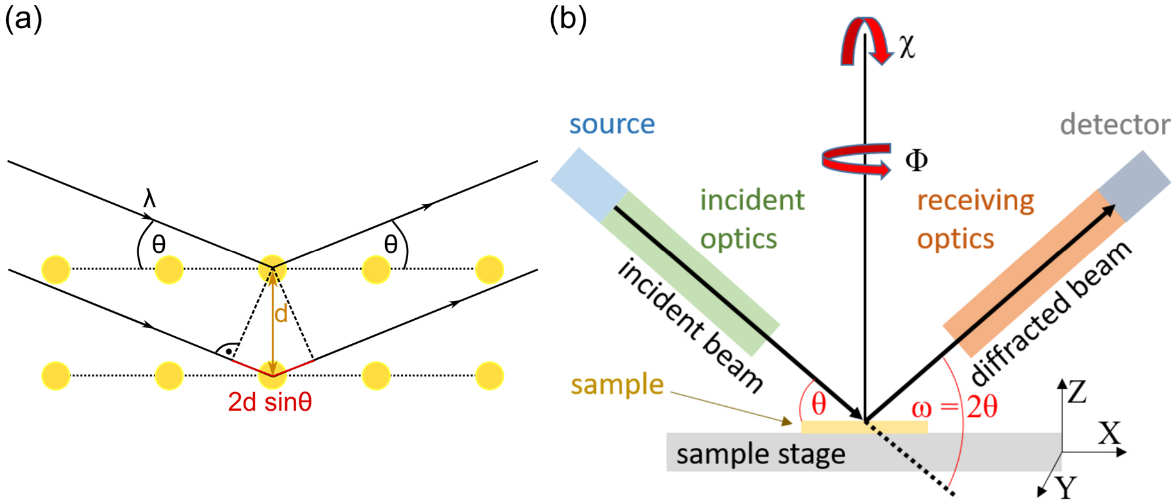

Figure 4-7: (a) Geometric visualization of Bragg's law with the incident beam being diffracted at the layers of atoms in the angle θ, depending on the distance of the lattice planes d and the wavelength λ. (b) Schematic arrangement of the parallel beam four-axis goniometer setup and the optical path with corresponding variable axis with angles θ, ω, χ (tilting), Φ (sample rotation).

In contrast to measurements performed in Bragg-Brentano geometry, larger defocusing of the beam is avoided in parallel beam geometry. In the used setup, a parallel beam is achieved by passing the divergent X-ray beam through a multilayered mirror (Göbel mirror) and an aperture. The obtained beam consists of parallel individual X-ray beams that reach the substrate surface at the same incident angle. The sample is positioned in a horizontal position on a sample stage. This setup allows thin film measurements under different angles to perform e.g., gracing incidence scans, rocking curve scans, pole figure scans, and also reciprocal space maps. More information on these techniques can be found in literature[303].

This work focuses on the performed 2θ/ω-scans, which are particularly suited for the mostly polycrystalline, but still oriented (textured) nature of the investigated films and multilayer stacks grown on single crystalline substrates. For epitaxial layers, further pole-figure measurements, rocking curves and additional in-plane investigations would be of interest, which is dependent on the film thickness (sufficient crystalline volume) and crystalline quality, as well as the used setup i.e. intensity, scan speed, step-width, number of data points and achievable signal-to-noise ratio. In the following chapter 4.5.2, the also used X-ray reflectivity will be introduced.

For 2θ/ω-scans, an alignment for the correct height (half-cut intensity) is performed in Z and ω, followed by an alignment to the Bragg plane of the single crystalline substrate (alignment to substrate reflection) to achieve the maximum possible intensity. The scan itself is a symmetric scan, where the primary and secondary arm are moved simultaneously at the same angular speed. In this configuration, diffraction is always obtained from planes parallel to the surface, which is mainly used for textured films. Different Bragg planes can be investigated by moving different angles like χ and ω. For the 2θ/ω measurements, an XRD pattern showing intensity in counts per second in dependence of 2θ in degree is given. In general, a reflection is characterized by position, intensity, width and shape including asymmetry. For powders, the 2θ angle is only dependent on the lattice parameters (spacing of the layers). By expecting the crystal class or determining it from a Laue pattern, parameters defining the crystal structure (lattice parameters a, b, c, α, β, γ) can be determined, including the space groups of the phases. Further analysis is possible by comparing the obtained patterns showing characteristic reflections with reference results e.g., from Powder Diffraction Files (PDF) respectively Crystallographic Information Files (CIF), which are collected in data bases such as the ICDD (International Center for Diffraction Data) data base. With this, compounds with different phases and structures can be identified and distinguished. For thin film, performing Rietveld refinement is difficult due to texture effects. A disadvantage of XRD for thin film characterization is the potentially difficult data analysis including e.g., the nearly impossible deconvolution of strain/stress and compositional changes (like in HfO_x[145]) both leading to shifts of reflection positions in 2θ. Also, instrumental influences as well as alignment problems (e.g., wrong height) play a role. Additionally, the width of the reflection is dependent on grain size that is often interconnected with film thickness, and to compositional as well as strain gradients.

Polymorphism in HfO_x: An important characteristic relevant to this work is the structural similarity of the polymorphous HfO_x (as described in chapter 2.1.5), which is characterized by the possible presence of multiple phases with only a small variation of the lattice parameters. This can result in very similar diffraction patterns. Exemplary simulated XRD patterns of polycrystalline powders from corresponding PDF and CIF data are shown in Figure 4-8. The monoclinic phase represents the thermodynamically stable phase at ambient conditions for both powders and films (m-HfO_2, space group $P2_1/c$ or also $P2_1/a$, ICDD 00-034-0104[123, 124]) with the characteristic $(\bar{1}11)$ reflection in the XRD pattern at $2\theta \approx 28.3°$. Next to this, a tetragonal phase (t-HfO_2, space group $P4_2/nmc$, ICDD 01-078-5756[126]) and a cubic phase (c-HfO_2 - $Fm\bar{3}m$, ICDD 04-011-9018) can be stabilized at higher temperatures. Both phases have a characteristic reflection at $2\theta \approx 30°$. This is also true for the pressure-stabilized orthorhombic phases oI-HfO_2 (space group *Pbca*, ICDD 01-083-0808) and oII-HfO_2 (*Pnma* or also *Pmnb*, ICDD 04-013-7323) in powders. These phases are also often assigned to the crystal structure of thin films which are stable at ambient conditions, mainly due to their similarity of the XRD patterns. The metastable, polar ferroelectric phases, referred to as an orthorhombic phase (o-HfO_2 or oIII-HfO_2, space group $Pca2_1$[130]) and the rhombohedral phase (r-$Hf_{0.5}Zr_{0.5}O_2$ - $R3$ or $R3m$[127]) also have similar reflections at $2\theta \approx 30°$ (not shown for $R3$). Additionally, an oxygen vacancy-stabilized rhombohedral phase of HfO_x can be stabilized in undoped, oxygen-deficient films (theoretical: r-$HfO_{1.5}$/experimental: r-$HfO_{1.7}$ - $R3m$[128]).

X-rays are mainly scattered by the electrons/electron density surrounding the nuclei. The scattering factor increases with the atomic number Z. In HfO_x, the scattering process is thus dominated by the Hf sublattice. As a consequence, one HfO_x phase with a defined Hf sublattice but slight differences in the O sublattice cannot be distinguished by XRD. However, these changes can potentially lead to drastic property changes of the films (e.g., non-polar vs. polar).

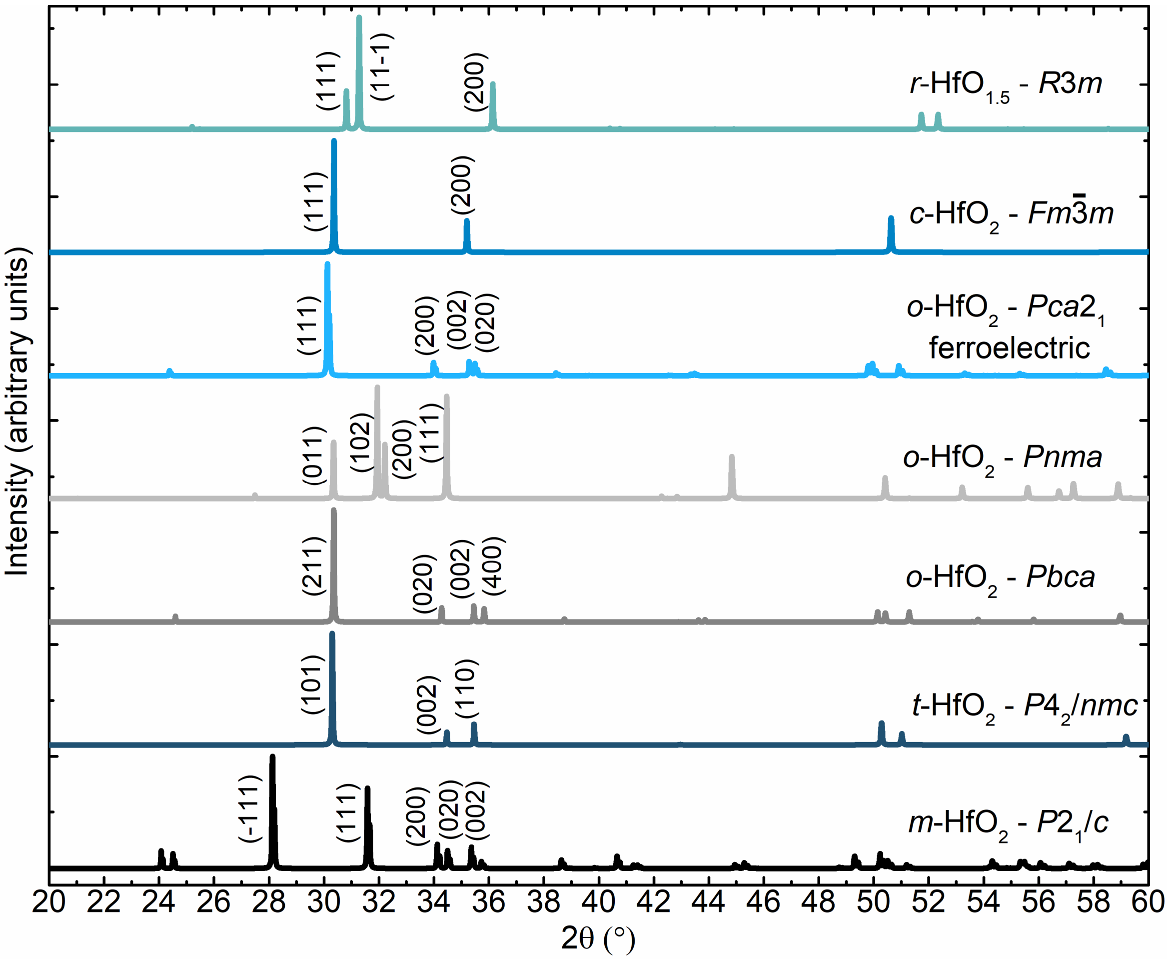

Figure 4-8: Exemplary XRD patterns of polycrystalline powders simulated using VESTA[129], with information from ICDD PDF and corresponding crystallographic information files (for $P2_1/c$, $P4_2/nmc$, *Pbca*, *Pnma* and $Fm\bar{3}m$) and DFT calculations (for $Pca2_1$ [130, 131] and $R3m$[128]). The lattice parameters and simulated pattern of the *r*-HfO$_{1.5}$ phase is very close to those obtained from experimental data[128]. The most-relevant reflections for the discussions in this work are indexed.

In principle, a distinction of these similar phases from XRD patterns of polycrystalline bulk (powder) samples can be done by analyzing the occurring splitting of the characteristic reflections. As an example, the (200) reflection of the cubic HfO$_2$ splits into (200), (002) and (020) in the $Pca2_1$ orthorhombic structure, while (111) of the cubic structure splits into (111) and $(11\bar{1})$ when undergoing a transition to the rhombohedral structure ($R3m$). This is accompanied by a shift towards larger diffraction angles, due to the smaller unit cell present.

For thin films, the distinction of the phases from XRD patterns especially from 2θ-scans is challenging, due to the similarity of these phases, which are all distorted variants of the fluorite structure ($Fm\bar{3}m$). This is in particular relevant for highly-textured or even epitaxial films showing only a low number of reflections (sometimes even only one reflection in the XRD pattern).[128, 145, 152] Due to the mentioned interconnection of effects leading to shifts and broadening of reflections, a distinction is challenging. This can result in an incorrect assignment of a phase to a specific crystal structure from absolute diffraction angles where characteristic 2θ reflections are found. A clear identification requires huge efforts. For highly textured films of a very good crystalline quality, it might be possible to determine the crystal structure using a combination of different diffraction techniques such as out-of-plane and in-plane scans, even though this has been proven to be very elaborate.[127, 128] To give an example: In oxygen-deficient

HfO_x, a $(111)_r$ reflection is visible in the XRD patterns from the out-of-plane 2θ-scans, however, a $(11\bar{1})_r$ reflection is not visible.[128, 145] Additionally, the $(111)_r$ reflection of the experimentally deduced structure is located at lower 2θ angles than expected from the simulated powder pattern. This is likely to be a result of the differing composition ($HfO_{1.7}$ versus $HfO_{1.5}$). Furthermore, reflections obtained for oxygen-deficient HfO_x films are found to show an increased broadening with higher oxygen-deficiency, which can lead to additional uncertainties. From in-plane measurements, a $(11\bar{1})_r$ reflection was found next to the $(111)_r$ reflection but only with a difference of $2\theta \approx 0.25°$.[128] Additional pole figure measurements can help to reveal texture and preferred orientation of these highly textured layers. However, the identification of the phases in HfO_x represents a challenging and elaborate task even for films of good crystalline quality.

In XRD patterns obtained from polycrystalline films, the mentioned peak splitting might be usable to distinguish the phases. However, for slightly textured but not epitaxial films, a distinction becomes again challenging due to the aforementioned effects (e.g., missing reflections, changed intensity ratio of reflections, shift and broadening of reflections) and also much lower intensities obtained due to the reduced volume of the films when compared to bulk samples. A distinction of phases gets even more challenging for phase mixtures in a film leading to potentially overlapping reflections in the XRD patterns. Then also the performance of pole-figure or other in-plane measurements and the interpretation of corresponding data becomes difficult.

XRD experimental: Structural investigations using XRD in this work were carried out using a Rigaku SmartLab diffractometer with a rotating 9 kW Cu anode (K_α-radiation, $\lambda \approx 1.54$ Å). For measuring (highly-)textured films of good crystalline quality (chapter 5.5 - HfO_2 films grown on Pt, chapter 6.1.1 – oxygen-engineered 20 nm thick HfO_x films grown on *c*-cut Sapphire), a 2-bounce Ge(200) monochromator (2×Ge(200) with very high resolution of 0.01°) and an incident slit of 2 mm was used (0.5 – 1 °/min, 0.01 ° steps). This arrangement was also used to measure 200 nm thick HfO_x films grown on SiO_2/Si (chapters 6.1.2 and 6.1.3) and 10 nm thin HfO_x films grown in the MBE system on top of TiN/SiO_2/Si (0.5 °/min, 0.03-0.05 ° steps). To obtain higher intensities, the slit size was increased to 5 mm and a secondary graphite monochromator was used for measuring mixed or annealed samples and HfO_2-based reference stacks (chapters 5.1, 5.2 and 5.3), which are lower crystalline quality. The same was done for XRD investigations on external ferroelectric samples (Fraunhofer IPMS CNT), 10 nm thin HfO_2-based stacks (CEA-Leti) and polycrystalline Ge-Sb-Te-based stacks (CEA-Leti). All measurements were performed using 2θ/ω-scans with a height alignment as well as substrate alignment (*c*-cut Sapphire (006) $2\theta \approx 41.67°$; Si (004) $2\theta \approx 69.14°$; MgO (002) $2\theta \approx 42.93°$). For all samples, 2θ/ω-scans were performed and diffraction patterns are given as intensity over 2θ. The gracing incidence configuration, often used for polycrystalline thin film measurements was not used to maintain a good comparability of all samples, and especially with textured films. In a gracing incidence setup, a fixed incident angle (often between 0.5 ° and 5 °) is used while the secondary arm is moved. In general, higher intensities can be achieved as a consequence of diffraction in a larger interaction volume. In this work, a sufficiently high intensity was obtained due to the used setup with a rotating anode for the performed symmetric 2θ-scans. Additional test measurements in gracing incidence configuration and comparison measurements of project partners (results not shown) revealed a good comparability and the achievement of similar XRD patterns from both configurations.

As a big advantage to obtain the XRD patterns of many samples such as the multitude of different irradiation samples presented in this work in a reasonable time, a measurement routine based on a four-sample stage was established. Four samples were placed on a stage with a glass plate at four individual positions (Figure 4-9). Using an automated routine, which was controlled by the Rigaku measurement software, the samples could be aligned and measured ($2\theta/\omega$-scan) one after another with the same optics. Therefore, the script includes rotations by 90 ° and movements in x- and y-direction of the stage. The distance between the samples is necessary to prevent unwanted scattered X-rays from neighbor samples from reaching the detector.

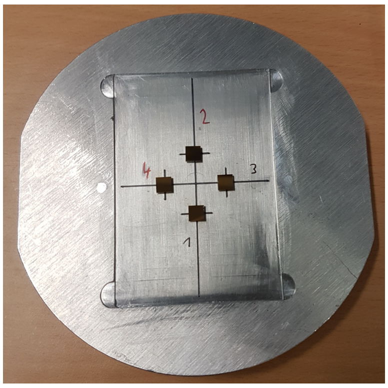

Figure 4-9: Four-sample stage with four exemplary 5×5 mm² samples placed at the positions 1-4. This stage is then mounted to the XRD setup. The distance between the samples is necessary to prevent interference from unwanted scattered X-rays from neighbouring samples.

4.5.2 X-ray reflectivity

X-ray reflectivity (XRR) is an X-ray based technique for determining layer thickness, density and (interface) roughness of thin films. The X-ray beam is moving at a grazing incidence angle, usually from about $2\theta = 0°$ to $2\theta = 6° - 10°$. An example is shown in Figure 4-10, where contained information in the pattern are labeled.

At incident angles smaller than the critical angle, the X-ray beam is reflected. As soon as the incidence angle exceeds the critical angle, part of the radiation penetrates the layer. The critical angle gives information about the density of the layer. When the angle of incidence is further increased, the penetration of the X-ray radiation increases, with one part being reflected or transmitted to the surface of the underlying layer (interface). This radiation can emerge again at the surface of the layer. This leads to constructive and destructive interferences which results in visible oscillations of the measured intensity, depending on 2θ. From the periodicity of these oscillations the layer thickness can be determined, while the drop in overall intensity provides information about the contrast in densities between the individual layers (or substrate) as well as the surface roughness. Information about the surface or interface roughness is also obtained from the weakening of the oscillations with increasing 2θ, where weaker oscillations usually correspond to higher roughness values. It is also possible to investigate and get useful information from multilayer structures with more layers. This requires a more challenging fitting routine to extract reasonable information which is less challenging for single layers or epitaxial stacks of good crystalline and interface quality. Fitting of patterns obtained from two layers can already be challenging. [303, 304]

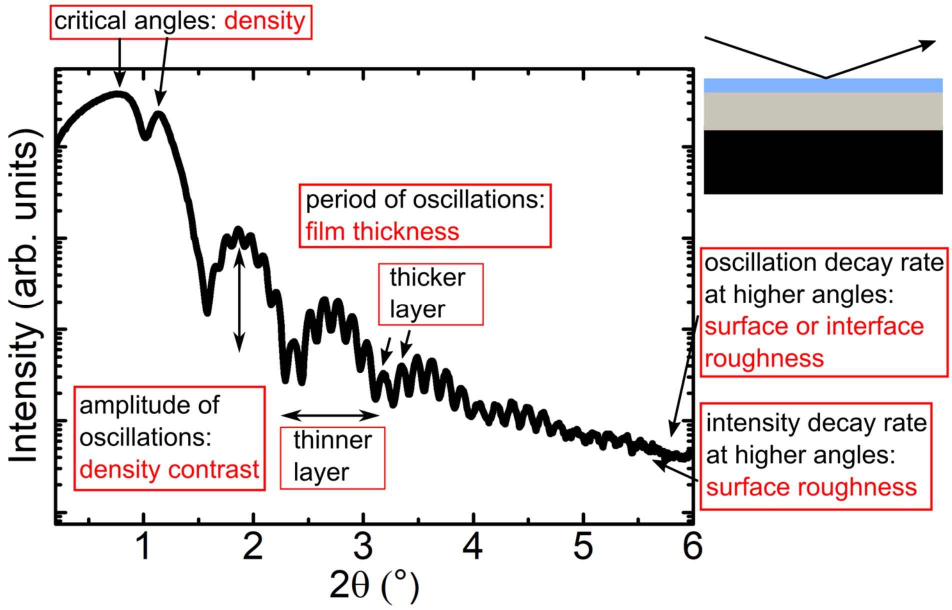

Figure 4-10: Exemplary XRR pattern with information like density, film thickness and surface roughness obtained from critical angle, slope and oscillations. Figure drawn from experimental data of a HfO_2 film grown on TiN/*c*-cut Sapphire. Labeled with information from[304].

XRR experimental: The XRR investigations performed in this work were conducted at the same Rigaku SmartLab diffractometer as described in the previous chapter using a similar setup, but without a secondary monochromator for those samples that were measured using a Graphite monochromator for XRD. Data analysis was performed utilizing the RCRefSim[305] software to extract layer thicknesses, densities and roughnesses by comparing simulated patterns obtained from a model structure with the measurement curve.

4.5.3 X-ray photoelectron spectroscopy

X-ray photoelectron spectroscopy (XPS) is a non-destructive characterization technique to obtain qualitative and quantitative information of solid samples, like composition and chemical bonding which is mainly used for thin films due to its surface sensitivity (max. 10 nm). The technique is based on the photoelectric effect and the occurring photoemission processes. Bound photoelectrons from core levels of atoms are irradiated with monochromatic X-rays (like Al K_α or Mg K_α), which absorb the photon energy hν and are emitted into vacuum with a kinetic energy E_{kin} when the binding energy E_b is exceeded (formula (9)).[306, 307]

$$E_b = h\nu - E_{kin} - \phi_{spec} \tag{9}$$

with ϕ_{spec} as the work function of the analyzer (spectrometer). A schematic representation of the emission process and energy relations is given in Figure 4-11 (a). Spectrometers and therefore measurements can be calibrated by measuring metallic reference samples such as Ag and Au. In general, all elements from lithium to uranium can be detected, while hydrogen and helium are not investigated due to their small photoelectron cross section.[306] A concentric hemispherical analyzer is required to separate the emitted photoelectrons by their kinetic energy, which can then be detected by a detector (channel plate). It consists of two concentric hemispheres at which different negative potentials are applied. A change of these potentials allows for filtering of electrons, so only photoelectrons with a certain energy can pass the analyzer. The electrons are collected and multiplied at a multi-channel electron multiplier and converted to a readable signal. Obtained spectra are usually given as intensity in counts per second (cps) versus the binding energy (E_b). An example survey of a $Hf_{0.5}Zr_{0.5}O_2$ film can be seen in Figure 4-11 (b).

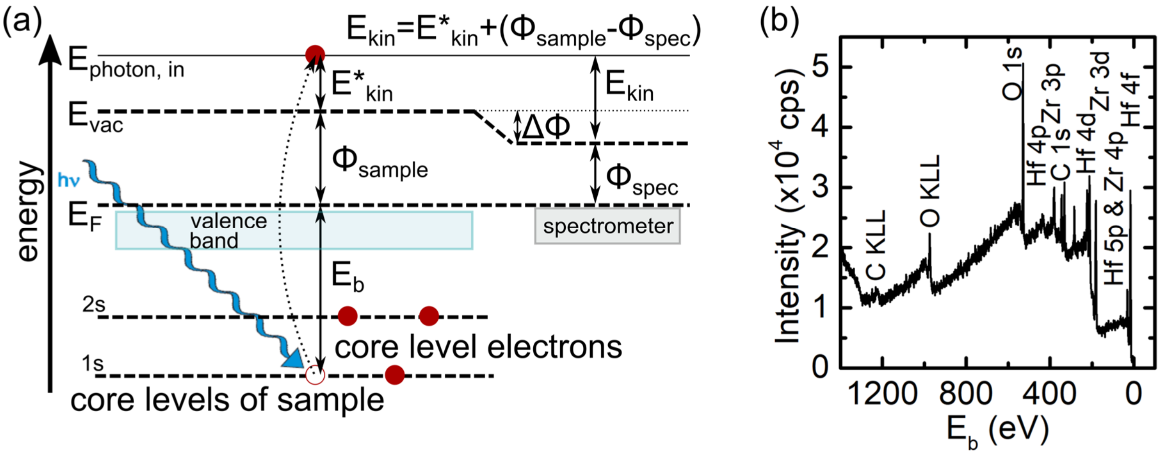

Figure 4-11: (a) Energy scheme of the emission of a photoelectron (red) with energy relations of sample to spectrometer work function. (b) Exemplary XPS survey of a 14 nm thick $Hf_{0.5}Zr_{0.5}O_2$ film that was grown on *c*-cut Sapphire with most important lines labeled.

Depending on the material and core level (orbitals) from which a photoelectron is emitted, it has a characteristic kinetic energy. Additionally, the number of detected electrons is proportional to the number of atoms in the sample. With this, the composition of a sample as well as additional information about the chemical bonding and chemical environment like oxidation states can be determined. The binding energy is shifted depending on the electron density of the probed atom (chemical shift), giving higher values for a higher positive oxidation state as a consequence of extra coulombic interaction between core electron and ion core. To obtain information from spectra, an identification of all peaks is necessary which includes the analysis of position, intensity and additional features like spin-orbit splitting, Auger lines or satellite peaks that can occur from different physical phenomena. The main lines in the spectra can directly be connected to the emitted photoelectrons from core levels and valence band which are the Hf 4f, Hf 5p, Hf 4d, Hf 4p, Zr 4p, Zr 3d, Zr 3p and O1s lines for $Hf_{0.5}Zr_{0.5}O_2$. Characteristic s lines for Hf and Zr are also visible. Carbon is seen on the top of the surface, if the films were exposed to non-ultra-high vacuum conditions prior to the measurements. Characteristic spin-orbit splitting of p-, d- and f-level emission lines in doublets occurs due to the splitting of the energy levels (spin angular momentum and orbital angular momentum). For the Hf 4f line as being relevant to this work, a splitting into Hf $4f_{7/2}$ and Hf $4f_{5/2}$ with an area ratio of 4:3 is obtained (compare chapters 5.1, 6.1.1). Auger lines can occur in the spectra as a result of the de-excitation of an excited state. After an electron emission from a core level, an electron from a higher core level fills the created hole. The energy is transmitted to another electron, which is emitted its core level (for oxygen e.g., leading to a visible O KLL line). In a similar fashion, X-ray fluorescence can occur, where the absorption of X-rays of a specific energy results in the re-emission of X-rays with a different energy. “Shake-up“- and „shake-off“-satellite lines can be induced by a simultaneous excitation of electrons in an atom, where a part of the energy of an emitted electron is transferred to a resting electron, which can be excited to an energy level below (shake-up) or above the vacuum energy (shake-off). These energy losses lead to satellite lines at higher binding energies than expected. Additionally, a loss of kinetic energy of the electrons due to the excitation of plasmons is possible (collective vibrations of the electron gas).[306-308]

The surface sensitivity of XPS originates from the mean free path of the electrons. This path describes the distance electrons travel in a solid without inelastic scattering and is limited due to the kinetic energies of the electrons, losing a fraction of their kinetic energy in inelastic collisions. For increased depth, the detection of discrete signals is limited and inelastic interactions lead to a background in the spectra. The usage of hard X-rays at a synchrotron can be used to increase the mean free paths and get a larger probing depth. [138, 306-308]

XPS experimental: In this work, XPS investigations were conducted at a PHI Versaprobe 5000 Spectrometer located at the Darmstadt Integrated System for Battery Research (DAISY-BAT). The used Al K_α radiation has a wavelength of 8.36 Å, which is corresponding to an energy of 1486,6 eV. To increase the intensity and probe a larger depth, a detection angle of 75° was used. Therefore, a typical maximum photoelectron free mean path of about 6 nm is expected.[145] To avoid the accumulation of charges on the surface, conductors are usually grounded. To investigate the insulating samples in this work, a dual beam charge neutralizer was used, which is composed of Ar ions and low-energy electrons.

As oxygen-deficient hafnium oxide is prone to surface oxidation, which hinders a proper investigation of the oxygen content in the films, these samples were transferred from the MBE growth chamber to the XPS system in a UHV vacuum suitcase (presented in chapter 6.1.1) without breaking the UHV conditions. All other investigated samples were exposed to air prior to the XPS investigations.

The spectrometer was calibrated to the Au Fermi edge and 4f emission lines. If a carbon signal was obtained in the spectra, peak positions can be corrected based on the position of the C1s at 284.8 eV.[309] The consideration of a shift is relevant for investigations of the chemical environment. Composition of single metals (like Hf:Zr ratio) are not affected by shifts. The Fermi level of the insulating m-HfO_2 grown on insulating *c*-cut Sapphire was aligned to the Fermi edge obtained for related films, corresponding to the energy of the valence band maximum of the O 2p band. In these measurements, a reference C 1s signal was not obtained, which is a consequence of the excellent UHV conditions during in-vacuum transfer to the XPS system.

Quantitative information is obtained from the spectra by analyzing the integrated peak intensities for different elements and their ratio (Hf to Zr, Hf to O), which was performed using the CASA XPS software[310]. Prior to the analysis, a Shirley-type background was subtracted. The used peak shapes are Gaussian-Lorentzian (30 %) functions for the Hf 4f and Zr 3d peaks and an asymmetric Doniach-Sunjic profile for metallic contributions of Hf. The used fit constraints are based on literature reports by Morant *et al.*[311] and Sharath *et al.*[138], using a peak splitting of 1.71 eV for Hf^{4+} and Hf^{X+} (sub)oxide doublets and 1.67 eV for Hf^0 doublets. As the integrated intensity is dependent on both device-specific factors and the effective cross-section of the investigated atoms (measure for the interaction between X-rays and electronic orbitals), a so-called sensitivity factor S for each element for the whole used setup has to be utilized to calculate the HfO_x composition with equation (10):

$$atomic\ ratio\ of\ Hf\ to\ O = \frac{I_{Hf\ 4f}}{I_{O\ 1s}} \times \frac{S_O}{S_{Hf}} \tag{10}$$

with $I_{Hf\,4f}$ and $I_{O\,1s}$ representing the integrated intensity of the Hf 4f and O 1s peaks, respectively, and S_{Hf} and S_O representing the respective sensitivity factors (2.639 and 0.711)[312]. Similar sensitivity factor values and therefore calculated compositions can be obtained using the built-in values of the PHI spectrometer. To obtain a simple ratio of two metal ions (e.g., Hf to Zr content in $Hf_xZr_{1-x}O_2$), the XPS software-internal quick fit solution gives a very good approximation. The calculation is based on the same principle. It should be mentioned that due to the described measurement- and sample-specific factors a sample composition uncertainty of up to 10 % can occur. Therefore, the discussion of trends and not only of absolute values obtained from single samples is considered. [138, 306-308, 310]

4.5.4 (Scanning) transmission electron microscopy and related techniques

Transmission electron microscopy (TEM) and scanning transmission electron microscopy (STEM) are important tools for material investigations (of atomic resolution) including information about composition and crystalline structure of samples. Both systems have in common that their working principle is relying on high-energy electron beams created in electron guns with acceleration voltages of today tens to hundreds of keV (e.g., 200 kV) for the investigation of electron transparent samples. The systems differ in the arrangement of different lenses guiding the electron beam and different detectors. Therefore, different characterization methods are usable. A schematic of the basic structure of a TEM and STEM, as well as the different detector geometries is given in Figure 4-12.

In conventional TEM, Bragg contrast is mainly used for imaging (besides density/thickness contrast and phase contrast in high-resolution TEM), which relies on the same principles as the diffraction of X-rays on crystal lattices. The de Broglie wavelength of the electron(s) at 200 keV is about 2.5 pm or 0.025 Å, which is in the range of the lattice plane spacings of a crystal. Diffraction occurs, if the Bragg condition is fulfilled (compare chapter 4.5.1).

For example, crystals/grains oriented with a prominent zone axis along the optical axis of the instrument fulfill the Bragg condition and appear dark in a bright-field (BF) image. The condenser lens system in TEM is used to achieve a wide, parallel(ized) beam. Usually, bright-field (BF) and dark-field (DF) imaging can be used in TEM, which is determined by the objective lens aperture. As the sample should be in a magnetic field that is as uniform as possible, it is technically located “in” the objective lens (which is a two-part lens). Additionally, high-resolution TEM (HRTEM) images (phase contrast) can be obtained by recording the spatial wave amplitude distribution in the image plane.[313, 314]

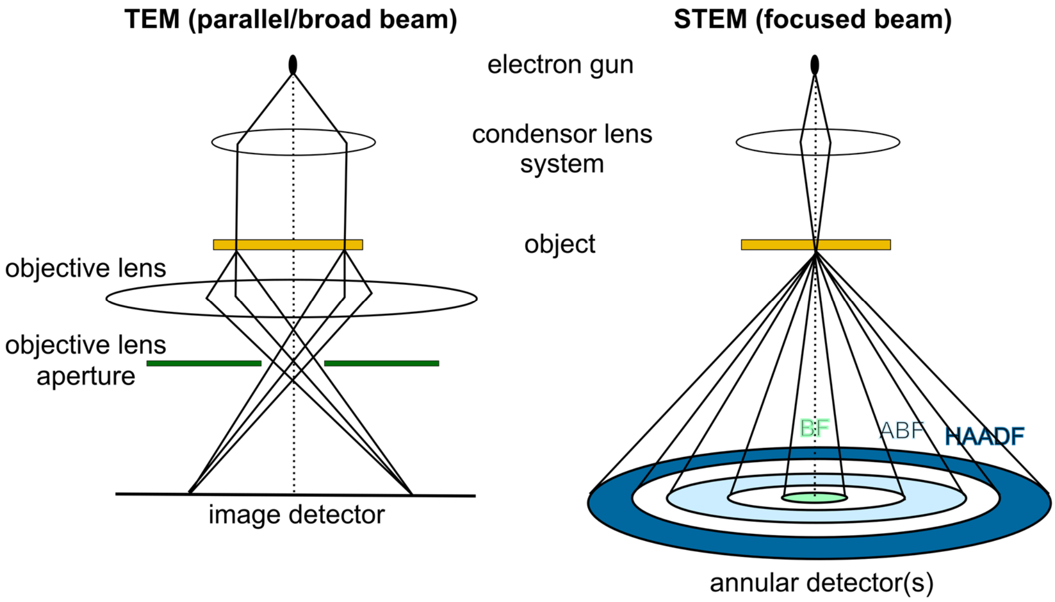

Figure 4-12: Schematic setup of a TEM (left) and a STEM (right) with electron beam paths. Redrawn using information from literature[313-315]. Note that these are simplified representations (without a two-part objective lens drawn for TEM; without a first crossover drawn). Additionally, a schematic representation of different STEM annular detectors used for image recognition in different modes (BF, ABF and HAADF), dependent on the angular range of the (diffracted) electron beam.

In STEM, the electron beam is focused by a condenser lens system on the sample, creating a beam that is scanned across the area under investigation. This beam is diffracted and (elastically and inelastically) scattered by the interaction with the sample. The electrons containing information about the sample can be detected using different annular detectors located at different scattering angles from the optical axis. Dependent on the detector geometry and camera length, different information can be obtained.

By selecting the angular range of the annular detector(s), bright-field (BF), annular dark-field (ADF) and high-angle annular dark field (HAADF) imaging is possible (see in Figure 4-12). The BF detector is located on the optical axis of the microscope, therefore only detecting electrons scattered or diffracted at a very small angular range or unscattered electrons. At larger angular range above 10 mrad up to usually 50 mrad (at 200 keV), ADF mode is reached, while at even larger angular range, HAADF mode is typically achieved. Here, the intensity of the detected electrons holds information about the atomic number Z of the atoms of the probed sample ($I \sim Z^2$)[316]. Higher probability of scattering of electrons at these large angles is obtained for heavier elements when compared to lighter elements (Rutherford scattering). With this, it is possible to e.g., reveal individual HfO_x grains in HAADF-STEM images and also distinguish (and index) different orientations of grains (crystallites).[313, 314]

Conventional STEM can be also named 2D-STEM due to the imaging using a (scintillator-based) “single pixel” detector (reciprocal space/k-space). Different information of the electrons can be analyzed, depending on the distances of sample to detector and lens configuration (camera length). Due to the interaction of the incident electron beam with the sample, X-rays are produced. From the characteristics X-rays qualitative and quantitative information about the composition of the sample can be gained by using energy-dispersive X-ray spectroscopy (EDX). Also, electrons can be inelastically scattered when being transmitted through the sample. This is the basis for the electron energy-loss spectroscopy (EELS) mode using a “1D detector” (2D detector, integrated along one dimension to a 1D signal). This mode can give information e.g., about band transitions, ionization of atoms and phonon excitations. As an example, this is of huge interest for HfO_x films with different oxygen content, where EELS can be used to distinguish and further analyze excitations of core-level electrons, which are given as characteristic edges. The 2D-STEM scanning (2D real space) together with the 1D EELS data collection (1D energy space) results in a 3D dataset, leading to the name 3D-STEM.

Diffraction of electrons can be used to record 2D diffraction patterns. With selected area electron diffraction (SAED) in TEM mode, a parallel beam on the sample is used and a field limiting, virtual aperture limits the region from which the diffraction pattern is generated (selected area of 150 nm in diameter in the used experimental setup in this work). Spatial resolution can be obtained utilizing a semi-converged electron beam in the nanobeam electron diffraction (NBED) mode. At small beam convergence (e.g., 5 mrad), spot-like diffraction patterns can be achieved. Technically, this is done using the condenser lens system in TEM mode. By precessing the electron beam in a conical geometry around the central axis of the microscope, precession electron diffraction (PED) is performed, improving the quality of diffraction patterns by integrating over several diffraction conditions. Two-dimensional diffraction patterns can be also recorded in STEM mode when the incident parallel beam is scanned across the sample, which leads to scanning precession electron diffraction (SPED). The complex dataset obtained can be analyzed using a so-called pattern matching routine utilizing e.g., the ASTAR or pyxem software package(s)[317, 318]. Scanning the beam in two dimensions and recording 2D diffraction patterns results in a 4D dataset, which makes SPED a part of the 4D-STEM methodology.[319]

As being relevant for this work, automated crystal orientation mapping (ACOM) can be applied on SPED datasets by template matching using databases (for structural parameters, e.g., from CIF) for different crystalline phases. This template matching during ACOM allows the extraction of two types of information from the SPED datasets: 1) orientation and 2) phase information. During this routine, probability values are assigned for each real space position (each pixel of the map) to match theoretical NBED patterns to experimental patterns. The best fitting phase to the experimental diffraction patterns per real space pixel is used. To confirm the validity of the recognized phases in the ACOM dataset, the available NBED patterns can be rotationally/azimuthally averaged for the classes created in the template matching routine. With this, positionally averaged, azimuthally-integrated NBED (position averaged NBED – PANBED) patterns are created, which can be compared e.g., to XRD patterns of the probed samples.[313, 314, 317, 320-322]

(S)TEM experimental: In this work, the analysis of hafnium oxide- and Ge-Sb-Te-based samples is focused on obtaining crystallographic information from atomic resolution imaging in high-resolution TEM (HRTEM) mode, HAADF-STEM and ABF-STEM mode, as well as NBED mode for obtaining crystalline features and crystallographic information from SPED/ACOM/PANBED. Most of the (S)TEM investigations in this work were performed by the Advanced Electronic Microscopy Division from TU Darmstadt in close collaboration with the RRAM Subgroup of the Advanced Thin Film Technology Division. For HAADF-STEM and ABF-STEM, as well as HRTEM imaging, a JEOL JEM ARM-200F operated with an acceleration voltage of 200 kV was utilized. HAADF imaging was performed at a beam convergence angle of 25 mrad, while SPED datasets were acquired with a convergence angle of 5 mrad on a Quantum Detectors MerlinEM direct electron detector. ACOM (phase and orientation maps) was achieved using the ASTAR software package[317, 323], while averaging the SPED datasets was performed using HyperSpy[324] and OpenCV[325] packages. More information about the python-based rotational averaging routine of the 4D-STEM dataset discussed in chapter 6.1.2 can be found in a publication uploaded to the open repository TUdatalib[326]. In principle, the used microscopy setup is capable of being used for additional advanced experiments, such as *in situ* heating or *in situ* biasing[327] and electron beam induced current (EBIC) imaging, if specific *in situ* TEM holders are used. Some samples were recently prepared for such tasks, but a discussion of results is beyond the scope of this work.

Prior to (S)TEM investigations, electron transparent lamellae of the sample have to be prepared, usually done in a focused ion beam (FIB) system. For the samples relevant to this work, a JEOLJIB-4600 FIB system was used to prepare lamellae in cross-sectional geometry. To prevent damaging of the sample during Ga ion beam irradiation, a 100 nm thick Pt layer was deposited by sputtering on top of the stacks prior to FIB preparation (see also chapters 4.2 and 6.1.2). For the STEM samples as discussed in chapter 5.5, lamellae were cut from devices already containing about 250 nm of Au and 100 nm of Pt. Preparation and analysis of external Ge-Sb-Te-based samples (chapter 4.7) was performed at CEA-Leti/CNRS-LTM in Grenoble.

4.6 Characterisation of the electrical properties

In general, a multitude of different techniques can be used to investigate different electrical properties of layers and devices. This chapter provides information about investigations of the electric polarization and resistive switching characteristics with a focus on the measurements as conducted in this work.

4.6.1 Electric polarization measurements of potentially ferroelectric stacks

The change of ferroelectric polarization with applied field resulting in ferroelectric hysteresis loops can be investigated using different methods. Those are mainly based on the measurement of the switching current or polarization charge response which are stimulated by applying an electric field across the ferroelectric material. Here, four prominent methods used in general will be shortly introduced[328-330]:

(1) A simple approach is the usage of a Sawyer-Tower circuit with a reference capacitor mounted in series with the ferroelectric. The voltage-drop across the reference capacitor occurring when a voltage is applied is proportional to the polarisation charge of the ferroelectric, which can then be determined. It is a fast and simple method, but parasitic effects and the absence of sufficiently precise reference capacitors are limitations.

(2) A similar method but using a reference resistor instead of a capacitor is the so-called “shunt method”. Here, the switching current is measured as a voltage-drop which is numerically integrated to obtain a value for the polarization charge.

(3) A very precise, but more complex method is the so-called “virtual ground method”, where the current is obtained from the voltage-drop occurring over a feedback resistor on an operational amplifier. The electric field across the resistor is proportional to the change of polarization over time.

(4) In the so-called current step method, an excitation current is applied across the ferroelectric which results in a voltage-drop that is measured. Here, no direct reference is necessary.

Experimental: P-E loops of samples presented in chapter 5.2 were obtained using a TF Analyzer 2000 P-E loop tracer by aixACCT Systems GmbH equipped with the corresponding FE module. This setup is a commercial setup based on a virtual ground method. The devices under test are capacitors, which were contacted in a custom-build probe station as described in literature[331] using 25 μm diameter tungsten tips fixed to micropositioners. The system was tested using a ferroelectric reference sample supplied by Fraunhofer IPMS CNT in Dresden containing a 10 nm HZO layer, which was also used to establish a measurement routine for thin hafnia-based stacks prepared in this work, not only thicker PZT-based stacks. P-E investigations were performed using dynamic hysteresis measurements with a single triangular waveform with a frequency of 1 kHz. Samples were pre-poled (or pre-polarized) setting a positive or negative pre-polarization pulse (amplitude 2 – 3 MV/cm) to create a defined polarization state. This is important, as obtained P-E loops are dependent on the history of the sample (electrical and mechanical treatments).

Additional tests were performed using beryllium copper as well as tungsten tips connected to a Lakeshore TTPX cryogenic probe station which is usually used for measurements at the Keithley 4200 Semiconductor Characterization System (further described in the next chapter). This was done to exclude detrimental effects of the contacting. Also, trials including up to 500 wake-up cycles were conducted. As the measured samples showed undesired leakage as discussed in chapter 5.2, positive-up-negative-down (PUND) measurements were also tested, where two pulses of positive polarity are applied one after another, followed by two triangular negative pulses. This can be used to separate leakage and actual polarization, as for real ferroelectric behavior the first pulse switches the polarization, while the second pulse is giving leakage as well as dielectric contributions to the switching only. External samples i.e. ferroelectric samples exposed to heavy ion radiation as discussed in chapter 6.2.2 were characterized at Fraunhofer IPMS CNT in Dresden (see chapter 4.7).

4.6.2 Resistive switching in HfO_2-based single memory devices

All electric investigations on single (not integrated) devices (results presented in chapters 5.2, 5.3, 5.4, 5.5 and 6.2.2) were performed using a Keithley 4200 Semiconductor Characterization System[332], short “Keithley 4200-SCS” in combination with a Lakeshore TTPX cryogenic probe station. The system was connected to two source measure units (SMU1 and SMU2), which are used to provide and measure current and voltage simultaneously. All measurements were performed under ambient conditions. In general, the probe station is also usable for low temperature (cooling down to 5 K using liquid He) and higher temperature (up to 400 K) measurements in a vacuum chamber. Additionally, pulse measure units (PMUs) can be equipped for pulse measurements using a remote amplifier switch (4225-RPM) to switch from SMU to PMU and to reduce noise generated due to long wire length. However, this is beyond the scope of this work.

Different measurement routines for leakage, electroforming, reset, set and endurance testing were carried out using the software called Keithley Interactive Test Environment (KITE). For quasi-static DC measurements, beryllium copper tips were used to contact bottom and top electrode of the devices under test, where current compliant voltage sweeps were applied to the Au top electrode layer using SMU1, while the bottom electrode was grounded using SMU2. The sputtered Au/Pt top electrode layers as described in chapter 4.2 with a comparably large thickness are necessary for the manual contacting of the tip without too much force to avoid breaking of the tips or pinching the devices, which would lead to a shortcut. Pt is used as an adhesive layer for the thicker Au layer grown in top. Current-voltage sweeps were conducted, which gives typical current-voltage curves (I-V curves). In this work, the absolute value of the current is plotted in all cases. Due to the constant top electrode area of about 900 μm^2 of all single devices, a current instead of a current density is given, allowing the direct comparison of all measurement results. Contacting was achieved by utilizing an optical microscope to place the 25 μm diameter tips on the 30 μm × 30 μm top electrode patches. The setup is depicted in Figure 4-13. An additional image can be found in literature[152]. More information about the Keithley 4200-SCS can be found elsewhere[332].

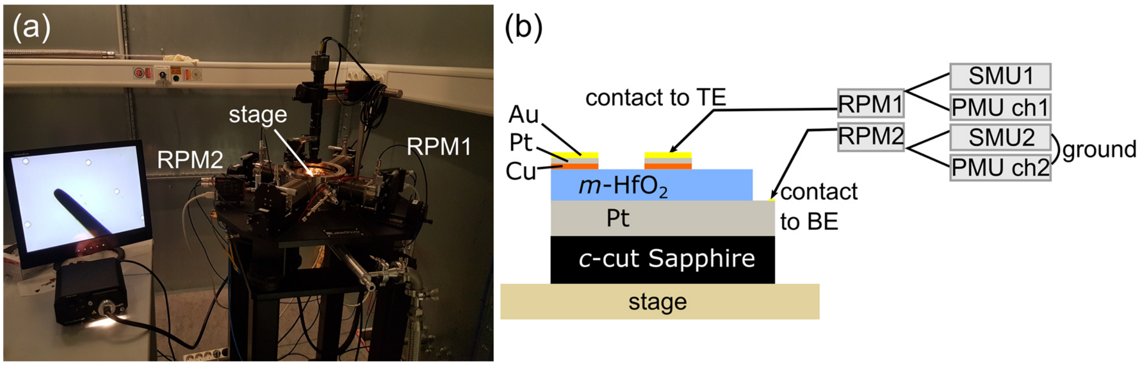

Figure 4-13: (a) Keithley measurement setup with a contacted device and a part of the top electrode tip visible on the monitor screen, (b) Schematic setup of a contacted device to RPMs and SMUs (and potentially usable PMUs). The arrows represent contact tips.

A system-internal current compliance (cc) was used to prevent a hard-breakdown of devices during forming/set. For the reset, no limiting cc is used, however, 0.1 A were utilized to protect the electronics of the Keithley 4200-SCS. If this cc is reached when the reset routine is carried out, no reset is possible and the device is considered as being "stuck" in the LRS. In this work, leakage current measurements were always performed sweeping from – 200 mV to 200 mV and back, with values of the leakage current obtained at – 200 mV (cc = 10^{-3} A). In this work, resistive switching characterization was performed by applying a voltage and measuring the current. Important parameters used for the different studies performed on single devices (capacitor stacks) are listed in the following:

(1) For resistive switching tests of potentially ferroelectric devices (chapter 5.2), a voltage of -5 V (cc = 10^{-4} A) was applied to Au/Pt/TiN/HZO/TiN devices for forming and up to ± 20 V for reset attempts.

(2) Au/Pt/HfO_2 or HZO/Pt devices (chapter 5.3) were characterized using ± 7 V during forming, ± 1.1 V to ± 1.4 V during reset and ± 4.5 to ± 5 V for the set with cc varied from 10^{-5} to 5×10^{-4} A for both, BRS and URS. 20 – 50 cycles were performed.

(3) For the resistive switching comparison of Au/Pt/Cu/HfO_2/Pt and Au/Pt/HfO_2/Pt devices as presented in chapter 5.4, forming was performed using ± 4 V

(cc = 10 – 100 μA), reset using max. – 1.1 V and set using ± 2 – 4 V with a cc of either 100 μA or 1 mA. 50 to more than 100 (endurance) cycles were performed.

(4) The oxide thickness-dependency study with Cu top electrodes (chapter 5.5) was carried out using 7 V for 20 nm and 15 nm HfO_2-containing samples and 4 V for thinner stacks (cc = 1 mA). The reset was always carried out applying – 1 V, while for the set routine a maximum voltage of 4 V was applied for 20 nm and 15 nm HfO_2-containing samples and 2 V for thinner stacks (cc = 1 mA).

(5) Resistive switching tests on Au/Pt/HfO_x/TiN devices (chapter 6.2.2) exposed to 5×10^{12} ions/cm^2 and a non-irradiated reference sample were carried out using an applied voltage of – 4 V (cc = 10^{-5} A) for forming, 2.3 V for reset and – 2.5 V for set (cc = 1 mA).

(6) Resistive switching measurements of integrated OxRAM and PCRAM devices with a transistor (1T1R) were conducted separately at different characterization systems as described in the next chapter 4.7.

4.7 External sample preparation and characterisation

Some samples discussed in this work have been prepared by cooperation partners, which is described in this chapter. Additionally, electrical and scanning transition electron microscopic (STEM) characterization was performed by the cooperation partners CEA-Leti, LTM CNRS and Fraunhofer IPMS CNT.

(1) 100 nm thick polycrystalline TiN bottom electrodes that were polished by chemical-mechanical polishing (roughness < 0.4 nm) were provided by CEA-Leti. These layers were grown on top of SiO_2/Si wafers from $TiCl_4$ and NH_3 precursors in an atomic layer deposition (ALD) process. ALD is a chemical vapor deposition technique known as an important tool for semiconductor processing and industrial use that is based on a sequential deposition of precursor molecules and self-limiting reactions controlled by added precursors, potential oxidizers and deposition cycles. Therefore, a precise thickness at Å- or monolayer-level can be achieved. Additionally, excess precursors or oxidizers can be removed from the system between the subsequent cycles to prevent reactions in the gas phase and control the thin film growth.[333] The usage of this industry-relevant technique results in a faster growth compared to films grown in an MBE setup.

(2) The irradiation samples for structural and OxRAM characterization (compare chapters 6.1.2 and 6.2.1) were prepared at CEA-Leti. These samples contain about 10 nm thin m-HfO_2 films grown at about 300 °C by ALD from $HfCl_4$ and H_2O precursors on TiN (~80 nm) and SiO_2 (~150 nm)-covered Si wafers. Working electronics were achieved by integrating the thin HfO_2 layers integrated as OxRAM in a 130 nm CMOS BEOL process, including NMOS transistors (n-type metal-oxide-semiconductor field-effect transistors) with a silicon oxide gate of 660 nm width and 500 nm length. The TiN/Ti top electrode was achieved by sputtering. For electrical characterization of the memory cells exposed to 1×10^{12} ions/cm^2, a larger transistor of 6700 nm width had to be used to provide sufficient current flow. The devices were patterned by utilizing lithography and etching steps to produce cells of various diameters. This work focuses on 400 nm diameter memory dots for the arrays and single devices with a diameter of 500 nm. More details and results can be found in literature as presented at the RADECS 2020 conference[63]. Electrical programming and measurements

were carried out by utilizing a cascade microtech bench with an Agilent B1500 parameter analyzer. Additional information can be found elsewhere[63].

(3) Ferroelectric samples for irradiation experiments have been prepared at Fraunhofer IPMS CNT. A 10 nm thin TiN bottom electrode was grown on highly boron-doped silicon wafers by utilizing an atomic layer deposition (ALD) system from $TiCl_4$ and NH_3 precursors at a deposition temperature of 450 °C. On top, three different amorphous, doped hafnium oxide layers have been deposited to create three different Metal-Ferroelectric-Metal (MFM) stacks: 20 nm thin hafnium-silicon-oxide (HSO), 20 nm thin hafnium-zirconium-oxide (HZO) or 10 nm thin HZO. Precursors of $HfCl_4$ and $SiCl_4$, H_2O as the oxidizing reactant and Ar as a purging gas were used to grow HSO films, respectively. A silicon doping concentration of around 3 at% was achieved by using a precursor cycling ratio of 16:1. Similarly, HZO films were produced using $HfCl_4$ and $ZrCl_4$ as the precursors with a cycling ratio of 1:1 to achieve $Hf_{0.5}Zr_{0.5}O_2$ (Hf:Zr 1:1 composition). Film thicknesses were controlled by the number of total deposition cycles. The TiN top electrode was fabricated by reactive sputtering (Ti target in nitrogen/argon atmosphere) at low temperature to avoid *in situ* crystallization of the hafnium oxide-based layer during deposition. A polar ferroelectric phase (space group $Pca2_1$) was achieved afterwards by crystallizing the doped hafnium oxide layers in N_2 atmosphere by rapid thermal processing treatment for 20 s at a temperature of 650 °C for HSO and by furnace annealing at 400 °C for 1 h for HZO containing stacks. The three different stacks are shown schematically in chapter 6.2.2. To get working MFM capacitors for electrical characterization, Ti/Pt contact dots (0.15 - 0.006 mm^2) were deposited by electron beam evaporation on top of the TiN top electrode layer utilizing a shadow mask. Afterwards, the TiN top electrode material between the contacts was removed by a wet etching step to form separated MFM capacitors. Voltage-dependent polarization (corresponding P-E calculated from oxide layer thickness) hysteresis measurements were performed on an Aixacct TF 3000 FE analyzer, using a triangular waveform and a frequency of 1 kHz in dynamic hysteresis measurements. From the resulting P-E and corresponding I-V loops, the characteristic values like remanent polarization, saturation polarization and coercive field are obtained. Cycling was performed with an amplitude of 3 MV/cm. For poling prior irradiation, a triangular pulse of positive or negative amplitude of 3 MV/cm was applied to set the respective state.

(4) Phase-change layers and memories have been prepared at CEA-Leti. Four different 100 nm thick full-sheet layers (no electrical contacts) have been grown: amorphous $Ge_2Sb_2Te_5$ (*a*-GST), crystalline $Ge_2Sb_2Te_5$ (*cry*-GST), amorphous Ge-rich GeSbTe (*a*-GGST) and crystalline Ge-rich GeSbTe (*cry*-GGST). GST films have been grown at 60 °C on SiO_x/Si in a single target sputtering process, while GGST films have been grown utilizing a co-sputtering process from a Ge and a GST target to achieve a combination of 45 % Ge and 55 % GST225.[211] Crystalline layers were achieved by post-deposition annealing of as grown amorphous samples at 450 °C for 15 min. A 10 nm SiN encapsulation layer was deposited on top via sputtering to prevent unwanted oxidation of the phase-change layer. Electrical measurements were performed on state-of-the-art wall-based PCRAM devices embedded in the BEOL fabrication of 4kb arrays integrated in the Memory Advanced Demonstrator

(MAD) of CEA-Leti, which is based on 130 nm CMOS technology. More details can be found in literature as presented at the RADECS 2020 conference[281].

For STEM analysis, the phase-change memory samples were prepared utilizing focused ion beam (FIB) milling in a FEI dual beam Helios 450S. Each sample was protected by a platinum layer to ensure surface protection from the Ga ion beam. An operation voltage of 30 kV was used for rough milling, followed by a reduction in the range of 2 – 8 kV to limit surface damages. Before STEM examination, samples were cleaned from hydrocarbon contamination by an oxygen-argon plasma. High-angle annular dark field (HAADF)-STEM analysis was performed at 200 kV using a double-aberration-corrected FEI Titan Ultimate TEM equipped with a high-brightness electron source, a Gatan Tridiem energy filter with Dual EELS and a Gatan US1000 CCD camera for nano-beam diffraction pattern acquisition. A probe corrector was used to obtain a beam current of about 200 pA, maintaining nanometer resolution. The electron energy loss spectra and diffraction scans were performed using standard tools, which are included in the Gatan Digital Micrograph software. EDX spectrometry was done utilizing the Super X detector system. To avoid damaging the Ge-rich GST alloys special care was taken in the control of the electron dose.

All crystallographic investigations using XRD were carried out as described in chapter 4.5.1 at TU Darmstadt. Combining the resources such as growth techniques and characterization methods of different research groups has led to a fruitful cooperation of the project partners, especially when focusing on industry-relevant TiN electrodes prepared by sputtering or ALD, thin ferroelectric layers and stacks, and integrated OxRAM and PCRAM on a wafer scale in contrast to lab-scale $30\times30\,\mu\text{m}^2$ patches on $5\times5\,\text{mm}^2$ samples. The results obtained utilizing the described characterization techniques of all prepared samples are presented and discussed in the following chapters 5 & 6.

5 Properties of hafnium oxide-based films and switching characteristics of resistive memory devices

This chapter focuses on the properties of hafnium oxide-based resistive switching devices. It is divided into 6 different parts.

First, HfO_2 was doped with Zr (mixing of HfO_2 with ZrO_2). For this, a co-evaporation routine was established based on the simultaneous usage of a Hf and a Zr metal source. The aim of this study was to achieve mixed $Hf_xZr_{1-x}O_2$ thin films of various composition in a controllable manner (section 5.1).

A subsequent aim was to transfer the hafnium zirconium oxide growth to highly-oriented TiN (111) electrodes and to prepare potentially ferroelectric $Hf_{0.5}Zr_{0.5}O_2$ stacks (abbreviated as HZO). These stacks include a TiN top electrode growth and a post-deposition annealing step. HZO was chosen since it is probably the most-promising candidate for BEOL integration of HfO_2-based ferroelectrics.[171] The progress from individual layer growth to a combined stack preparation and the characterization of corresponding physical properties via XRD, XRR, XPS as well as electrical measurements towards ferroelectric stacks are discussed (section 5.2).

In the main part of this chapter (sections 5.3, 5.4 and 5.5), the resistive switching properties of monoclinic and amorphous HfO_2- and HZO-containing stacks with Pt electrodes and HfO_2-containing stacks with a Cu top electrode are presented. First, stacks with only Pt electrodes (top and bottom) are investigated with a focus on 1) the possibility to achieve resistive switching and 2) the potential influence of ZrO_2/HfO_2 mixing in HZO compared to pure HfO_2 samples (section 5.3). In a subsequent study, the resistive switching behavior of Pt/HfO_2/Pt devices is compared to the behavior of Cu/HfO_2/Pt devices with a focus on different possible switching mechanisms (TCM versus ECM – section 5.4). In the last resistive switching study in this chapter, the HfO_2-thickness dependency of Cu/HfO_2/Pt ECM devices is investigated with a focus on the underlying switching and conduction mechanisms (section 5.5).

In an additional section (5.5), occurring difficulties related to the preparation technique of devices ("with IBE" versus "without IBE" – compare chapter 4.3) are discussed to explain the high leakage currents obtained. This includes (S)TEM/SPED investigations. In the last section 5.7, all results are summarized.

5.1 Mixing HfO_2 with ZrO_2

Doping of HfO_2 with Zr was started to obtain mixed $Hf_xZr_{1-x}O_2$ thin films of various composition in a controllable manner. This corresponds to a mixing of HfO_2 and ZrO_2, which leads to the creation of a solid solution of $Hf_xZr_{1-x}O_2$. For this, a co-evaporation procedure was established using electron beam evaporation of Hf and Zr from individual metal sources simultaneously and oxidation using an oxygen plasma. The films were grown at 300 °C substrate temperature on *c*-cut Sapphire substrates. A schematic stack is shown in Figure 5-1 (a)).

To get a broad composition range, the sum of the Hf and Zr evaporation rate was kept constant (0.7 Å/s) and the desired compositions were controlled by adjusting the individual evaporation rate (controlled via QCM control - compare chapter 4.1.3, equation (7)). The obtained values for the $Hf_xZr_{1-x}O_2$ films are given in Table 5-1 as calculated composition and growth-controlled composition, respectively. The measured compositions (Hf:Zr content) of the layers via XPS investigations are also listed. Exemplary XPS spectra including a fitting of the Hf $4f_{7/2}$ and Hf $4f_{5/2}$, and Zr $3d_{5/2}$ and Zr $3d_{3/2}$ lines are shown for the $Hf_{0.5}Zr_{0.5}O_2$ film in Figure 5-1 (b), confirming the desired composition. This routine was performed for the whole sample series based on reports from literature[138, 311, 334, 335]. Full control of the composition was possible and validated by XPS results, showing only minor deviations of the film composition from QCM calibration values (growth-controlled composition, Hf:Zr ratio). However, it has to be mentioned that the growth control remained challenging, as the overall growth pressure and the growth rates were fluctuating more than expected. This is likely a consequence of the different vapor pressures of the evaporated metals and the background pressure from the oxygen plasma. Possibly, a lower overall rate (sum of the rates) might have been beneficial. However, the usage of lower rates would not have allowed the control of such a broad range of compositions and was therefore not reasonable. Furthermore, not all rates are stable rates for the respective sources. The stability of a rate is a complex phenomenon that depends on different parameters such as filling level of the source, beam power and background pressure, among others. Additionally, the simultaneous stabilization of the individual Hf and Zr rates using one deposition controller with only one remote control remained challenging. An automated deposition of the layer was not possible, as the individual rates were not stable without manual adjustments. The obtained layer thicknesses are also listed in Table 5-1, as derived from XRR fits (patterns given in Figure 5-1 (c)).

Table 5-1: Calculated, growth-controlled and XPS compositions as well as obtained film thicknesses derived from XRR measurements of the $Hf_xZr_{1-x}O_2$ films grown on *c*-cut Sapphire substrates.

calculated composition	growth-controlled composition	XPS composition (Hf:Zr)	XRR thickness
HfO_2	HfO_2	-	12.5 nm
$Hf_{0.86}Zr_{0.14}O_2$	$Hf_{0.86}Zr_{0.14}O_2$	$Hf_{0.88}Zr_{0.12}$	12.0 nm
$Hf_{0.79}Zr_{0.21}O_2$	$Hf_{0.81}Zr_{0.19}O_2$	$Hf_{0.79}Zr_{0.21}$	13.1 nm
$Hf_{0.72}Zr_{0.28}O_2$	$Hf_{0.72}Zr_{0.28}O_2$	$Hf_{0.70}Zr_{0.30}$	13.9 nm
$Hf_{0.65}Zr_{0.35}O_2$	$Hf_{0.64}Zr_{0.36}O_2$	$Hf_{0.60}Zr_{0.40}$	13.7 nm
$Hf_{0.58}Zr_{0.42}O_2$	$Hf_{0.58}Zr_{0.42}O_2$	$Hf_{0.57}Zr_{0.43}$	12.8 nm
$Hf_{0.51}Zr_{0.49}O_2$	$Hf_{0.51}Zr_{0.49}O_2$	$Hf_{0.50}Zr_{0.50}$	14.0 nm
$Hf_{0.44}Zr_{0.56}O_2$	$Hf_{0.45}Zr_{0.55}O_2$	$Hf_{0.45}Zr_{0.55}$	13.8 nm
$Hf_{0.36}Zr_{0.64}O_2$	$Hf_{0.38}Zr_{0.62}O_2$	$Hf_{0.40}Zr_{0.60}$	12.2 nm
$Hf_{0.29}Zr_{0.71}O_2$	$Hf_{0.28}Zr_{0.72}O_2$	$Hf_{0.31}Zr_{0.69}$	11.4 nm
ZrO_2	ZrO_2	-	10.5 nm

Similar film growth times lead to slightly varying layer thicknesses, where especially the mixed oxide films tend to get thicker (e.g., $Hf_{0.5}Zr_{0.5}O_2$). As there was no significant difference found in the overall density of the layers, this result might be a consequence of a changing crystalline quality and/or fluctuations of the overall evaporation rate. The crystal structure and phase composition of the layers was examined using XRD (Figure 5-1 (d)). As the substrate temperature used during growth was 300 °C, the films are found to be polycrystalline. In Hf-rich $Hf_xZr_{1-x}O_2$ films, reflections of the highest intensities are found at around $2\theta \approx 28.4°$, 34.6° and 35.6°, while in Zr-rich $Hf_xZr_{1-x}O_2$ films, the strongest reflections are found at $2\theta \approx 30.3$ °, 34.8° and 35.7°. This is congruent with literature reports, where these reflections were assigned to the monoclinic symmetry with a high phase fraction expected in Hf-rich $Hf_xZr_{1-x}O_2$ films and to a tetragonal phase fraction being dominant in Zr-rich films.[336, 337]

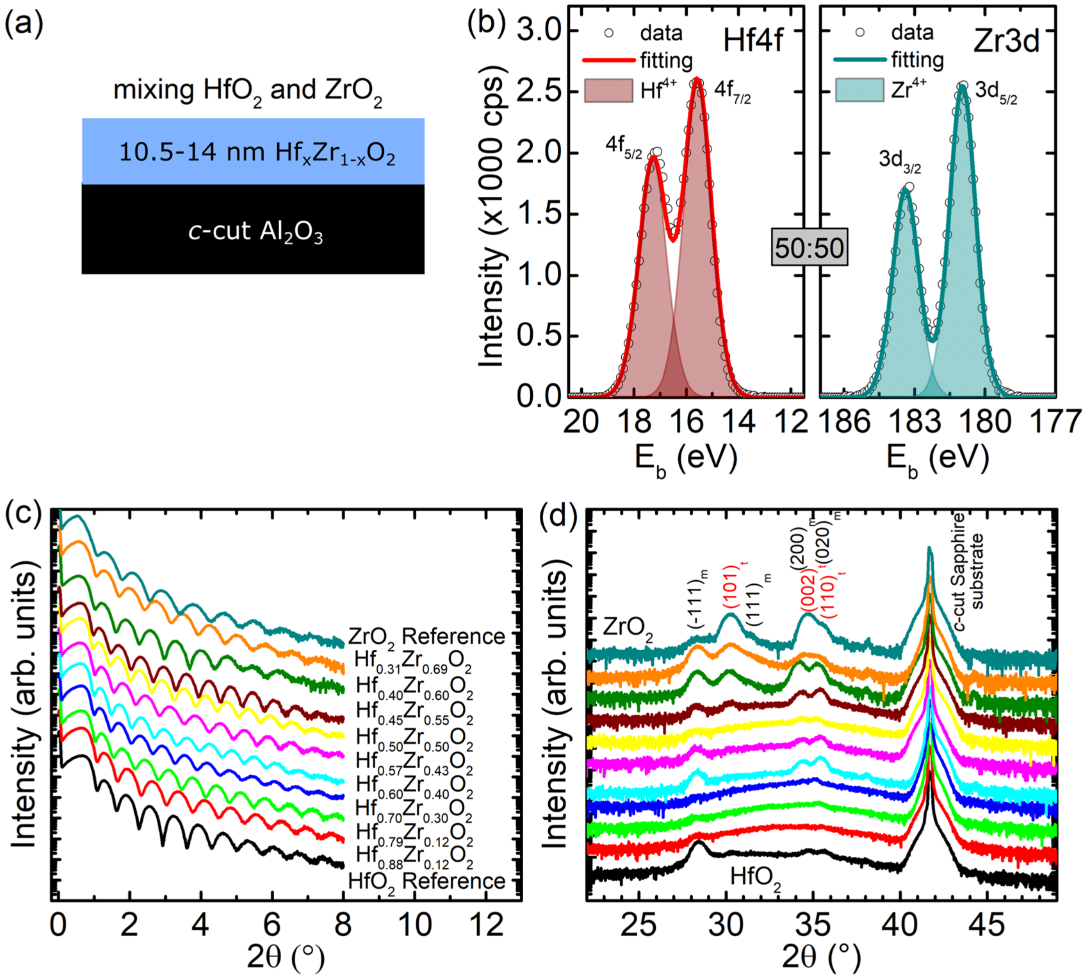

Figure 5-1: (a) Schematic of the stacks containing $Hf_xZr_{1-x}O_2$ films on *c*-cut Sapphire. (b) Exemplary XPS spectra and fits of the Hf4f and Zr3d lines corresponding to the $Hf_{0.5}Zr_{0.5}O_2$ film. A Shirley-type background was subtracted. (c) XRR patterns of the $Hf_xZr_{1-x}O_2$ films of different composition grown on *c*-cut Sapphire. Note that the given compositions are the measured (XPS) compositions, while HfO_2 and ZrO_2 act as references. (d) XRD patterns of the $Hf_xZr_{1-x}O_2$ polycrystalline films of different composition grown on *c*-cut Sapphire, crystallizing in a monoclinic (indexed in black) and potentially tetragonal structure (indexed in red). Note that an orthorhombic, cubic or rhombohedral structure is also possible. The increased background ("broader bump") between 30° and 38° stems most likely from an interface effect between *c*-cut Sapphire substrate and $Hf_xZr_{1-x}O_2$ film due to for example the possible formation of nano-crystallites. This result is comparable to literature reports on pure HfO_x films grown on c-cut Sapphire.[145]

As these literature reports have only discussed annealed layers (as grown amorphous films), a direct relation to the presented results is not straightforward. Additionally, a clear assignment of the quite broad reflections at $2\theta \approx 30.3$ °, 34.8° and 35.7° remains challenging due to the similarity of reflection positions of the different reported similar phases of HfO_2 (and also the polymorph ZrO_2), as discussed thoroughly in chapter 4.5.1. Those reflections can be assigned to the reported cubic, tetragonal, orthorhombic or rhombohedral and even monoclinic phase of hafnium oxide (e.g., ICDD 00-034-0104, 04-011-9018 or 01-078-5756). This includes the non-centrosymmetric polar phase (space group $Pca2_1$). In the following, $(111)_o$ is used to label the potentially present (111) reflection of the polar orthorhombic (ferroelectric) phase.

Nevertheless, the following conclusions can be drawn:

- Fully oxygen-saturated HfO_2 films are known to usually crystallize in the monoclinic structure when grown on *c*-cut Sapphire substrates.[128, 145] The presence of a small reflection at around $2\theta \approx 30.3$ ° as seen in Figure 5-1 (d) could indicate a small fraction of a slightly oxygen-deficient, rhombohedral phase, as recently reported by Kaiser e*t al.*[128] for HfO_x films.
- Furthermore, some films (e.g., $Hf_{0.6}Zr_{0.4}O_2$) show a lower crystallinity with lower intensities of the reflections. This could point to a different crystallization behavior of the formed $Hf_xZr_{1-x}O_2$ phases in dependence of the Hf:Zr ratio.
- Hf-rich films tend to crystallize in the monoclinic phase, while the Zr-rich films contain a higher phase fraction of the cubic, tetragonal, orthorhombic or rhombohedral phase. In the context of literature reports, a tetragonal or a rhombohedral structure is more likely than a cubic or orthorhombic structure. [128, 336, 337] Overall, a precise composition control of the films was possible as confirmed by XPS results and the obtained crystal structures of the layers as seen from XRD patterns is found to be in accordance with literature.

5.2 Towards a polar crystalline phase for ferroelectric stacks

After successful growth of the $Hf_xZr_{1-x}O_2$ layers in the MBE system, about 12 nm thick $Hf_{0.5}Zr_{0.5}O_2$ (HZO) layers were grown on titanium nitride (TiN) conducting bottom electrodes. On top of the HZO/TiN stack, a TiN top electrode was deposited (schematically shown in Figure 5-2 (a)). The aim was a controlled fabrication of the polar orthorhombic phase with ferroelectric properties, which may be achieved in two different ways:

- First, HZO films may be directly forced to grow in the polar orthorhombic crystalline structure on top of a substrate or bottom electrode e.g., by inducing a strain to the hafnium oxide-based film during growth as reported for epitaxial Y-doped HfO_2 grown on ITO[198] and later shown for HZO grown on LSMO[124]. Therefore, in this work, films have been grown on high-quality, highly-textured, (111)-oriented TiN bottom electrodes on *c*-cut Sapphire substrates. The bottom electrode texture could promote the growth of an oriented orthorhombic phase and thus induce a preferred crystallographic direction.
- Second, an orthorhombic phase in HZO films can be achieved by post-deposition annealing of TiN/HZO/TiN stacks (here: subsequent heating of the whole stacks after top electrode deposition) as reported by Park *et al.*[201], among others.

The oxide layer thickness of 12 nm was chosen based on literature reports, where good ferroelectric properties of HZO films were found for layer thicknesses between 5 and 15 nm[201]. The chosen thickness in this study is further in accordance with the results presented in the previous chapter, where a good thickness and composition control of the $Hf_xZr_{1-x}O_2$ layers was possible for similar thicknesses. A lower thickness was believed to potentially show increased undesired leakage currents. The layer thickness was verified using XRR (compare pattern in

Appendix Figure 1 with well-defined oscillations up to 2θ ≈ 6°, revealing a good quality of both the oxide and the (111)-oriented TiN bottom electrode). The film composition of Hf:Zr 1:1 was chosen as HZO is probably the most promising ferroelectric candidate for BEOL integration[171] with good ferroelectric properties reported for the given thickness range[338].

Approach to directly grow of a polar orthorhombic phase on TiN bottom electrodes: The XRD results of an as grown as well as an annealed (600 °C, 20 s, 380 Torr N atmosphere) TiN/HZO/TiN stack can be seen in Figure 5-2 (b). For both cases, the HZO films are polycrystalline (monoclinic & orthorhombic/tetragonal/cubic/rhombohedral), showing similar reflection positions with a significantly high monoclinic phase fraction. In connection with the corresponding electrical results (shown and discussed later in this chapter) and in comparison to literature[203, 339], it can be stated that it is unlikely that the formation of the polar orthorhombic phase was successful, neither during growth on textured (111)-oriented TiN electrodes at 300 °C directly nor after post-deposition annealing. There are no structural changes towards a polar orthorhombic phase occurring during annealing of already crystalline HZO films.

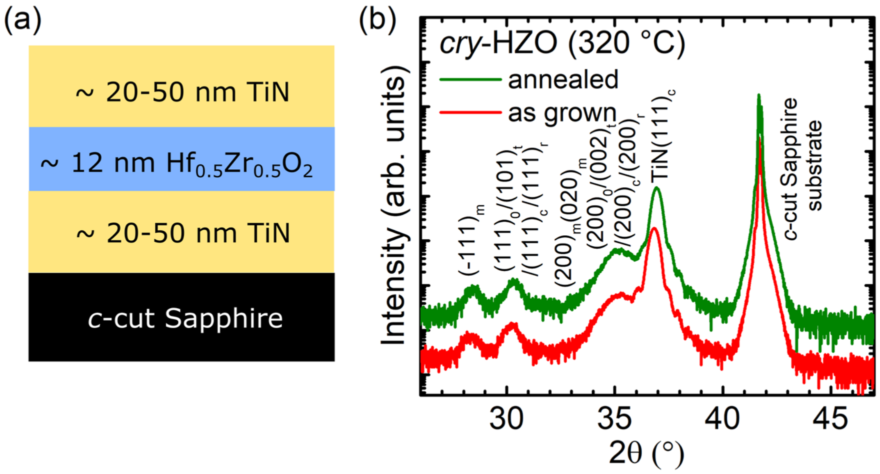

Figure 5-2: Schematic representation of the TiN/HZO/TiN stacks prepared and investigated, (b) XRD patterns of as grown (red) and post-deposition annealed (green; 600 °C for 20 s) TiN/HZO/TiN stacks of polycrystalline nature.

The result obtained after annealing further underlines literature results[203, 339], where a transformation from the monoclinic to the polar orthorhombic phase in doped hafnium oxide films is reported to be impossible. Instead, it was stated, that a transition from an amorphous through an intermediate tetragonal phase to the polar orthorhombic phase is possible during quenching of the sample right after a post-deposition annealing step[3, 203]. For this, an as grown amorphous HZO layer sandwiched between two electrodes are required.

Approach to achieve a polar orthorhombic phase by post-deposition annealing: To test this approach, different TiN/HZO/TiN stacks have been grown containing an amorphous HZO layer for further post-deposition annealing experiments. The results of an exemplary annealing experiment are shown in Figure 5-3. The single crystalline c-cut Sapphire substrates have the characteristic (006) reflection at around 2θ = 41.67° (Figure 5-3 (a)). This reflection was used for the substrate alignment performed prior to the 2θ-scans and is therefore always found at this fixed angle. Reflections corresponding to the films grown on top can show characteristic shifts in 2θ, depending on the phases formed. Consequently, the 2θ angle (position) of a certain film reflection can be discussed with respect to the substrate peak position and therefore also between different films (relative shifts). For different laser heating annealing conditions in N_2

atmosphere, reflections in an angular range between 2θ = 30.25 – 30.4° (Figure 5-3 (b)) are visible. The reflections can again be assigned to different phases of HZO with no clear differences visible. A potential slight shift towards larger angles for a higher annealing temperature of 600 °C suggests a smaller out-of-plane lattice parameter for the films annealed at higher temperatures. This could be related to a loss of oxygen in the HZO layer.

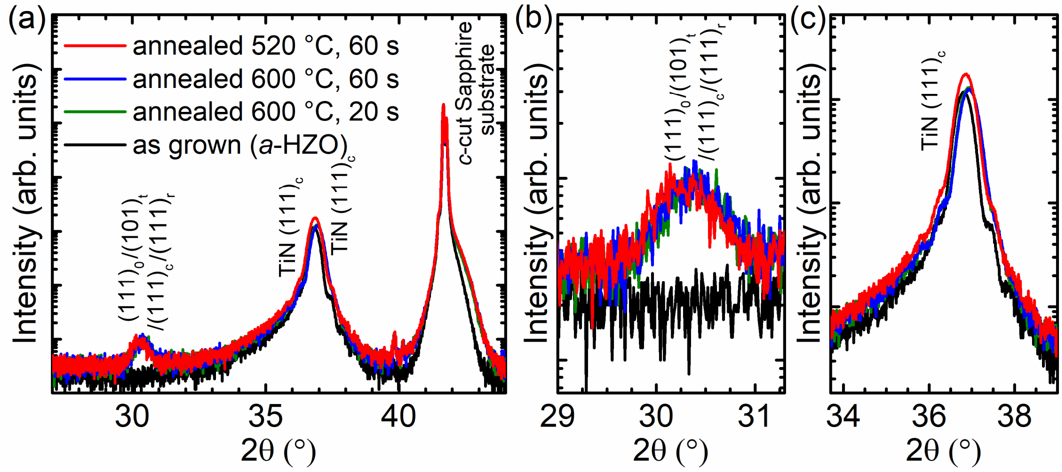

Figure 5-3: XRD patterns of exemplary post-deposition annealing attempts (heating rate: 15 – 20 K/s, holding time: 20 – 60 s with an IR laser system in 380 Torr nitrogen atmosphere) of HZO-containing stacks. Annealed HZO layers are (at least partially) crystallized, showing a characteristic reflection at around 2θ = 30.25°, which could be assigned to the polar orthorhombic phase of HZO.

A shift of the TiN (111) reflection towards larger diffraction angles as seen in Figure 5-3 (c) is also indicative for a decrease of the out-of-plane lattice constant of the cubic structure of TiN, which could point towards an oxidation of the TiN bottom electrode layer (towards TiON). The (111) reflection of TiN is usually found at 2θ ≈ 36.66° (ICDD 00-038-1420), while for an increased oxygen content, the (111) reflection of a potentially formed TiO_xN_y preferably shifts to angles 2θ ≈ 37° (ICDD 01-084-4872). Furthermore, the intensity and number of Laue oscillations visible for as grown TiN are reduced after annealing. This could be a result of a decreased sharpness of the TiN/HZO interface, which might be a result of the formation of a TiO_xN_y interfacial layer.

Similar post-deposition annealing experiments have been conducted on HZO-containing stacks grown on (001)-oriented MgO substrates, where (200)-oriented TiN bottom electrodes can be achieved. This opens the possibility to induce a different strain on the HZO layer from the bottom electrode during growth and also during post-deposition annealing. An exemplary stack and XRD result are shown in Appendix Figure 2. Due to their epitaxial relationship/matching lattice parameters, the TiN (200) and the MgO (002) reflection overlap (2θ ≈ 42.6° and 42.9°, respectively). However, the visible Laue oscillations confirm a smooth growth of the highly-textured MgO bottom electrode. Similar to the results obtained in Figure 5-3 for stacks prepared on *c*-cut Sapphire, the initially amorphous HZO layer is crystallizing (at least partially) during annealing, revealing a reflection at 2θ ≈ 30.2°, which can be again assigned to different crystalline structures. Interestingly, the different substrate and therefore TiN bottom electrode orientation leads to an additional reflection at 2θ ≈ 35.35° and therefore an additional orientation of the HZO layer. The presence of only two reflections in the XRD patterns could be an indication for the presence of a cubic phase. However, neither the absolute diffraction angles nor the difference between the maxima match any of the expected values of potential phases in question. Due to the texture of the layer and the low crystalline volume, a distinction of potential phases is not possible from the XRD pattern.

Electric polarization measurements: To further investigate which phase of HZO is present or dominant in the discussed stacks (and additional attempts), voltage-dependent electric polarization measurements were carried out. The presence of a polar orthorhombic phase can only be proven by electrical investigations. A representative curve valid for all devices consisting of annealed HZO-containing stacks described in this chapter is shown in Figure 5-4 (a). A reference P-V curve of a common non-annealed Pt/*m*-HfO_2/TiN stack is shown in (b).

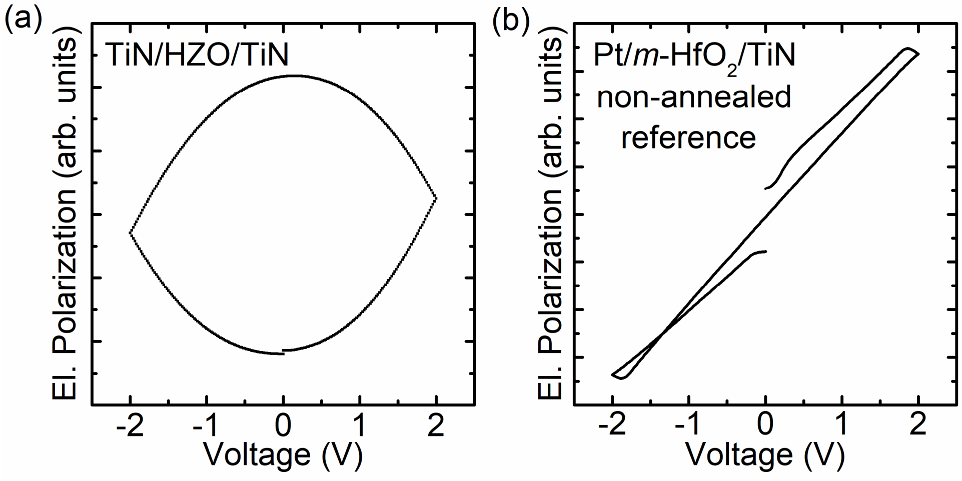

Figure 5-4: Electric polarization measurement curves for (a) an annealed TiN/HZO/TiN stack showing a leaky behavior and (b) a reference Pt/HfO_2/TiN stack showing dielectric behavior.

Overall, the electrical measurements for devices of all post-deposition annealed stacks containing HZO films with a possibly polar orthorhombic structure showed the visible open loops (a), which are connected to high leakage currents. Unfortunately, a proper P-E loop as it would be expected for ferroelectric samples (compare chapter 2.2) was not obtained. The high leakage completely inhibits the application of these stacks as ferroelectric memory devices. In principle, a polar orthorhombic (ferroelectric) phase could be present, but the electrical measurements are dominated by leakage. Thus, the presence of a polar phase cannot be confirmed. Measurements of reference Pt/HfO_2/TiN RRAM devices containing TiN and HfO_2 showed the expected linear dielectric P-E behaviour of devices containing an insulating HfO_2 layer. The reference devices are composed of a similar TiN bottom electrode but a Pt top electrode and a monoclinic HfO_2 layer without Zr grown at 300 °C. These stacks were not post-deposition annealed. Additional experiments (as described in chapters 4.1.3, 4.2 and 4.3, results not shown) resulted in similarly leaky P-E loops. Those experiments included the usage of differently prepared TiN electrodes, increased temperature during TiN electrode and HZO layer growth, different annealing procedures using an infrared laser, a furnace annealing step or an annealing procedure performed using the heater of the MBE growth chamber, different gases and pressures up to a maximum of the used systems (e.g., laser annealing in max. 380 Torr nitrogen/argon atmosphere) to maintain safe experimental environment, different electrical measurement approaches like the usage versus avoidance of pre-poling, or the usage of possible wake-up cycling or PUND measurements. These results are therefore not presented in this work.

However, the question arises why all P-E loops of potentially ferroelectric devices show a leaky behavior. In general, reasons for leakage in dielectrics/ferroelectrics are manifold, including different influences by charge carrier injection in the layer, which is dependent on a variety of different mechanisms but also preferential breakdowns and leakage paths along grain boundaries are possible. [135, 136, 340] Additionally, dielectric materials tend to dissipate energy due to the movement of electrical charges in the material stimulated by an alternating electric field as a general principle. This leads to the generation of heat. The lost energy is called dielectric loss.[341] Possible influences on the leakage of the presented stacks in this chapter can be also found in the following points:

(1) <u>HZO growth process in the MBE system:</u>

Besides the Zr-doping and mentioned difficulties of the film growth control, which could have an effect on the Hf/Zr distribution in the layer, especially the oxygen content is crucial for the conductivity characteristics and leakage of the film. As known from literature[128, 145], an increased number/density of oxygen vacancies in pure HfO_2 films can lead to an increase in conductivity up to a fully conducting layer. As Kaiser *et al.* [128, 145] have shown, this is especially true for the oxygen-deficient rhombohedral phase of hafnium oxide, showing similar XRD patterns than they are obtained from measurements on polar orthorhombic films. From the presented XRD results, no distinction can be made. A slight oxygen-deficiency induced in ferroelectric films is believed to facilitate the formation of the polar orthorhombic phase and potentially enhance ferroelectric properties, while a larger oxygen-deficiency is proposed to be highly detrimental. [184, 186-192] Nevertheless, the presence of a slightly decreased relative density of the HZO layers (compare Appendix Figure 1) compared to fully stoichiometric $Hf_{0.5}Zr_{0.5}O_2$ with a density of 9.79 g/cm^3 [64, 131] does not directly point towards an increased oxygen vacancy density in the presented layers. This is deduced from observations made on oxygen-deficient HfO_x, where an increased oxygen deficiency is accompanied by an increase of the HfO_x layer density.[145]

As the growth of amorphous HZO films in the given stack configuration in a reactive MBE chamber was performed for the first time, exact details on the influences were not known. Therefore, a slight oxygen-deficiency (compare to chapter 5.1) cannot be fully excluded. Recently, the preparation of stacks containing polycrystalline, ferroelectric $Hf_{1-x}Zr_xO_2$ films grown by plasma assisted atomic oxygen deposition was demonstrated.[200] The main differences to the discussed stack growth (compare chapter 4.1.3) were the higher temperatures used for oxide layer growth and the obtained growth pressures, which Zacharaki *et al*. found to be one order of magnitude lower than observed during growth of films presented in this chapter. Additionally, films were grown on single crystal Ge substrates and not on TiN/*c*-cut Sapphire. Increasing growth kinetics could lead to the desired results, which might be achieved by higher temperature growths of HZO and TiN layers. This was not possible in this work as the HZO layers were found to be crystallizing in the undesired monoclinic phase at increased temperatures, possibly due to the overall increase of the temperature in the chamber during co-evaporation of Hf and Zr (two heat producing sources simultaneously). Cooling of the MBE chamber wall by liquid nitrogen during deposition could mitigate this issue. Reduced growth pressures could also allow a better rate control during growth.

(2) TiN bottom and top electrode growth:

The top electrode is exposed to air immediately after removal of the TiN/HZO/TiN stack from the growth chamber, while the bottom electrode comes into contact with atmospheric oxygen after the preparation of an electrically contactable surface spot by ion beam etching (IBE). In both cases, a formation of TiO_xN_y interface layers is possible, if the TiN is not fully nitrogen-saturated. For the high temperature bottom electrode, 4-point resistivity measurements revealed resistivity values of about 50 – 200 $\mu\Omega$cm, which is in the expected range for a stoichiometric TiN bottom electrode. Therefore, especially the low growth temperature of the TiN top probably results in a poor layer quality and a potential nitrogen deficiency. Indications for this were found in corresponding quick-tests utilizing a handheld multimeter (increased electrical resistance). The TiN oxidation is likely to further increase during the annealing process and the TiO_xN_y layer formed, thus functioning as a so-called scavenging layer. This is directly related to the described phenomenon of a possible oxygen-deficiency in the HZO layers, which means that the nitrogen-deficient TiN electrodes can extract oxygen from the initially dielectric HZO layer, creating oxygen vacancies in the HZO during annealing. This in turn would lead to the observed leakage currents. As an additional consequence, the formation of a polar orthorhombic phase might be inhibited. In literature, the formation of TiO_xN_y as an interface layer is known. However, its occurrence and effects in the ferroelectric properties of the ferroelectric layers has been reported to be a quite complex phenomenon[193, 342, 343], mostly due to the direct interaction of the TiN and TiO_xN_y with the oxide layer. The movement of oxygen ions during P-E measurements can also lead to a formation of an interface layer. These complex phenomena are not yet fully understood and subject to further research as mentioned in chapter 2.2.

(3) Post-deposition annealing process (temperature, time, gas background pressure):

In literature, a variety of different post-deposition annealing procedures using various parameters are discussed, which strongly depend on the materials, stack design, growth technique and subsequent further preparation of the stacks, where annealing temperature, time and background gases etc. are adjusted to achieve the desired polar phase. A commonly used annealing tool is flash heating. Possibly, annealing procedures used in this study are not optimized to achieve an overall crystalline polar orthorhombic phase. As an example, parts of the HZO layers could still be amorphous. The used ramping parameters as well as holding time and annealing temperature might not result in a sufficiently high thermal budget in the stacks allowing the required formation of a tetragonal phase during annealing and the polar ferroelectric phase after quenching. Additionally, the background pressure was limited to a maximum of 380 Torr due to the vacuum chamber limitations, which might not be sufficient to prevent oxygen and nitrogen from being removed from the residual HZO and TiN layers, respectively, during annealing.

(4) Ion beam etching process:

In the IBE process used to provide an accessible spot for electrically contacting the bottom electrode, two major detrimental effects on the HZO layer can occur. a) Increased heat can be produced, which promotes diffusion processes and can increase leakage currents. This is prevented by utilizing liquid nitrogen cooling of the samples during etching. b) The high ion energy used for the etching process can additionally cause for example re-deposition of material at the edge of an etched hafnium oxide layer (edge of a device). This could create a conductive path between top and bottom electrode and result in an unwanted overall conductive device. This is believed to be prevented by stopping the etching process at the hafnium oxide surface and not etching fully down to the bottom electrode surface (compare chapter 4.3.). These problems arose after the study on HZO-containing stacks was conducted and have therefore not been further included in the preparation of additional samples. Further discussions regarding the influence of the IBE process on device properties are presented in chapter 5.6.

Most likely, the overall leaky behavior of differently prepared stacks is a consequence of a combination of several factors.

Further attempts: As seen from this quite extended list of possibilities, problems are manifold and many different interconnected parameters influence the overall film properties. However, a few further attempts to understand the behavior and to find solutions towards the achievement of ferroelectric properties were conducted.

First, a further optimization of the TiN electrodes was aimed by increasing the temperature during growth. As for the top electrode preparation by MBE this approach is quite limited, a sputtering approach was used. XRD patterns of first TiN growth attempts on *c*-cut Sapphire substrates utilizing RF sputtering in N_2/Ar-atmosphere at 5 different growth temperatures are shown in Appendix Figure 3 (a). All films were found to be amorphous without any characteristic cubic reflections visible in the XRD patterns. The corresponding lowest resistivity values of about 1500 $\mu\Omega$cm are therefore exceeding the values obtained for high temperature TiN bottom electrode films grown in the MBE system (about 50 – 200 $\mu\Omega$cm) by at least one order of magnitude. A further optimization and crystallization of the layers with the used sputtering system was not possible due to the limited background pressure and heating capabilities. Quick XPS investigations (results not shown) also revealed Sn and Nb impurities in the layers, which are most likely impurities originating from the inside of the sputtering chamber itself. Additionally, a slight nitrogen deficiency was indicated, which is likely a result of the utilized sputtering from a TiN target in an insufficient background pressure environment. The performance of RF or DC sputtering using a pure Ti target with sufficient nitrogen background pressure in a different sputtering chamber might be a more promising approach.

Second, Pt top electrodes were used to provide a more chemically inert top electrode material (stacking from top to bottom: *ex situ* magnetron sputtered Pt/amorphous HZO grown in the MBE system/(111)-oriented TiN bottom electrode grown in the MBE system/*c*-cut Sapphire substrate). For direct comparison, post-deposition annealing (after electrode sputtering) was performed in a similar manner (60 s at 500 – 600 °C in 380 Torr Ar atmosphere). The XRD pattern of an annealed Pt top electrode-containing sample in comparison to the pattern obtained from an annealed TiN top electrode-containing samples is shown in Appendix Figure 3 (b) as an example. The formation of a polar orthorhombic phase might be also possible in a stack with a Pt electrode as reported by Park et *al.*[183] Unfortunately, all tested stacks again showed an unexpected high leakage. This indicates that the expected electrode-related difficulties are not only limited to the top electrode, but additional challenges (HZO growth, annealing process and bottom electrode) remain.

In a final approach to obtain a better understanding of the HZO-containing stacks and the HZO layer itself, DC leakage current measurements and resistive switching attempts were conducted on post-deposition annealed TiN/HZO/TiN devices. This was also performed to test, if resistive switching is possible. The general possibility to obtain resistive and ferroelectric switching in doped hafnium oxide-based stacks was reported in literature[172]. Interestingly and in contrast to the observed leaky behavior in P-V measurements (AC characteristics), the measured devices were found to be in the HRS from DC leakage current measurements (around 10^{-10} – 10^{-7} A at 200 mV for a $30\times30\ \mu m^2$ top electrode area). Forming was achieved by applying a negative voltage (Figure 5-5 (a)), however, the expected reset could not be observed. Increasing positive or negative voltage applied did not result in a proper reset either (b).

The obtained current-voltage curves reveal kind of a step-wise reset with increasing absolute values of negative voltage up to 20 V applied. This behavior was observed for multiple samples and devices. Overall, resistive switching for all tested stacks containing post-deposition annealed HZO layers failed with no real trend deducible. The reason for the failed reset attempts and an absence of a hard-breakdown at such high applied voltages still remain unclear. Nevertheless, the results reveal that the stacks are not fully conducting, neither as-prepared devices nor devices after step-wise reset.

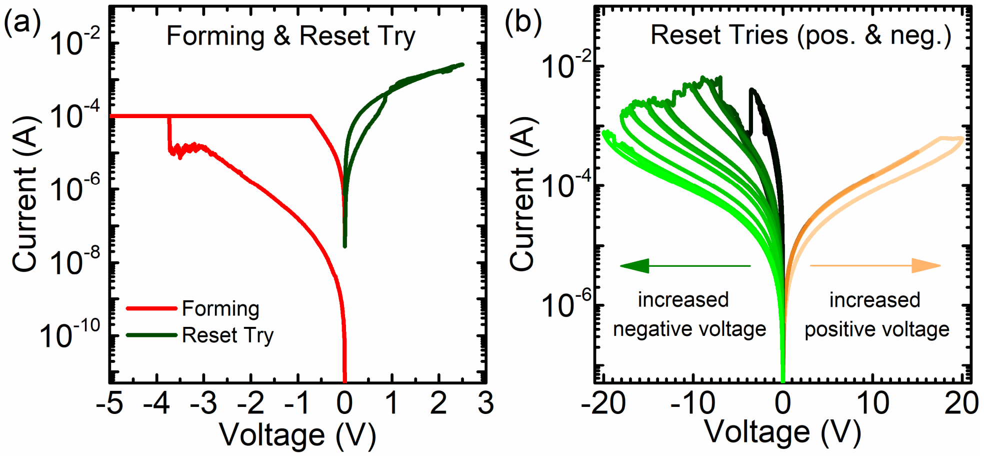

Figure 5-5: Resistive switching characteristics of post-deposition annealed TiN/HZO/TiN devices with a potentially polar orthorhombic crystalline structure. (a) Achieved forming step and failed first reset (reset try). (b) Partial/step-wise resets seen for negative and positive voltage up to ±20 V applied.

Summary: Hafnium oxide films were successfully doped with Zr to achieve $Hf_xZr_{1-x}O_2$ films. Overall, a good control of the composition was possible. Films with the most interesting composition of $Hf_{0.5}Zr_{0.5}O_2$ (HZO) for ferroelectric applications were transferred to substrates covered with a TiN bottom electrode. Different post-deposition annealing attempts on amorphous stacks with a TiN top electrode grown on top, led to a possible formation of a polar orthorhombic phase, characterized using XRD. Unfortunately, all devices were found to be leaky in the subsequent voltage-dependent electric polarization measurements. Further attempts to improve the stacks or to understand the obtained behavior revealed even more challenges. The reason for the leaky P-E loops and the impossible reset obtained from resistive switching attempts still remain unclear. Further comprehensive studies are required, as many different parameters are influencing each other. There are several possible steps, that can lead to a better understanding of the material system and potentially ferroelectric properties of TiN/HZO/TiN devices with lower leakage:

- It has been revealed that a stoichiometric TiN top electrode growth is mandatory to prevent the formation of unwanted TiO_xN_y layers, which could be achieved by DC sputtering.
- An improved growth of low temperature HZO films can support the achievement of better results. This could be done using parameters close to reported values[200] and additional chamber wall cooling.
- The high variety of influencing parameters and occurring challenges have revealed that it is highly recommended to conduct further studies taking the described findings into account; and to systematically change single parameters one after another in subsequent studies, including especially detailed post-deposition annealing as well as IBE studies.

5.3 Resistive switching characteristics of Pt/HZO/Pt- and Pt/HfO_2/Pt-based devices

To get a better understanding of the HZO material system, resistive switching of non-annealed HZO-containing devices was tested and compared to the behaviour of pure HfO_2-containing devices. The HZO and HfO_2 functional layers were grown in the MBE with different crystallinity (amorphous films grown at RT versus monoclinic films grown at about 300 °C), and sandwiched between sputtered Pt electrodes, providing a more inert electrode system than present for TiN electrode-containing stacks. These devices are aimed to serve as proof of principle stacks for resistive switching of HZO-containing stacks and to investigate possible impacts of the growth kinetics, when an increased growth temperature is used (compared to films grown at room temperature). Those stacks were not post-deposition annealed and are not aimed to be ferroelectric.

In more detail, the different possible switching modes were investigated from voltage-dependent resistive switching measurements (DC voltage sweeps). XRD patterns of the four different stacks (Pt/stoichiometric HZO or HfO_2 films grown on Pt-covered *c*-cut Al_2O_3 substrates at 300°C and RT, respectively) are shown in Figure 5-6. XRR patterns of HZO or HfO_2 films on Pt are shown in the insets. Those were measured without the top electrode layers to simplify the extraction of film thicknesses, which becomes extensively harder with an increasing number of layers. Schematic representations of the four different HZO-based stacks are also given. The absence of characteristic reflections in the XRD patterns indicates that the HfO_2 and HZO films grown at RT are amorphous, whereas the films grown at 300 °C are crystalline with a characteristic ($\bar{1}11$) reflection of the monoclinic phase at around 28.33°. From the characteristic XRR oscillations, a Pt bottom electrode layer thickness of about 60 nm and an oxide layer thickness of about 11 – 12 nm was obtained, as well as a low (surface/interface) roughness below 1 nm.

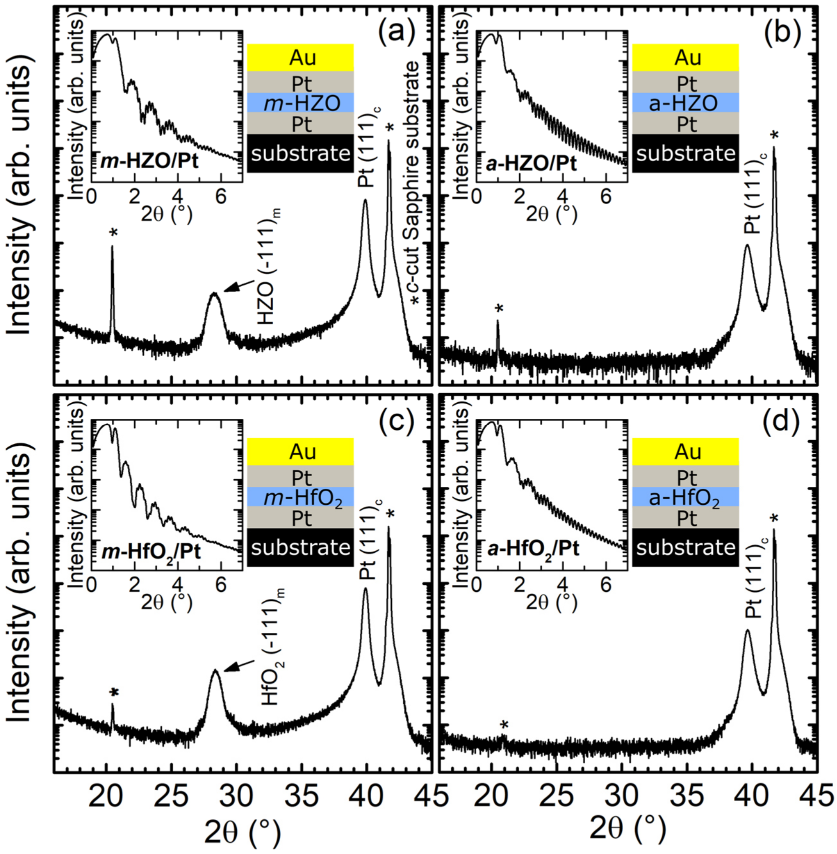

Figure 5-6: XRD and XRR patterns of stacks with a) *m*-HZO film grown at 300 °C, b) *a*-HZO film grown at RT, (c) *m*-HfO_2 film grown at 300 °C, (d) *a*-HfO_2 film grown at RT. The (111) reflection of the cubic Pt cubic electrodes and the *c*-cut Sapphire substrates are also visible.

A schematic representation of the layer thicknesses of the stackings can be obtained from Figure 5-7 (a). The Pt bottom electrode quality, especially roughness, was checked additionally by atomic force microscopy (see Appendix Figure 4). Crystalline HZO and HfO_2 films might in general show a slightly lower roughness when compared to amorphous films, which is a result of the different growth kinetics.

In Figure 5-7 (b) and (c), exemplary bipolar resistive switching current-voltage curves with set with positive voltage polarity (blue) and reset with negative polarity (green) of devices containing (b) *m*-HZO and (c) *a*-HZO are shown. In contrast to the switching attempts on post-deposition annealed TiN/HZO/TiN samples presented in the previous chapter, proper bipolar resistive switching including forming, set and reset operation is possible. All devices were found to be fully functional. The as grown stacks are thus not fully conducting and the growth of HZO films at both 300 °C and RT seems to result in well-defined dielectric oxide layer. An additional interesting characteristic of the presented symmetric devices containing both a Pt bottom and top electrode is the occurrence of non-polar switching. In other words, similar set and reset operations can be performed regardless of the polarity, at least in a limited voltage range to prevent set during the reset routine.

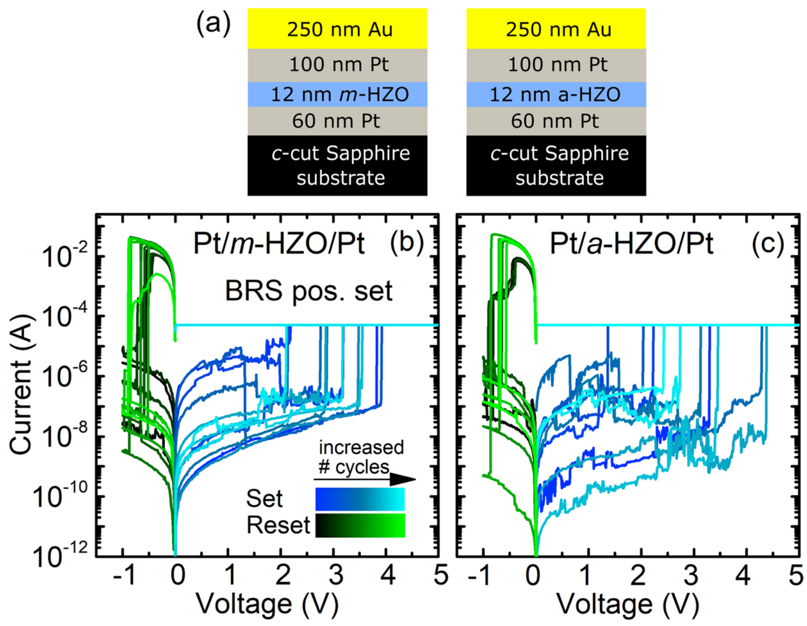

Figure 5-7: (a) Schematic representation of the investigated stacks and corresponding BRS I-V curves of (b) *m*-HZO- and (c) *a*-HZO-containing stacks. The color coding from dark to light blue/green indicates the increased number of cycles for set/reset, respectively.

As an example, for the possible unipolar resistive switching characteristics obtained, current-voltage curves of monoclinic HZO are presented in Figure 5-8, for (a) positive and (b) negative voltages applied. Additional examples for the other stack types are shown in Figure Appendix-5.

Overall, the switching characteristics are found to be quite similar for all stack types, independent of the polarity of the voltage or the type of oxide in the stacks. However, a large set voltage variance and an overall high cycle-to-cycle variability is obtained, which is likely to be a result of a Joule-heating dominated switching mechanism (TCM). The usage of Pt top and bottom electrode as inert electrodes strongly promotes the formation and rupturing of an oxygen vacancy filament dominated by thermal effects (Joule heating) especially in URS mode. However, also for BRS, where the valence change mechanism can exist, a dominance of the thermochemical mechanism is possible. This can be also seen from the required low reset voltages around or below -1 V. The presented results are according to literature, where non-polar switching was found in Pt/HfO_2/Pt based devices. [153, 154, 156]

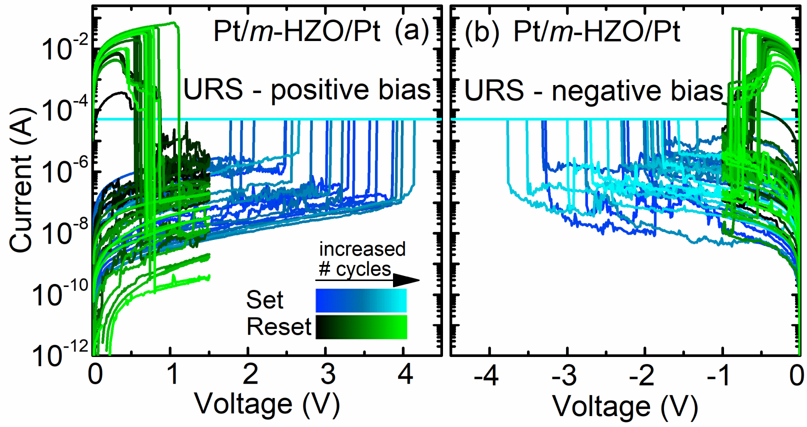

Figure 5-8: Current-voltage curves for URS of *m*-HZO-containing devices under (a) positive bias voltage polarity and (b) negative bias voltage polarity. The color coding from dark to light blue/green indicates the increased number of cycles.

Additionally, a low endurance and a non-uniform behavior is typical. A deep reset seen as a large current jump in the reset process is considered to be the result of a highly- or fully-dissolved conductive filament, resulting in the presence of a deep HRS. The subsequent (re)formation of a conductive filament is then achieved at increased set voltages. The high current compliance required for a successful set operation and possible current overshoots are likely to be contributing to the non-uniform behavior.

Cumulative probabilities of the forming, set and reset voltages obtained for devices of the four different stacks for negative set and reset (URS) are shown in Figure 5-9. A cumulative probability plot is a graphical representation of the empirical cumulative distribution function of the data. It is created by plotting each measurement value against the fraction of all values that are less than or equal to that value, therefore assigning probabilities to each data point. With this, the probability of being above or below a particular value is given, which can be useful for comparing different datasets.

The major difference in the presented dataset is found for the forming voltages (Figure 5-9 (a), where devices containing amorphous oxide layers tend to shown larger forming voltages than devices containing crystalline layers. This is in accordance with literature, where grain boundaries present in crystalline oxides are seen as preferential sites for oxygen defect agglomeration and potential paths for conductive filament formation. This position is believed to be energetically more favorable than a segregation in bulk HfO_2.[76, 134-137]

For reset (b) and set (c) voltages, no direct impact of the Zr-content is observed for 30 measured devices (of each sample). A reduction of the operation voltages by Zr-doping (mixing) cannot be confirmed. However, in contrast to literature, the presented results were obtained from HZO-containing devices and not from devices with a 9 at% Zr-doped HfO_2 switching layer.[147-150] Comparing the forming voltages of devices containing crystalline *m*-HZO versus *m*-HfO_2, lower values are found for *m*-HfO_2-containing devices. Due to the chemical similarity of Hf and Zr, this was not expected to be seen for a Hf:Zr 1:1 mixture. The nature of this effect is yet unclear.

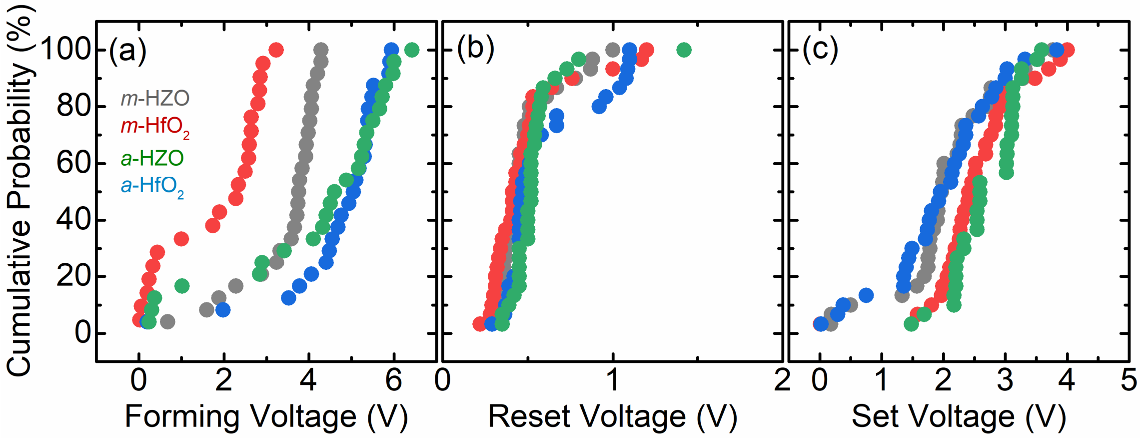

Figure 5-9: Cumulative probability plots of (a) forming voltage, (b) reset voltage and (c) set voltage for the four different investigated stacks. Values were obtained from URS with negative set and reset voltages for 30 devices each. Note that in the shown plots absolute values are given.

Deeper analysis of these stacks including further switching measurements or any further switching using annealed HfO_2- or HZO-containing devices was not performed. However, the obtained results of this comparative study have proven resistive switching functionality of amorphous and monoclinic hafnium oxide-based devices, mainly independent of the Zr-doping. The results obtained from the working devices with chemically inert Pt electrodes have further revealed that the amorphous film growth itself is most likely not directly causing the leakage and switching problems discussed in the previous chapter 5.2 for P-E and I-V investigations.

5.4 Resistive switching characteristics of Pt/HfO_2/Pt devices and Cu/HfO_2/Pt devices

As the resistive switching characteristics and corresponding mechanisms are not only depending on the type of insulator but also on the nature of the top electrode (e.g., chemically active electrode versus chemically inert electrode), electrode-dependent characteristics of Cu/10 nm HfO_2/Pt devices were studied and their behavior compared to the characteristics obtained for Pt/10 nm HfO_2/Pt devices, using different operation modes. The Pt/HfO_2/Pt stack is similar to the stack used for the investigations discussed in the previous chapter, but not the same sample. In contrast to a Pt electrode, a Cu electrode can be used as an active electrode to establish a Cu conductive filament. Those ECM devices show switching characteristics preferably based on an electrochemical metallization mechanism and are of interest for non-volatile memory applications. A further motivation for the conduction of this study is the potential use of HfO_x-based ECM devices as selectors, as they can show threshold switching behavior (compare chapters 2.1.2, 2.1.3 and 2.4).

Schematic device stackings of both samples under investigation are shown in Figure 5-10 (a). The stoichiometric hafnium oxide films are ($\bar{1}$11)-oriented (textured) monoclinic films, while the Pt bottom electrode layer is cubic and (111)-oriented, as shown in the previous chapter. In Figure 5-10 (b), the cumulative probability plots of Cu/HfO_2/Pt (orange) and Pt/HfO_2/Pt (grey) devices are shown.

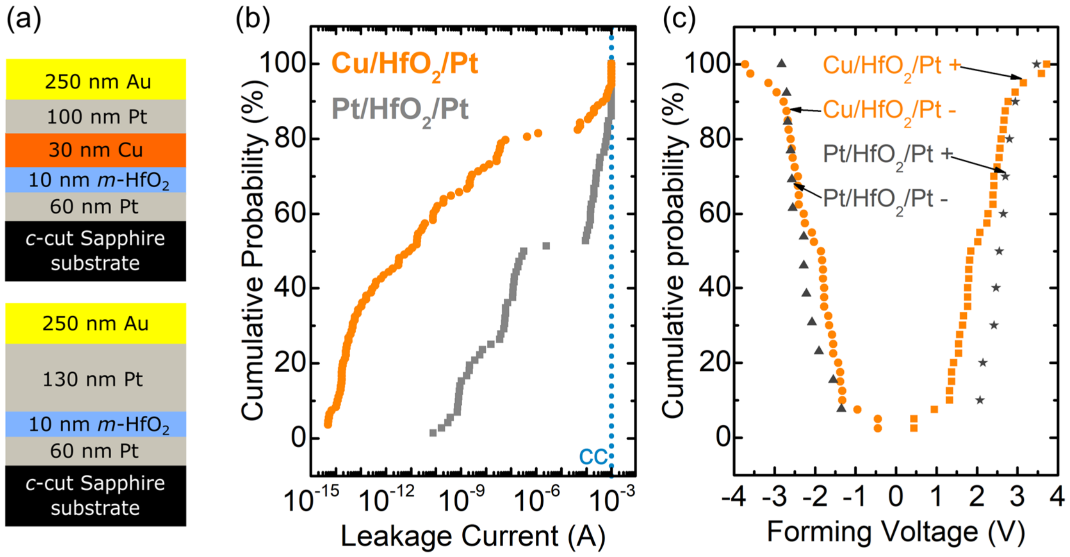

Figure 5-10: (a) Schematic device stacks with a Cu versus Pt top electrode and (b) cumulative probability plot of the leakage current for the two different stacks. Pt top electrode-based devices have much higher leakage currents than Cu top electrode-based devices. Note that the devices size (top electrode area) is 30×30 µm². The dotted line labeled cc marks the value of 1 mA used as the current compliance. (c) Cumulative probability plot of the forming voltage for both stacks for positive and negative polarity with the lowest values obtained for Cu/HfO_2/Pt stacks for positive voltages.

Overall, Cu/HfO_2/Pt devices show lower initial leakage currents than Pt/HfO_2/Pt devices. 88 out of 108 devices could be formed, while 20 devices were already stuck in the LRS with a high initial leakage current at the used current compliance of 1 mA. $Pt/HfO_2/Pt$ devices show a comparably high average leakage current of about 0.35 mA (75 devices measured) with 31 devices with a leakage current above 0.01 mA and 27 devices with a leakage between 0.01 mA and 10 nA. 17 devices were found to have low leakage of below 10 nA.

The reason for the high leakage currents in $Pt/HfO_2/Pt$-based devices when compared to $Cu/HfO_2/Pt$ devices could be related to the presence of different conduction mechanisms, dependent on the top electrode to insulator interface. Due to the simultaneous growth of the HfO_2 layers of both stacks (and the Pt bottom electrode underneath), the oxide layers have the same properties. Further investigations are required in the future to fully understand the obtained differences.

In Figure 5-10 (c), the forming voltage distributions (cumulative probabilities) of both device types are shown for both polarities (negative and positive voltage). As most of the $Pt/HfO_2/Pt$ devices showed a high initial leakage current, forming was performed on 23 devices only. For devices with a higher initial leakage current, a reset step was first required (not included in the presented plots). The obtained forming voltages are found to be around 1.5 – 3 V (absolute value). In contrast, the forming voltages of $Cu/HfO_2/Pt$ devices are dependent on the applied voltage polarity. For negative voltages applied, values are found between -2 and -4 V, which is similar to the values obtained for $Pt/HfO_2/Pt$ devices. On contrast, slightly lower voltages are obtained for positive polarity. This is in accordance to literature reports and most probably a result of two different switching mechanisms occurring.[96, 104, 105, 159, 344] Both, unipolar and BRS switching in $Pt/HfO_2/Pt$ devices is dominated by thermal effects (TCM), which is stabilizing a conductive filament composed of oxygen vacancies (Hf metal rich and O depleted volume). In contrast, BRS with a forming/set under positive bias in $Cu/HfO_2/Pt$ devices is dominated by an electrochemical metallization mechanism with a Cu metal filament being formed. If a positive voltage is applied to the top electrode, Cu ions diffuse into the oxide layer from the top to the bottom electrode during the forming process. In this case, the electrochemical metallization mechanism is energetically dominating a potentially also relevant valence change mechanism. Consequently, Cu ion formation and migration leading to the stabilization of a metal filament is favored over the formation of an oxygen vacancy filament. In contrast, Cu ion migration under negative voltage bias is suppressed, as the cations are repelled by electric field. The reset under negative bias is occurring due to a mixture of effects from electric field and Joule heating, often reported to be dominated by heat effects.[100, 104, 105]

Exemplary current-voltage curves are presented in Appendix Figure 6 and Appendix Figure 7, which are in accordance with the discussed results presented in Figure 5-10 (c). It is shown that a switching of devices of both device stack types under all possible polarities is possible (negative forming/set & negative reset; positive forming/set & positive reset; negative forming/set & positive reset; positive forming/set & negative reset). The reset voltage values of all four operation modes for both stack types are similar and always below 1 V (absolute values). Larger absolute reset voltage values in the range of 1.2 V to 1.5 V lead to an undesired set process after the actual reset. This results in a hard-breakdown of the devices that keeps being stuck in the LRS afterwards. Therefore, applied voltages were chosen to not exceed 1.1 V for all samples in the reset routine (absolute values). The occurring non-polar switching in $Pt/HfO_2/Pt$ was already discussed in the previous chapter.

Representative current-voltage curves (50 cycles) of a Pt/HfO_2/Pt device are shown in Figure 5-11. Unipolar resistive switching (URS) was performed using negative set and reset (a), while bipolar resistive switching (BRS) was performed using negative set and positive reset (b). As this study focuses on the physical behavior of the switching to obtain a better understanding of the device physics, the necessary performance of only a few numbers of cycles was sufficient and a high endurance as required for real applications was not tested.

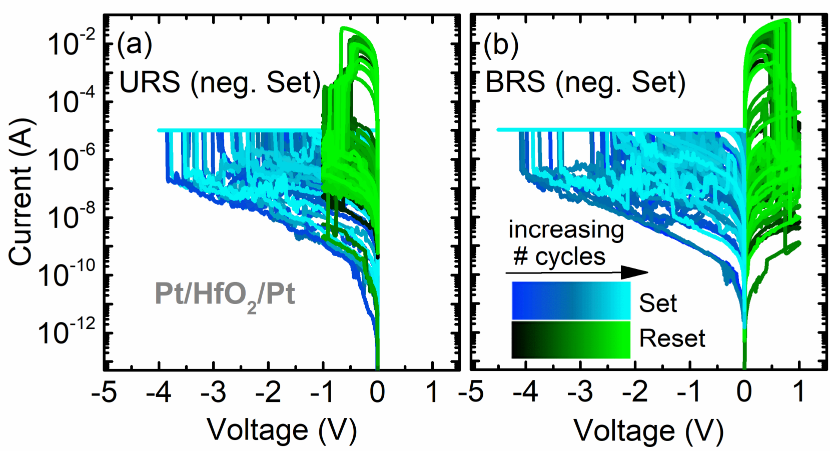

Figure 5-11: Representative 50 endurance cycles of Pt/HfO_2/Pt devices of (a) URS (negative set) and (b) BRS (negative set). These results are indicating a non-polar switching behavior with a large operation voltage variance visible.

Overall, both switching operations lead to a stable switching independent on the operation mode, however, a huge variance can be observed for both cases (set voltage: about 0.5 – 4 V; reset voltage: about 0.4 – 1 V). The switching process is subject to a dominant thermochemical mechanism, as discussed in chapter 5.3. As a consequence, it is reasonable to assume that a valence change mechanism only plays a minor role. A large variance of the set voltage in subsequent cycles occurs mostly when the corresponding reset after a set leads to either a high or low current (in the HRS). For the subsequent set, a much lower or a much larger set voltage is then required, respectively. The change is induced by temperature effects, where the highest temperature region in the vicinity of the conductive filament leads to a change of the filament shape or rupture length compared to the previous (or subsequent) cycle. A filament is ruptured to a different length in the subsequent cycle(s), which is leading to different resistances of the respective HRS. The occurring current jumps (high average resistance ratio of 10^6) stress the switched device in every cycle. However, more than 100 stable switching cycles could be achieved.

As this chapter focuses on the switching characteristics of Cu/HfO_2/Pt devices, all four possible switching modes are shown in Figure 5-12. The behavior of Cu/HfO_2/Pt devices is discussed in more detail in the following. For all modes, stable resistive switching was found but not all cycling operations lead to a similar result. In general, the bipolar resistive switching in Cu/HfO_2/Pt devices is found to be dependent on the initial forming/set polarity, where larger voltages are required for negative polarity.

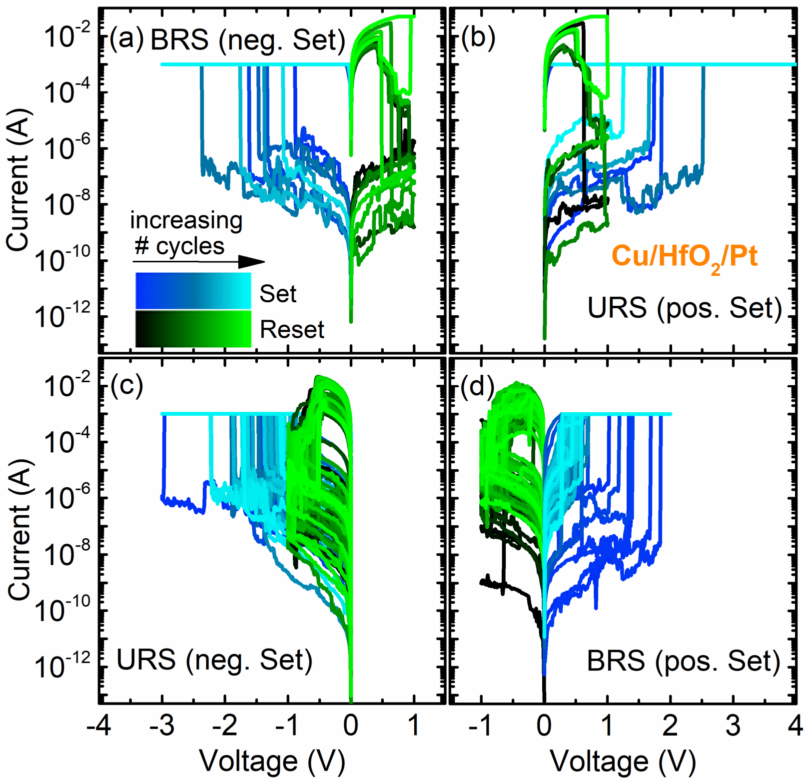

Figure 5-12: Representative cycles of a Cu/HfO₂/Pt devices of (a) BRS (negative set), (b) URS (positive set), (c) URS (negative set) and (d) BRS (positive set), all showing a different behavior strongly dependent on the operation mode. After the last shown reset routine in positive polarity ((a) and (b)), the devices face a hard-breakdown (permanent set to the on state).

First, the BRS with negative set (Figure 5-12 (a)) and the URS with positive set (b) show a low endurance (max. 20 cycles before hard-breakdown; devices stuck in LRS). For the URS (c) and BRS (d) with a negative reset operation, a better performance expressed by a larger number of possible cycles is observed (50 shown, more than 100 cycles possible).

Second, the overall memory window of the devices (here given as a current ratio between the LRS and HRS) is dependent on the operation mode. For the BRS (Figure 5-12 (a)) and URS (b) with a positive reset operation, a high variance of the operation voltages in only a small number of cycles and large variation of the HRS current after the reset processes is found. URS with a negative reset operation (c) leads to a similar large current jump occurring during the reset ($\approx 10^5$), with a variance of the set voltage between 0.5 and 3 V (absolute values). In contrast, this is not found for BRS with a negative reset operation (d), where the memory window is much lower ($\approx 10^3$). Therefore, also the set voltage variance is reduced ($\approx 0.2 - 1$ V). Smaller current drops in reset lead to a more stable switching overall. However, there is a sufficiently large current flowing for proper set and reset functionality and a large memory window is maintained over more than 100 cycles.

While positive set operation leads to the stabilization of a conductive filament composed of Cu in Cu/HfO₂/Pt (d), it is reasonable to assume that an oxygen vacancy filament is stabilized when a negative voltage is applied for the set process (c). A rupturing of the metal filament in the subsequent negative reset occurs predominantly by Joule heating for both cases. For BRS with negative set and positive reset operation, an electrochemical mechanism is dominant, but the motion of Cu ions during forming/set can lead to a possible superimposition of electro- and thermochemical mechanisms. This could result in the presence of a mixed (hybrid) filament.

The low endurance for positive reset (Figure 5-12 (a)) is therefore likely caused by a detrimental interaction of Cu ion migration with the actual rupturing process of an oxygen vacancy-based filament. This can lead to an unwanted set during the actual reset routine, which is difficult to prevent. For URS using positive operation voltages, a Cu metal filament is formed during set. In the dissolution/rupturing process caused by Joule heating during reset, Cu ions move away from the conductive filament region close to the Cu top electrode, however metal ions from the active electrode could re-stabilize a conductive filament (driven by a mixture of thermal effects and electric field applied). This hypothesis could explain the resulting visible hard-breakdown and low endurance found in URS for positive bias voltage polarity (Figure 5-12 (b)).

In summary, several differences were found when comparing the switching characteristics of Pt/HfO_2/Pt and Cu/HfO_2/Pt devices overall. Pt/HfO_2/Pt devices show a thermochemical mechanism-based non-polar switching behavior and a large memory window with a high operation voltage variance. In contrast, investigations of especially the BRS characteristics (positive set and negative reset) in Cu/HfO_2/Pt devices revealed an improved device stability. In accordance with literature, this is attributed to an operation based on the formation and rupturing of a Cu metal conductive filament. Further, the set voltages seem to be reduced with increasing cycles, which indicates a formation and stabilization of a Cu conductive filament that is probably not dissolved to a large extent in the reset process (quite conductive HRS after reset and low forming voltage in subsequent set process). The complex switching mechanism and a possible model for the filament formation and rupturing in Cu/HfO_2/Pt-based devices, which can be influenced by electric field and created heat, is further discussed in chapter 5.5 for stacks containing dielectric layers of different thickness.

5.4.1 Current compliance-dependent switching and potential threshold switching

An additional motivation for the investigation of the presented stacks was the potential use of HfO_x-based devices as selectors (compare chapter 2.1.2 and 2.4), which will be now shortly discussed. In the presented studies, the required threshold resistive switching (TRS) was not observed.

For stable resistive switching in Pt/HfO_2/Pt-based TCM devices, a high current compliance in the set processes (100 μA and 1 mA) lead to an instable switching, while for switching using a lower current compliance (10 μA), no significant impact on the number of endurance cycles or the stability was found for all switching polarities. During forming, stable filaments were achieved by using a current compliance of 10 – 100 μA (stable LRS). This could be a result of the conductive filament thickness achieved and the overall heat produced in the vicinity of the filament during switching, both tending to increase with larger current compliance. A lower current compliance is considered to result in the formation of a weaker filament and a reduced heat production within the stack, which lowers the probability of unfavored ionic motion and ion distribution effects. A very low current compliance however may lead to an insufficient current flowing to establish a stable conductive filament in the dielectric layer. Therefore, the cycling discussed in this chapter was performed using a current compliance of 10 μA for Pt/HfO_2/Pt devices.

In contrast, the usage of current compliance of 10 μA and 100 μA for forming/set processes of Cu/HfO_2/Pt in ECM devices resulted in a lowered endurance. At a high current compliance of 1 mA, however, a more stable BRS (positive forming/set, negative reset) was achieved (potentially leading to the formation of a thicker filament). Possibly, the creation of Cu ions at the top electrode interface, their motion and the creation (nucleation and growth) of a Cu filament starting from the Pt bottom electrode requires larger currents. The Cu/HfO_2/Pt memory devices were therefore switched using a current compliance of 1 mA.

In literature[224], a current compliance dependence of the BRS (non-volatile switching with a stable LRS) and TRS (filament formed in a set process, but volatile switching with unstable LRS) in Cu/HfO_2/Pt based devices is reported. Stable non-volatile switching was obtained using a current compliance of 100 μA, while (volatile) TRS was reported for set operation with current compliance of 10 μA and 1 μA. This dependency could not be confirmed by the results presented in chapter 5.4. Instead, stable memory switching with the mentioned lowered endurance was obtained. A possible explanation could be an occurring current overshoot during forming/set for higher current compliance values. The current compliance control of the measurement setup has a delay that is expected to be in the μs-range, during which a current overshoot accompanied by high Joule heating can occur.[152, 332] A conductive filament can be established on a shorter timescale and therefore continue growing during the delay time. This can lead to thicker filaments formed than expected and a corresponding non-volatile memory behavior. This is also valid for the tested Pt/HfO_2/Pt devices. At even lower current compliance values (e.g., 1 μA), no filament was formed at all, which was seen from conductance values that were found to be far below $1G_0$ ($G_0 = 2e^2/h$ with e being the elementary charge and h the Planck constant). The formation of the thinnest possible conductive filament leads to a conductance of about $1G_0$. This represents the narrowest point of the filament with one oxygen vacancy or one metal atom connecting the electrodes and can be used as an indicator for an established or ruptured filament.[75, 345]

In literature, different stackings with HfO_x as a switching layer showing threshold switching are reported[53, 112, 164, 223, 224], where TRS is not only dependent on the current compliance but also on the ion species. The usage of a Ag electrode is reported to simplify the achievement of threshold switching in comparison to Cu. This could stem from different effects: (1) A larger work function difference between the used electrodes seems to support TRS. (2) The interface energy of the filament should be much larger than the interface energy of a formed cluster.[224] (3) Additionally, the higher mobility of the Ag ions and the occupation of interstitial sites in the HfO_x layer might play a role. It was further shown that the switching performance in Ag/HfO_2/Pt films can be controlled by a preformed oxygen vacancy filament.[53, 223] This can also be a promising approach for Cu-based selector devices. Here, additional Cu-doping of the HfO_x layer[164] can increase ion mobility and potentially also necessary interface energies and trap states. It should be kept in mind that these effects further depend on temperature and oxide layer thickness.[112, 167]

5.5 Thickness-dependent resistive switching in Cu/HfO$_2$/Pt-based ECM devices

As downscaling of devices is a key feature of electronics in general and also relevant for different kinds of RRAM devices that are promising candidates for 3D-integration, there is a large interest in related studies. Investigations of the switching properties of Cu/HfO$_2$/Pt-based devices can help to get a better understanding of a) the underlying switching mechanisms of ECM devices with a Cu conductive filament in general and b) the properties of HfO$_2$-based dielectric layers in dependence of the oxide layer thickness in particular. In the presented study, bipolar resistive switching with positive forming/set and negative reset operation of Cu/HfO$_2$/Pt devices with different HfO$_2$ layer thickness (20 nm – 3 nm) was conducted. The stacking of the electrical devices is shown schematically in Figure 5-13 together with a HAADF-STEM and an ABF-STEM image of atomic resolution of a stack containing a 10 nm thick HfO$_2$ layer sandwiched between a Pt bottom and a Cu top electrode. A good crystallinity of the oxide is confirmed. Crystalline grains with a length of 10 nm are connecting both electrodes.

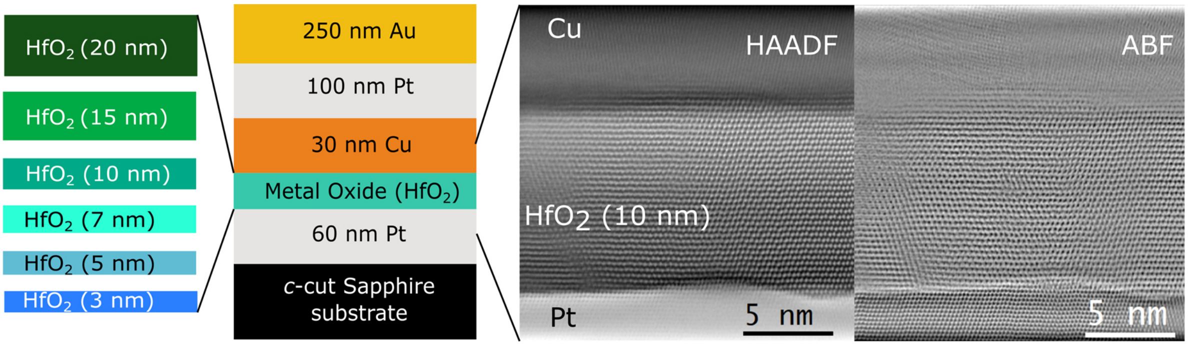

Figure 5-13 Schematic representation of the device stacks with different HfO$_2$ layer-thicknesses (20nm, 15nm, 10 nm, 7 nm, 5 nm, and 3 nm) on Pt bottom electrodes and *c*-cut Sapphire substrates, with Au/Pt/Cu top electrode layers. Additionally, a high-angle annular dark-field image (HAADF) showing the presence of a crystalline 10 nm HfO$_2$-film sandwiched between the two metal electrodes (Cu - dark; Pt - bright) and a high crystallinity of the 10 nm thick HfO$_2$ film is given. In the annular bright-field image (ABF), the crystalline nature of the electrodes can be seen. An Average Background Subtraction Filter (ABSF) was applied to the initial STEM images.[346] Figure partially reproduced with permission from[347]. The original publication is licensed under a Creative Commons Attribution 4.0 License (CCBY) and published by AIP Publishing.

The hafnium oxide films were found to be monoclinic films (*m*-HfO$_2$; space group $P2_1/c$; XRD patterns in Figure 5-14 (a)), while the Pt bottom electrode is cubic ((111)-oriented). The intensity of the characteristic ($\bar{1}11$) reflection of monoclinic HfO$_2$ decreases for thinner oxide layers due to the lower crystalline volume (interaction volume with the X-rays). For the 3 nm thin film, the reflection is of low intensity, which is additionally caused by the small crystallite sizes and close to the resolution limit of the measurement setup. Representative switching curves of devices containing hafnium oxide layers of different thickness are shown in Figure 5-14 (b). For all samples, the devices are working under positive set and negative reset, as described in the previous chapter. Electroforming as well as subsequent reset and set was performed on devices to investigate the resistive switching characteristics in more detail. To allow a reasonable comparison, devices with a similar HRS current (1.0×10^{-11} A) were used.

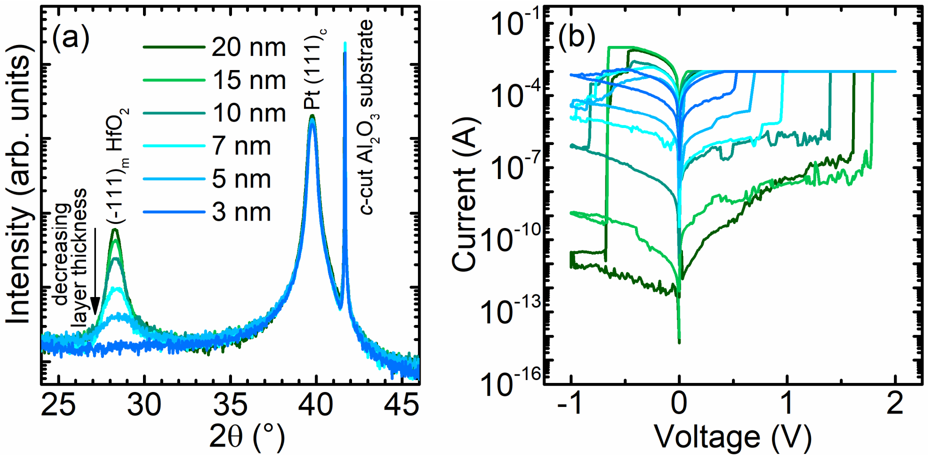

Figure 5-14: (a) XRD patterns of the *m*-HfO_2 films of different thickness grown on top of cubic Pt bottom electrodes and *c*-cut Sapphire substrates, (b) Representative current-voltage curves obtained from devices of the six different stacks. A change from an abrupt to a more gradual reset with increasing oxide layer thickness is visible. Figure partially reproduced with permission from[347]. The original publication is licensed under a Creative Commons Attribution 4.0 License (CCBY) and published by AIP Publishing.

5.5.1 Bipolar resistive switching characteristics, filament formation and rupture in Cu/HfO_2/Pt ECM devices with varying oxide layer thickness

To get a first insight in the electrical device performance, the forming voltages of the six different stacks were investigated. Those are found to be oxide layer thickness-dependent (Figure 5-15), which is in accordance to literature on HfO_2-based RRAM[100, 132, 162] Devices containing thicker hafnium oxide layers tend to require higher voltages to reach a critical electric field in the dielectric HfO_2 for a successful forming process. This trend cannot only be seen from the representative current-voltage curves for the six different stacks (a), but in more detail also from the cumulative probability plot (b).

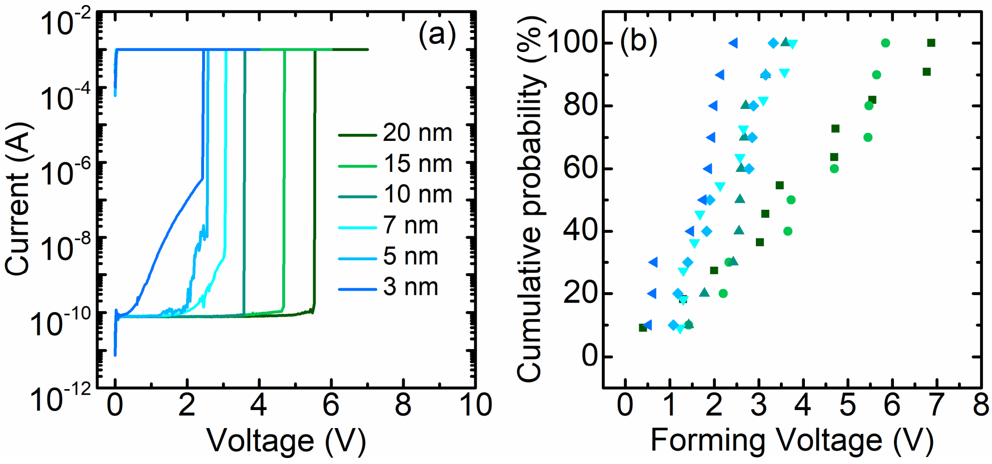

Figure 5-15: (a) Current-voltage curves of the forming process (cc = 1 mA), (b) cumulative probability plot of the forming voltage obtained from devices of all six samples with varied oxide layer thickness (10 devices each). Figure partially reproduced with permission from[347]. The original publication is licensed under a Creative Commons Attribution 4.0 License (CCBY) and published by AIP Publishing.

Devices containing 20 nm and 15 nm thick HfO_2 films have an average forming voltage of about 4 V, while for thinner samples containing 10 – 5 nm thin HfO_2 and 3 nm thin HfO_2 films average voltages of about 2.5 V and 2 V were found, respectively. Also, it becomes obvious that the forming voltage variance is larger for thicker samples (voltages up to about 7 V).

The most interesting feature was found in the current-voltage curves for the reset (Figure 5-16 (a)). With decreasing oxide layer thickness from 20 nm down to 3 nm HfO_2, there is a continuous change from an abrupt (sharp and deep reset, high nonlinearity) to a more gradual reset visible. The current in the HRS after the reset ranging from 10^{-12} A to 10^{-4} A is therefore by multiple orders of magnitude lower in thicker devices than in thinner ones. The measurement curves were additionally compared to the quantum conductance G_0 (= $2e^2/h$), which was used as an indicator for a ruptured or possibly non-ruptured (still connected) filament. The current-voltage curve for G_0 was added to Figure 5-16 (a) in red. For stacks containing HfO_2 films of 20 nm down to 7 nm thickness, the HRS current drops below G_0 during the reset. The conductive filament can therefore be considered as being ruptured. For thinner stacks, the current stays above G_0 even after the reset. It is reasonable to assume that the conductive filament is not completely ruptured in 3 nm and 5 nm thick films. A thin connection between both electrodes via an oxygen vacancy-based conductive filament in the actual HRS is likely. The difference in the current levels of the LRS and HRS of such devices is then a result of the filament width. Devices in the HRS contain a much thinner filament than devices in the LRS. This is directly linked to the overall current flowing through the overall device during the reset process. The cumulative probability of the maximum reset current (max. reset current) is shown in Figure 5-16 (b), while the cumulative probability of the HRS current is shown in (c).

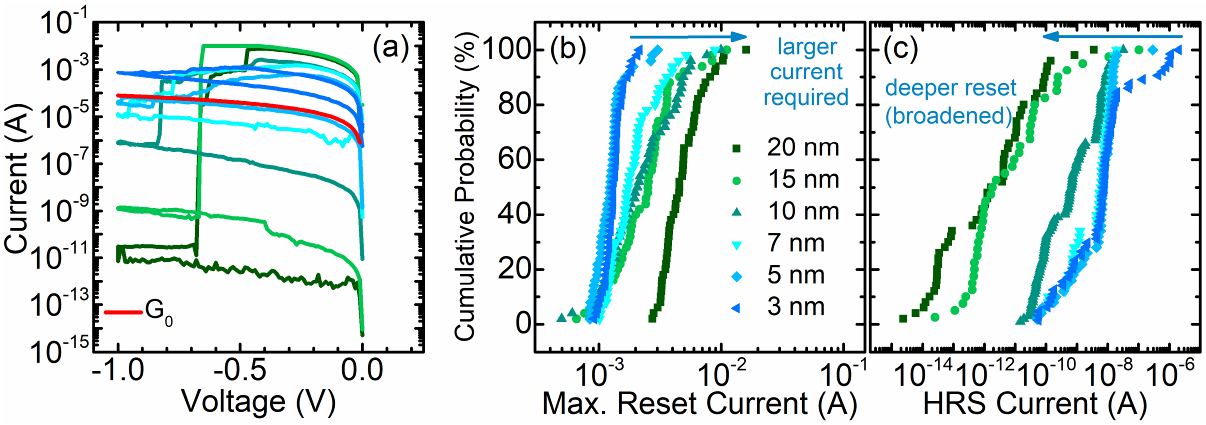

Figure 5-16: (a) Representative current-voltage curves of the reset process for devices of the six different stacks. Additionally, the curve of G_0 is included (red). For the reset, a maximum voltage of -1 V was applied to prevent a hard-breakdown of the devices by oxygen vacancy filament-formation. (b) Cumulative probability of the maximum reset current and (c) cumulative probability of the HRS current after the reset. Blue arrows label the increase of the oxide layer thickness. Figure partially reproduced with permission from[347]. The original publication is licensed under a Creative Commons Attribution 4.0 License (CCBY) and published by AIP Publishing.

The trend shows that in devices containing thicker oxide layers, a larger current of about 4.5×10^{-3} A is required to achieve a reset (compare also Figure 5-16 (b) to (a)) when using the same reset routine (maximum voltage of – 1 V applied). The HRS current of devices containing 20 nm and 15 nm thick HfO_2 switching layers (1.6×10^{-12} A) is more than 1000 times lower than the HRS current of thinner devices (8.0×10^{-9} A) after the reset. This corresponds to a deeper reset in thicker films (Figure 5-16 (a)). Additionally, a broadening/larger variance of the HRS current for thicker stacks is seen in Figure 5-16 (c) when compared to thinner stacks, which is equivalent to a higher HRS variance. In the subsequent set (see Figure 5-17 (a)), a similar broadening is visible for thicker devices with 20 nm and 15 nm HfO_2 layers (up to 4 V), while thinner devices show a uniform set voltage distribution in the cumulative probability plot (in average about 0.5 V, maximum set voltage about 1.8 V). A good visualization of the larger variance obtained for thicker devices is to use a HRS current versus set voltage plot as given in Figure 5-17 (b). The different behavior can be easily seen from the clustering values and the two ellipses drawn around them to represent values of thinner devices (dark blue) and thicker devices (green). Data have been obtained from measurements of five devices per oxide layer thickness.

It can be summarized that devices containing 10 nm, 7 nm, 5 nm, and 3 nm HfO_2 show a high HRS current (average about 3×10^{-9} A for 10 nm and 7 nm stacks and about 1×10^{-8} A for 5 nm and 3 nm stacks), a small HRS current variance (about 1×10^{-8} A – 1×10^{-10} A) and low set voltages (about 0.3 V – 0.7 V). In contrast, thicker devices containing 20 nm and 15 nm HfO_2 layers show lower HRS currents (average $< 1\times10^{-9}$ A) and a larger variance of about 1×10^{-8} A – 1×10^{-14} A as well as larger values and variance of the set voltage (about 0.5 V – 4 V). These changes are accompanied by a more abrupt reset obtained for thicker devices, changing to a more gradual reset visible in the current-voltage curves of thinner devices.

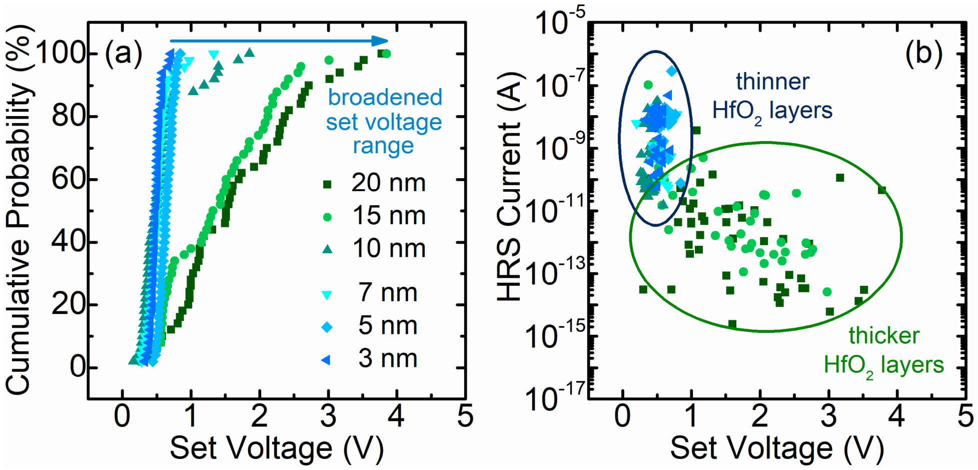

Figure 5-17: (a) Cumulative probability of the set voltage. The blue arrow marks an increasing oxide layer thickness. (b) HRS current versus set voltage correlation plot for devices containing HfO_2 layers of different thickness. Values of thinner films are marked with a dark blue ellipse, while values of thicker films are marked with a green ellipse. Figure partially reproduced with permission from[347]. The original publication is licensed under a Creative Commons Attribution 4.0 License (CCBY) and published by AIP Publishing.

To explain the observed behavior, the following qualitative model is suggested for the presented resistive switching series, where a change of the resistive switching mechanism with varying oxide layer thickness is assumed (Figure 5-18).

When a positive voltage is applied to the top electrode of the devices, while the bottom electrode is grounded, Cu atoms of the Cu electrode are ionized and migrating as Cu ions towards the Pt electrode, where they start forming a conductive Cu filament, growing towards the Cu electrode. As soon as the electric field reaches the critical required value, a conductive Cu filament is established that connects both electrodes in this forming process. The forming (and set) process is based on an electrochemical mechanism. During the subsequent reset process, the conductive filament in thicker HfO_2 films (7 – 20 nm) is ruptured, while in thinner films (3 nm and 5 nm) the filament is only getting thinned (not ruptured), as seen from the G_0 values in Figure 5-16 (a). With decreasing oxide layer thickness, the ruptured conductive filament shows a larger gap, i.e. a not or less conducting part between electrode and filament part. This is corresponding to an abrupt reset in the current-voltage curves. It is reasonable to assume that the thickness-dependent reset behavior stems from the combination of two forces involved: field-induced electromigration and thermal effects/Joule heating. In the reset process of thicker films (15 nm and 20 nm HfO_2), the conductive filament is ruptured by a combination of both with a large contribution of Joule heating. A large current flow is required to reach the necessary critical field for rupturing the filament. Therefore, large Joule heat is created in the vicinity of the conductive filament, which strongly supports ion formation and migration, finally resulting in the rupturing of the filament in a process including a comparably weak oxidation. This is in accordance with the Joule heating-dominated reset behaviors reported in ECM devices containing oxide switching layers of comparable or larger thickness (15 nm – 40 nm).[104, 105] As a consequence, the filament is strongly dissolved (larger gap), which results in the aforementioned deep HRS and the abrupt reset characteristics. The large fluctuations of the HRS current levels after each reset in thicker stacks (20 nm and 15 nm) and the operation voltage variance observed is then also directly related to a dominant thermal-based mechanism and a quite brutally dissolution of the filament. In contrast, electric field-induced ion migration dominates the reset process in thinner films (3 nm and 5 nm).

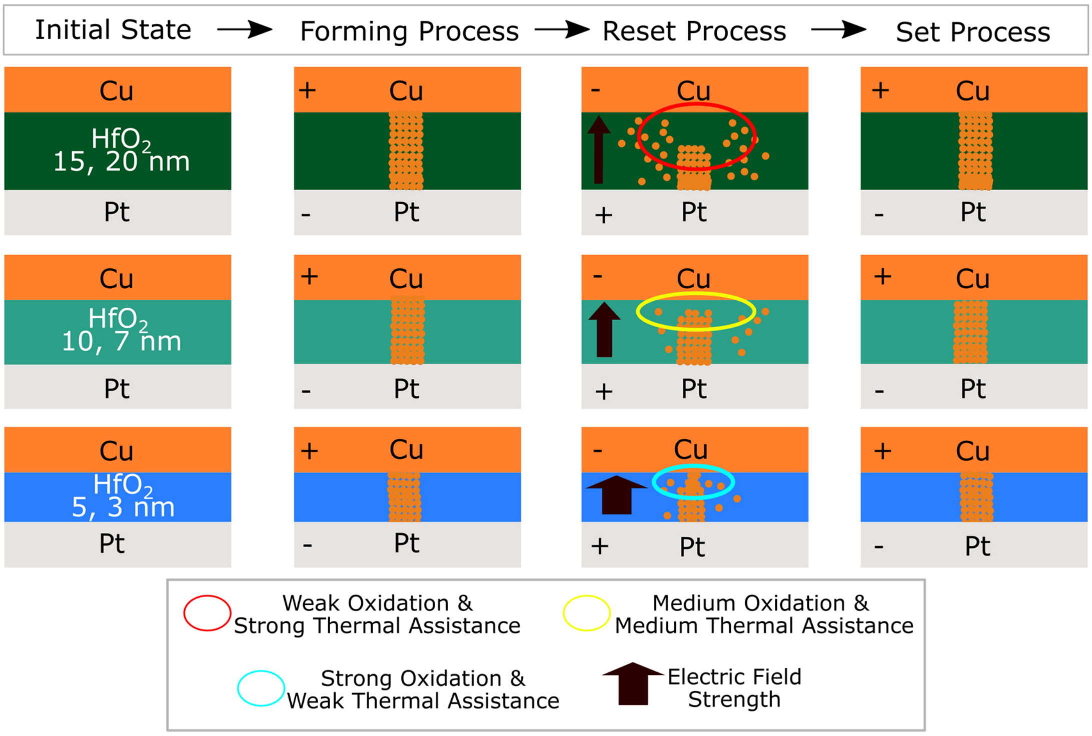

Figure 5-18: Conductive filament formation and rupturing model (reset process) for $Cu/HfO_2/Pt$ devices containing HfO_2 layers of various thickness (20 – 3 nm). In thick devices, the reset process is dominated by thermal effects, while with decreasing thickness, the thermal assistance in the reset process is getting less dominant. After the reset in 3 nm and 5 nm thick films, the filament is not completely ruptured, but thinned. The electric field influence on the reset process therefore increases. Black arrows indicate the electric field strength in the oxide layer. Figure partially reproduced with permission from[347]. The original publication is licensed under a Creative Commons Attribution 4.0 License (CCBY) and published by AIP Publishing.

The relatively large electric field present in the thinner films, leads to a strong electric field-induced oxidation and only a weak thermal assistance, where the conductive filament is thinned but not ruptured. In devices containing 7 nm and 10 nm thick HfO_2 layers, an intermediate (medium) oxidation and Joule heating-assisted mechanism is present, in which the conductive filament is ruptured in close vicinity of the Cu electrode. The overall mechanism can be called a thermally-assisted electrochemical mechanism. The conductive filament gets reconnected to the top electrode (or thickened in 3 nm and 5 nm films) in the subsequent set process when the required set voltage is applied. In the presented qualitative model, the conductive Cu filament is not fully dissolved in the reset process. This is supported by the current levels of the HRS found after the reset, which are higher than the ones observed in pristine devices. Therefore, the forming voltages are higher than the set voltages required after the first reset. However, the presence of conductivity-modifying remanent Cu ions or protons as reported in literature[166, 348] to influence resistive switching cannot be fully excluded, but it is unlikely to result in conductance levels of several G_0 as observed in the presented study. It should be mentioned that for the model as shown in Figure 5-18, a filament of similar diameter for all HfO_2 film thicknesses and an overall uniform filament thickness (cylindrical shape in 3D) for each oxide layer thickness was chosen to simplify the representation. The actual filament diameter can slightly vary over its length, especially in 3 nm and 5 nm thin HfO_2 films, as discussed above. Additionally, the shape of the conductive filament in 3D can be more cone-like.[349]

S. Chen and I. Valov have reported[100] that the best overall switching performance, represented by a compromise between a good resistance ratio and low and narrow operation voltages, is found for 30 nm Cu/10 nm HfO_2-based devices. This is in accordance with the results obtained in this work. The used 30 nm thick Cu top electrode was chosen by coincidence, as the reported literature study[100] was published after the samples of the study presented in this chapter were prepared. A 10 nm thick HfO_2 switching layer was believed to show the optimum performance, as high leakage currents are suppressed (layer not too thin), while allowing a comparably simple field-accelerated ion migration through the oxide (layer not too thick).

5.5.2 Conduction mechanisms in Cu/HfO_2/Pt ECM devices with varied oxide layer thickness

As a second part of the thickness-dependency study, the conduction mechanisms of 20 nm, 10 nm and 3 nm thick HfO_2 films in the set process (positive voltage) were analysed from the current-voltage curves of devices of the HRS to obtain a deeper understanding of the device behavior. The current-voltage curves are given in Figure 5-19 in log-log scale.

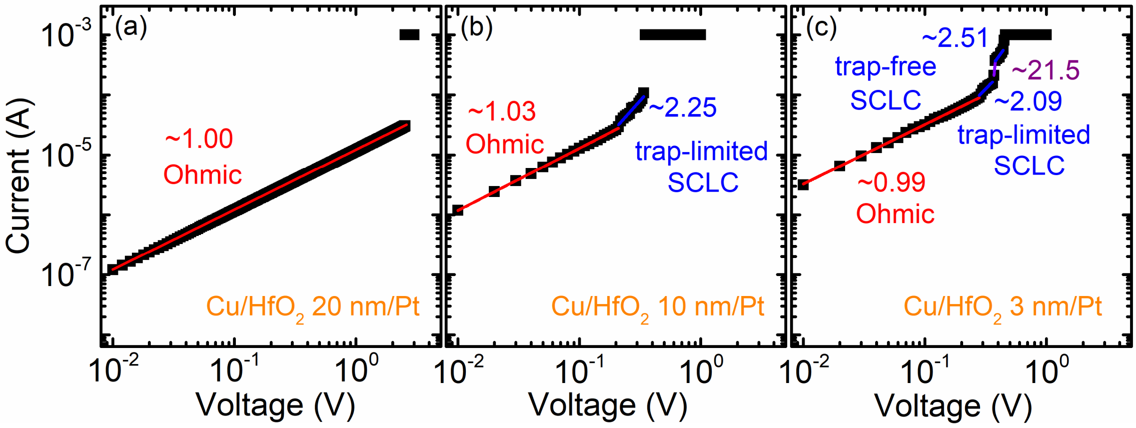

Figure 5-19: Representative current-voltage curves of the HRS obtained in the set process of devices containing (a) 20 nm, (b) 10 nm and (c) 3 nm thick HfO_2 layers. By fitting the slope plotted in log-log scale, ohmic (red fit) and trap-limited/trap-free SCLC conduction (blue fit) can be assigned, dependent on the oxide layer thickness and the applied voltage. Additionally, the slope corresponding to the trap-filled SCLC is shown in purple. This mechanism only occurs for a very short time between trap-limited SCLC and trap-free SCLC. Figure partially reproduced with permission from[347]. The original publication is licensed under a Creative Commons Attribution 4.0 License (CCBY) and published by AIP Publishing.

From the slopes of the corresponding linear fits, an assignment to a certain conduction mechanism is possible. For 20 nm thick HfO_2, the current-voltage curve can be well represented by a linear fit with a slope of 1, which corresponds to an ohmic conduction in the HRS, based on thermally induced electrons (Figure 5-19 (a)). For 10 nm thick HfO_2, the ohmic conduction can be fitted with a slope of 1.03 up to 0.3 V, while a second fit is required for the data at higher voltages which gives a linear fit with the slope of 2.25 (b). It is likely that this corresponds to a trap-limited space-charge-limited conduction (SCLC), as the slope is close to 2. For 3 nm thick HfO_2 (c), four linear fits are required to fit the data points. Up to 0.3 V, a slope of 0.99 is obtained indicating ohmic conduction, while at larger voltages three different slopes above 2 are present. From 0.3 V – 0.45 V, a slope of 2.09 is obtained, corresponding to a trap-limited SCLC. At a voltage of around 0.5 V, a current jump occurs, which is best fitted by using a linear fit with a slope of 21.5. At around 0.55 – 0.7 V, the slope of the corresponding linear fit is 2.51. These fits correspond to regions where a trap-filled SCLC and a trap-free SCLC are likely to be present, respectively. The variation of the current-voltage curves is a result of the changed conduction mechanism caused by different filling levels of the trap states with injected electrons. At larger voltages, the conductive filament connects both electrodes and a current jump to the current compliance of 1 mA is observed. A qualitative model is shown in Figure 5-20.

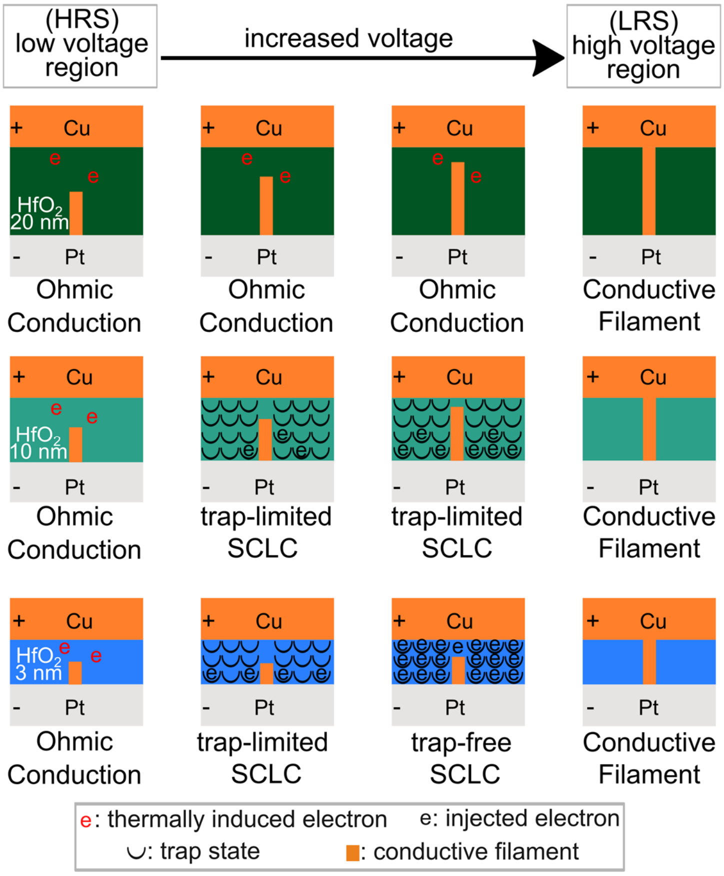

Figure 5-20: Schematic representation of the conduction model for $Cu/HfO_2/Pt$ devices containing HfO_2 layers of three thicknesses (20 nm, 10 nm and 3 nm). With increasing oxide layer thickness, the conduction changes from ohmic to ohmic plus additional SCLC. Note that an additional representation for the trap-filled SCLC is not given, as it only occurs for a very short time between trap-limited SCLC and trap-free SCLC. Figure partially reproduced with permission from[347]. The original publication is licensed under a Creative Commons Attribution 4.0 License (CCBY) and published by AIP Publishing.

In thicker films, the ohmic conduction occurs by thermally-induced electrons. The electric field strength is not sufficiently large for an injection of electrons into the HfO_2 layer (weak injection). Electron injection only occurs for thinner films (10 nm and 3 nm), when the electric field strength is sufficiently high at higher voltages. Here, trap-limited SCLC is present, which is accompanied by a filling of the trap states with electrons. As soon as all trap states are filled (in 3 nm thick films), the current suddenly increases. At larger voltages, a trap-free SCLC is present. When the set voltage is reached, the conductive Cu filament is connecting both electrodes. The presented plots (Figure 5-19) are given as current versus voltage plots, while theoretically an electric field-dependent current density is used. However, in real devices, a rupturing of the filament leads to a gap after the reset process, which cannot be exactly quantified. The real electric field present during the subsequent set process can therefore not be determined. As a consequence, a real field-dependency cannot be given and fittings are usually obtained from current-voltage curves. The presence of SCLC-based mechanisms $Cu/HfO_2/Pt$ devices is in accordance with literature.[118] However, the presented results reveal a thickness-dependence and a change of the conduction mechanism.

In summary, oxide thickness-dependent resistive switching characteristics were investigated in the presented study, where stable BRS was obtained for all stacks and no TRS was found. For this BRS, models for both the switching mechanism and the conduction mechanisms (set) of $Cu/HfO_2/Pt$ ECM devices were developed. The reset process in devices containing thicker HfO_2 layers was found to be dominated by thermal effects (thermally-assisted mechanism) in ECM resistive switching devices. With decreasing oxide layer thickness, the thermal effects were found to be decreasing, while the reset process gets more and more dominated by oxidation due to a comparably stronger electric field in the layers. The oxide layer thickness has also an influence on the conduction mechanism. A change of the conduction mechanism in the HRS was found, where thicker films show ohmic conduction and thinner films additionally show SCLC conduction by injected electrons at increasing voltages applied.

5.6 Impact of the preparation workflow on electrical properties of devices

For the thickness-dependent resistive switching studies (chapter 5.5), initially two preparation workflows were used to achieve two similar series of $Au/Pt/Cu/HfO_2/Pt/$*c*-cut Sapphire stacks with varying HfO_2 thickness (6 samples each – stack configuration shown schematically in Figure 5-21 (a)).

The first series of samples contained 6 *in vacuo*-capped samples that were structured using an ion beam etching (IBE) procedure (“**with IBE**”), introduced in chapter 4.3 (compare Figure 4-5). It was aimed to establish a procedure for future preparations of oxygen-deficient HfO_x-containing stacks with a Cu top electrode, where *in vacuo* capping is required to prevent unwanted further oxidation of the oxide layers.

The second series of samples was designed as a reference series, containing samples that were *ex situ*-covered with top electrode material after the optical lithography procedure, which does not include an IBE step (“**without IBE**”). The different preparation of these two stacks was further described in chapter 4.1.3 and 4.3. A schematic representation of the workflow was presented in Figure 4-5.

The 6 samples prepared “without IBE” could be used for switching investigations, showing resistive switching (as presented in chapter 5.5). Most devices of those samples showed a reasonably low initial leakage current (HRS) and could be formed. In contrast, devices prepared from stacks “with IBE” for HfO_2 layer thicknesses of 15 nm – 3 nm showed high initial leakage currents and were stuck in the LRS (in current compliance of 10^{-3} A). Representative current-voltage curves of the corresponding leakage measurements are shown in Figure 5-21 (a). Only for the sample containing a 20 nm HfO_2 switching layer, several devices were found to be in the HRS (see cumulative probability plot in (b)).

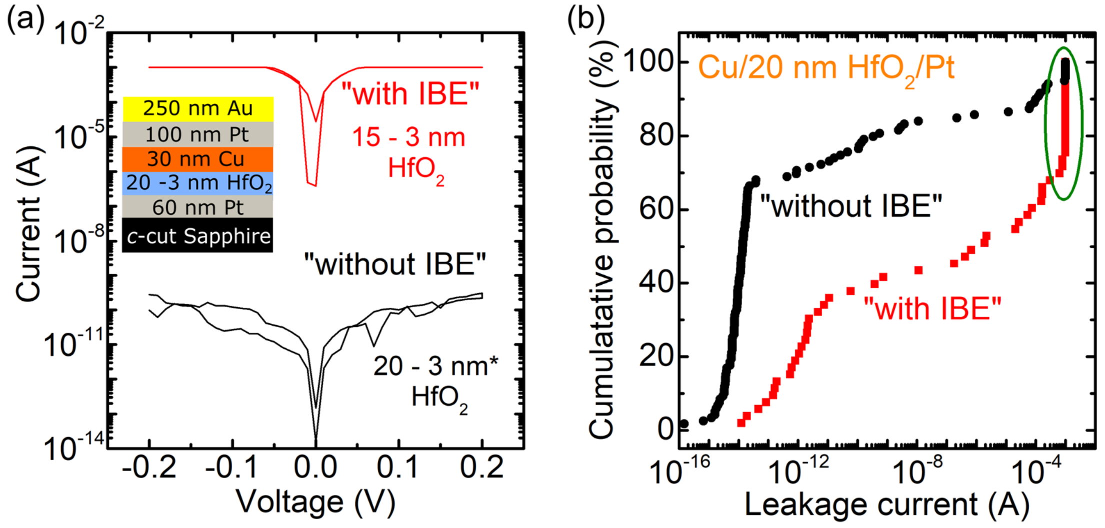

Figure 5-21: (a) Schematic device stack of “with IBE” and “without IBE” samples with corresponding leakage curves. 15 – 3 nm thick HfO_2 samples prepared using IBE (“with IBE” -red) were found to be leaky, while all stacks prepared “without IBE” (black) showed a reasonably low leakage. * Note that this is a simplified representation, as thinner layers were found to show an increased leakage current in average for “without IBE” devices. However, several devices with a leakage current of 10^{-11} A were found for all stacks with different oxide layer thicknesses, as presented in chapter 5.5. (b) Cumulative probability plot with leakage current values of “without IBE” and “with IBE” Cu/20 nm HfO_2/Pt devices. Overall, “without IBE” devices show lower leakage currents with most devices being found in the HRS with leakage currents around 10^{-15} A, which even might be below the detection limit of the measurement system (insulating devices in their pristine state). About 10 of 50 Cu/20 nm HfO_2/Pt devices prepared “with IBE” were found to be stuck in the LRS (green ellipse).

Devices from the samples containing 20 nm HfO_2 layers from both preparation workflows were switchable. However, for the 20 nm “with IBE” sample, larger leakage currents were found overall, with 10 devices stuck in the LRS (leakage at current compliance of 10^{-3} A, reset failure for negative voltage with cc of 10^{-2} A). For thinner “with IBE” stacks containing HfO_2 layers of 15 nm – 3 nm thickness, all measured devices (10 – 20 per stack) were found to be stuck in the LRS (curve in Figure 5-21 (a)). To better understand the differences obtained for “without IBE” versus “with IBE” samples and possible problematic preparational influences, the impact of the two preparation workflows with a focus on “with IBE” samples was examined using scanning precession electron diffraction (SPED). This is discussed in the following.

A closer look into the microstructure using the SPED technique revealed potential differences of the “with IBE” versus “without IBE” samples (see Figure 5-22). SPED is used to obtain nanobeam electron diffraction (NBED) patterns for each pixel of a 2D map. A template matching routine combines these NBED patterns with a list of user-defined templates (monoclinic for HfO_2 and cubic for Cu and Pt). Orientation and phase maps are generated through probability values. For all presented stacks, the same pattern matching routine was used. The acquired experimental NBED patterns which are obtained locally from the nanocrystal are matched with the simulated NBED patterns.

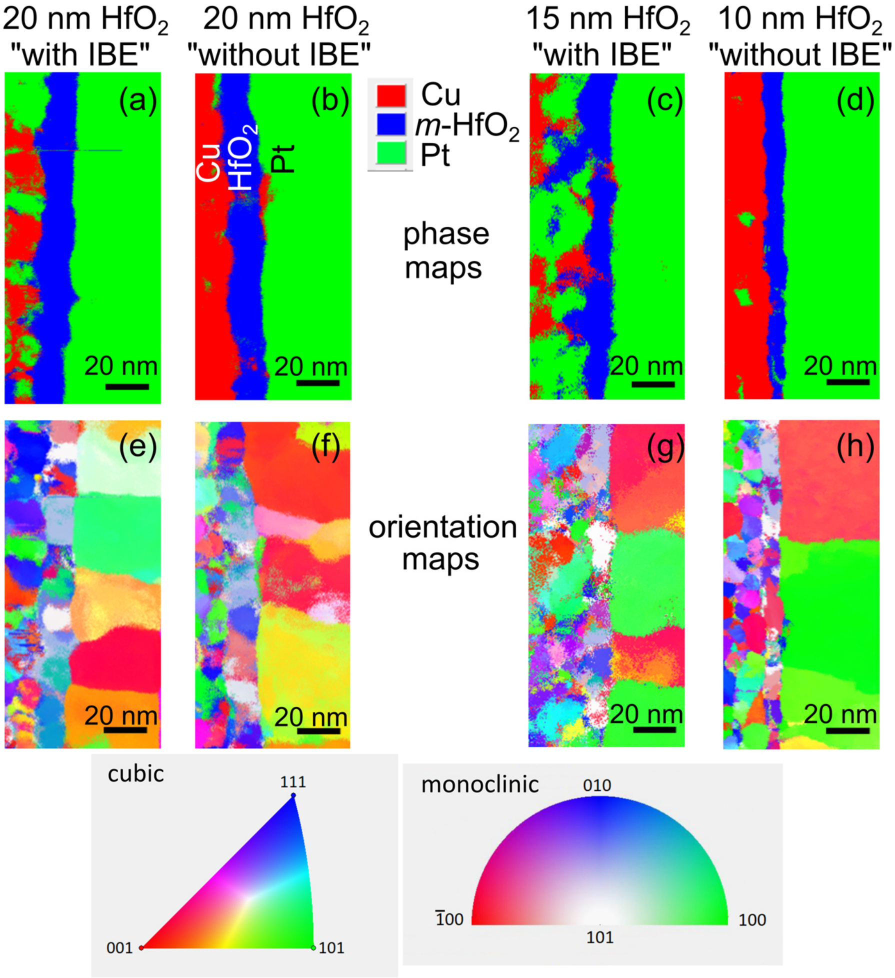

Figure 5-22: Phase and orientation maps obtained for Cu/HfO_2/Pt devices prepared “with IBE” and “without IBE”. Lamellae were cut from the middle of 30 µm × 30 µm devices. Phase maps of a Cu (red)/m-HfO_2 (blue)/Pt (green) (a) “with IBE” sample containing 20 nm HfO_2, (b) “without IBE” sample containing 20 nm HfO_2, (c) “with IBE” sample containing 15 nm HfO_2, (d) “without IBE” sample containing 10 nm HfO_2. (e)-(h) show the corresponding orientation maps. Color wheels for the monoclinic (for HfO_2) and cubic structure (for Pt and Cu) are given at the bottom of the figure. The knowledge about these phases originates from XRD investigations (see chapter 5.5, Figure 5-14).

From the phase and orientation maps, three important features are revealed:

- All HfO_2 layers are closed, continuous layers with a monoclinic structure as seen from the phase maps (blue layers).
- While for “without IBE” samples a clear distinction between the top electrode layers is possible in the phase maps, a potential phase mixture of the Pt (green) and Cu (blue) top electrode layers is obtained for “with IBE” samples in the phase maps (Figure 5-22 (a) – (d)). This is generally possible but considered unlikely and will be discussed in the following in more detail.
- From the orientation maps, different grain sizes are indicated for the Cu top electrode for “with IBE” versus “without IBE” samples. This could stem from the different growth methods used to prepare these Cu layers (MBE versus sputtering – compare chapter 4.1.3).

In this context, two explanations can be given for the observed differences of the leakage values for “with IBE” versus “without IBE” devices:

(1) The high leakage currents found in “with IBE” devices could be a consequence of a possible intermixture of the top electrodes, as seen in Figure 5-22 (a) and (c). Increased heat induced during IBE could have led to the movement of Cu ions through the thin HfO_2 layers, forming a conductive path. This narrow path might not be distinguishable from the HfO_2 layer in the presented phase maps, but a temperature-induced intermixing of Cu and Pt could be visible. However, a clear reason for such an intermixture during layer growth or during IBE cannot be given. A direct damage of the top surface of the HfO_2 switching layer, potentially creating oxygen vacancies, is not possible, as the device surface is protected by a photoresist layer during etching. This is supported by the presence of working 20 nm HfO_2-containing devices. Additionally, there are a few more things that argue against this first potential explanation:

    First, high temperatures are required for sufficient Cu ion movement that could have led to a visible intermixture with Pt or even a filament formation in the HfO_2 layer. Additionally, this increased temperature has to be present for a longer time than the maximum used etching time of 15 min.[350-352] This is not likely, as during the short IBE process cooling of the sample stage with liquid nitrogen was used to prevent undesired heating effects. Furthermore, increased heat is believed to lead to a further hardening of the photoresist (further cross-linking). As a consequence, the photoresist would only be hardly removable afterwards which was not the case. Thus, also a failure of the cooling during etching is very unlikely. Additionally, a very similar IBE process led to a successful preparation of working Pt/PZT/LNO (lanthanum nickelate) ferroelectric[331] and Pt/HfO_x/TiN VCM devices (not yet published). However, these stacks do not contain a Cu top electrode layer.

    Second, the visible intermixture of Cu and Pt in the orientation maps of “with IBE” samples could be a result of misindexing during pattern matching. The same matching routine was used for all stacks, established from the “without IBE” SPED dataset. However, the Cu top electrodes of “with IBE” and “without IBE” samples were grown using two different deposition techniques (MBE versus sputtering – compare chapter 4.3), which results in at least slightly different layers. A potentially larger misindexing than expected could be present for “with IBE” results, which is especially supported by the quite chaotic image shown in Figure 5-22 (c), where a kind of disarranged HfO_2 layer can be seen.

(2) The high leakage currents found in “with IBE” devices could also be a consequence of a variety of other detrimental damages induced by IBE, like the creation of potential leakage paths at the side parts of devices. In general, IBE can lead to different damages. A schematic representation of some potential effects at the surface of the HfO_2 layer of the prepared devices is given in Figure 5-23.

    In this work, IBE was carried out using a 150 W Ar plasma. The etching process for the preparation of Cu/HfO_2/Pt devices was stopped at the HfO_2 surface controlled by endpoint detection (compare chapter 4.3). The stopping was done by closing the shutter in front of the substrate as soon as no Cu signal is present in the spectra detected by a mass spectrometer. However, at this point also the HfO_2 layer is partially etched away. This becomes more severe for higher roughnesses of the layers, where the endpoint detection is more challenging.

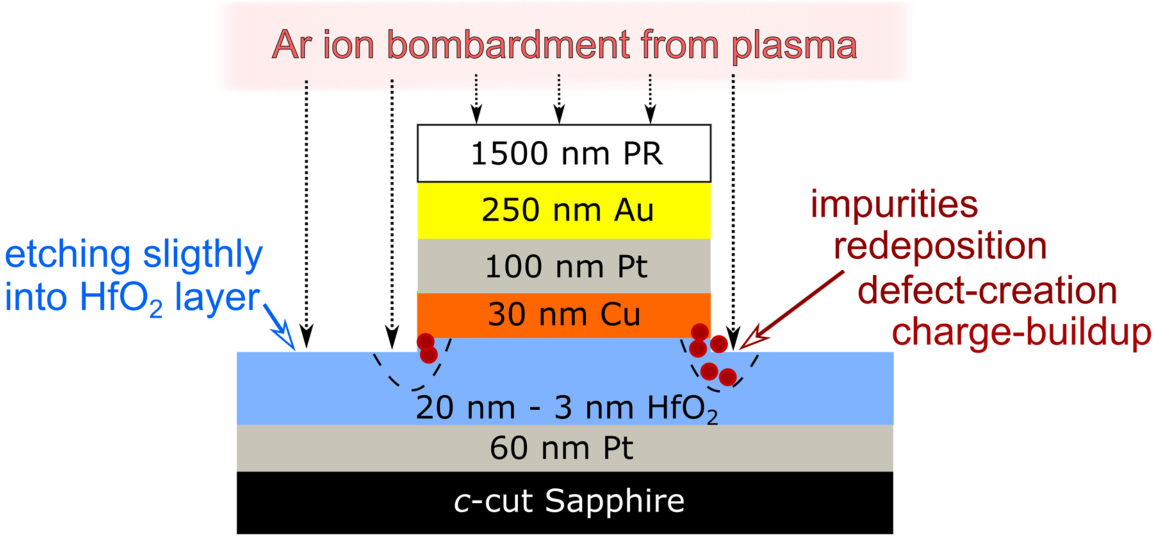

Figure 5-23: Schematic representation of an IBE process to create devices from a stack (photoresist/Au/Pt/Cu/HfO_2/Pt/substrate) right before the end. Effects (represented by red dots) like a deposition and movement of impurity atoms and ions, redeposition of material, defect-creation or charge-buildup can occur, likely at the edges and in a small volume of the HfO_2 layer (dashed line). Figure/layer thicknesses are not drawn to scale.

At the edges of the devices, where the HfO_2 layer is in contact with the Cu top electrode layer, several detrimental effects induced by IBE can occur.[297] A few examples are listed in the following:

- Impurities can be deposited on top of any layer and metal atoms/ions can penetrate and move inside the layers. This can lead to conductive paths in the oxide layer or to a modification of the conduction mechanism of the devices due to dopants. In principle, impurities can stem from etching of the sample holder, stage, shutter or the chamber wall.
- Additionally, a redeposition of etched material like Hf is possible, which would result in similar effects. Further, the occurrence of preferential sputtering[334] of HfO_2 can lead to the creation of a conductive path at the edges (oxygen removed preferentially), consisting of a Hf-rich volume.
- A charge-buildup can occur at the interface between conducting and insulating materials as a result of ion exposure. This can lead to increased leakage currents or even result in a dielectric breakdown.

Although the IBE process is similar for all samples (20 – 3 nm HfO_2 thickness), the induced damage is likely to more heavily impact thinner stacks. This is supported by the presence of switchable devices found in “with IBE” 20 nm thick HfO_2-layer containing devices, while devices of thinner stacks (15 nm HfO_2 thickness and below) were found to be stuck in the LRS. The thickness of 20 nm for the HfO_2 layers could be close to or at the layer thickness limit for still working devices.

If stacks are etched down to the bottom electrode surface, the potential damaged edge surface area increases. Then, effectively the full dielectric/oxide layer thickness is potentially affected, which is believed to increase the possibility to render devices non-functional. This could have been the case for some of the TiN/HZO/TiN stacks (compare chapter 5.2, next to the potential TiO_xN_y interlayer formation). In general, the induced damage is likely to be increased by higher etching powers. A reduction of the etching power could therefore be beneficial.

In summary, the high leakage found in etched devices ("with IBE") could be related to induced effects such as heat (and a potential intermixture of the top electrode layers) or complex damage effects, like impurity deposition or charge-buildup at the edges of devices or interfaces. Further studies can give further insights in the driving forces leading to these leakage currents. Energy-dispersive X-ray spectroscopy (EDX) studies performed on the (S)TEM lamellae could reveal a potential intermixture. Of particular interest would be an investigation by EDX with high resolution of the edge region of devices to possibly detect signals from impurities. Additionally, more information could be collected from repetitions of the IBE process with new stacks and changed etching parameters (e.g., lower power). Another etching step at low power after the main etching procedure could be included to clean the edges of the prepared devices from possibly conductive material. The obtained results are a solid basis for the creation of a functioning device preparation workflow using dry etching, which is required for the successful reproducible production of (*in vacuo*-capped) oxygen-deficient HfO_{x}-based devices.

5.7 Summary and Outlook – Mixed $Hf_xZr_{1-x}O_2$ films and resistive switching of hafnium oxide-based memory devices

In the first part of this work, different influences on the properties of hafnium oxide-based films and devices for potential ferroelectric or resistive switching applications were investigated.

First, a co-deposition process of Hf and Zr using two separate electron guns and *in situ* oxidation utilizing an oxygen plasma was successfully established. Mixed $Hf_xZr_{1-x}O_2$ thin films of desired compositions were achieved in a controllable manner, which was validated by XPS results. XRD investigations revealed the polycrystalline nature of these films grown on *c*-cut Sapphire substrates. In a second step, the growth of $Hf_{0.5}Zr_{0.5}O_2$ (HZO) films with the probably most-interesting composition for ferroelectric applications was transferred to highly-oriented TiN bottom electrodes and another TiN layer was grown as a top electrode, which resulted in the creation of TiN/HZO/TiN stacks. These stacks were post-deposition annealed to potentially achieve a ferroelectric orthorhombic phase of the HZO-films. Unfortunately, all devices were found to be leaky in voltage-dependent electric polarization measurements. Additionally, proper resistive switching was found to be inhibited. This is most likely a consequence of a combination of different influencing factors, like top electrode and oxide layer growth, post-deposition annealing steps and the used ion beam etching procedure. The growth of stoichiometric TiN top electrodes as well as HZO films at potentially higher growth temperatures seems mandatory, potentially using recently published literature values[200] and additional chamber wall cooling. The conducted studies provide important insights into the growth of HZO films and TiN/HZO/TiN stacks in the MBE system and point out preparation aspects that need to be included in new systematic growth series as well as annealing and ion beam etching studies for the achievement of ferroelectric devices.

In a third part, the resistive switching properties of monoclinic and amorphous HfO_2- and HZO-containing stacks with Pt electrodes were investigated. Devices of all four different stacks were switchable with the expected trend towards higher forming voltages in devices containing amorphous layers compared to crystalline (monoclinic) layers. This study further revealed no significant influence of the Zr-doping (mixing) on the switching properties of the TCM devices, which were subject to a large (expected) set voltage variance. The most important result of this study is that the growth of *a*-HZO at RT results in a good layer quality and switchable devices. Therefore, the leakage problems obtained in previous potentially ferroelectric TiN/HZO/TiN devices and the inhibited resistive switching are most likely not directly caused during the growth of the HZO films.

In a forth study, the switching behavior of Pt/HfO_2/Pt and Cu/HfO_2/Pt devices was investigated. Dependent on the top electrode material Pt or Cu, different switching mechanisms (TCM versus ECM) were found for URS (negative operation voltages) in Pt/HfO_2/Pt and BRS (positive forming/set and negative reset voltages) in Cu/HfO_2/Pt devices as the most-stable switching modes. Additionally, the potential appearance of threshold resistive switching (TRS) was investigated by varying the current compliance during forming/set. However, TRS was not observed in Pt/HfO_2/Pt and Cu/HfO_2/Pt devices, which could be related to occurring current overshoots during forming/set.

A fifth study was focusing on the resistive switching behavior in Cu/HfO_2/Pt devices with different oxide layer thickness. A qualitative model for the observed transition from a gradual reset to an abrupt reset occurring with increasing oxide layer thickness was developed, with a strongly Joule heating-assisted resistive switching in ECM devices containing thicker oxides and an electric field-dominated process in devices containing thinner oxides. Additionally, a change of the conduction mechanism(s) in the set process was found, again dependent on the oxide layer thickness. Thicker films have ohmic conduction, while thinner films show SCLC conduction by injected electrons at increasing field.

In a sixth part, it was found that different leakage currents observed in devices are dependent on the preparation workflow ("with IBE" versus "without IBE"). By utilizing SPED, a potential intermixture of the Cu and Pt top electrode layers was found in etched samples, which could have a crucial impact on the electrical properties of the device stacks. Moreover, more complex damage effects could occur during etching with high power, like impurity deposition or charge-buildup at the edges of devices. The occurring detrimental effects should be further investigated and have to be prevented in the future to achieve a well-reproducible preparation workflow for devices structured by ion beam etching.

6 Heavy ion irradiation of HfO_x- and Ge-Sb-Te-based materials and emerging memories

Different types of ionizing radiation are ubiquitous in our daily environment from natural sources or artificial sources. This includes nuclear power plant, aviation/aerospace and medical environments. In the frame of the project WAKeMeUP, this work provides a comparative study on the radiation resilience of emerging non-volatile memory technologies towards ionizing radiation and their suitability for potential applications in harsh-radiation environments. The heavy ion irradiation experiments were performed at the X0-beamline at the UNILAC accelerator of the GSI Helmholtzzentrum fuer Schwerionenforschung in Darmstadt (Germany). Phase-Change Memory (PCM/PCRAM), Oxide-based Random-Access Memory (OxRAM) and ferroelectric capacitors were exposed to high-energy (1.635 GeV) Au ions using a constant flux of 5×10^8 ions/cm²s, and varying the fluences from 1×10^9 up to 1×10^{13} ions/cm² to investigate potential changes on the electrical device performance. Heavy ion radiation is characterized by a high energy and a high ionization potential. As for the investigated emerging memories, the information storage is not directly charge-based, an increased resilience towards ionizing radiation was expected when compared to charge-based memories.

Next to the evaluation of the suitability for harsh environmental applications of the emerging non-volatile memory technologies, a second purpose of the heavy ion irradiation study was to investigate possible mechanisms of data loss due to heavy ion irradiation and induced changes. The properties of hafnium oxide-based resistive and ferroelectric memories as well as Ge-Sb-T-based phase change memories strongly depends on the crystal structure/crystallinity, microstructure and composition of the active material. Potentially induced phase transitions and defects in general can have a direct influence on the functionality of the emerging memories. So far, reports on these phenomena are scarce. Therefore, full-sheet layer samples were exposed to heavy ions for investigations of the effect on the structural properties of the hafnium oxide- and Ge-Sb-Te-based materials used as oxide-based resistive and ferroelectric as well as phase-change layers.

In this chapter, structural (XRD), microstructural (STEM) and electrical investigations are combined and the results compared to obtain a better understanding of general mechanisms in emerging memory technologies exposed to heavy ions. In a first study, irradiation-induced phase transitions in highly-textured (section 6.1.1) and less textured/polycrystalline, stoichiometric and oxygen-deficient HfO_x full-sheet layers (sections 6.1.2 and 6.1.3) are presented. These structural results are combined with electrical results obtained from HfO_2-based OxRAM (section 6.2). Similar studies connecting structural and electrical investigations are presented for Si- and Zr-doped HfO_x ferroelectric layers and capacitors (section 6.2.2) as well as Ge-Sb-Te-based phase-change materials and memory arrays (section 6.4). Finally, the results are summarized (section 6.5).

6.1 Phase transitions in HfO_x films exposed to Au swift heavy ions

In this chapter, phase transitions induced by Au heavy ions in HfO_x films are presented. First, the phase transition of textured, (stoichiometric) monoclinic films to (substoichiometric) oxygen-deficient rhombohedral films grown on *c*-cut Sapphire substrates is discussed and compared to as grown (oxygen-engineered) oxygen-deficient films. Additionally, results obtained for irradiated textured, oxygen-deficient rhombohedral films are shown. Those experiments were designed to obtain a better understanding of the phase transition mechanism in HfO_2 films exposed to heavy ions.

Second, phase transitions obtained for films of less textured/polycrystalline nature grown on Si substrates (wafers) with and without a TiN bottom electrode are discussed. Investigations of the micro- and nanostructure give more insights into the nature of the phase transition, also with respect to applications. The structural results are directly connected to electrical results of irradiated OxRAM and to structural and electrical results obtained for non-irradiated (as grown) hafnium oxide films and single devices (capacitor stacks).

6.1.1 Crystalline-to-crystalline phase transition in textured, stoichiometric HfO_2 and oxygen-deficient HfO_x films exposed to heavy ions

To obtain a better understanding of the reported ion-beam induced phase transition in hafnium oxide[11, 238-240, 249, 250] and to investigate if the reported results on hafnium oxide powders also apply to thin films, stoichiometric hafnium oxide films were irradiated with Au ions of 1.635 GeV energy with fluences ranging from 1×10^9 to 7×10^{12} ions/cm^2. As the dependency on the oxygen content is of great interest, an additional series of oxygen-engineered (intentionally grown oxygen-deficient) hafnium oxide films were irradiated. The textured film growth on c-cut Sapphire substrates facilitates the analysis of structural changes by XRD (characterized by a low number of orientations/reflections). As shown schematically in Figure 6-1, three sample series (A, B, C) were investigated.

Series A contains textured, stoichiometric monoclinic HfO_2 films (m-HfO_2). Those samples have been exposed to Au ions of different fluence to investigate the effect of the heavy ions on the crystalline structure.

Series B contains oxygen-engineered HfO_x films. This series contains samples ranging from stoichiometric HfO_2 to substoichiometric $HfO_{1.1}$. The highly-textured films were grown under controlled, continuously decreasing oxidation conditions (compare chapter 4.1.3). The good controllability of the growth parameters opens the possibility to achieve a set of films within a broad range of oxygen content (engineering the oxygen content). The substoichiometric films are named “oxygen-deficient HfO_x” in the following. These oxygen-engineered samples were not irradiated but used as a comparison series for the irradiated films. In combination with *in vacuo* XPS investigations, the oxygen-deficiency can be directly verified. Due to the similarity of the XRD patterns of oxygen-deficient hafnium oxide films with hafnium oxide powders (and the polymorph zirconium oxide), it was believed that oxygen-deficient HfO_x films are also of tetragonal nature.[138] However, it was recently published[128, 145], that the oxygen-deficient phase of hafnium oxide is a (oxygen vacancy) defect-stabilized rhombohedral phase, which was first described as a slightly distorted low temperature cubic phase (called a pseudocubic phase; compare chapters 2.1.5 and 4.5.1). The determination of the crystal structure of thin hafnium oxide films is in general challenging due to the low crystalline volume and the similarity of the crystal structures like the cubic, tetragonal and several orthorhombic phases of hafnium oxide, differing only by relatively small structural distortions. Those phases are hardly distinguishable by XRD as discussed in chapter 4.5.1. Texture, strain and a low interaction volume in XRD leads to various changes in the XRD pattern, like a shift of the reflection positions, additional reflection broadening or the absence of reflections in patterns obtained for highly-textured films. In the original publication[293] connected to the presented data in this chapter, the substoichiometric phase of hafnium oxide was labeled to be a tetragonal phase. In this work and the following discussion, the suboxide will be labeled as r-HfO_x, according to the current state of research.[128]

Series C contains highly-textured, oxygen-deficient, rhombohedral HfOx films. These films were irradiated at different ion fluences from 1×10^9 to 7×10^{12} ions/cm² and structural changes were investigated using XRD.

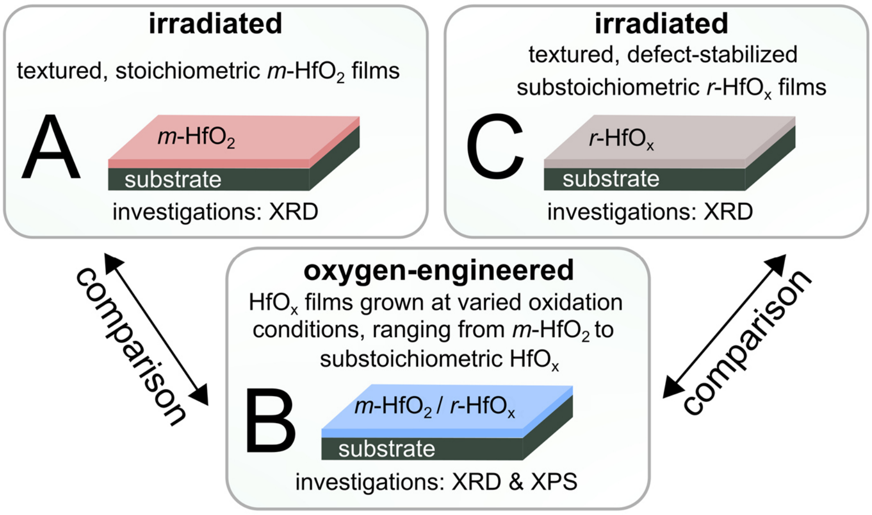

Figure 6-1: Schematic overview of sample series A (irradiated stoichiometric, monoclinic hafnium oxide), series B (non-irradiated oxygen-engineered hafnium oxide) and series C irradiated (oxygen-deficient hafnium oxide) mainly containing monoclinic and rhombohedral hafnium oxide films grown on *c*-cut Sapphire substrates. Series A, B and C were characterized using XRD, while for series B containing oxygen-engineered films, XPS investigations were performed. Partially reproduced from[293] with permission. The original publication is licensed under a Creative Commons Attribution 4.0 License (CCBY) and published by IEEE. In the original publication, the rhombohedral phase was labeled as a tetragonal phase.

The results obtained after irradiation for series A and series C can be directly compared to as grown, oxygen-engineered films of series B, as presented in the following. In Figure 6-2, the XRD patterns of all three series are shown. The irradiation-induced structural changes of m-HfO_2 films irradiated at high fluences of 3×10^{12} up to 7×10^{12} ions/cm² are visible in Figure 6-2 (a). Reflections of the as grown film (black curve) can be assigned to the $(\bar{1}11)$, (111), (200) and (020) planes of the monoclinic phase (space group: $P2_1/c$) at diffractions angles of $2\theta \approx 28.4°$, 31.7°, 34.4° and 34.8°, respectively. A beam-induced crystalline-to-crystalline phase transition from the monoclinic to a phase of higher symmetry is observed with increasing fluence, where the intensities of the monoclinic reflections decrease, while those of the reflections visible at $2\theta \approx 30.3° - 30.5°$ and $2\theta \approx 35.3° - 35.5°$ increase. Those can be assigned to reflections of different phases (compare chapter 4.5.1), corresponding e.g., to the (101) and (002) planes of the tetragonal phase ($P4_2/nmc$) or the (111) and (200) planes of the rhombohedral phase ($R3m$) of HfO_x[128], respectively. A detailed discussion on these phases is given later in this chapter.

Analogous to the increasing irradiation fluence for series A, a similar trend is visible with decreasing oxygen content ($HfO_2 - HfO_{1.1}$) for oxygen-engineered HfO_x films of series B (Figure 6-2 (b)). For the highest oxidation conditions, the monoclinic phase of stoichiometric HfO_2 is present (grey curve), while the monoclinic reflection is gradually reduced in intensity with an appearance of a rhombohedral phase for decreasing oxidation conditions, as shown in literature[128, 145]. The corresponding (111) reflection shifts towards larger diffraction angles with decreasing oxygen content of the layers. For the least oxidized $HfO_{1.1}$ film, a transition to a hexagonal closed packed hafnium oxide phase (*hcp*-HfO_x) is visible.

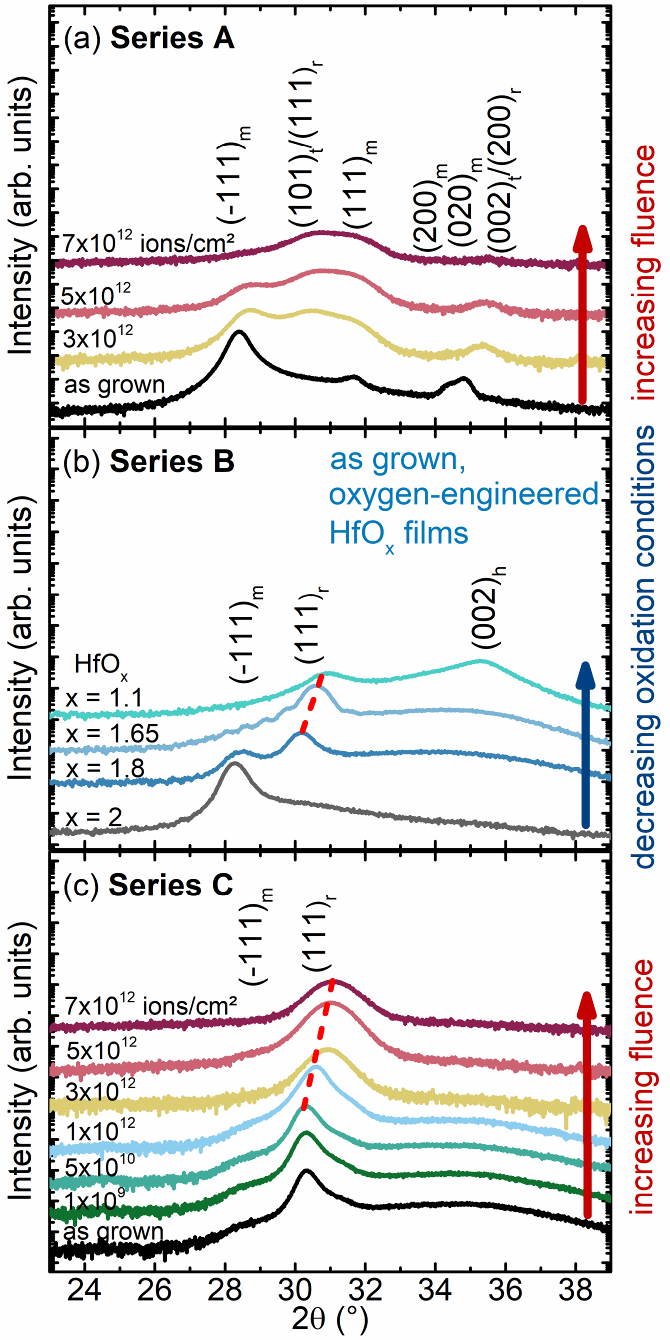

Figure 6-2: (a) XRD patterns of textured *m*-HfO_2 films revealing a phase transition from the monoclinic (m) to most likely the rhombohedral (r) phase of hafnium oxide with increasing fluence. As a comparison, the reflections corresponding to the tetragonal (t) phase of HfO_x are given, as for irradiated HfO_2 powder samples, a phase transition from the monoclinic to the tetragonal phase was reported.[11] (b) XRD patterns of as grown, oxygen-engineered HfO_x films of four different compositions, showing a similar phase transition with decreasing oxidation conditions and a shift of the rhombohedral (111) reflection towards larger diffraction angles. $(002)_h$ marks the diffraction angle of the hexagonal (002) reflection of hexagonal HfO_x close to metallic Hf (ICDD 00-038-1478). (c) XRD patterns of irradiated *r*-HfO_x films, showing a shift of the (111) reflection. Dotted red lines are guides to the eye. Partially reproduced from[293] with permission. The original publication is licensed under a Creative Commons Attribution 4.0 License (CCBY) and published by IEEE. In the original publication, the rhombohedral phase was labeled as tetragonal.

Changes in the XRD patterns can also be seen in irradiated, directly grown defect-stabilized *r*-HfO_x films of series C (Figure 6-2 (c)). The reflection at $2\theta \approx 30.3°$ corresponds to the (111) reflection of rhombohedral HfO_x[**128**]**.** At fluences below 1×10^{12} ions/cm^2, the rhombohedral phase seems to be stable, with no visible changes in the XRD patterns. At a fluence of 1×10^{12} ions/cm^2 and above, the $(111)_r$ reflection gradually shifts towards larger diffraction angles ($2\theta \approx 30.3°$, 30.55°, 30.9°, 31.0°, 31.1°). Additionally, a broadening of the reflections visible after irradiation can be a result of an increased number of defects in the crystal lattice.

Based on these obtained changes, the following points will be discussed in further detail:

- Due to the similarity of the XRD patterns obtained from series A and series B, the two sample series can be compared. Including the XPS results obtained from series B, a description of the irradiation-induced phase transition in HfO_2 films from the monoclinic to the most likely rhombohedral phase can be given. → see (1)
- The monoclinic to rhombohedral phase transition found in films is directly comparable to the irradiation-induced transition from the monoclinic to tetragonal phase reported for powder hafnium oxide.[11] Additionally, a rough quantitative description of the phase transition can be given. → see (2)
- The XRD results obtained from as oxygen-deficient rhombohedral HfO_x films of series C, which were exposed to heavy ions can be directly compared to results obtained from oxygen-engineered films of series B. → see (3)

(1) As recently reported[128, 145] and discussed above, the substoichiometric phase in hafnium oxide is found to be a rhombohedral phase. Due to the similarity of the XRD patterns of series A and series B (Figure 6-2), the beam-induced phase transition observed for thin films exposed to heavy ions can be assigned to a crystalline-to-crystalline phase transition from the monoclinic to the rhombohedral phase of hafnium oxide.
Further, the direct growth of oxygen-engineered HfO_x films in combination with *in vacuo* XPS investigations allows the estimation of the oxygen content of the films of series B. The obtained values can be directly related to irradiated films of series A (and C), even though such XPS measurements could not be performed on irradiated HfO_x samples due to a significant surface oxidation oxygen-deficient layers of several nanometers after getting in contact with air.[132, 145] To prevent this for series B, a vacuum transfer unit was utilized to maintain ultra-high vacuum conditions avoiding surface oxidation during sample transfer.

The Hf 4f and O 1s spectra of the four samples of series B with differing oxygen content have been plotted in Figure 6-3 (a). More details on the ratios of the peak areas used for the calculation of the oxygen content are given in (b). Pictures of the vacuum suitcase and transfer chamber used for the transfer from the MBE to the XPS vacuum chamber are shown in (c). After subtraction of a Shirley-type background, peak fitting with a Gaussian-Lorentzian function (GL(30)) for all Hf^{4+} and Hf^{X+} ($x < 4$) states and with a Doniac-Sunjic (DS(0.16)) function were performed. The area ratio for the Hf $4f_{7/2}$ to Hf $4f_{5/2}$-peak is 4:3. Position constraints (energy difference) for the Hf^{X+} peak splitting of 1.71 eV and for Hf^0 of 1.67 eV were used based on literature reports.[138, 311, 312]

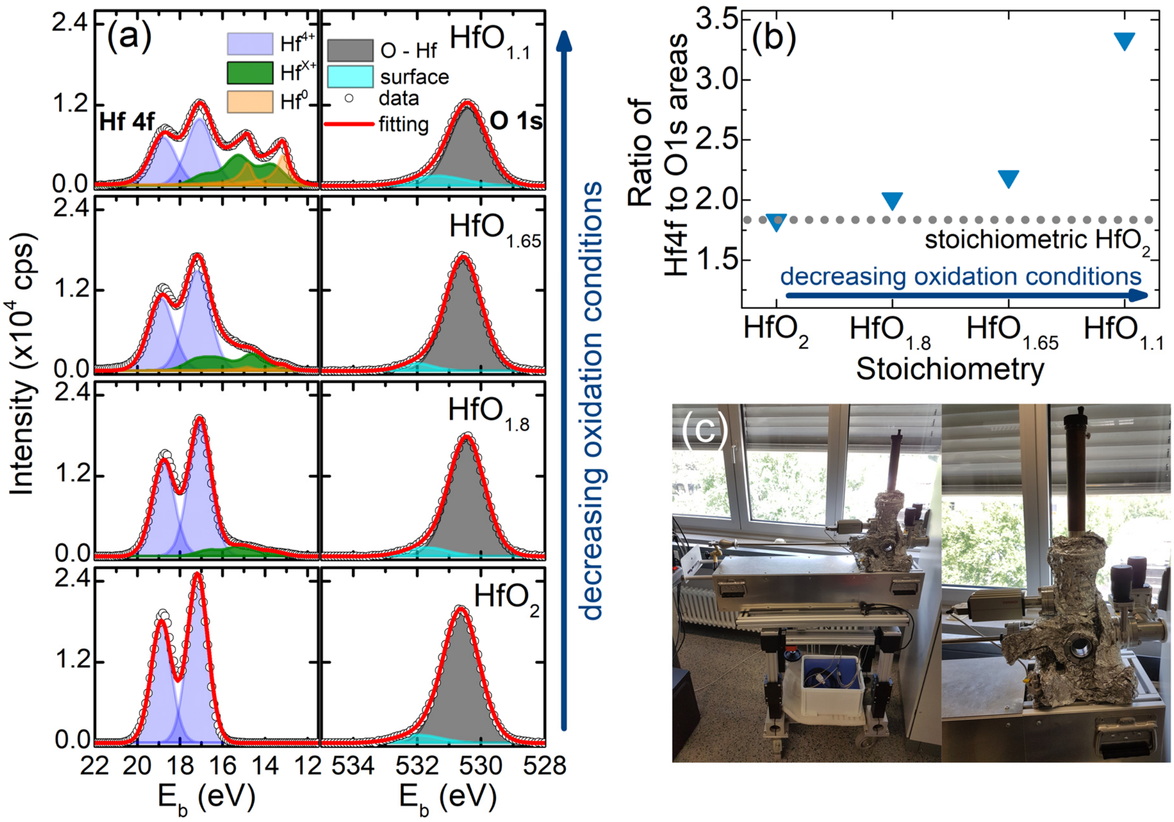

Figure 6-3: (a) XPS spectra with fits of the Hf $4f_{7/2}$ and Hf $4f_{5/2}$ (left) and O 1s (right) lines of the oxygen-engineered films of series B. The purple area corresponds to the Hf^{4+} state, orange to metallic Hf^{0} and green is the convolution of Hf^{X+} sub-oxide states. The O 1s fits include contributions from oxygen bound to Hf (grey) and to surface adsorbates (turquoise). (b) Decreasing oxidation conditions during the growth of the oxygen-engineered films result in an increased ratio of the Hf 4f to O 1s area, compared to the initial ratio for stoichiometric HfO_2 (dotted grey line), and obtained varying composition of HfO_x films (HfO_2, $HfO_{1.8}$, $HfO_{1.65}$, $HfO_{1.1}$). (c) Vacuum transfer unit with turbo pump and vacuum chamber as used for the *in vacuo* transfer from MBE to XPS system. (a) and (b) reproduced from[293] with permission. The original publication is licensed under a Creative Commons Attribution 4.0 License (CCBY) and published by IEEE.

In all films, the Hf^{4+} state of the Hf 4f signal is the predominant in the spectra. For the stoichiometric HfO_2 sample only Hf^{4+} states (purple) are observed, while the areas of possible Hf^{X+} sub-oxide states (convolution given in green) and Hf^{0} metal states (orange) increase with decreasing oxidation conditions. The Hf^{X+} suboxide states could be fitted by using one or two doublets for all films. From the area ratio (Figure 6-3 (b)) and the atomic sensitivity factors for Hf and O (2.639 and 0.711, respectively[312]) using equation (9) – chapter 4.5.3, the approximate film compositions were calculated to be **HfO_2** (fully oxidized reference sample), **$HfO_{1.8}$**, **$HfO_{1.65}$** and **$HfO_{1.1}$**, respectively. The XPS results therefore reveal a gradual decrease of the oxygen in the HfO_x layers with decreasing oxidation conditions during film growth. In combination with the XRD results (Figure 6-2), a stabilization of the rhombohedral phase by oxygen defects (most likely oxygen vacancies) is likely, which is according to latest literature reports.[128, 145]

In the context of the described analysis, the following points should be mentioned: a) The values were obtained using the O 1s peak of oxygen bound to hafnium (grey), excluding the surface contribution part of the O 1s peak (adsorbates/hydroxide - light blue). b) Due to the usage of an insulating Sapphire substrate and the absence of a reference C 1s signal, the spectrum of the most oxidized (HfO_2) sample was aligned to the energy of the valence band maximum of the O 2p band prior to the analysis (compare chapter 4.5.3). For all other samples, the positions were matching well already. c) For XPS analysis, in general an error of about 10 % is considered. Absolute values may slightly vary. However, the obtained results are reasonable and in accordance to expectations with a clear trend obtained for a sample series of four samples.

Comparing the results of series B (XRD and XPS) with those of series A (XRD), the following conclusions can be made:

- Due to the similarity of the XRD patterns of irradiated hafnium oxide of series A and oxygen-engineered films of Series B, a similar phase transition from the monoclinic to rhombohedral phase of hafnium oxide can be assumed.
- This transition is likely to be a result of induced oxygen vacancies. For series A, these are beam-induced defects, while for series B, the oxygen vacancies are introduced during the growth of oxygen-deficient films directly. From the similarity of the XRD patterns of series A and B, also an approximate composition of the film exposed to 7×10^{12} ions/cm^2 can be assumed (as an example). The $(111)_r$ reflection is located at $2\theta \approx 30.6^\circ$ in the XRD patterns of the oxygen-engineered $HfO_{1.65}$ film (series B, compare Figure 6-2), which matches well with the diffraction angle obtained for the reflection of the sample exposed to 7×10^{12} ions/cm^2 (series A). Therefore, a similar composition of $HfO_{1.65}$ can be assumed after irradiation.

(2) The phase transition observed in films of series A (as shown in Figure 6-2 (a)) can be compared to literature results obtained from irradiated HfO_2 powder (bulk) samples**[11, 238-240]**, where a strikingly similar trend in the XRD patterns is found (similar reflections visible). However, a monoclinic to tetragonal phase transition is reported for powders. As discussed above, the phase transition in films is believed to be also a crystalline-to-crystalline phase transition but from the monoclinic to the rhombohedral phase of HfO_x. This assumption is based on the latest results obtained for as grown oxygen-engineered films.**[128]**

For HfO_2 powder samples, A. Benyagoub[11] has described the irradiation-induced phase transition mechanism from the monoclinic to the tetragonal phase based (also) on the creation of oxygen defects. Defects are expected in the films after a first ion impact, while a subsequent second impact of the defective volume leads to the transformation of the phase. This is a double-hit process, corresponding to defective track overlaps (compare chapter 3.2). Such double impacts are likely to be dominant for fluences around 10^{12} ions/cm^2 and above. This is matching the presented results for HfO_2 films. Further, for the conducted experiments with heavy ions with an energy in the GeV range, the interaction of the ions with matter is also dominated by ionization and electronic excitation processes (electronic energy loss). For 1.635 GeV Au ions, the electronic energy loss in *m*-HfO_2 films with a density of 9.68 g/cm^3 is about 52.8 keV/nm, according to TRIM-2010 code[235] calculations. This value is by far exceeding the reported threshold of about 18 keV/nm for the phase transition in hafnium oxide powders[11], pointing out that a beam-induced phase transition is expected.

For a quantitative analysis of the phase transition, a statistical approach (based on Poisson statistics - compare chapter 3.2) can be used as done for powder hafnium oxide.[11, 240] For thin films, a similar approach is chosen, where the overall integral intensities of the monoclinic and rhombohedral reflections (or tetragonal in the original publication[293]) were used to determine their respective phase fraction as a function of the ion fluence (using equation (5), chapter 3.2). In Figure 6-4, the rhombohedral phase fraction in dependence of the fluence is shown with additional values calculated from literature reports[11, 240] for the tetragonal phase for comparison. With increasing fluence, a larger amount of rhombohedral phase is found (about 51 % at 3×10^{12} ions/cm², 71 % at 5×10^{12} ions/cm² and 80 % at the highest chosen fluence of 7×10^{12} ions/cm²). At the same time, the amount of monoclinic phase is reduced. The plotted phase fraction data points of the rhombohedral phase can be fitted using a sigmoidal function as described by Gibbons[248], following equation (6) – see chapter 3.2. It is assumed that (i) the spatial distribution of the ion impacts is stochastic and characterized by Poisson statistics and (ii) the phase transition occurs only in track overlapping zones. For the given fit (red curve), $n = 2$ represents the double impact scenario, while $\Delta C(\infty)$ (the maximum concentration increase at saturation) is 80 %. A damage cross section σ of about $7.4(\pm0.25)\times10^{-13}$ cm² (or $74(\pm2.5)$ nm²) is deduced.

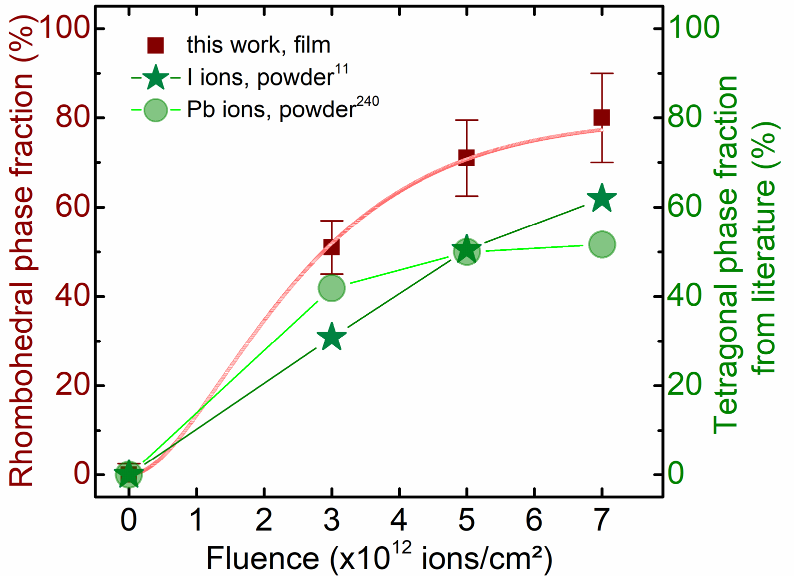

Figure 6-4: Representation of the increasing rhombohedral (red) phase fraction in hafnium oxide films (this work) with sigmoidal fit and comparison to literature values obtained from powder samples (green) showing an increasing tetragonal phase fraction after irradiation. These were calculated from data reported in literature[11, 240] of experiments with 250 MeV I and 2.31 GeV Pb ions. Linear connections between stars are a guide to the eye. Partially reproduced from[293] with permission. The original publication is licensed under a Creative Commons Attribution 4.0 License (CCBY) and published by IEEE.

To get an idea how meaningful these results are, a comparison to literature results is reasonable. Therefore, tetragonal phase fraction values were calculated using the given parameters by A. Benyagoub[11, 240] and B. Schuster[11, 240] for the sigmoidal function. The results are plotted in Figure 6-4 in green in direct comparison to the data presented in this work (red). Overall, the obtained values are in good accordance with the values estimated from literature reports, considering the high electronic energy loss of the presented irradiations with Au ions. Damage cross-sections are found to be in the lower nm²-region. However, the obtained rhombohedral phase fractions in irradiated hafnium oxide thin films are slightly larger than the values calculated from literature (51 – 61 % at about 7×10^{-12} ions/cm², with $\sigma \approx 4.8\times10^{-13} - 1.01\times10^{-12}$ cm²) for the tetragonal phase fraction. It needs to be noted that the comparisons for volume fractions in this work are determined for thin films to give a rough approximation, whereas the referenced studies use power diffraction data.

(3) Irradiated defect-stabilized *r*-HfO_x films of series C are showing similar features, like shift or broadening of reflections in the XRD patterns (as shown in Figure 6-2 (c)) as described for series A and series B. The as grown rhombohedral phase is stable with no visible changes of position or intensity in the XRD patterns below a fluence of 1×10^{12} ions/cm^2 ($2\theta \approx 30.3°$). At higher fluences of 1×10^{12} to 7×10^{12} ions/cm^2, the diffraction angle 2θ of the $(111)_r$ reflection shifts towards larger values ($2\theta \approx 30.55°$, 30.93°, 31.0°, 31.1°; see red dotted line in Figure 6-2 serving as a guide to the eye for the gradual shift). This shift represents a decrease of the out-of-plane lattice constant of the rhombohedral phase and is visualized in Figure 6-5 (red; as a relative shift to the $(111)_r$ 2θ angle of irradiated films) together with the oxygen-engineered results for comparison (blue; $2\theta \approx 30.17\,°$ ($HfO_{1.8}$), 30.6 ° ($HfO_{1.65}$) and 30.9 ° ($HfO_{1.1}$)).

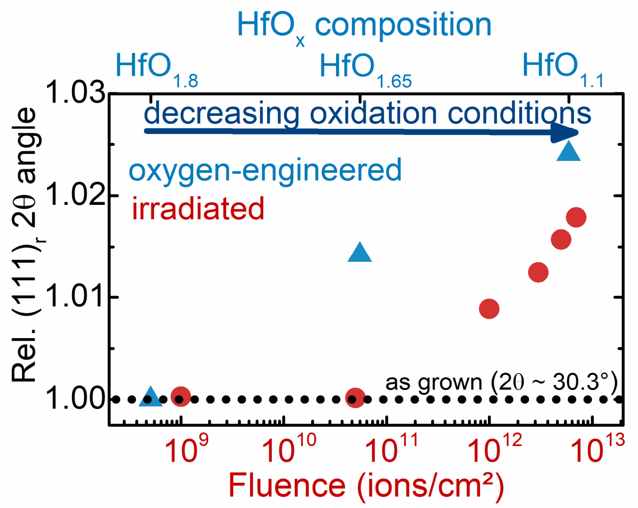

Figure 6-5: Relative (Rel.) 2θ diffraction angle of the rhombohedral (111) reflection as a function of fluence (red dots). With decreasing oxidation conditions in oxygen-engineered films and corresponding lower oxygen content, the rhombohedral reflection (blue triangles) shows a similar shift. The dotted black line marks the position of the as grown references. Figure partially reproduced from[293] with permission. The original publication is licensed under a Creative Commons Attribution 4.0 License (CCBY) and published by IEEE. In the original publication, the rhombohedral phase was labeled as tetragonal.

Combining again XRD and XPS results, the creation of oxygen vacancies is the predominant mechanism for structural changes caused by heavy ion irradiation also in *r*-HfO_x films of series C, which are transformed to even more oxygen-deficient films. Similar to series A, the fluence threshold where changes are observed (around 1×10^{12} ions/cm^2) seems to be linked to a track overlapping phenomenon. In the case of irradiated *r*-HfO_x films, the structural similarity between related phases (cubic, tetragonal, orthorhombic, rhombohedral) does not allow a distinction from the XRD patterns. Therefore, a clear description of a possible phase transition from the rhombohedral to any other phase is not possible at this point. A further transition towards a hexagonal phase might be possible, as seen from the results obtained from oxygen-engineered films of series B, which might not yet be visible in the XRD of films exposed up to 7×10^{12} ions/cm^2. Therefore, additional irradiation experiments at much higher fluences are expected to be necessary.

The results presented on irradiated textured stoichiometric and (substoichiometric) oxygen-deficient hafnium oxide films can be summarized as follows:

Textured, monoclinic hafnium oxide films exposed to Au ions likely undergo a defect-induced (oxygen vacancies) phase transition from the monoclinic to a rhombohedral phase. This transition is fluence-dependent, starting in the region where defective track overlapping occurs. A first ion impact leads to the creation of a defective volume, while a second impact leads to a transformation of the phase. For as grown, textured, defect-stabilized rhombohedral hafnium oxide films exposed to heavy ions, the XRD patterns reveal a decrease of the out-of-plane lattice constant with increasing irradiation fluence. The observed changes can be directly correlated to an induced further decrease of oxygen content in the HfO_x films. These conclusions are based on a comparison to XRD and XPS results obtained from non-irradiated, oxygen-engineered HfO_x films, revealing a strikingly similar phase transition occurring with decreasing oxygen content.

6.1.2 Irradiation-induced phase transition in polycrystalline stoichiometric HfO_2 films grown on SiO_x/Si and TiN/SiO_2/Si

To come closer to real applications, where the growth on Si wafers (also with an additional bottom electrode) is relevant, HfO_2 films were grown on SiO_x/Si and TiN/SiO_2/Si substrates and irradiated with Au heavy ions of similar conditions as presented in the previous chapter. A schematic representation of the stacks is shown in Figure 6-6 (a). The thickness of the stoichiometric monoclinic hafnium oxide films grown in the MBE system on SiO_x/Si was chosen to be 200 nm to provide sufficient probing volume for structural investigations. Those are referred to as 200 nm thick m-HfO_2 films. In contrast, 10 nm thin m-HfO_2 films were grown on industrial TiN bottom electrodes on SiO_2-covered Si wafers. Those stacks are close to stackings used for the preparation of real devices (but without a top electrode).

In Figure 6-6 (b), (c) and (d) the XRD patterns of samples before and after irradiation with different fluences are shown. As grown 200 nm thick m-HfO_2 films grown on (001)-oriented Si and the native SiO_x layer are polycrystalline (Figure 6-6 (b) and (c)), showing reflections of the monoclinic phase (space group $P2_1/c$). Similar to XRD data shown for films grown on c-cut Sapphire (chapter 6.1.1), the $(\bar{1}11)_m$ reflection at $2\theta \approx 28.4°$ has the highest (integral) intensity. Heavy ion irradiation with 1.635 GeV Au ions again induces a crystalline-to-crystalline phase transition again to the rhombohedral phase of HfO_x, starting at fluences around 1×10^{12} ions/cm^2. With increasing fluence, a gradual progress is obtained, with the highest intensity of the $(111)_r$ reflection at $2\theta \approx 30.5°$ (at 8×10^{12} ions/cm^2). The reflection visible in the range of $2\theta \approx 32° – 34°$ corresponds to the forbidden Si (200) reflection of the Si substrate to due Umweganregung[353]. Intensity and shape are dependent on the Φ-position (planar horizontal rotation of the sample during XRD).

As discussed already in chapter 6.1.1, it is difficult to distinguish various similar phases of the polymorphic hafnium oxide in thin films by XRD 2θ-scans. However, due to the similarity to the results presented in the previous chapter for irradiated monoclinic HfO_2 and rhombohedral oxygen-engineered HfO_x films, it is reasonable to assign the crystalline phase occurring after irradiation in the polycrystalline films again to the defect-stabilized rhombohedral phase of hafnium oxide.

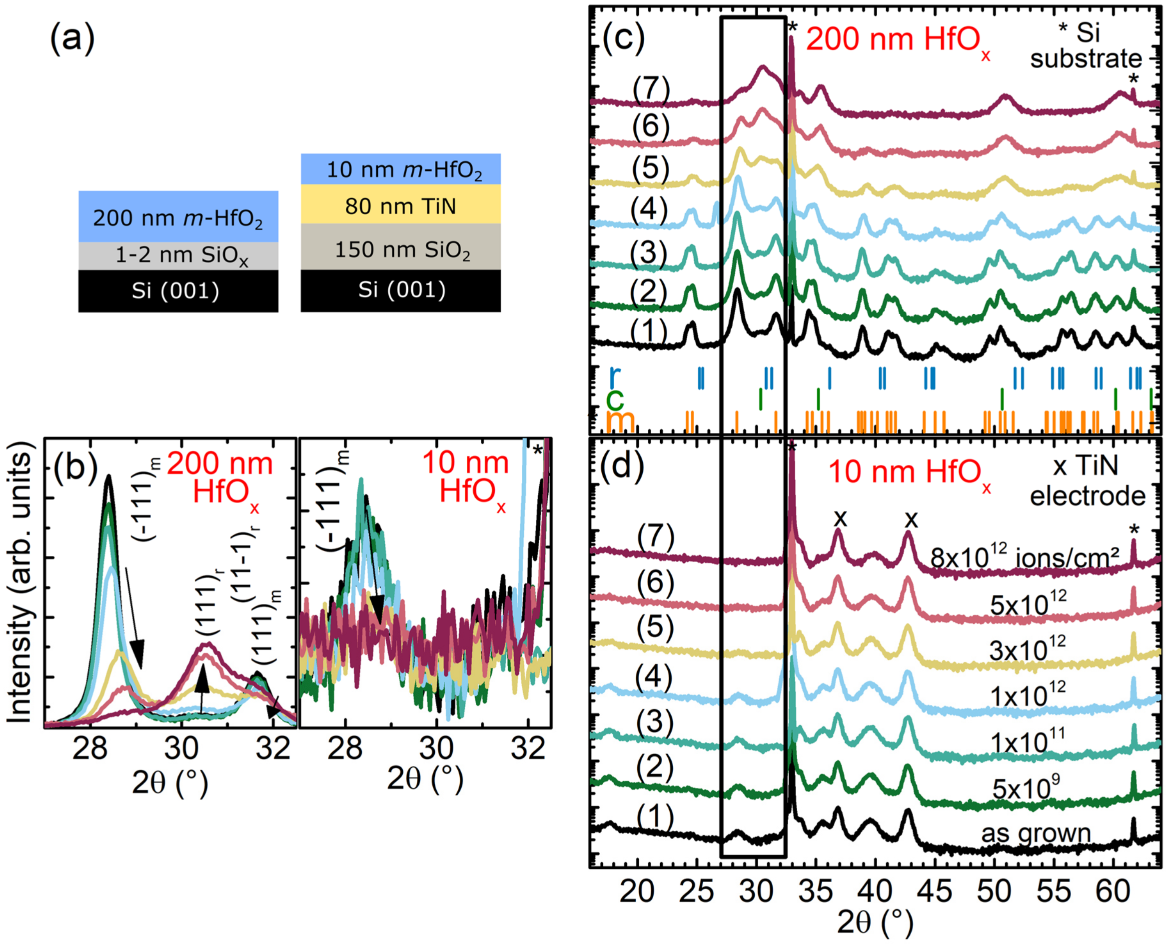

Figure 6-6: (a) Schematic representation of the two series of samples containing 200 nm thick *m*-HfO$_2$ and 10 nm thin *m*-HfO$_2$. (b) Detailed views of the XRD patterns in the region of the $(\bar{1}11)_m$ and $(111)_r$ reflections as marked in (c) & (d) with a black box. Similar changes as discussed in chapter 6.1.1 are visible. Reflections corresponding to the monoclinic and rhombohedral phase are marked with m and r, respectively. Trends occurring with increasing fluence are illustrated with black arrows. The potentially occurring $(11\bar{1})_r$ reflection position is also labeled. (c) XRD patterns of thick HfO$_2$ films before (1) and after irradiation ((2)-(7)) on SiO$_x$/Si substrates. A phase transition from the monoclinic (orange ticks)[123, 124] to a rhombohedral phase (blue ticks) [128] of hafnium oxide after irradiation is visible. Additionally, due to the similarity of the rhombohedral to the cubic crystal structure, the reference pattern of a cubic phase of hafnium oxide is given (green ticks)[126]. Note that the given rhombohedral reference is created based on theoretical DFT results for *r*-HfO$_{1.5}$.[128] In real films, diffraction angles in experimental patterns are closer to those seen in the cubic reference pattern. (d) XRD patterns of 10 nm thin HfO$_2$ films on TiN/SiO$_2$/Si. A decrease in intensity is visible with no directly observable crystalline-to-crystalline phase transition. Si substrate reflections are marked with a *. TiN electrode reflections are marked with an x. Figures (a) and (b) are partially reproduced with permission from[354], https://doi.org/10.1021/acsnano.2c04841. The original publication is licensed under a Creative Commons Attribution 4.0 License (CCBY) and published by American Chemical Society. The rhombohedral (111) reflection was initially labeled as cubic (111). A simulated reference pattern of the rhombohedral structure was added.

Additionally, a slight increase of the reflection located at $2\theta \approx 31.5^\circ$ for the highest fluence of 8×10^{12} ions/cm^2 could indicate the presence of a rhombohedral $(11\bar{1})$ reflection. However, a clear statement is challenging and in the theoretical pattern, the rhombohedral (111) and $(11\bar{1})$ reflections are found at $2\theta \approx 30.8^\circ$ and 31.3° and the intensities are reversed ($I(11\bar{1})_r > I(111)_r$, compare Figure 4-8). From reported experimental data[128] (similar reported lattice parameters as theoretical data), a lower difference of the diffraction angles of the rhombohedral (111) and $(11\bar{1})$ reflections ($2\theta \approx 30.6^\circ$ and 30.8°) was revealed, which could be a result of a different oxygen content of the layers and thus a differing unit cell. The difference observed in films could also be a matter of texture, as even polycrystalline films can show a preferential growth direction (presented later in this chapter as obtained from electron microscopy results).

The phase transition from the monoclinic to the rhombohedral phase is accompanied by reflection shifts in the XRD patterns for both phases with increasing fluence. This could be an indication for an increased number of induced defects (like oxygen vacancies) in the crystalline structure with changing unit cell parameters. In terms of absolute values, reflections corresponding to the rhombohedral phase are always located at 2θ angles between the diffraction angles of reflections of the reference cubic and rhombohedral powders. This points to slightly different unit cell constants and correspondingly to different unit cell sizes, which might indicate that the phases have different oxygen contents. The absolute diffraction angle of the $(111)_r$ reflection is more in accordance with the experimental results obtained from highly-textured r-$HfO_{1.7}$ than to the calculated rhombohedral reference pattern.[128] Additionally, a broadening of the reflections visible after irradiation (Figure 6-6) can be associated to a reduced average grain size (of the grains corresponding to each phase, respectively) on one hand, or on the other hand again to an increased number of defects in the crystal lattice and a larger variation of lattice parameters (potential coexistence of several HfO_x phases with different values of x).

As grown 10 nm thin m-HfO_2 films deposited on $TiN/SiO_2/Si$ by ALD are also polycrystalline, but with a lower number of reflections visible in the XRD patterns (Figure 6-6 (b) & (d)) and a much lower intensity due to the lower interaction volume when compared to 200 nm thick films. At a fluence of 1×10^{12} ions/cm^2, the intensity of the monoclinic $(\bar{1}11)$ reflection at $2\theta \approx 28.45°$ starts to be reduced until it is no longer visible. This study was conducted in close collaboration with CEA-Leti – Grenoble, where the ALD grown films have been prepared (see chapter 4.7). These layers are relevant for resistive switching studies as presented in chapter 6.2.1. For comparison, 10 nm HfO_2 films grown in the MBE setup on TiN/SiOx/Si (for growth parameters see chapter 4.1.3) were irradiated. The corresponding XRD patterns are given in Appendix Figure 8. Overall, both series containing 10 nm thin HfO_2 films are showing very similar changes of the crystalline structures visible in XRD, as the intensity of the monoclinic reflections decrease continously with higher fluences. In contrast to the observations made in thicker films, there is no evidence for a crystalline-to-crystalline phase transition in thinner films. This can be a result of different effects, like an overall reduced intensity and signal-to-noise ratio due to the lower crystalline quality, amorphization or a fragmentation of the crystalline grains. An overall reduced intensity and a poor signal-to-noise ratio due to the lower crystalline quality can be excluded. However, amorphization and grain fragmentation need to be still considered.

As the precise nature of the ion-induced changes on the nm-scale cannot be resolved by XRD, additional STEM investigations were performed, allowing a microstructural analysis based on a spatially resolved dataset. First, BF-STEM (Figure 6-7 (a)) and HAADF-STEM ((b)-(d)) analysis was performed on the as grown 200 nm thick $HfO_2/SiO_2/Si$ stacks with a Pt protection layer on top, revealing columnar HfO_2 grains with a length of several tens of nm to more than 100 nm (in vertical direction).

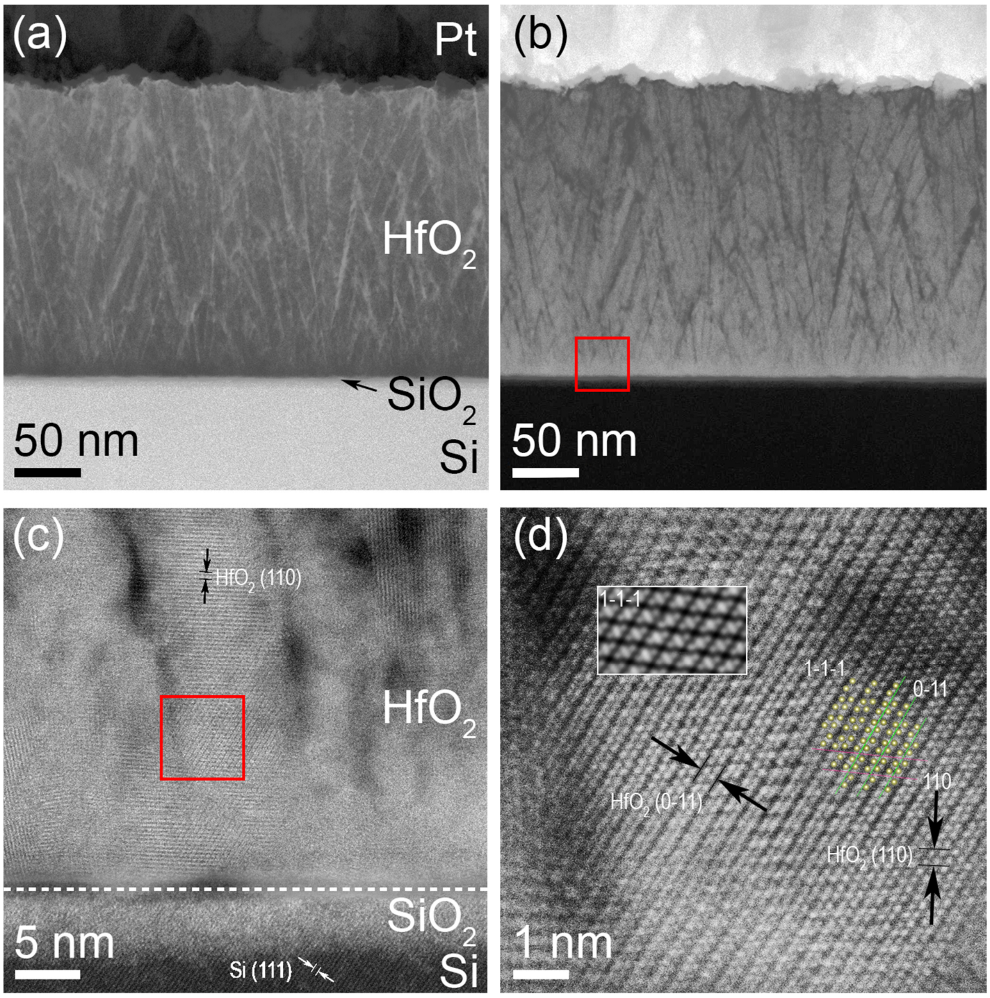

Figure 6-7: (a) BF-STEM image of the as grown $HfO_2/SiO_2/Si$ stack with a Pt protection layer on top. Columnar grains of the HfO_2 films are visible. (b) HAADF-STEM image of the same area. (c) High-resolution HAADF-STEM image of the area marked by a red square in (b), revealing the polycrystalline nature of the HfO_2 film, an amorphous SiO_2 layer and a single crystalline Si substrate. The dashed line indicates a change in displayed contrast. (d) High-resolution HAADF-STEM image of the area marked by a red square in (c), with lattice spacings.

From the red square in Figure 6-7 (b) right across the $HfO_2/SiO_2/Si$ interfaces, an atomic-resolution image was acquired as seen in (c). The HfO_2 film is found to be highly crystalline and of polycrystalline nature as seen from XRD analysis (compare Figure 6-6). Two lattice spacings for HfO_2 and Si are given exemplarily. The dashed line in Figure 6-7 (c) indicated a change in displayed contrast to allow for a visualization of the lattice planes in both HfO_2 and SiO_2/Si. This is necessary due to the difference in Z-contrast of these layers as ^{14}Si is light compared to ^{72}Hf. The SiO_2 is found to be amorphous while the Si substrate is a single crystal. A high magnification HAADF-STEM image of the area marked by a red square in Figure 6-7 (c) is given in (d), with different lattice distances marked for the visible HfO_2 grains. In the inset in (d), a multislice simulation of the given $(1\bar{1}\bar{1})$ viewing direction is given. It is important to mention that the lattice planes of $(\bar{1}11)$, $(11\bar{1})$, $(1\bar{1}\bar{1})$ and $(\bar{1}\bar{1}1)$ are identical in the monoclinic crystal structure (*hkl* ≡ *-hk-l* ≡ *-h-k-l* ≡ *h-kl*). A differentiation is only possible from high-resolution images acquired from two dimensions of the same area.

To obtain a better understanding of the phase transition on a microstructural level, further STEM investigations, including automated crystal orientation mapping (ACOM) were performed on samples containing 200 nm thick (Figure 6-8) and 10 nm thin (Figure 6-9 – ALD HfO_x) hafnium oxide films before and after irradiation. Template matching during ACOM allows the extraction of two types of information from the scanning precession electron diffraction (SPED) datasets: orientation and phase information.

Due to the gradual changes observed in the XRD patterns (compare Figure 6-6) and the high chance of detecting different crystalline phases after the phase transition at high fluences above 1×10^{12} ions/cm^2, irradiated samples which were exposed to 5×10^{12} ions/cm^2 were chosen and compared to as grown, non-irradiated samples. In the XRD patterns (Figure 6-6) these films are labeled with (6) and (1), respectively.

It is important to mention that for the pattern matching routine next to the monoclinic phase ($P2_1/c$), a cubic phase of hafnium oxide was used (space group $Fm\bar{3}m$, ICDD 04-011-9018), as the rhombohedral nature of substoichiometric hafnium oxide was not known at that time. Oxygen-deficient HfO_x was reported to be present in a defect-stabilized cubic structure.[145] The lattice parameters were believed to be very similar to the cubic phase used as an input for the pattern matching, probably with a slight distortion of the unit cell. Therefore, also in the original publication of the ACOM and XRD data, the oxygen-deficient phase of hafnium oxide was labeled to be a cubic phase (c-HfO_x).[354] This phase can be described as a pseudocubic phase due to the only slightly distorted nature when compared to a perfectly cubic symmetry ($\alpha \approx 89.56°$, compare Table 2-1, chapter 2.1.5). In this work and the following discussion, it will be named again r-HfO_x, according to the recently reported rhombohedral phase of hafnium oxide.[128] However, the input structure for the pattern matching is labeled as the used cubic phase.

In Figure 6-8, cross-sections of 200 nm thick HfO_2 films before (a) and after irradiation (b) are presented in HAADF contrast. Grain boundaries are visible as dark lines in (a), while a rather diffuse image with only a small number of dark lines is found in (b). In the ACOM orientation map of the as grown sample (c), the granular microstructure can be identified, showing the columnar HfO_2 grains in more detail. It becomes evident that the texture of the as grown m-HfO_2 films grown on SiO_2/Si is given in the columnar grain structure mainly, which is present after/above the first 20 nm of smaller HfO_2 grains. After irradiation (d), a significant grain fragmentation is visible (grains reduced to sizes below 10 – 30 nm). Orientations of the grains can be seen from the given color wheels for both the monoclinic and cubic crystal structure (input). Overall, the grain orientations are more randomized and an increased grain boundary density is present after irradiation when compared to as grown films. In the phase map of the as grown sample (e), approximately 91 % of the phase is assigned to the monoclinic phase, while 9 % is cubic. The crystalline-to-crystalline transition obtained from XRD is directly confirmed by the ACOM phase map results after irradiation (f) with 58 % monoclinic and 42 % cubic phase fractions.

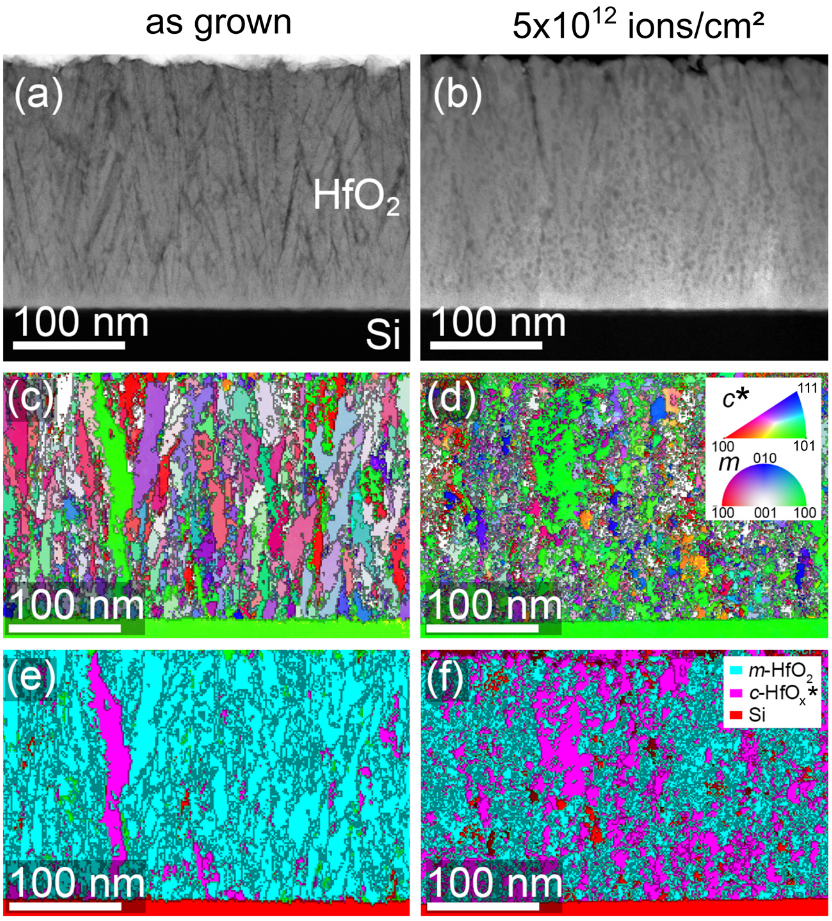

Figure 6-8: (a) HAADF-STEM image of the as grown 200 nm $HfO_2/SiO_2/Si$ stack with a Pt protection layer on top, revealing columnar grains of the HfO_2 films. (b) HAADF-STEM image of the $Pt/HfO_2/SiO_2/Si$ stack exposed to 5×10^{12} ions/cm². (c) ACOM orientation map of the as grown sample each color represents an orientation. A significant grain fragmentation after irradiation is revealed. Color wheels for the cubic and monoclinic structures are included. (d) ACOM orientation map of the sample exposed to 5×10^{12} ions/cm². (e) ACOM Phase map of as grown sample with a high fraction of *m*-HfO_2. Misorientation parts (>10°) and phase boundaries are given in grey. (f) ACOM phase map of the sample exposed to 5×10^{12} ions/cm², revealing a higher fraction of the cubic phase. *** Note that the pattern matching routine was performed using a cubic structure of hafnium oxide (space group: ICDD 04-011-9018, a ≈ 5.06 Å) as first reported in literature[145] for the oxygen-deficient phase occurring in HfO_x. Lattice parameters are close to the recently found rhombohedral phase.[128] Due to this similarity, the cubic and rhombohedral phases can hardly be distinguished in STEM/SPED (ACOM).** Figure reproduced with permission from[354], https://doi.org/10.1021/acsnano.2c04841. The original publication is licensed under a Creative Commons Attribution 4.0 License (CCBY) and published by American Chemical Society.

The ACOM phase maps were created using the ASTAR software package[317] from the SPED dataset acquired on the as grown (non-irradiated) sample. Visible colors mark the grains for which the given monoclinic and cubic HfO_x and cubic Si crystal structures are matched. A template matching routine was followed using template databases for both the monoclinic and cubic hafnium oxide phases, assigning probability values for each real space position (each pixel of the map). Simulated nanobeam electron diffraction (NBED) patterns were matched to experimental NBED patterns acquired at the nanocrystals of the samples. The same image processing and template matching parameters were used for the pattern matching of both ACOM maps.

In addition, the positionally averaged, azimuthally-integrated NBED patterns (position averaged NBED – PANBED) for the monoclinic and cubic phase were extracted by applying the ACOM map labels from (f) (see Appendix Figure 9). Those were used to confirm the validity of the recognized phases (monoclinic versus cubic) in the dataset. Therefore, XRD patterns of the as grown and irradiated (5×10^{12} ions/cm^2) sample and theoretical positions of reflections as well as Bragg intensities are given as bar plots together with the converted 2θ plots of the PANBED diffraction data. These results clearly reveal that a distinction of the two phases in question was possible by this method. Additional information on the workflow of integrating a 4D-STEM SPED dataset is provided in an open repository including the raw data of the presented study on 200 nm thick hafnium oxide films.[326] It should be mentioned that the analysis is limited in diffraction angle resolution by the used beam convergence in the SPED experiment of 5 mrad at 200 kV electrons equaling 17° Cu K_α radiation. Based on this, a distinction of the cubic and rhombohedral phase by means of SPED techniques is not possible, however, a pattern matching routine using structural model of the rhombohedral phase is believed to lead to similar results.

Using the obtained pattern matching routine that led to the presented phase and orientation maps (Figure 6-8), it was also possible to achieve a good phase recognition of the as grown oxygen-deficient films presented by Kaiser *et al.*[128, 145] (corresponding ACOM results are not yet published), well-separated from the monoclinic phase of hafnium oxide. Those films have a lower film thickness of 20 nm, which is increasing the difficulty to create a reasonable pattern matching routine due to the low probed volume and consequently lower number of grains (less data points). Therefore, it was easier to establish a pattern matching routine from the SPED dataset of 200 nm thick films and apply this routine to thinner films. The successful transfer further underlines the similarity of the cubic and rhombohedral phase, as the pattern matching routine created from a cubic phase well-matches films experimentally found to be of rhombohedral nature. Therefore, the usage of a cubic phase in the pattern matching procedure is reasonable.

In a similar fashion, the obtained pattern matching routine was applied also for the as grown and irradiated 10 nm thin HfO_x films. Corresponding HAADF-STEM images and orientation maps are shown in Figure 6-9. Initially (Figure 6-9 (a)), the grains in 10 nm thin HfO_2 films were vertically at least as large as the film thickness and horizontally larger than the image field of view. The microstructure of the thin films before irradiation resembles the initial 10 nm of the as grown 200 nm thick films (compare Figure 6-8) with an overall slightly lower texture. This could be a result of the growth by ALD, utilizing organic precursors and a much faster growth rate. Therefore, on one hand more defects and impurities are probably present in the films and on the other hand the different growth kinetics led to a lower texture, when compared to films grown in an MBE setup by electron evaporation of the metal plus oxidation via oxygen plasma.

After ion exposure, again an occurring grain fragmentation with a lateral size reduction is revealed by high-resolution STEM images and phase orientation maps, similar to the findings in 200 nm thick films (Figure 6-9 (b)). In vertical direction, the film thickness of 10 nm determines the (maximum) size of the grains. It is important to mention that for all films (shown in Figure 6-8 and Figure 6-9), the microstructural investigations reveal crystalline grains after irradiation and consequently a pure crystalline-to-crystalline phase transition. There are no traces of amorphization visible after irradiation.

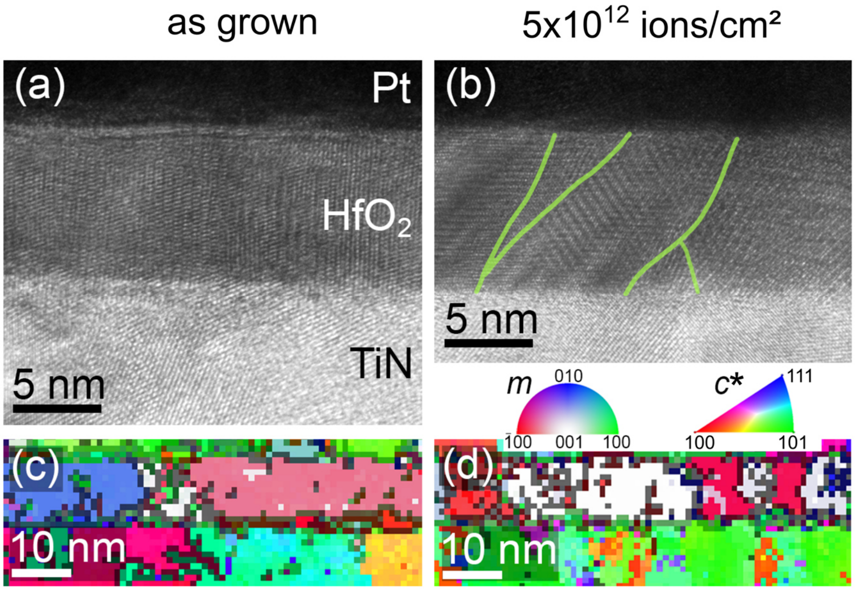

Figure 6-9: (a) HRTEM image of the as grown 10 nm HfO$_2$/TiN stack with a Pt protection layer on top. One single grain is visible in the given field of view. (b) Representative HRTEM image of the Pt/HfO$_2$/TiN stack exposed to 5×10^{12} ions/cm². Significantly smaller grains are identified. Grain boundaries in the HfO$_2$ layer are highlighted by the green lines. (c) ACOM orientation map of an as grown stack. Each color represents a different orientation as seen from the color wheel for the cubic and monoclinic structures. Grey indicates misorientation (>20°) and phase boundaries. (d) ACOM orientation map of a sample exposed to 5×10^{12} ions/cm². Note that the TiN and Pt layer are also included in the map. *** Note that the pattern matching routine was performed using a cubic structure of hafnium oxide (space group: ICDD 04-011-9018, a ≈ 5.06 Å) as first reported in literature[145] for the oxygen-deficient phase occurring in HfO$_x$. Lattice parameters are close to the recently found rhombohedral phase.[128]** Figure reproduced with permission from[354], https://doi.org/10.1021/acsnano.2c04841. The original publication is licensed under a Creative Commons Attribution 4.0 License (CCBY) and published by American Chemical Society.

Due to the low volume of the films and consequently a lower number of data points usable for pattern matching, the obtained phase information have lower statistical significance. However, it is reasonable to assume a similar phase transition as obtained from 200 nm thick films also occurring in 10 nm thin films. Therefore, the vanishing of the intensities of the monoclinic reflections in the XRD patterns of 10 nm thin HfO$_2$ films at high fluences (see Figure 6-6) is not a result of an overall reduced intensity and signal-to-noise ratio due to the lower crystalline quality and not a result of irradiation-induced amorphization, as all films are found to be crystalline. The vanishing intensities can solely be explained by a beam-induced grain fragmentation of the crystalline grains. A pure crystalline-to-crystalline phase transition is revealed, which is directly confirmed by the presented STEM (ACOM) results. This could have been otherwise falsely identified as amorphization.

The STEM investigations have been proven to be extremely valuable to get a detailed picture of the nature of the phase transition, as the interaction volume of coherent crystalline regions of one orientation has shown to be not sufficient to obtain resolvable intensities in the XRD patterns. The ACOM maps further confirm the elongated grains grown along the ($\bar{1}11$) direction for 200 nm thick films (and 10 nm thin films, where grains have the lateral size of the thickness of the layer) being present in the films before and after irradiation. This is in accordance with the observations made from the XRD patterns.

In literature, different transitions are reported, depending on the used irradiation parameters, HfO_2 material and initial crystal structure. Dhanunjaya *et al.*[249] reported a topological grain fragmentation in HfO_2 films exposed to 100 MeV Ag heavy ions with fluences of 3×10^{12} ions/cm² - 1×10^{14} ions/cm², revealed by field emission scanning electron microscopy. These results are in accordance with the presented results. In this work, the presented pattern matching results from SPED datasets additionally show a beam-induced grain fragmentation at nanometer resolution on cross-sections of HfO_x films.

(HR)TEM-based studies, like presented by Suvorova *et al.*[252] also focus on the structural evolution in hafnium oxide-based films. A possible transition from an orthorhombic to the tetragonal phase of HfO_2 was found after 160 MeV Xe ion exposure in La-doped HfO_2 films, obtained by a utilizing HRTEM and electron diffraction. No grain fragmentation or indications of amorphization were observed. The films were found to be of nanocrystalline nature. Ion energies were changed between 24 and 160 MeV and a constant fluence of 5×10^{11} ions/cm² was used. In comparison to the experimental results presented in this work, this fluence is below the expected threshold fluence in the 10^{12} ions/cm²-range (assuming similar energies and ions), where grain fragmentation was found. It is reasonable to assume that the observed beam-induced crystalline-to-crystalline phase transition based on a double impact (as discussed in chapter 6.1.1) is directly connected to the grain fragmentation observed in films, occurring only at high fluences (as presented in this chapter).

The results of this study can be summarized as follows:

- A beam-induced crystalline-to-crystalline phase transition from the monoclinic of hafnium oxide to the most-probably rhombohedral phase occurs in 200 nm thick and 10 nm thin HfO_2 films at high fluences, similar to the results presented in chapter 6.1.1.
- The vanishing of the intensities of the monoclinic reflections in the XRD patterns of the 10 nm thin HfO_2 films at high fluences (see Figure 6-6) are the result of a beam-induced grain fragmentation of the crystalline grains. A pure crystalline-to-crystalline phase transition is revealed, which is directly confirmed by the presented STEM (ACOM) results.
- Overall, it is clearly revealed that a full set of structural data consisting of both XRD results combined STEM-ACOM results for micro- and nanocrystalline analysis is beneficial for reliable interpretations of irradiation-induced changes.

6.1.3 Irradiation-induced phase transition in polycrystalline oxygen-deficient HfO_x films grown on SiO_x/Si and TiN/SiO_x/Si

Similar to the experiments already presented for stoichiometric 200 nm thick HfO_2 films, oxygen-deficient HfO_x films grown on SiO_2/Si substrates were irradiated. This is also directly comparable to results obtained from the irradiated highly-textured, oxygen-deficient series of samples grown on *c*-cut Sapphire substrates as presented in chapter 6.1.1. Schematic stacks of the samples and corresponding XRD patterns of the investigated series containing 200 nm thick HfO_x and HfO_y films are shown in Figure 6-10. Both non-irradiated films contain rhombohedral and monoclinic hafnium oxide phases. However, HfO_x films are less oxygen-deficient than HfO_y films, as they are grown using a lower oxygen flow (compare chapter 4.1.3).

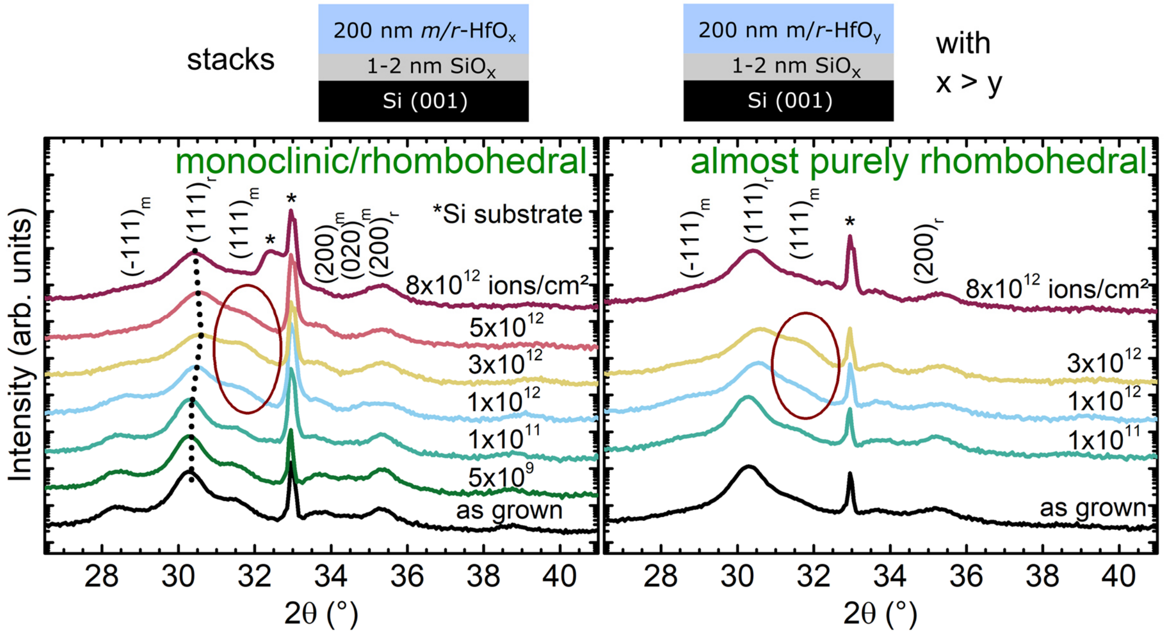

Figure 6-10: XRD patterns of 200 nm thick *m*/*r*-HfO$_x$ and m/*r*-HfO$_y$ films grown on SiO$_x$/Si substrates before and after irradiation with up to 8×10^{12} ions/cm². A shift of the rhombohedral (111) reflection is visible. Note that there were no experiments performed with 5×10^9 and 5×10^{12} ions/cm² for the HfO$_y$ sample series.

HfO$_x$ films consist of a mixture of monoclinic and rhombohedral phases, visible from the characteristic $(\bar{1}11)_m$ and $(111)_r$ reflections with the highest intensity at $2\theta \approx 28.3°$ and 30.3°, respectively. At fluences above 1×10^{12} ions/cm², the monoclinic $(\bar{1}11)$ reflection is shifted to $2\theta \approx 28.8°$ and its intensity decreases. The phase fraction is reduced, accompanied by the already described phase transition to the rhombohedral phase. In the XRD patterns of HfO$_y$ films in contrast, only a low intensity is found for the $(\bar{1}11)$ and (111) reflections of the monoclinic phase before irradiation. The presence of a phase mixture in as grown films could be related to the large film thickness, as the influence of strain from the substrate on the grown layer is reduced with increasing thickness, resulting in a relaxed structure. Additionally, a polycrystalline layer is likely to be grown on top of an amorphous interlayer (oxidized Si surface).

For both series, a shift towards larger diffraction angles of the $(111)_r$ reflection ($2\theta \approx 30.3°$ (as grown) – 30.6° (3×10^{12} ions/cm²)), comparable to the result obtained after irradiation of rhombohedral hafnium oxide films grown on *c*-cut Sapphire substrates (compare Figure 6-2 in chapter 6.1.1) is visible. Additionally, a broadening of the reflection occurs. Interestingly, the $(111)_r$ reflection shifts towards lower angles at higher fluences of 5×10^{12} ions/cm² ($2\theta \approx 30.4°$) and 8×10^{12} ions/cm² ($2\theta \approx 30.4°$). This could be a result of a relaxation of the out-of-plane lattice parameter of the rhombohedral phase occurring, if a large number of defects is introduced in the structure.

Furthermore, the occurrence of an increased intensity for the reflection at $2\theta \approx 31.7°$ is seen (red ellipses). This reflection can either be assigned to the $(111)_m$ reflection of as grown layers ($2\theta \approx 31.6°$) or to a potentially occurring $(11\bar{1})_r$ reflection. This is best seen for HfO$_x$ films exposed to 5×10^{12} ions/cm². At 8×10^{12} ions/cm², the intensity of this reflection is reduced. For the observed (200) reflections, it is difficult to determine a clear trend, mainly due to the low intensities and additional broadening. The transition to a monoclinic phase showing a $(111)_m$

reflection is unlikely due to the reverse transition occurring in irradiated monoclinic films (compare previous chapters) with decreasing oxygen content in the structure at higher fluences. The presence of a rhombohedral (11$\bar{1}$) reflection is more likely. The quite large film thickness and the growth on SiO$_x$/Si substrates seem to be favoring this kind of transition, possibly due to the polycrystalline nature (and behavior closer to bulk) of the 200 nm thick hafnium oxide films. This seems to be not or less significant in irradiated textured films grown on c-cut Sapphire substrates (chapter 6.1.1). However, more experiments are required to provide a more fundamental understanding.

As an additional series, 10 nm thin oxygen-deficient HfO$_x$ films grown in the MBE system on top of a TiN electrode were irradiated to discuss the structural changes based on XRD investigations. The corresponding XRD patterns of the fluence study can be seen in Figure 6-11 together with a schematic representation of the as grown stack. This study is directly comparable to the irradiation studies performed on 10 nm thin HfO$_2$ films (MBE – Appendix Figure 8 and ALD – Figure 6-6) as described in the previous chapter.

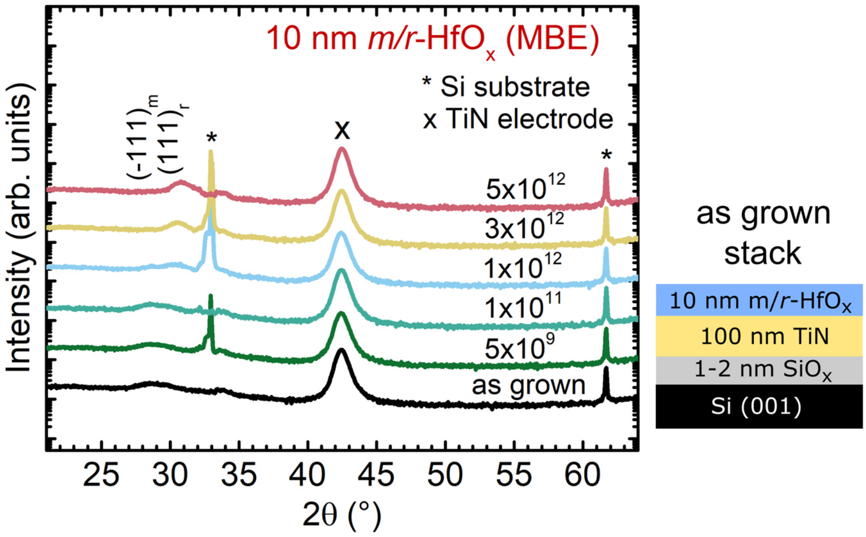

Figure 6-11: XRD patterns of as grown and irradiated 10 nm thin oxygen-deficient HfO$_x$ films grown on TiN/SiO$_x$/Si with a low overall intensity of the hafnium oxide reflections due to the low volume of the layer. The (111)$_r$ reflection shifts towards larger diffraction angles with increased fluence. Note that the highest fluence is 5×10^{12} ions/cm² and no sample was exposed to 8×10^{12} ions/cm². Substrate reflections are marked with a *, while x marks the cubic (200) reflection of the TiN bottom electrode.

Overall, reflections that can be assigned to the hafnium oxide layer are of low intensities due to the low thickness of the layers and the resulting low interaction volume in XRD. The small crystallite size and increased oxygen-deficiency further leads to a reflection broadening in the as grown film. For non-irradiated films, a low intensity reflection at $2\theta \approx 28.8°$ is visible, which could be assigned to the ($\bar{1}$11)$_m$ reflection (usually found around $2\theta = 28.3°$). However, the used growth conditions are similar to the ones used to prepare the oxygen-deficient films as shown in Figure 6-10 (b) and this deficiency is expected for this series as well. Due to the low interaction volume, potentially occurring low intensity features can hardly be observed. Two reflections ($2\theta \approx 28.8°$ and $2\theta \approx 30.3°$) could be identified in the pattern of the as grown film and the patterns of films exposed to 5×10^{9} and 1×10^{11} ions/cm². The reflection at $2\theta \approx 28.8°$ vanishes at increased fluences, while the one at $2\theta \approx 30.3°$ seems to increase in intensity. This could indicate a crystalline-to-crystalline phase transition as seen for the monoclinic to rhombohedral transition. Additionally, the presence of strain induced during growth of the quite thin layers can lead to a shift of the reflection (changed unit cell parameters). The observed reflection at $2\theta \approx 28.8°$ could therefore correspond to a $(\bar{1}11)_m$ reflection of (strained) monoclinic phase overlapping with a $(111)_r$ reflection of the defect-stabilized rhombohedral phase (mixture of monoclinic and rhombohedral phases). This becomes more evident when looking at the shape of the $(111)_r$ reflection at higher fluences, which are less broadened and of higher intensity. With increasing fluence, a shift towards larger diffraction angles is again observed, starting at a fluence around 1×10^{12} ions/cm².

The observed grain fragmentation in 10 nm thin monoclinic films exposed to 5×10^{12} ions/cm² as presented in chapter 6.1.2 and the accompanied vanishing intensities of the $(\bar{1}11)_m$ reflection in the XRD patterns at high fluences raise the question why there are reflections visible in XRD patterns of 10 nm thin oxygen-deficient rhombohedral films. Grain fragmentation might be hindered by the presence of sub 10 nm sized grains that might be growing with increasing radiation fluence instead. Additional investigations are required in the future to obtain a better understanding of the observed behavior for both 200 nm thick oxygen-deficient hafnium oxide films grown on SiO_x/Si as well as 10 nm thin oxygen-deficient hafnium oxide films grown on TiN/SiO_x/Si. This could include the irradiation of oxygen-deficient amorphous films, where a rhombohedral phase could be stabilized at high fluences, similar to the monoclinic phase stabilized after the irradiation of stoichiometric amorphous HfO_2 films, reported in literature[250].

6.2 Correlation of induced structural changes in HfO_2 with electrical properties of OxRAM

Irradiation experiments on full-sheet layers have revealed ion-induced changes such as a phase transition from the monoclinic to the rhombohedral phase of hafnium oxide by means of XRD and STEM investigations. For real applications, working devices have to be created, which require the presence of electrodes. Further the size of the devices is much lower when compared to full-sheet layer samples. However, irradiation-induced changes of e.g., the electrical performance of devices can occur. For the 10 nm thin *m*-HfO_2 films grown by ALD (compare XRD pattern in in chapter 6.1.2), 1T1R arrays based on access transistors and corresponding OxRAM cells are tested. Additionally, electrical measurements on irradiated single 1R memory cells with 10 nm *m*-HfO_2 films prepared in the MBE system are performed. The results can be correlated directly to the structural findings discussed in chapter 6.1.2 and also to the shown XRD results in Appendix Figure 8.

6.2.1 Resistive switching behavior of 1T1R arrays with HfO_2-based OxRAM cells exposed to heavy ion radiation

4kb 1T1R arrays (660 nm transistor gate width) were irradiated with 1.635 GeV Au ions of three different fluences (5×10^{9} ions/cm², 5×10^{10} ions/cm² and 1×10^{12} ions/cm²). NMOS transistors are used to access the TiN/Ti/HfO_2/TiN memory cells and limit the current during forming and set. The resistance values over 10^4 cycles for the 1T1R arrays exposed to 5×10^{9} ions/cm² and 5×10^{10} ions/cm² are given in Figure 6-12. The median as well as quartile 1 and 3 are given for the more than 3000 tested devices for 10^4 cycles. Scanning electron microscopic cross section images showing the OxRAM integration scheme and the memory stack can be found in the conference paper by Guillaume *et al.*[63]

After irradiation with a fluence of 1×10^9 ions/cm² (Figure 6-12 (a)), the 1T1R arrays are fully functional. Compared to the usual behavior of non-irradiated arrays (not shown) there are no irradiation-induced resistance changes detected. The LRS mean values are about 7.9 – 8.0 kΩ, while the HRS values vary from about 500 kΩ – 580 kΩ. The memory window (HRS to LRS resistance ratio) of about 70 is maintained for at least 10^4 cycles. These results can be given with a good statistical certainty[355], as more than 3000 devices were measured. A good performance is still preserved after irradiation with 5×10^{10} ions/cm² (b). Here, a slightly larger fluctuation of the HRS values (29400 V kΩ – 42000 kΩ) is visible, resulting in a memory window of 33 – 50.

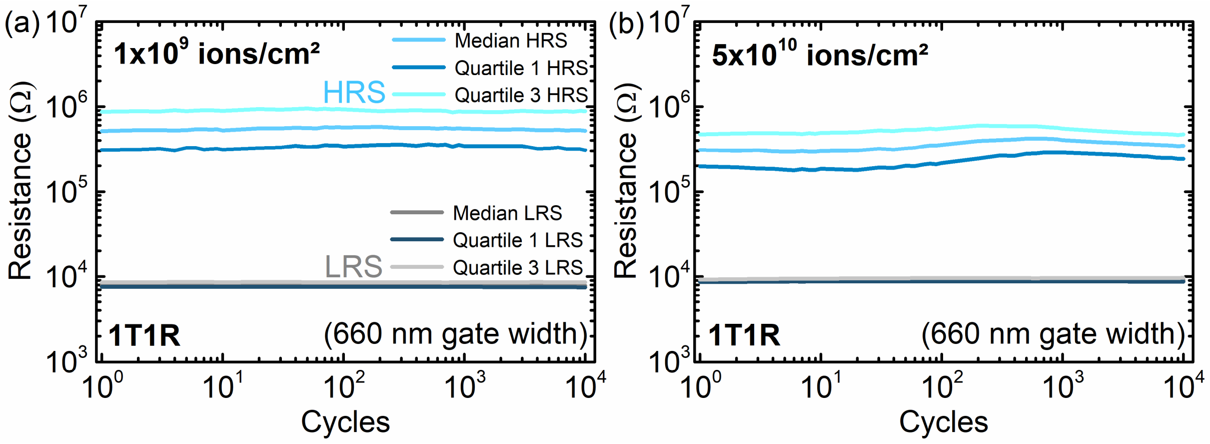

Figure 6-12: Resistance versus 10^4 cycles for a 1T1R array with HfO_2-based OxRAM devices. A clear memory gap is present between the LRS (grey) and HRS (blue) mean values (as well as quartile 1 and 3) for 3072 devices after irradiation at a fluence of (a) 1×10^9 ions/cm² and (b) 5×10^{10} ions/cm². Data presented at RADECS conference with similar figure printed in the conference proceedings[63]. Partially reproduced with permission from[354], https://doi.org/10.1021/acsnano.2c04841. The original publication is licensed under a Creative Commons Attribution 4.0 License (CCBY) and published by American Chemical Society.

At higher fluences, a significant impact on the access transistor functionality is observed (Figure 6-13), as seen from the drain current versus drain voltage curves of irradiated transistors (1T) with a gate width of 660 nm.

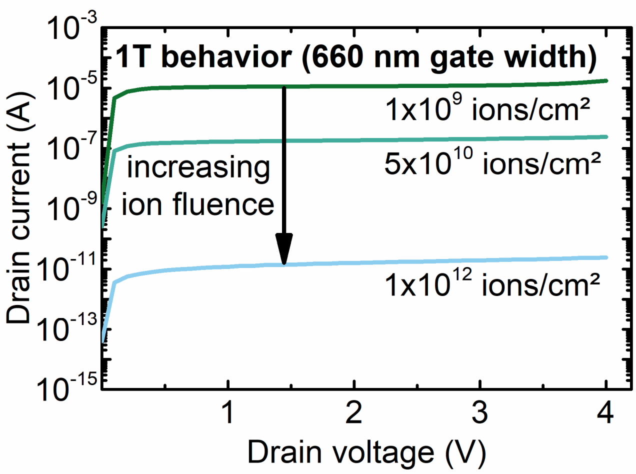

Figure 6-13: Drain current-drain voltage curves of single NMOS transistors with a gate width of 660 nm after irradiation (at a gate voltage of 1.3V). The curve obtained for 1×10^9 ions/cm² also represents a curve typically observed for a non-irradiated transistor (not shown). With increasing fluence, lower currents are measured overall. Data presented at RADECS conference with similar figure printed in the conference proceedings[63]. Partially reproduced with permission from[354], https://doi.org/10.1021/acsnano.2c04841. The original publication is licensed under a Creative Commons Attribution 4.0 License (CCBY) and published by American Chemical Society.

With increasing fluence, lower output currents can be achieved (1.7×10^{-5}, 2.4×10^{-7} and 2.4×10^{-11} A at a drain voltage of 4 V after exposure to 1×10^{9}, 5×10^{10} and 1×10^{12} ions/cm², respectively). This result is in accordance with literature results obtained on silicon oxide gate transitors[10], where a reduced conduction was attributed to a creation of interface defects between gate oxide and channel. Additionally, a shift of the threshold voltage can occur due to defects induced in the gate oxide (not shown; compare additional electrical results presented in literature[63]). These effects can explain the minor fluctuations of the resistance values after irradiation with 5×10^{11} ions/cm², as the access periphery might be partially damaged already.

The impact on the access transistors further leads to a loss of the automated access routine used to address the memory cells via the 660 nm gate width transistors for the arrays exposed to the highest tested fluence of 1×10^{12} ions/cm². However, single memory cells could still be accessed by connecting a larger gate width transistor (6700 nm) in series. With this, sufficiently high current could be provided to switch and cycle the cell even after ion exposure to 1×10^{12} ions/cm². Exemplary resistance versus 10^4 cycles are shown in Figure 6-14. For the first 10 cycles, the memory cell seems to be stuck in the LRS. However, a recovery probably due to a redistribution of oxygen vacancies by cycling of the cell is visible, accompanied by two distinct resistance states. For at least 10^4 cycles, a memory window of 5 – 20 is maintained. Additional electrical results regarding the transistor performance, the impact of the irradiation on the 1T1R arrays programmed in three different states (LRS, HRS, pristine state), the impact of Si implantation of the HfO_2 layer on the switching properties as well as the performance of 1R cells for up to 10^7 endurance cycles can be found elsewhere[63].

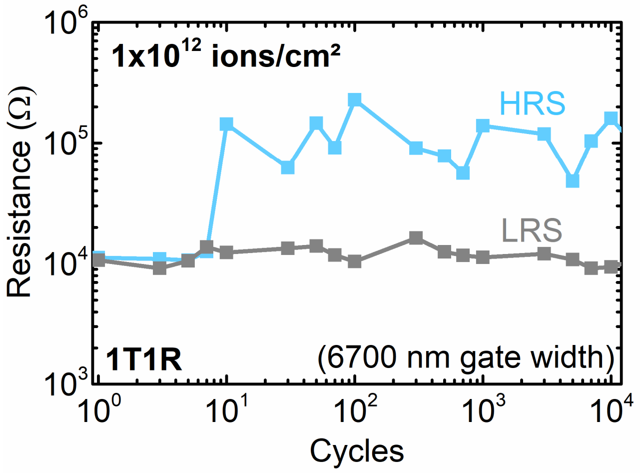

Figure 6-14: Resistance versus 10^4 cycles of a 1R HfO_2-based OxRAM cell irradiated at a fluence of 1×10^{12} ions/cm² and accessed by utilizing a 6700 nm gate width transistor. Data presented at RADECS 2020 conference. Data presented at RADECS conference with figure printed in the conference proceedings[63]. Partially reproduced with permission from[354], https://doi.org/10.1021/acsnano.2c04841. The original publication is licensed under a Creative Commons Attribution 4.0 License (CCBY) and published by American Chemical Society.

Compared to full-sheet layers, device sizes for electrical applications are much smaller. In chapter 6.1.2, the fluence-dependent impact on the crystal structure of 5×5 mm² full-sheet layers was discussed. Device sizes of the OxRAM cells in the 1T1R arrays are only about 160000 nm² (1.6×10^{-9} cm²) small. This results to a much lower number of ions impacting on each device (e.g., 1600 ions in average at a fluence of 1×10^{12} ions/cm²). Assuming a damage cross section of about 74 nm² of the ion tracks in HfO_2 as deduced in chapter 6.1.1 in irradiated hafnium oxide films, the areal track coverage can be calculated. Considering the occurrence of overlapping tacks, a coverage of about 52 % at a fluence of 1×10^{12} ions/cm^2 and 100 % at the highest fluence for full-sheet layers of 8×10^{12} ions/cm^2 can be assumed. A similar calculation with the cross-section value of 48 nm^2 given by Benyagoub for powder HfO_2 in literature[11] leads to calculated coverage values of 52 % (at 1×10^{12} ions/cm^2) and 98 % (at 8×10^{12} ions/cm^2). This clearly shows, that track overlapping cannot be ignored and effects like an increased number of irradiation-induced defects or a phase transition become more severe at higher fluences.

In this context, it is remarkable that the functionality of OxRAM devices that were exposed to 1×10^{12} ions/cm^2 is still preserved. The results show that the HfO_2-based resistive memory devices are very radiation hard. For even higher fluences, it is reasonable to assume that the induced defects and the increasing track overlap, which are resulting in a phase transition from the monoclinic to the rhombohedral phase in HfO_x, leads to a drastic change of the electrical properties. According to investigations on as grown samples including oxygen-deficient HfO_x films by Sharath *et al.*[132] and also from the physical property (electrical conductivity) results reported by Kaiser *et al.*[145], the memory device conductivity is expected to increase drastically with decreasing oxygen content. Assuming a similar behavior after 1.635 GeV Au heavy ion irradiation, where more oxygen defects are introduced in the HfO_2 layer and the phase transition observed in irradiated monoclinic HfO_2 films (see chapter 6.1.2) to the rhombohedral phase, the following conclusion can be drawn: Up to a fluence of 1×10^{12} ions/cm^2, the memory devices are overall functional but the CMOS transistors (access periphery) fail. At higher fluences, when a larger amount of rhombohedral phase is formed, the resistive memory cells are expected to get/remain fully conducting. This would correspond to a loss of the memory state (HRS) and a lost functionality of the devices.

6.2.2 Resistive switching behavior of an irradiated single 1R memory cell containing 10 nm *m*-HfO_2 films grown in the MBE system

1R memory cells (Au and Pt top electrode layers/10 nm HfO_2 layer/TiN bottom electrode grown on a Si substrate as seen from the schematic in Figure 6-15 (a)) were tested before (as grown reference) and after irradiation (5×10^{12} ions/cm^2).

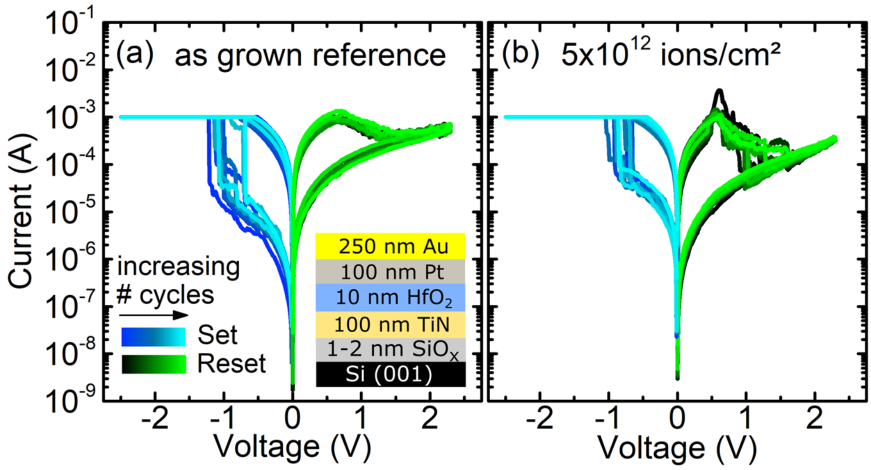

Figure 6-15: Current-voltage characteristics of a Pt/10 nm HfO_2/TiN device (a) before (as grown Reference) and (b) after being exposed to 5×10^{12} ions/cm². Resistive switching is achieved in both devices.

Two current-voltage curves are shown in Figure 6-15, revealing a similar behavior of both stacks (a) before and (b) after irradiation (10 cycles tested each). It is important to mention that the devices for the resistive switching experiments were prepared using the full-sheet layer $HfO_x/TiN/SiO_x/Si$ samples after the irradiation experiments and after the XRD investigations performed. Corresponding XRD results are shown in Appendix Figure 8.

First of all, both devices could be switched and there is no big difference visible in the current-voltage characteristics. After irradiation with 5×10^{12} ions/cm^2, the presence of an electrically conductive rhombohedral phase is expected to lead to a high conductivity[128, 145] of the hafnium oxide-based device and most likely to a non-recoverable loss of the memory (no HRS, no reset would be possible). Such an extremely detrimental characteristic is not observed in the given case. Devices were found to be in the HRS with an acceptably low initial leakage current measured. The presence of an electrically conductive rhombohedral phase of oxygen-deficient HfO_x phase is not seen. This phenomenon is most likely a result of a passivation layer (significant surface oxidation layer)[132, 145] that has formed on top of the of the oxygen-deficient HfO_x when the samples were exposed to air before device preparation (top electrode growth, more than one year after the irradiation experiment). This almost perfectly stoichiometric HfO_2 layer most probably acts as the active switching layer in devices after heavy ion exposure of 5×10^{12} ions/cm^2. Thus, a conductive layer with a modified electronic structure by introduced oxygen vacancies is not obtained.

However, there are some differences visible in the current-voltage characteristics. The set distribution obtained after irradiation seems to be narrower, with a possibly larger overall HRS current ($6\text{-}18\times10^{-6}$ A versus $1\text{-}3\times10^{-6}$ A; HRS in kΩ-range, LRS below 1 kΩ). This is accompanied by an overall lower memory window (max. 40 versus max. 120). Additionally, for the first few cycles after irradiation, an abrupt switching was obtained, which is not seen in the current-voltage curves of the as grown reference device. This could be related to a redistribution of oxygen vacancies. Overall, a further discussion of the switching data and a possible connection to the beam-induced phase transition (chapter 6.1.2 and Appendix Figure 8) is only reasonable with sufficient statistical evidence. Thus, further investigations on irradiated devices that were prepared with electrodes before the irradiation experiments are required. With this, also the performance of memory cells exposed to ions of high fluence can be tested, giving results independent of degraded CMOS transistors. Moreover, a comparison of resistive switching results of non-irradiated and irradiated *in vacuo* capped oxygen-deficient HfO_x-containing devices can be useful.

6.3 Heavy ion irradiation induced phase transitions in doped hafnium-oxide ferroelectric layers and electrical properties of ferroelectric capacitors

The influence of (1.635 GeV Au) heavy ion irradiation on the stability of the hafnium oxide-based ferroelectric layer and capacitor functionality was investigated, connecting irradiation-induced phase changes observed by XRD with ferroelectric properties of three different ferroelectric stacks (see Figure 6-16). These stacks contain a) a 20 nm thick Si-doped HfO_2 layer (HSO; in the following Figures marked in a reddish colour scheme), b) a 20 nm thick $Hf_{0.5}Zr_{0.5}O_2$ layer (HZO; yellowish/sand colour scheme) and c) a 10 nm thick $Hf_{0.5}Zr_{0.5}O_2$ layer (brownish colour scheme) sandwiched between TiN electrodes, grown on SiO_x/Si substrates cut from Si wafers. This extensive study was performed in collaboration with Fraunhofer IPMS CNT in Dresden (external samples – see chapter 4.7) with the aim to better understand beam-induced changes in hafnium oxide-based ferroelectrics.

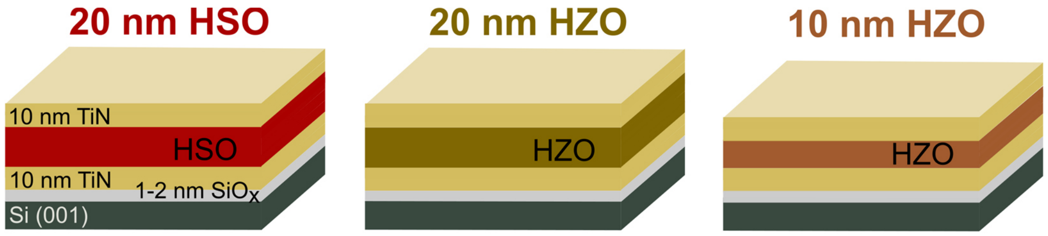

Figure 6-16: Schematic drawings showing the irradiated ferroelectric stacks containing 20 nm HSO (Si-doped HfO_2), 20 nm HZO or 10 nm HZO (Zr-doped HfO_2) layers sandwiched between two TiN electrodes on top of a SiO_x/Si substrates.

Structural investigations using XRD: The XRD patterns of the investigated stacks are shown in Figure 6-17 with a non-irradiated (as grown) reference given in grey and increased ion fluences ranging from 1×10^{10} to 7×10^{12} ions/cm². As grown stacks with 20 nm HSO and 20 nm HSO (Figure 6-17 (a) and (b)) consist of a mixture of the monoclinic phase (space group $P2_1/c$, ICDD 00-034-0104) with characteristic reflections at $2\theta \approx 28.5°$ and $2\theta = 34° - 35°$, and a possible mixture of tetragonal, cubic and orthorhombic phases (characteristic reflections at $2\theta \approx 30.5°$ and $2\theta = 35° - 36°$). For the as grown stack containing 10 nm thick HZO (Figure 6-17 (c)), there is no or only a very small amount of the monoclinic phase present (low intensity between $2\theta = 34° - 35°$). The main characteristic reflection is located at $2\theta \approx 30.5°$. (Theoretical powder) reference patterns of the monoclinic, ferroelectric orthorhombic, tetragonal and cubic phase of HfO_2 based on reported structures are shown in Figure 6-17 (d).[123, 124, 126, 130, 356] As already discussed, the ferroelectric orthorhombic, tetragonal, other non-polar orthorhombic or the cubic structure of thin film HfO_x can only be hardly distinguished by means of XRD. In the given 2θ-scans of these thin, strained and oriented films, a separation of the phases is not possible (compare chapter 4.5.1). However, the presence of a large amount of the polar orthorhombic phase is confirmed by the measurable electric polarization of the samples, which is presented later in this chapter. Therefore, the reflections found at $2\theta \approx 30.5°$ and $2\theta = 35° - 36°$ can be mainly assigned to the (111) and (200) planes of the orthorhombic phase ($Pca2_1$). This result is in accordance with literature results obtained from films which were prepared with the same preparation workflow.[130]

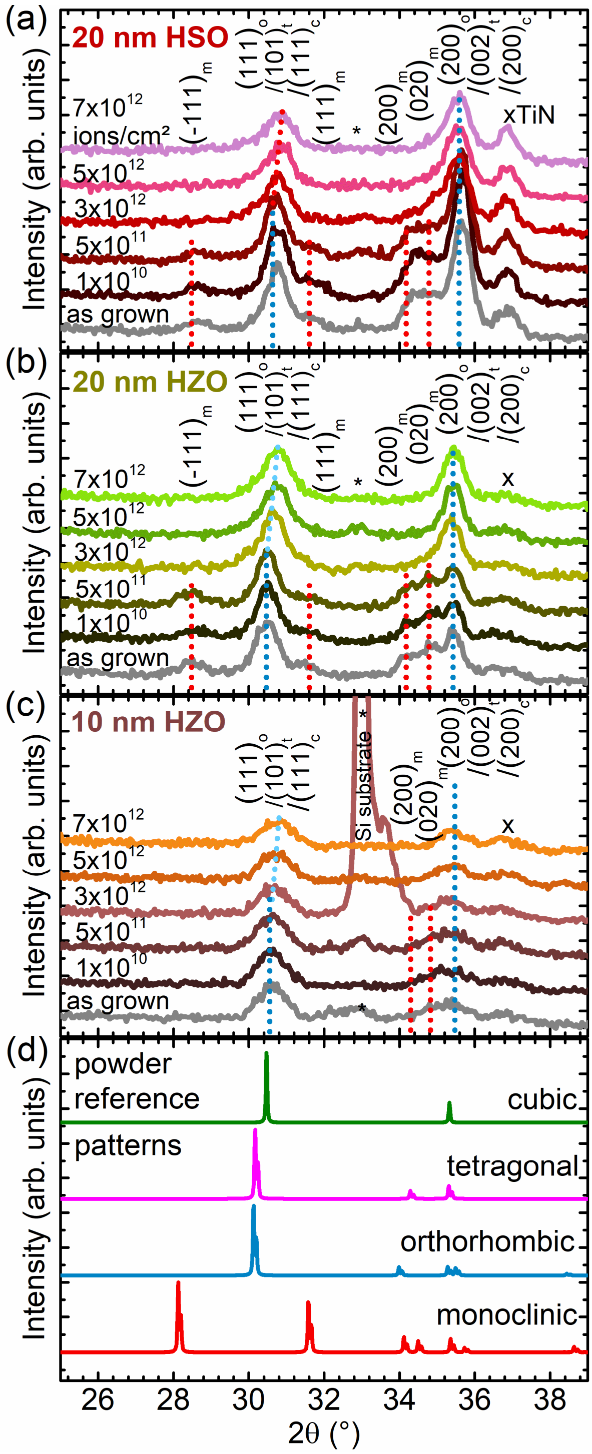

Figure 6-17: XRD patterns of doped ferroelectric hafnium oxide films before and after irradiation, containing (a) 20 nm HSO, (b) 20 nm HZO and (c) 10 nm HZO. With increasing ion fluence, a shift of the initially (111)$_o$ reflection towards larger diffraction angles occurs. Monoclinic reflections vanish at fluences above 5x10^{11} ions/cm². (d) Theoretical powder reference patterns of the monoclinic, polar orthorhombic, tetragonal and cubic phase of HfO$_2$, created based on previously reported structures.[123, 124, 126, 130, 356] The (111)$_c$ reflection of the TiN electrode is marked by x. The Si-substrate reflections located between 2θ = 32.5° - 34° are assigned to the Si (200) reflection due to Umweganregung[353] and is not related to the ferroelectric layer. Partially reproduced with permission from[131]. The original publication is licensed under a Creative Commons Attribution 4.0 License (CCBY) and published by AIP Publishing.

After ion exposure, four visible major characteristics in the XRD patterns can be pointed out:

- Up to a fluence of 5×10^{12} ions/cm^2, no intensity changes or shifts of the reflections in 2θ are recognisable.
- At increasing fluences, the reflections assigned to the monoclinic phase disappear (at 2θ ≈ 28.5° and 2θ = 34° – 35°) from the XRD patterns.
- A continuous shift of the reflection located at 2θ ≈ 30° towards larger diffraction angles is visible (starting above 5×10^{11} ions/cm^2).

These observations are described in more detail in the following and connected to the ferroelectric properties, such as the field-dependent electric polarization results (P-E characteristics) of devices to obtain a more extensive understanding of the basic physical mechanisms present in hafnium oxide-based ferroelectric memories exposed to heavy ion radiation.

Electrical investigations of ferroelectric capacitors: In Figure 6-18, the P-E characteristics obtained before (grey - Ref.) and after heavy ion irradiation are presented. Additionally, the results obtained after 10000 post-cycles after the irradiation and tests shown are provided. These experiments were performed for devices based on 20 nm HSO, 20 nm HZO and 10 nm HZO exposed to heavy ions of different fluences (1×10^{10}, 5×10^{11} and 2.4×10^{12} ions/cm^2).

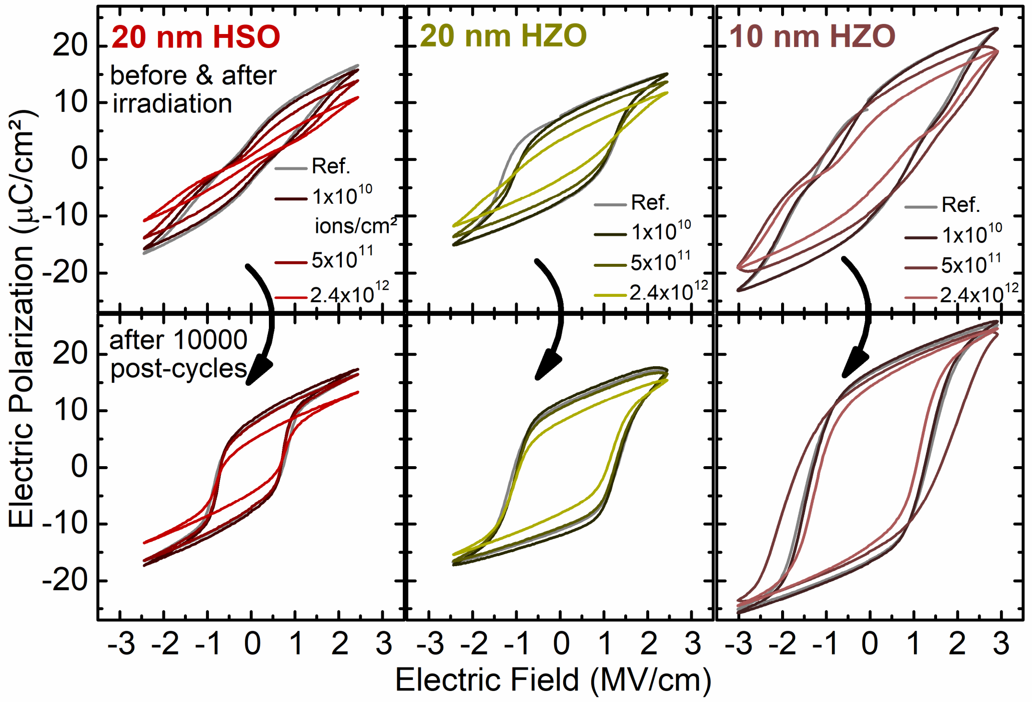

Figure 6-18: Field-dependent electric polarization curves before (grey – Ref.) and after exposure to different fluences (top) and after 10000 post-cycles (bottom). The induced pinching of the polarization hysteresis loops is reversed after cycling and the loops are re-opened, showing ferroelectric behavior. Additionally, the loop of a non-irradiated, but cycled reference sample (grey) is shown. Partially reproduced with permission from[131]. The original publication is licensed under a Creative Commons Attribution 4.0 License (CCBY) and published by AIP Publishing.

Overall, all stacks were found to be ferroelectric, showing a typical ferroelectric loop with two distinct remanent polarization states. Consequently, the observed reflection in the XRD patterns at around 2θ = 28.5° and 2θ = 34° – 35° (Figure 6-17) can be assigned to the non-centrosymmetric ferroelectric orthorhombic (space group $Pca2_1$) phase of the ferroelectric layers. Fractions of other phases are likely, especially at higher fluences, which will be discussed further in this chapter.

At a fluence of 1×10^{10} ions/cm^2, no significant influence of the heavy ions on the P-E characteristics are visible, while at increased fluences (5×10^{11} and 2.4×10^{12} ions/cm^2) a pinching of the loops accompanied by a gradual reduction of the remanent polarization (P_r) and saturation polarization (P_S) are observed for all three stacks. The characteristic values are listed in Table 6-1. In this study, only positive polarization and coercive field values are given from the representative plots. To carry out a detailed analysis, absolute values are listed However, absolute values can suffer from statistical errors. Therefore, the discussion is limited to observed trends.

Table 6-1: Remanent polarization (P_r) and saturation polarization (P_S) values obtained for the three stacks before irradiation (Ref.) and at various fluences.

Ferroelectric	Ref.	1×10^{10} ions/cm^2	5×10^{11} ions/cm^2	2.4×10^{12} ions/cm^2
20 nm HSO	$P_r \approx 3.7\ \mu C/cm^2$ $P_S \approx 16.6\ \mu C/cm^2$	$P_r \approx 3.0\ \mu C/cm^2$ $P_S \approx 15.8\ \mu C/cm^2$	$P_r \approx 1.7\ \mu C/cm^2$ $P_S \approx 13.9\ \mu C/cm^2$	$P_r \approx 0.6\ \mu C/cm^2$ $P_S \approx 10.9\ \mu C/cm^2$
20 nm HZO	$P_r \approx 7.6\ \mu C/cm^2$ $P_S \approx 15.1\ \mu C/cm^2$	$P_r \approx 7.1\ \mu C/cm^2$ $P_S \approx 15.1\ \mu C/cm^2$	$P_r \approx 5.9\ \mu C/cm^2$ $P_S \approx 13.7\ \mu C/cm^2$	$P_r \approx 3.4\ \mu C/cm^2$ $P_S \approx 11.8\ \mu C/cm^2$
10 nm HZO	$P_r \approx 10.7\ \mu C/cm^2$ $P_S \approx 23.1\ \mu C/cm^2$	$P_r \approx 10.4\ \mu C/cm^2$ $P_S \approx 23.1\ \mu C/cm^2$	$P_r \approx 9.8\ \mu C/cm^2$ $P_S \approx 19.0\ \mu C/cm^2$	$P_r \approx 6.2\ \mu C/cm^2$ $P_S \approx 19.1\ \mu C/cm^2$

Overall, HZO-containing stacks show larger values when compared to the HSO-containing stacks, as also known from literature, which could be related to a different crystallographic texture of the films.[130] Especially the stacks containing 10 nm thin HZO films show a high polarization, both before and after being exposed to Au heavy ions. This is related to the lower or missing monoclinic phase fraction in thinner films.[130]

Remarkably, the reduced polarization values can be recovered, and the pinching of the P-E loops can be reopened by applying wake-up field cycles (Figure 6-18). The P_r and P_S values are increasing (e.g., P_r of 20 nm HSO: 8.2 $\mu C/cm^2$ (1×10^{10} ions/cm^2), 7.3 $\mu C/cm^2$ (5×10^{11} ions/cm^2), 4.6 $\mu C/cm^2$ (2.4×10^{12} ions/cm^2)) when compared to the values of non-cycled samples. The characteristic polarization values obtained after 10000 post-cycles are listed in Table 6-2.

Table 6-2: Remanent polarization (P_r) and saturation polarization (P_S) values obtained for the three stacks after 10000 post-cycles after irradiation at various fluences. Additionally, values of a non-irradiated, but cycled reference sample (Ref.) are shown.

Ferroelectric	Ref.	1×10^{10} ions/cm^2	5×10^{11} ions/cm^2	2.4×10^{12} ions/cm^2
20 nm HSO	$P_r \approx 7.7\ \mu C/cm^2$ $P_S \approx 16.5\ \mu C/cm^2$	$P_r \approx 8.2\ \mu C/cm^2$ $P_S \approx 17.3\ \mu C/cm^2$	$P_r \approx 7.3\ \mu C/cm^2$ $P_S \approx 16.4\ \mu C/cm^2$	$P_r \approx 4.6\ \mu C/cm^2$ $P_S \approx 13.3\ \mu C/cm^2$
20 nm HZO	$P_r \approx 11.0\ \mu C/cm^2$ $P_S \approx 16.9\ \mu C/cm^2$	$P_r \approx 11.5\ \mu C/cm^2$ $P_S \approx 17.2\ \mu C/cm^2$	$P_r \approx 10.3\ \mu C/cm^2$ $P_S \approx 16.5\ \mu C/cm^2$	$P_r \approx 7.9\ \mu C/cm^2$ $P_S \approx 15.4\ \mu C/cm^2$
10 nm HZO	$P_r \approx 16.8\ \mu C/cm^2$ $P_S \approx 25.1\ \mu C/cm^2$	$P_r \approx 16.8\ \mu C/cm^2$ $P_S \approx 25.7\ \mu C/cm^2$	$P_r \approx 15.6\ \mu C/cm^2$ $P_S \approx 23.5\ \mu C/cm^2$	$P_r \approx 14.3\ \mu C/cm^2$ $P_S \approx 24.5\ \mu C/cm^2$

Such a trend can also be observed for the coercive field values (E_C of 20 nm HZO (non-cycled): 1.1 MV/cm (Ref.), 1.0 MV/cm (1×10^{10} ions/cm²), 1.0 MV/cm (5×10^{11} ions/cm²), 0.7 MV/cm (2.4×10^{12} ions/cm²) vs. E_C (post-cycled): 1.3 MV/cm (Ref.), 1.3 MV/cm (1×10^{10} ions/cm²), 1.2 MV/cm (5×10^{11} ions/cm²), 1.0 MV/cm (2.4×10^{12} ions/cm²). All stacks showed slightly pinched P-E loops prior to ion exposure and cycling, which can be called an antiferroelectric-like behavior. The loops are opening during cycling, which is especially visible for 20 nm HSO- and 10 nm HZO-containing films. This is a commonly observed wake-up behavior in hafnium oxide-based ferroelectrics. [130]

A similar behavior is seen after post-cycling after irradiation. More statistics of the remanent polarization values after irradiation and subsequent post-cycling are given in the boxplots shown in Figure 6-19. The general trend towards a reduced polarization with increasing fluence is visible for all tested devices.

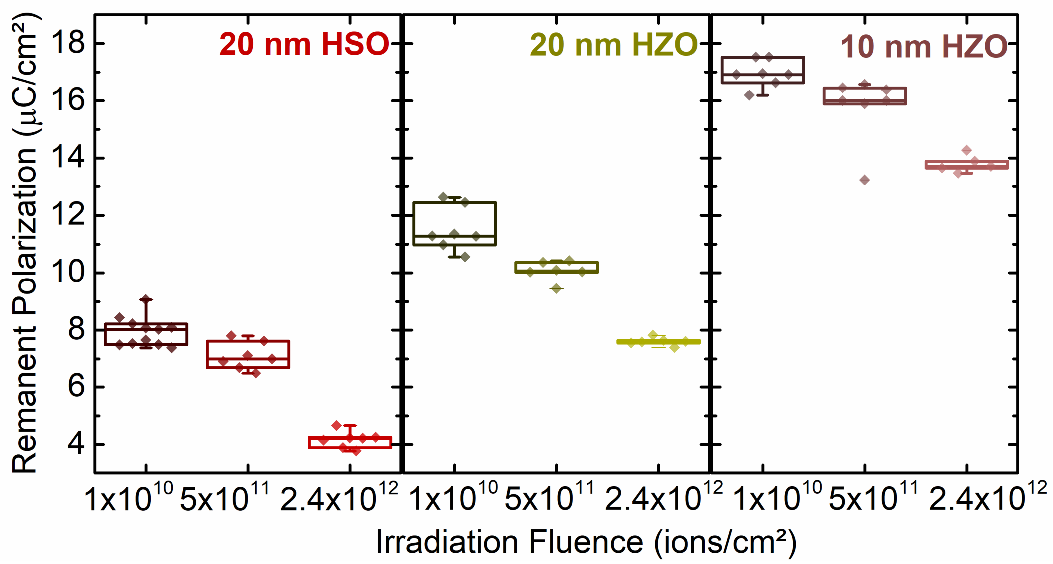

Figure 6-19: Values of the remanent polarization after irradiation and 10000 post-cycles for 6 to 10 devices per fluence. A clear trend to lower values with increased fluences is visible. Partially reproduced with permission from[131]. The original publication is licensed under a Creative Commons Attribution 4.0 License (CCBY) and published by AIP Publishing.

Additionally, the measured P_r values after post-cycling are found to not only be recovered but exceeding the polarization values of the non-irradiated and non-cycled reference samples. In the case of 20 nm thick HSO films, this result can be partially explained by the missing monoclinic phase fraction in the ferroelectric layers after irradiation and post-cycling, as discussed in the context of the XRD results shown in Figure 6-17. The non-irradiated reference stacks initially contained a small fraction of the non-polar monoclinic phase, which was reduced during irradiation and is not recovered during post-cycling. A detailed explanation is given in the following.

By correlating the beam-induced as well as the cycling-induced changes of the electric polarization to the XRD results, the following explanations for the described observations can be given:

(1) All prepared ferroelectric layers contain a large amount of the polar orthorhombic phase, which is mostly unaffected up to a fluence of at least 5×10^{12} ions/cm². However, oxygen

defects (most likely oxygen vacancies) are likely to be introduced by the electronic interaction of the Au ions with the layers as further described in (3) – see below. The observed minor changes of the polarization are a consequence of this increase of defects.

(2) The initially present monoclinic phase is most likely transformed to a phase of higher symmetry after 1×10^{12} ions/cm² exposure and above. This could be similar to the results discussed in chapters 6.1.1 and 6.1.2 for non-doped hafnium oxide film, where the presence of a rhombohedral phase after irradiation is likely. However, ferroelectric films contain additional dopants and are crystallized in the polar orthorhombic phase, which potentially leads to a different transition than obtained for initially monoclinic pure HfO_2 films. This could also lead to differences compared to the beam-induced transition of a rhombohedral phase of HfO_x to an even more oxygen-deficient phase as described in chapter 6.1.1.

(3) The visible shift of the orthorhombic (111) reflection from $2\theta = 30.5° – 30.75°$ (before irradiation) to $2\theta = 30.75° – 30.9°$ after being exposed to 7×10^{12} ions/cm² (compare Figure 6-17) can at first glance be a result of a) an introduction of oxygen vacancies or b) an induced phase transition. As discussed in chapter 6.1.1, irradiated rhombohedral hafnium oxide films show a similar shift of the reflections in the XRD patterns which could be connected to a decreasing oxygen content of the layers (increasing with increasing irradiation fluence). This could be accompanied by a further phase transition. As described by Nico Kaiser *et al.*[128, 145], a further decrease of the oxygen content in as grown, non-doped HfO_x films, which is equivalent to a further introduction of more oxygen vacancies, is directly accompanied by a continuous shift of the corresponding position of the reflection in the XRD patterns and a phase transition. Therefore, a beam-induced phase transition can be also presumed in ferroelectric hafnium oxide-based films exposed to heavy ions. The electronic energy loss in the ferroelectric layers is about 53 keV/nm (using a ferroelectric layer density of 8.79 g/cm²). The nuclear loss is as low as 68 eV/nm and the number of displacements per atom (dpa) in $Hf_{0.5}Zr_{0.5}O_2$ is only about 1×10^{-4}. Overall, a comparable crystalline-to-crystalline phase transition as described in chapter 6.1.1 (monoclinic to rhombohedral and rhombohedral to an even more oxygen-deficient phase) and in literature[11] (monoclinic to tetragonal) could be also induced in orthorhombic films. This transition is likely to be also relying on a defective track overlap, which becomes more probable with increasing ion fluence especially for values above 1×10^{12} ions/cm². However, the question arises to which phase the orthorhombic phase is transformed.

(4) A partial phase transition from a polar orthorhombic to a non-polar cubic or tetragonal phase is possible, which in accordance with the observation of the reduced polarization values after irradiation at high fluences and the visible shape of the loops. As the polarization is not fully vanishing after irradiation (7×10^{12} ions/cm²), the polar orthorhombic phase seems to be partially preserved even after extensive ion exposure. This is hardly visible in the XRD patterns, however, a split of the initially present orthorhombic (111) reflection into a defect-rich orthorhombic (111) and a cubic (111) reflection can be presumed, which are located at a very similar diffraction angle.

Vice versa, a reopening of the P-E loops by electric field cycling is a clear indication for a field-induced phase transformation to the ferroelectric orthorhombic phase. This has been shown in non-irradiated films for the transition from a tetragonal to the polar orthorhombic phase.[40, 357] In the presented cases, this corresponds to a transformation back from a non-polar phase to the initially present polar orthorhombic phase.

It cannot be clearly stated which non-polar phase is (partially) present after irradiation. The presence of a tetragonal phase is possible (comparable to non-irradiated stacks[40, 357]), however, also a cubic phase is possible. The latter is supported by the relative reflection angles of the phases in question. The presence of a cubic $Fm\overline{3}m$ phase with an expected $(111)_c$ reflection appearing at slightly larger angles than the coinciding $(111)_o$ and $(101)_t$ reflections is likely. In general, also a transition to the oxygen-deficient rhombohedral phase of hafnium oxide might be possible. However, the measurable electric polarization after irradiation confirms the presence of an insulating phase but the rhombohedral $HfO_{1.7}$ (or $HfO_{1.5}$) phase is reported to be electrically conducting.[128, 145] The presence of a small fraction of the rhombohedral phase (with e.g. a lower oxygen-deficiency) cannot be fully excluded, however, a beam-induced transition from the polar orthorhombic to a non-polar tetragonal or cubic phase is more likely.

(5) The intensity of the (111) reflections corresponding to the initial orthorhombic phase is decreasing and the peak width is increased. The full width at half maximum (FWHM) is changing from about 0.32° – 0.46° in 20 nm HSO, 0.34° – 0.45° in 20 nm HZO and 0.43° – 0.49° in 10 nm HZO films. A broadening of reflections was reported in chapter 6.1.1 in the context of introduced defects and a beam-induced grain fragmentation at ion fluences above 1×10^{12} ions/cm^2. Such a grain fragmentation is also presumed to occur in ferroelectric hafnium oxide-based films.

A direct connection to the ferroelectric properties is possible when looking at the P-E curves of HSO-containing stacks. Here, an interesting detail is visible. While all three stacks have initially shown a similar pinching of the loops (antiferroelectric-like behavior before irradiation or cycling), the slope of the loops differed. This indicates a difference of the relative permittivity, which is decreasing with increasing ion fluence. At the highest fluence of 2.4×10^{12} ions/cm^2 the reduction of permittivity even persists post-cycling. As a general trend, a lower relative permittivity indicates a reduction in symmetry. This could be related to an amorphization in ferroelectric hafnium oxide.[358] However, this effect can also be a result of the presence of a grain fragmentation and consequently nanocrystalline grains and an increased number of grain boundaries. This is equivalent to a larger disordered volume in the ferroelectric layer, leading to a reduction of permittivity.

Additionally, the P_S values are reduced initially, even though the same ferroelectric behavior is reached after post-cycling. This indicates a reduction of switchable orthorhombic phase in the initial case. In general, this can be explained again by the presence of phase transitions or by domain wall pinning effects due to the generation of oxygen vacancies. However, an increase in mechanical stress would alter the ferroelastic switching behavior[359], which does not match the observed behavior, as the values of the displacement current peaks do not shift in position (not shown).

(6) The increased polarization after cycling of irradiated films compared to the initial characteristics can be explained by a combination of different mechanisms, which become more obvious when analyzing the cycle-dependent P_S values (Figure 6-20). It should be

mentioned that an analysis of the P_S values was carried out instead of an analysis of the P_r values, as the P_r values consist of undesirable antiferroelectric components next to the ferroelectric components.

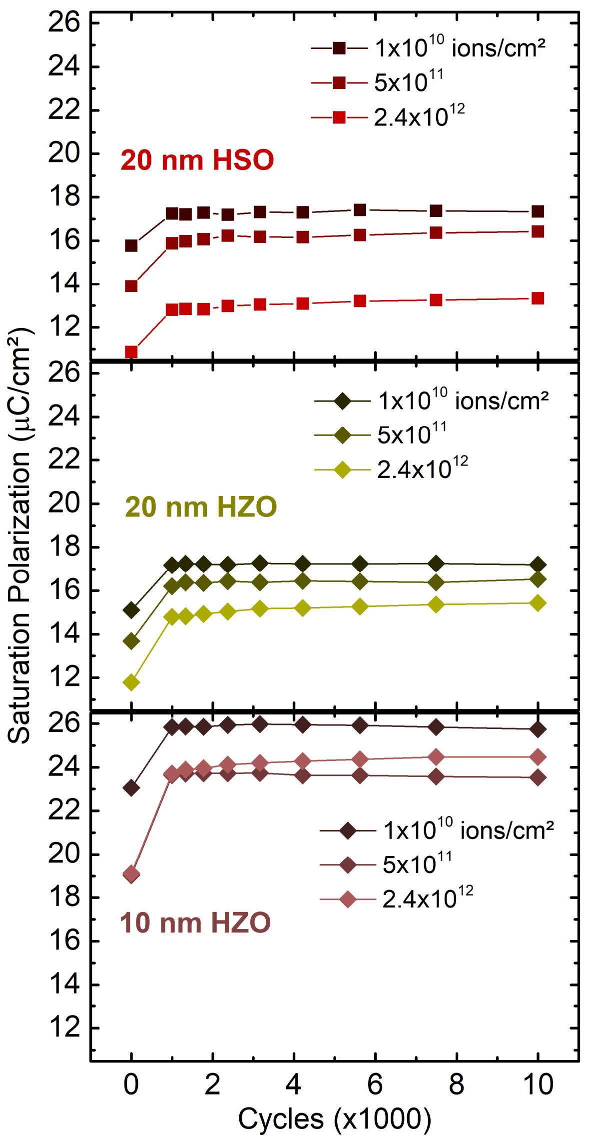

Figure 6-20: Evolution of the saturation polarization P_S in dependence of up to 10000 field-cycles (post-cycling) using an amplitude of 3 MV/cm. A significant increase after cycling is observed with a saturation reached after about 1000 cycles. For the largest fluence of 2.4×10^{12} ions/cm², P_S is even after cycling lower compared to samples exposed to lower fluences for all stack types. Partially reproduced with permission from[131]. The original publication is licensed under a Creative Commons Attribution 4.0 License (CCBY) and published by AIP Publishing.

The obtained results validate the aforementioned trends (in (5)), as for all three sample stack configurations the initial reduction of P_S after ion exposure is visible. Upon post-cycling, a large increase of the P_S after 1000 cycles occurs, while there are no significant changes observed for further cycling up to 10000 cycles (see values listed in Table 6-1 and Table 6-2). This is a contradiction to the common wake-up behavior, where a constant P_S is expected during electric field cycling.[359] Hence, the trend observed for irradiated and post-cycled samples has to be explained in a different way, either by a sudden wake-up or a superposition of classical and partial sudden wake-up. Sudden wake-up has only been observed when an electric field was applied to initially amorphous hafnium oxide-based stacks, leading to a field-induced crystallization, where the applied voltage allows a precise control of the crystallization process. This effect is usually showing Arrhenius-like behavior with an activation energy barrier of 0.45 V.[359] For the ferroelectric stacks presented in this work, the required amplitudes reported for this crystallization process are not reached.

In the given case, an irradiation-induced crystalline-to-crystalline phase transition accompanied by grain fragmentation occurs at large fluences. The grain fragmentation leads to an increased number of grain boundaries. Since the reduction of the P_S persists even after post-cycling for the samples exposed to large fluences above 1×10^{12} ions/cm², a phase transition from a non-polar phase (like the cubic or tetragonal phase) to the polar orthorhombic is much more likely to occur than an electric field-induced crystallization. The induced fragmentation of grains cannot be reversed. This field-induced phase transition appears to be consistent to the reported irreversible phase transition from the non-polar tetragonal phase to the polar orthorhombic phase in non-irradiated hafnium oxide-based ferroelectrics.[360, 361]

Additional polarization measurements of pre-poled capacitors: To get insights into the influence of the polarization state of the devices on their properties after heavy ion irradiation, pre-poled devices were investigated. In Figure 6-21, the field-dependent polarization hysteresis loops of devices poled negatively (neg.) and positively (pos.) prior to irradiation are shown.

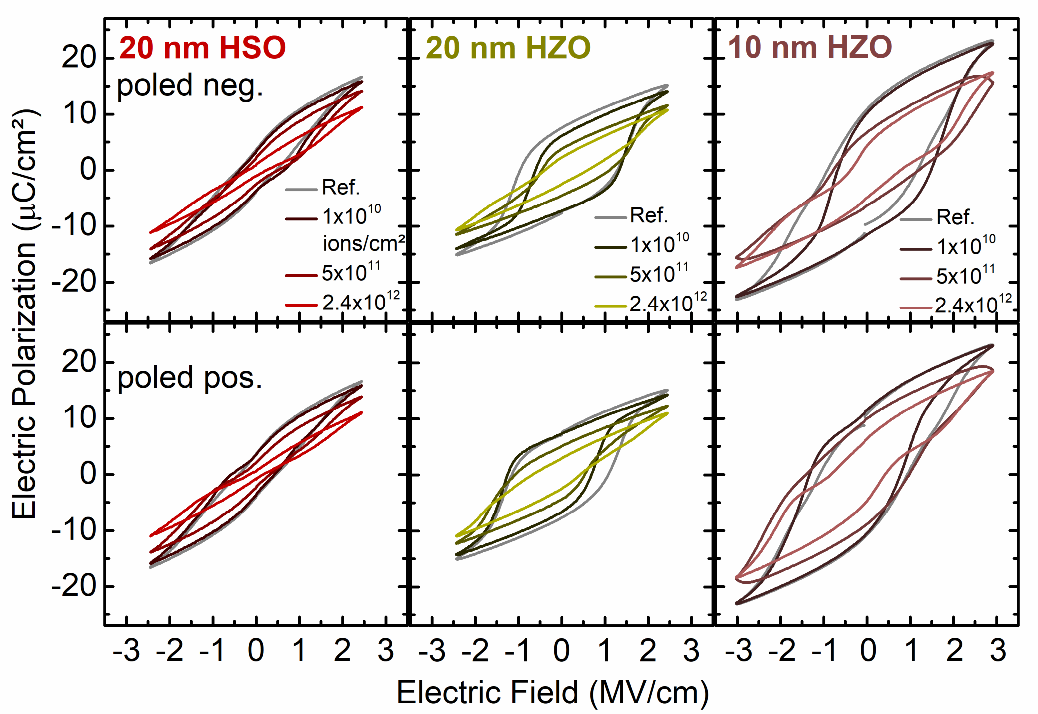

Figure 6-21: Field-dependent electric polarization hysteresis of capacitors poled prior to Au irradiation. A shift of the coercive fields to more positive or negative values are visible for samples poled negatively (top) or positively (bottom), respectively. Trends obtained for increasing fluences are similar to non-poled samples. Partially reproduced with permission from[131]. The original publication is licensed under a Creative Commons Attribution 4.0 License (CCBY) and published by AIP Publishing.

Overall, similar trends compared to the discussed results can be seen (compare to Figure 6-18). Additionally, a clear imprint is visible by the curve asymmetry, which is especially seen for HZO-containing samples compared to HSO-containing samples. Remarkably, there is a steeper switching transition for values around E_C found for all irradiated stacks. Additionally, the coercive field window ($2E_C$) is lower. In literature, imprint has been related to the presence of oxygen vacancies in ferroelectric layers.[130] The observed trend visible after irradiation of pre-poled samples cannot be explained by this only. Instead, again the induced phase transition next to the generated oxygen vacancies influence the domain dynamics, which results in the observed behavior. To get a deeper understanding of this behavior, further in-depth analysis of the oxygen vacancy dynamics in hafnium oxide-based films will be required in future studies.

Model and Summary: The results presented on irradiated ferroelectric Si-doped hafnium oxide- and hafnium zirconium oxide-based stacks can be summarized in a simplified model (Figure 6-22).

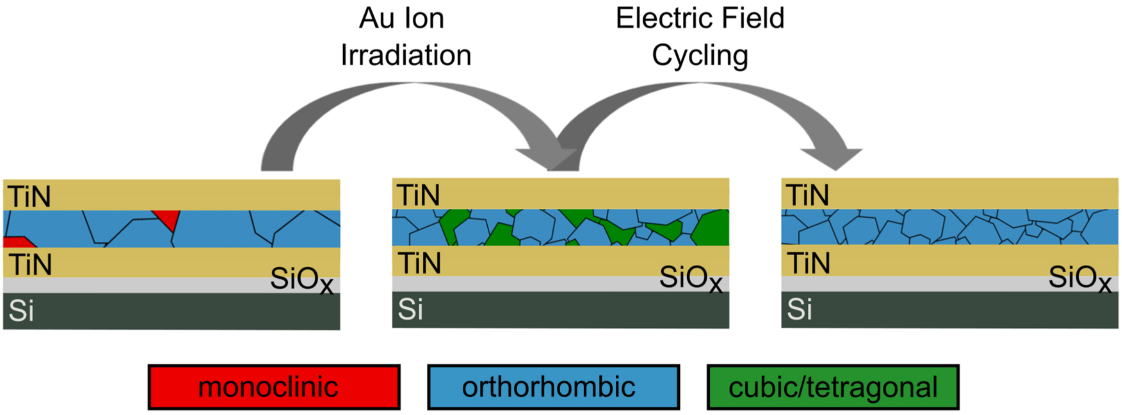

Figure 6-22: Schematic of the changes induced by heavy ion irradiation and post-cycling in ferroelectric hafnium oxide-containing stacks. A beam-induced phase transition of the monoclinic (red) and polar orthorhombic (blue) phase to non-polar a cubic or tetragonal (green) phase occurs, accompanied by grain fragmentation at high fluences. The non-polar phase can be (re)transformed to the polar orthorhombic phase upon field-cycling. In contrast, the induced grain fragmentation appears to be irreversible. Partially reproduced with permission from[131]. The original publication is licensed under a Creative Commons Attribution 4.0 License (CCBY) and published by AIP Publishing.

High-energy heavy ion irradiation leads to a phase transition from the polar orthorhombic to likely a non-polar cubic or tetragonal phase, which is accompanied by grain fragmentation. As a consequence, the ferroelectric properties degrade. These results were obtained from detailed electrical investigations combined with XRD analysis. Upon cycling, the non-polar phase is transformed back to the polar orthorhombic phase. Moreover, grain fragmentation and an increased fraction of grain boundaries can explain the reduction in remanent polarization, and the not fully-recoverable polarization for high fluences, while ferroelectric properties can be fully recovered by post-cycling for lower fluences. The study points out the high radiation resilience of hafnium oxide-based ferroelectric materials and capacitors and gives detailed insights into material characteristics after heavy ion irradiation in the electronic energy loss regime as well as device properties of ferroelectric capacitors upon cycling in general.

6.4 Heavy ion irradiation induced phase transitions in $Ge_2Sb_2Te_5$ and Ge-rich GST layers and electrical properties of phase-change memory

The influence of heavy ions on the stability of Ge-Sb-Te-based layers and corresponding phase-change memory devices in a 1T1R-array were investigated. Similar to the experiments conducted for hafnium oxide-based samples, fluence-dependent beam-induced crystallinity changes of full-sheet layers were investigated by XRD and STEM and connected to the switching performance of PCRAM. In contrast to hafnium oxide-based stacks, not only crystalline but also amorphous Ge-Sb-Te-based layers were investigated, as PCRAM is strongly dependent on the reversible amorphous-to-crystalline transition. Additionally, the composition of the phase-change layer plays an important role in the observed electrical behavior of PCRAM. Therefore, four different stacks were investigated (about 100 nm thick amorphous $Ge_2Sb_2Te_5$ (*a*-GST) films, crystalline $Ge_2Sb_2Te_5$ (*cry*-GST) films, amorphous Ge-rich GST (*a*-GGST) films and crystalline Ge-rich GST (*cry*-GGST) films; all capped with SiN encapsulation layer – see Figure 6-23) grown on SiO_x/Si (001) substrates cut from Si wafers.

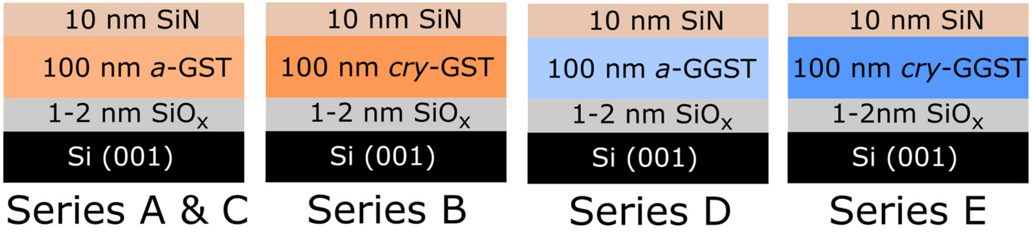

Figure 6-23: Schematic representations showing the irradiated phase-change memory stacks containing 100 nm *a*-GST, *cry*-GST, *a*-GGST and *cry*-GGST (full-sheet) layers with a 10 nm SiN encapsulation layer grown on top of a SiO_x/Si substrates.

Structural investigations using XRD: The XRD patterns of the GST-films are shown in Figure 6-24. Interestingly, dependent on the initial crystalline or amorphous nature of the phase-change layers, different trends are observed.

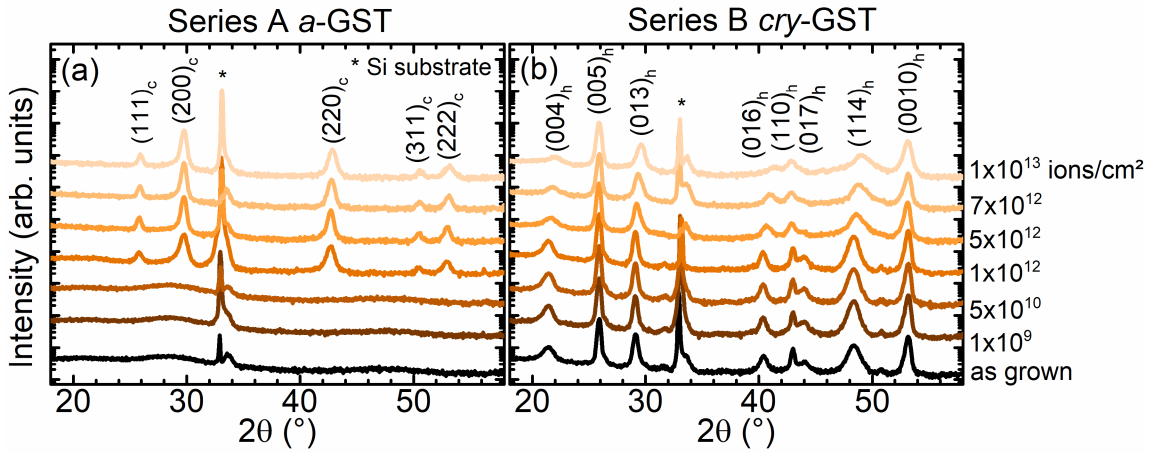

Figure 6-24: XRD patterns of as grown and irradiated GST-based samples consisting of amorphous $Ge_2Sb_2Te_5$ (*a*-GST, Series A) and crystalline $Ge_2Sb_2Te_5$ (*cry*-GST, Series B) with changes occurring at increasing fluence. Si substrate reflections are marked with a *. Partially reproduced with permission from[354], https://doi.org/10.1021/acsnano.2c04841. The original publication is licensed under a Creative Commons Attribution 4.0 License (CCBY) and published by American Chemical Society.

Initially amorphous GST (*a*-GST, series A) undergoes a crystallization to a cubic phase (space group $Fm\bar{3}m$, ICDD 00-054-0484) after exposure to 1×10^{12} ions/cm² and above (Figure 6-24 (a)). In contrast, initially crystalline GST layers (*cry*-GST, series B) do not face such drastic structural changes (Figure 6-24 (b)). Ion irradiation only leads to minor shifts and slight broadening of reflections attributed to the hexagonal phase of GST (space group $P\bar{3}m1$, trigonal crystal system, ICDD 04-020-8161) above 1×10^{12} ions/cm².

Since a threshold fluence for the observed phase transition in a-GST films is not visible from the XRD results with the chosen fluence steps, an additional sample series (C; XRD patterns in Figure 6-25) was irradiated including fluences of 5×10^{9}, 3×10^{11} and 5×10^{11} ions/cm².

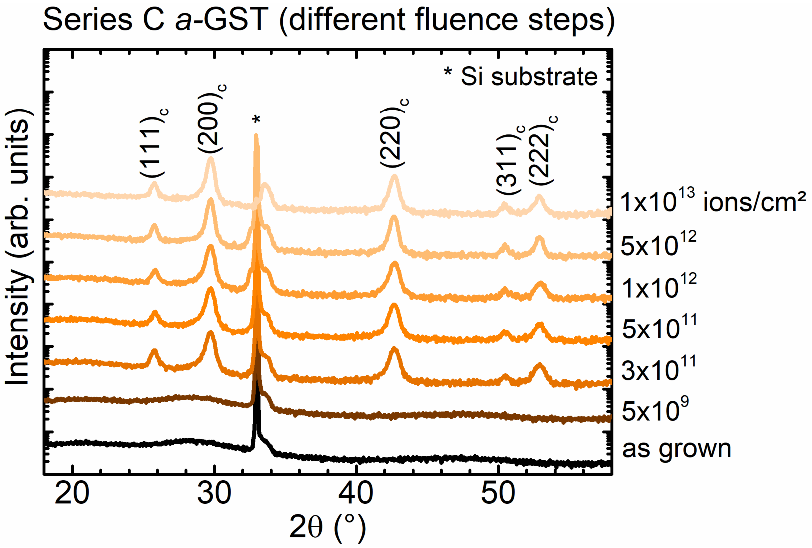

Figure 6-25: XRD patterns of as grown and irradiated amorphous $Ge_2Sb_2Te_5$ (a-GST) films of Series C, with different fluence steps compared to Series A. Starting at fluences of 3×10¹¹ ions/cm² and above, a-GST films crystallize in the cubic phase. Partially reproduced with permission from[354], https://doi.org/10.1021/acsnano.2c04841, https://pubs.acs.org/doi/suppl/10.1021/acsnano.2c04841/suppl_file/nn2c04841_si_001.pdf (supporting information). The original publication is licensed under a Creative Commons Attribution 4.0 License (CCBY) and published by AIP Publishing.

Combining the results of series A and C, the fluence threshold of phase transition of initially a-GST films to the cubic phase of GST can be narrowed down to a fluence between 5×10^{10} and 3×10^{11} ions/cm². For GGST-films differing trends are observed in the XRD patterns (Figure 6-26).

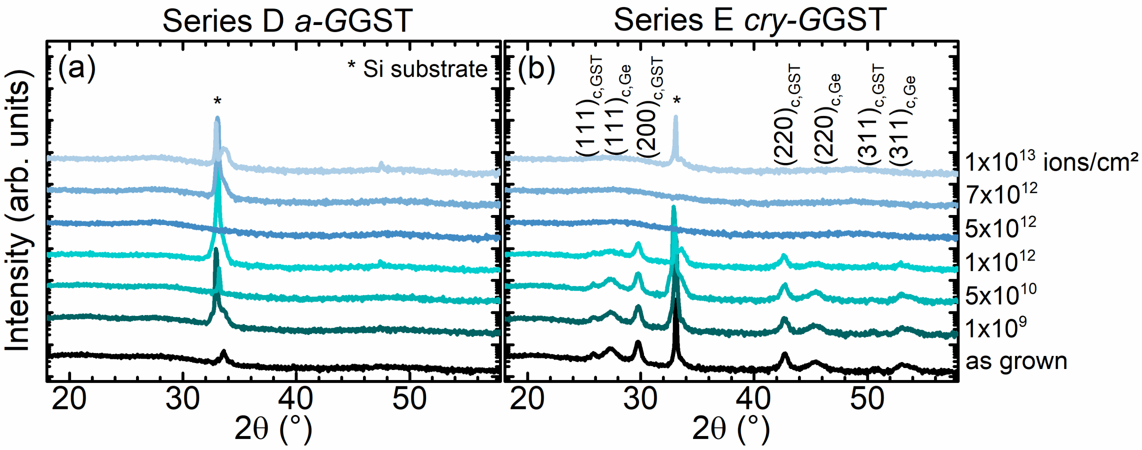

Figure 6-26: XRD patterns of as grown and irradiated GGST-based samples consisting of amorphous Ge-rich GST (a-GGST, Series D) and crystalline Ge-rich GST (*cry*-GGST, Series E) with changes occurring at increasing fluence in *cry*-GGST films only. Si substrate reflections are marked with a *. Partially reproduced with permission from[354], https://doi.org/10.1021/acsnano.2c04841. The original publication is licensed under a Creative Commons Attribution 4.0 License (CCBY) and published by American Chemical Society.

In initially amorphous Ge-rich GST (*a*-GGST, series D) films, there are no changes visible in the XRD patterns. The amorphous nature of these films seems to be still maintained even after exposure to a fluence as high as 1×10^{13} ions/cm². In contrast, for initially crystalline Ge-rich films (*cry*-GGST, series E), the reflections corresponding to the cubic phase of GST and cubic Ge (space group $Fd\bar{3}m$, ICDD 00-004-0545) vanish after ion exposure to more than 1×10^{12} ions/cm². Already at a fluence of 1×10^{12} ions/cm², gradual changes of the crystalline GST and Ge (typical phase separation in GGST) are visible when compared to the XRD patterns obtained at lower fluences.

From the four different sample series shown, dependent on the initial amorphous or crystalline nature as well as the composition of the Ge-Sb-Te-based films, different behaviors were found after exposure to high-energy heavy ions. This could be a result of three different phenomena, which will be discussed in the following:

(1) an overall temperature increase of the sample during ion irradiation
(2) bond-breaking occurring in the crystalline structure due to local temperature spikes
(3) a crystallization due to significant local temperature increase

As the ion flux during irradiation was not exceeding 5×10^{8} ions/cm²s, beam-induced temperature effects (overall sample heating) can be excluded. The overall sample temperature is estimated to be not higher than 60 °C and therefore far below the crystallization and melting temperature of the phase-change materials. Instead, the observed behaviors can be described as a result of two competing mechanisms - bond-breaking versus crystallization/bond-formation - caused by local thermal spikes around the ion trajectory. This is a consequence of the dominating electronic interaction of the high-energy Au ions with the Ge-Sb-Te-based layers, as the electronic energy loss in these films is as high as 34 keV/nm. The result is then determined by the dominating process (bond-breaking or crystallization).

In *cry*-GGST films, bond-breaking seems to be dominant, as the reflections of the crystalline phase vanish from the XRD patterns of *cry*-GGST films (see Figure 6-26) and an amorphous film is obtained after ion exposure of 5×10^{12} ions/cm² and above. Gradual changes, as seen for the *cry*-GGST films exposed to 1×10^{12} ions/cm² and for *cry*-GST films for fluences exceeding 1×10^{12} ions/cm² (see Figure 6-26 and Figure 6-24, respectively) can again be a result of a starting or partial bond-breaking.

In *a*-GST films (see Figure 6-24 and Figure 6-25), crystallization effects seem to be dominant, as a cubic crystalline structure is obtained after irradiation. It is reasonable to assume that the induced thermal spikes lead to a nucleation process and crystallite growth with corresponding bond formation. Interestingly, the necessary fluence for the amorphous to crystalline phase transition is significantly lower than the fluences observed for the transitions obtained for crystalline films (series B and E). For *a*-GGST films of series D (see Figure 6-26), there are no indications for a crystallization in the XRD patterns.

Overall, GGST films tend to have a higher radiation resilience than GST films, which especially holds true for the amorphous state. GGST layers tend to maintain the disordered phase, while this is less favorable in GST layers, where the crystalline phase seems to be more stable.

Investigation of microstructure and composition: To obtain a more detailed understanding, microstructural investigations were conducted and results combined with the XRD data to give possible explanations for the observed changes. EDX and HAADF-STEM images of *a*-GST exposed to 1×10^{13} ions/cm^2 and of *cry*-GGST exposed to 7×10^{12} ions/cm^2 are presented in Figure 6-27. For initially *a*-GST films, a crystalline structure with large grains is revealed after irradiation (a). The crystallization process is validated by the corresponding nano-diffraction patterns. Ge, Sb and Te are found to be well-distributed in EDX mappings. For initially *cry*-GGST, nm-sized crystallites are present, which is especially visible in the NBED patterns by few and low intensity nano-diffraction features (b). In EDX mappings, the characteristic segregation of Ge and Ge-Sb-Te phases in GGST is revealed, which is maintained even after irradiation at high fluences. These results confirm the aforementioned behavior of GGST films having a higher thermal stability also on a microscopic scale. The high thermal stability of the *a*-GGST films in particular is likely to be associated with the general higher temperature stability due to the higher binding energies of these films when compared to *a*-GST films.[211, 212, 362]

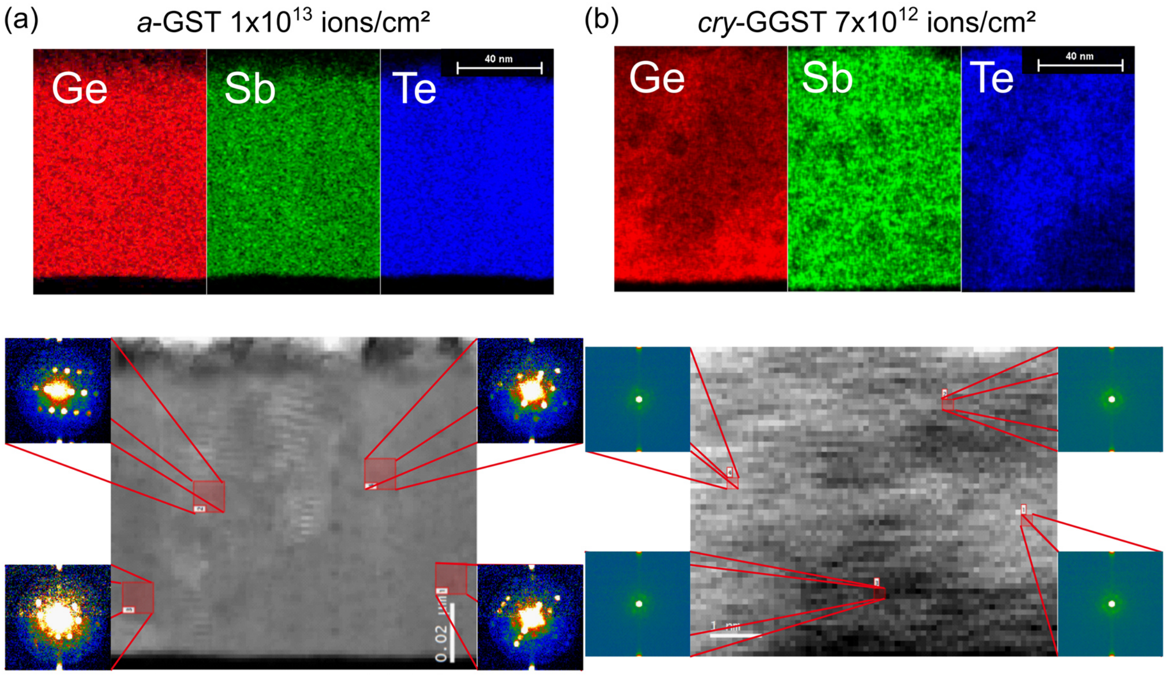

Figure 6-27: EDX and HAADF-STEM images with nano-diffraction patterns of (a) as grown amorphous $Ge_2Sb_2Te_5$ (*a*-GST) exposed to 1×10^{13} ions/cm² showing a crystalline structure with large grains and of (b) crystalline Ge-rich GST (*cry*-GGST) exposed to 7×10^{12} ions/cm² with nm-sized crystallites (visible from few and low intensity NBED patterns). EDX maps reveal a uniform distribution of elements for (a) *a*-GST and (b) *a*-Ge/GST segregation in *cry*-GGST. Reproduced with permission from[354], https://doi.org/10.1021/acsnano.2c04841. The original publication is licensed under a Creative Commons Attribution 4.0 License (CCBY) and published by American Chemical Society.

A comparable crystallization was observed by De Bastiani *et al.*[363] in as grown (non-irradiated) *a*-GST by Raman spectroscopy, where a reduction of initially present Ge-Te tetrahedral bonds occurred. Those tetrahedral bonds are a characteristic property of *a*-GST. Similar structural characteristics are likely in the presented *a*-GST films after ion exposure indicated by the obtained crystallization (XRD and STEM results) and the maintained uniform elemental distribution (of Ge, Sb and Te seen from EDX).

In contrast, the STEM results obtained from the initially cry-GGST films exposed to 7×10^{12} ions/cm² (Figure 6-27 (b)) show nanocrystalline features, which are not obtained in the XRD patterns. It is reasonable that the overall crystalline long-range order is affected by heavy ion irradiation at high fluence, while the short-range order is preserved. Additionally, the typical elemental distribution with Ge/GST-segregation is maintained as confirmed by EDX. Although the definition of phase-change materials includes the change between an amorphous and a crystalline state, the term “amorphous” may also relate to a nanocrystalline structure of still highly-disordered nature, especially if samples are only characterized by XRD. A preserved short range order in the films is also believed to be the origin of the increased background intensity visible in the XRD patterns $2\theta \approx 25° - 35°$ of all amorphous films, as it is present in reported XRD patterns of amorphous Ge-Sb-Te-based phase-change layers.[257, 258] Similar to the results obtained from irradiated *m*-HfO_2, phase transitions in *cry*-GST and *cry*-GGST occur at fluences above 1×10^{12} ions/cm², which is likely to be related to a mechanism based on defective track overlapping (as discussed for hafnium oxide in chapters 6.1.1 and 6.1.2). This is likely to be also the case in Ge-Sb-Te-based phase-change layers, where a large localized temperature is assumed to be required to induce a phase transition.

When directly comparing irradiated crystalline and amorphous films, ion irradiation is expected to introduce a higher disorder in crystalline layers (short- and long-range order is affected), where bond-breaking is likely. Reflection shifts or broadening in the XRD patterns can be a result of a gradual change of the out-of-plane lattice parameter, increasing with higher fluences. In *cry*-GST films, a hexagonal structure is still maintained, with only a slight loss of the initial order (larger diffraction angle corresponds to a smaller lattice constant). At larger fluence a larger damage is expected, especially at fluences, where track overlapping occurs (10^{12} ions/cm² region). In amorphous films with an initially higher disorder, localized heating (thermal spike) can lead to a crystallization. In *a*-GST films, a significantly lower threshold fluence (between 5×10^{10} and 3×10^{11} ions/cm²) is necessary for the amorphous to cubic GST transition (as mentioned above). This seems to be likely connected to single event effects than to the discussed defective track overlapping.

It is reasonable to assume that the different behavior observed for different phase-change layers after ion exposure is based on the different thermal conductivities of the materials. Heat transfer and corresponding local heating is dependent on the thermal conductivity of the individual material. A lower thermal conductivity in e.g., *a*-GST (about 0.19 W/m*K) when compared to *cry*-GST (about 1.58 W/m*K; hexagonal)[364], leads to an increased temperature of the ion-induced localized thermal spike. As a consequence, cubic nano-crystallites are formed in initially amorphous films. This trend is also valid for GGST-based films but with the addition of having larger binding energies when compared to GST-based films.

Electrical investigations of integrated 1T1R PCRAM: As phase-changes are the fundamental mechanism behind the functionality of phase-change memory cells, electrical tests of irradiated devices are required to assess their radiation hardness. Induced changes may have a crucial impact on the overall functionality, especially in terms of distinguishability of the on state (crystalline phase corresponding to the LRS) and off state (amorphous state corresponding to the HRS). Electrical measurements on as grown and irradiated state-of-the-art wall-based phase-change memory devices in a 1T1R arrangement were performed (compare chapter 4.7). Resistance values obtained as a function of fluence are shown in Figure 6-28. It should be mentioned that in GST-based PCRAM switching is often performed by reversibly changing between the cubic phase and the amorphous state, while irradiation and XRD investigations on full-sheet layers were performed only on hexagonal crystalline films. The initial crystal structure is a result of the preparation process. It is reasonable to assume a similar behavior of both, the hexagonal phase and the cubic phase of GST (e.g., with a thermal conductivity of about 0.57 W/m*K)[364].

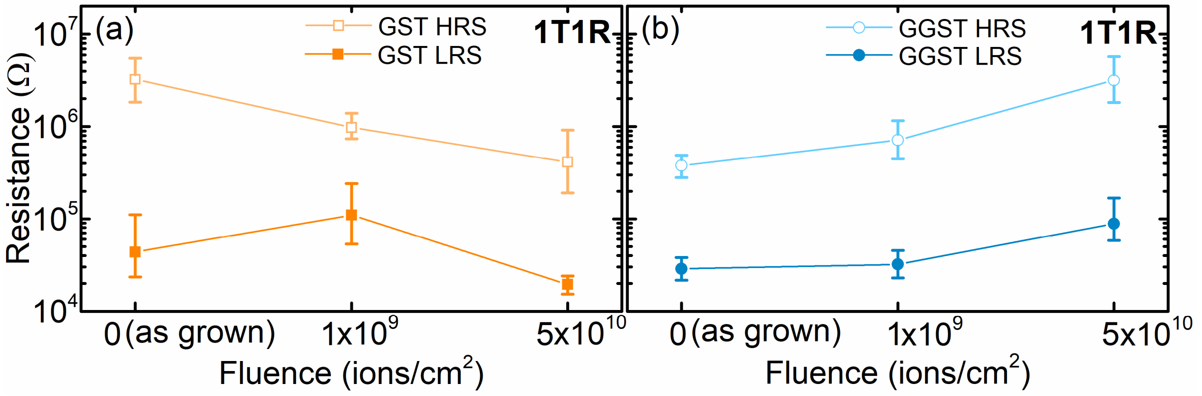

Figure 6-28: Median device resistance values including ±1σ values of (a) GST- and (b) GGST 4kb (1T1R) arrays for the LRS (after set) and HRS (after reset) as a function of fluence (250 devices each). The resistance values of GST-based devices decrease with increasing fluence, while for GGST-based devices, the resistance values increase. Reproduced with permission from[354], https://doi.org/10.1021/acsnano.2c04841. The original publication is licensed under a Creative Commons Attribution 4.0 License (CCBY) and published by American Chemical Society.

Similar to the radiation resilience of the full-sheet materials, integrated GGST-based PCRAM devices (electrode area 10^{-3} μm^2) also show a higher radiation resilience than GST-based devices. For both cases, a clear memory window is found for all samples. Before discussing the trends and possible reasons, it should be mentioned that only three (fluence) data points per memory stack were determined, which can only grant an observation on the overall trend and a larger data set would be required to be statistically more reliable. Electrical investigations 1T1R-arrays exposed to fluences above 5×10^{10} ions/cm² were tried, but the access transistors were damaged. This led to an inhibited data readout due to readout errors and even a full loss of addressing the transistors in several cases. However, the presented data with certain trends of the device resistances can function as a basis of a discussion, relating heavy ion irradiation-induced structural and electrical property changes.

In general, two different trends are visible in Figure 6-28. For GST-based films, a decrease of the overall HRS and LRS resistance occurs, while for GGST-based devices HRS and LRS resistance values increase (values given in Table 6-3).

Table 6-3: HRS and LRS resistances of as grown and irradiated PCRAM devices based on 100 nm thick GST and GGST films.

material & state/fluence	as grown	1×10^9 ions/cm²	5×10^{10} ions/cm²
GST HRS	3.2×10^6 Ω	9.8×10^5 Ω	4.2×10^5 Ω
GST LRS	4.4×10^4 Ω	1.1×10^5 Ω	1.9×10^4 Ω
GGST HRS	3.8×10^5 Ω	7.1×10^5 Ω	3.1×10^6 Ω
GGST LRS	2.8×10^4 Ω	3.2×10^4 Ω	8.8×10^4 Ω

The increase of the resistance in GST-based devices in the LRS after 1×10^9 ions/cm² exposure is likely to be a result of a structural relaxation. The drastic decrease of the LRS resistance and the reduced memory window occurring with increasing fluence can easily result in a loss of the memory state in GST-based devices at the highest fluence.

For GGST-based devices, the memory window is maintained or even increased. Two factors can explain this opposite trend:

(1) a possible irradiation-induced phase transition as seen from full-sheet layer experiments
(2) beam-induced detrimental effects on the CMOS access transistor functionality

In *cry*-GST and *cry*-GGST, phase transitions have only been observed at higher fluences than the ones used for electrical experiments of PCRAM. However, as the observed transition in *a*-GST films to the cubic phase of GST occurs at lower fluences between 5×10^{10} and 3×10^{11} ions/cm², which is close to the highest fluence of the electrical measurement, the resistance reduction especially of the HRS is likely to be caused by a possible begin of a phase transition (just initiated transition). The increased device conductivity occurring with higher fluence can be a result of an increasing number of localized structural changes. However, the detrimental effect on the access transistors cannot be excluded to have an influence on the measurement of the 1T1R-arrays. As described in chapter 6.2.1, OxRAM characterization has revealed that transistors are affected at 5×10^{10} ions/cm² and 1×10^{12} ions/cm², leading to an increasing overall resistance. As for GST-based devices the overall resistance is decreasing with increasing fluence also in the LRS, the detrimental process seems to be dominated by a starting or ongoing phase transition. In GGST-based devices, the resistance values of both, the HRS and LRS increase with increasing fluence, which is likely to be dominated by failures induced by affected access CMOS transistors. This is most likely caused by single event effects, as seen from the fluence range and also the small electrode area of about 10^{-3} μm² (10^{-9} nm²). At a fluence of 5×10^{10} ions/cm², only about 50 ions hit one memory cell on average. Despite the detrimental effects induced by the heavy ions in transistors of the 1T1R-arrays, the memory gap of GGST-based devices is maintained (good resistance range and ratio) and the device performance can be rated as excellent, even after 5×10^{10} ions/cm² exposure.

In literature, investigations of phase transitions in combination with electrical data are scarce. Some studies, using different projectiles such as light ions of low energy ions or protons[256, 257, 365] report that no significant changes occur in irradiated PCM. Even for high-energy heavy ions, only minor changes and small indications of a radiation-induced crystallization of amorphous Ge-Sb-Te-based layers were reported.[258] In context to literature, the presented irradiation experiments on PCM full-sheet layers were conducted at higher ion energy and in a similar fluence range (when compared to Kanda *et al.*[258]), clearly showing ion-induced phase transitions (amorphous-to-crystalline, crystalline-to-crystalline, and crystalline-to-amorphous phase transitions) as well as microstructural changes for films of different composition and crystallinity irradiated using identical ion beam conditions. This shows the importance of considering structural investigations of phase-change materials after irradiation experiments. This holds true in the given case especially for *a*-GST with a crystallization occurring at fluences right above 5×10^{10} ions/cm². Regarding literature reports on irradiated phase-change memory, mostly single event effects occurring at low fluences were reported with no significant changes of the electrical properties and functionality.[275-277, 279] For Ge-Sb-Te-based devices that were affected by 1.2 GeV Xe ions, again single event upsets were reported.[278] The reason for the memory loss was assumed to be a radiation-induced localized amorphization at the interface of the heating element and the phase-change layer.

The presented heavy (1.635 GeV Au) ion irradiation experiments in this chapter using clearly revealed beam-induced changes of the electrical characteristics of phase-change memory devices as a result of possible localized phase-changes due to bond-breaking and bond-creation in GST-based films, which is strongly supported by structural results obtained, while for GGST-based devices, changes are most likely (only) caused by affected CMOS access transistors. Overall, the presented memories are found to be radiation-hard, withstanding the exposure to large energy heavy ions and fluences.

6.5 Investigations of emerging memories exposed to heavy ions

On a greater, more general picture, some common but also differing effects occurring in hafnium oxide- and Ge-Sb-Te-based memory materials and electronics after ion exposure were revealed (as presented in sections 6.1 – 6.4).

In HfO_x-based materials and devices, no matter if serving as a dielectric, resistive switching or ferroelectric layer, two main influences on the characteristics are of great relevance: 1) induced defects and 2) induced phase transitions. Heavy ion irradiation induces defective tracks with defects in oxides, as preferentially oxygen vacancies. This can have a crucial impact on the materials properties. With increasing fluence, an increased number of defects is created. Especially resistive switching in oxide-based RRAM devices, where a conductive filament composed of oxygen vacancies is created and ruptured, is dependent on the number, distribution and movement of oxygen defects. Defect-induced phase transitions e.g., in hafnium oxide occur, if a specific electronic energy loss threshold is exceeded and at the same time the number of impacting ions is sufficient to achieve defective track overlapping,[11] which is the case for fluences around 10^{12} ions/cm^2.

In highly crystalline HfO_2 films, a defect-induced crystalline-to-crystalline phase transition from the monoclinic to a potentially rhombohedral phase accompanied by a significant grain fragmentation occurring in the high fluence regime was revealed by combining conventional methods such as XRD probing a macroscopic volume with high spacial resolution (S)TEM analysis. The study further underlines the drastic changes in the microscopic structure and induced phase transitions of the active materials. Especially in HfO_2-based ferroelectric memories, investigations of the crystal structure are of high importance, as ferroelectrics rely on a good crystalline quality. Additionally, the composition of the active layer has a direct effect on the ferroelectric properties of devices.

For Ge-Sb-Te-based phase-change materials, a quite similar conclusions can be drawn. Similar to ferroelectrics, their functionality relies on crystallinity (changes) and phase stability. The processes are not dominated by oxygen vacancies (in contrast to HfO_x-based materials) but by bond-breaking and bond-(re)creation, which is directly related to changes of the ordered or disordered state. Properties and ion irradiation-induced phase transitions strongly depend on the initial crystallinity and composition of the active layers. Changes can vary significantly and are found to be present within a larger fluence range when compared to results from experiments on HfO_x-based layers.

A good comparison of all memories can be done by comparing XRD patterns, which are showing different (but connected) beam-induced phase transitions. An overview of exemplary stacks and corresponding XRD patterns that serves as a summary for the observed phase changes as described in sections 6.1 – 6.4 is given in Figure 6-29.

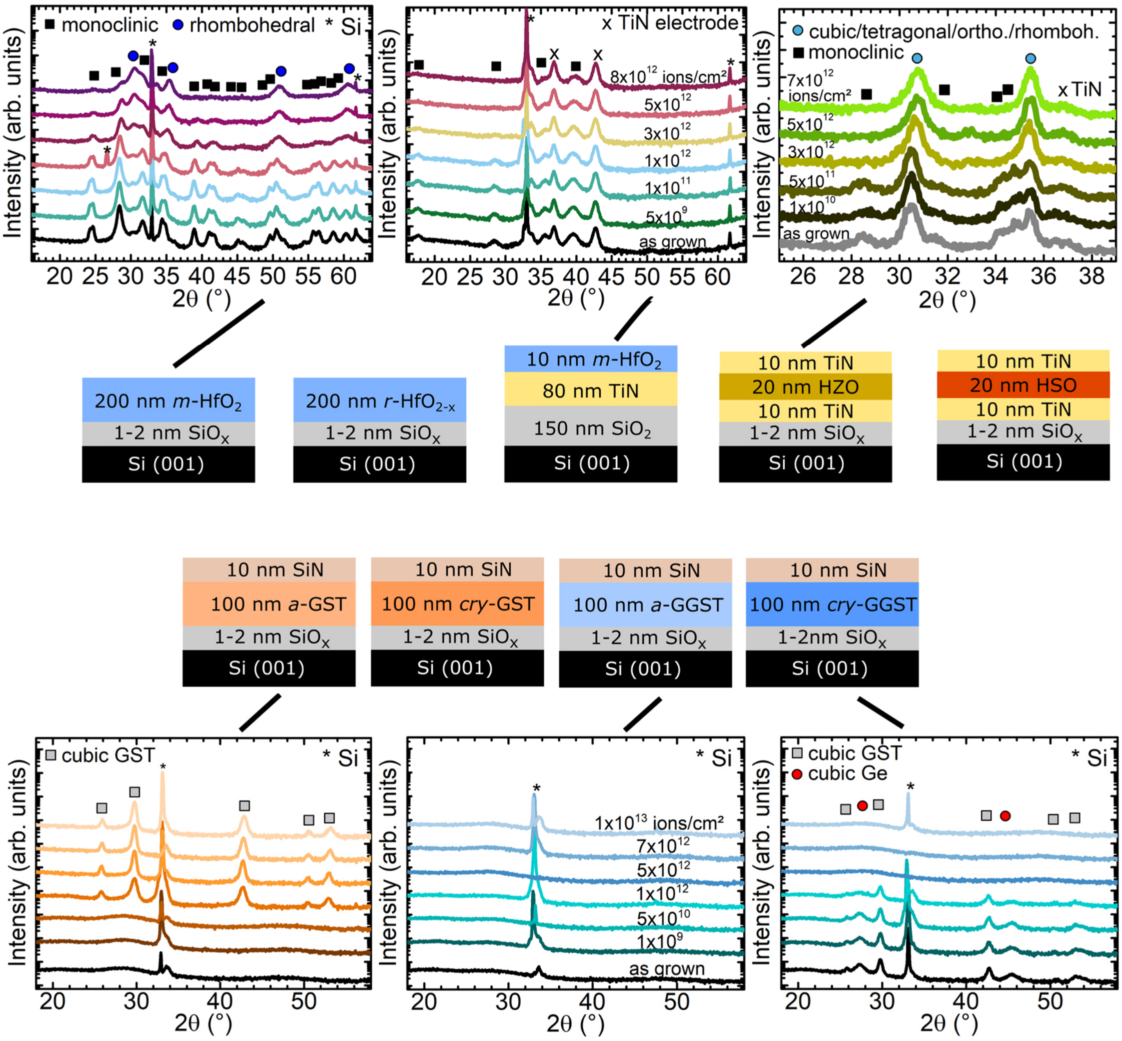

Figure 6-29: Schematic overview of HfO_2-, HfO_x-, Zr-doped HfO_2 (HZO)-, Si-doped HfO_2 (HSO)-, $Ge_2Sb_2Te_5$ (GST)-based and Ge-rich GST-based sample series. Representative XRD patterns of samples exposed to heavy ions are given, showing different structural changes. Note that these are only a few examples.

Overall, the Au heavy ion irradiation experiments have revealed that for all presented material systems the irradiation effects strongly depend on the initial crystallinity/crystal structure and composition of the active layers. Therefore, a combination of XRD, STEM and electrical investigations is highly adviced to overall obtain a clear picture in irradiated stacks as part of a general roadmap when interpreting irradiation data. This is not only of interest for the given case of high-energy heavy ions at high fluence, but also for other lighter ions or protons of lower energy and fluence. (Similar) irradiation-induced phase transitions accompanied by variations of physical or electrical properties can still occur but those are based on different mechanisms.

7 Conclusion and Outlook

In this work, relevant influences on the switching characteristics of three emerging memory types, in particular HfO_2-based resistive and ferroelectric memories as well as Germanium-Antimony-Tellurium (Ge-Sb-Te)-based phase-change memories and their response to heavy ion irradiation were investigated.

First, different influences such as doping, the electrode choice and the oxide layer thickness on the properties of hafnium oxide-based films and devices relevant for potential ferroelectric and resistive switching applications were addressed. Therefore, specifically designed HfO_x-based model systems were investigated. Second, heavy ion irradiation-induced effects on material characteristics with a focus on phase transitions as well as electrical switching properties of emerging memories were studied. The most important findings of this work are summarized in the following and an outlook for some attractive future studies is given.

7.1 Summary of the conducted studies

Synthesis of mixed $Hf_xZr_{1-x}O_2$ thin films and electrical properties of $Hf_{0.5}Zr_{0.5}O_2$-based devices: A co-evaporation process yielding $Hf_xZr_{1-x}O_2$ films was successfully established using a reactive molecular beam epitaxy deposition system. This routine is based on the simultaneous evaporation of material from a Hf and a Zr metal source using electron beams and a direct oxidation via a provided oxygen plasma. $Hf_xZr_{1-x}O_2$ thin films of 11 different compositions were grown in a controllable manner on *c*-cut Sapphire substrates. The good control of the composition and layer thickness was validated by XPS and XRR investigations, respectively. As the potentially most-promising compound for ferroelectric applications in BEOL integration is $Hf_{0.5}Zr_{0.5}O_2$ (HZO), the established $Hf_xZr_{1-x}O_2$ growth recipe was used to grow HZO films on a TiN bottom electrode and the layer was capped with an additional TiN or Pt top electrode. Post-deposition annealing studies of TiN/HZO/TiN stacks were performed, aiming a polar orthorhombic phase of the HZO-films and therefore measurable ferroelectric properties. However, all devices were found to be leaky in voltage-dependent electric polarization measurements and repeatable resistive switching was found to be not possible. These observations could be attributed to different potentially interconnected phenomena such as a formation of a non-stoichiometric and poorly conducting TiO_xN_y or insufficient post-deposition annealing and quenching steps.

Resistive switching in HfO_2-based TCM and ECM devices: To address possible influences on the resistive switching behavior of HfO_2-based devices, three different switching studies were conducted, focusing on the influences of crystallinity and doping, the electrode choice as well as the oxide layer thickness on the switching behavior.

- Devices of four different stacks containing monoclinic and amorphous HfO_2- and HZO-switching layers sandwiched between two Pt electrodes (Pt/HfO_2 or HZO/Pt) were found to be switchable with a non-polar behavior, which was attributed to a dominant thermochemical mechanism in devices with two chemically inert electrodes (TCM). A clear influence of the Zr-content on the switching behavior was not observed. The most important result of this study is that the growth of amorphous HZO at room temperature leads to a good layer quality and switchable memory devices could be prepared. Therefore, the high leakage and inhibited switching obtained in annealed TiN/HZO/TiN devices of the previous study are most likely not directly caused by the growth conditions of the HZO films.

- As the choice of the electrode can significantly affect the switching behavior of devices by determining the dominating switching mechanism, the resistive switching properties of HfO_2-based devices with a Pt top electrode and with a Cu top electrode were compared (Pt/HfO_2/Pt versus Cu/HfO_2/Pt). Two different dominating switching mechanisms were found i.e. a thermochemical mechanism in Pt/HfO_2/Pt (TCM) versus an electrochemical mechanism in Cu/HfO_2/Pt (ECM) devices, which is further depending on the switching mode. Most stable switching was found for URS for Pt/HfO_2/Pt (negative operation voltages) and BRS in Cu/HfO_2/Pt (positive forming/set and negative reset voltages). Additionally, the potential appearance of threshold resistive switching (TRS) was investigated. However, TRS was not observed for the tested devices, which could be related to occurring current overshoots during forming/set.
- A resistive switching study focusing on the influence of the oxide layer thickness in Cu/HfO_2/Pt ECM devices was conducted, revealing a transition from a gradual to a more abrupt reset occurring with increasing HfO_2 layer thickness. A qualitative model was developed for the underlying switching mechanism, which includes a strongly Joule heating-assisted resistive switching in ECM devices with thicker HfO_2 layers and an electric field-dominated switching in devices with thinner layers. Additionally, an oxide layer thickness-dependency of the conduction mechanisms was found, where devices containing thicker films show an ohmic conduction, while devices containing thinner films show SCLC conduction by injected electrons at increasing electric field in the set process. The obtained changing of the device properties dependent on the oxide layer thickness is considered an interesting finding for the community, as further downscaling of electronic components is of huge interest for emerging memory applications.

Overall, the designed studies on HfO_2-based model systems show a dependence of the switching characteristics of resistive switching devices on the choice of the electrodes and on the oxide layer thickness. Additionally, a growth routine was developed for Zr-doped HfO_2 films for potential ferroelectric applications. A precise control of the layer composition of the $Hf_xZr_{1-x}O_2$ films was achieved.

Heavy ion irradiation-induced phase transitions in HfO_x films: Stoichiometric and oxygen-deficient HfO_x full-sheet layers were exposed to high-energy Au heavy ions for investigations of the beam-induced phase transitions occurring in hafnium oxide.

- In HfO_2 films, a defect-based phase transition from the monoclinic to a rhombohedral phase was found. This conclusion was possible due to a comparison of XRD results of irradiated films to XRD and XPS results obtained from non-irradiated, oxygen-engineered HfO_x films of different stoichiometry ranging from HfO_2 to $HfO_{1.1}$, for which a strikingly similar phase transition was found with decreasing oxygen content. The irradiation-induced transition is fluence-dependent, starting in the region where significant defective track overlapping occurs. This result is in accordance to literature descriptions, where the phase transition mechanism in hafnium oxide powders was described as a double impact mechanism.[11] A first ion impact likely leads to the creation of a defective volume with introduced oxygen vacancies, while a second impact of this volume leads to a transformation of the phase along the ion trajectory. The transition only occurs if a threshold for the electronic energy loss of about 18 keV/nm is exceeded. This condition is fulfilled for the irradiated films, where 1.635 GeV Au ions lead to an electronic energy loss of about 53 keV/nm in the HfO_2 layers. In contrast to literature, where a tetragonal phase was found in powders after ion exposure[11], the occurring phase in HfO_x films can be attributed to the rhombohedral structure. However, it should be mentioned that a clear distinction of the different known hafnium oxide phases with a very similar crystal structures such as the tetragonal, rhombohedral or cubic phases by XRD remains challenging, especially for irradiated films showing a broadening of reflections with an increased number of induced defects at higher fluences. All these phases are structurally closely related, as the tetragonal or rhombohedral structures of hafnium oxide are slightly distorted variants of the cubic structure.

- By combining XRD analysis with STEM methods with a high special resolution, more details on the phase transition could be revealed. First, the crystalline-to-crystalline phase transition in HfO_2 films was confirmed by the results of a developed pattern matching routine performed on a recorded SPED dataset.[326] Second, the phase transition was revealed to be accompanied by a significant grain fragmentation in HfO_2 films exposed to 5×10^{12} ions/cm². With this information, the observed reduction of reflection intensities of the monoclinic phase after ion exposure in the XRD patterns of thin films could be explained by the obtained grain fragmentation and is not a result of an amorphization of the material.
- For as grown, oxygen-deficient rhombohedral hafnium oxide films exposed to heavy ions, a decrease of the out-of-plane lattice constant with increasing irradiation fluence is found from XRD investigations. This is likely related to an increase of induced defects in the form of oxygen vacancies.

Connection of heavy ion irradiation-induced phase transitions and electrical properties of HfO_2-based OxRAM, doped HfO_2-based ferroelectric capacitors for FeRAM applications as well as Ge-Sb-Te-based PCRAM: The obtained phase transition in HfO_2 can be correlated to results obtained from OxRAM characterization. Similarly, induced phase transitions in doped HfO_2-based ferroelectric layers and in Ge-Sb-Te-based phase-change layers can further be related to the obtained electrical performance of the respective emerging memories.

- For OxRAM exposed to high-energy heavy ions, a remarkable radiation-hardness was found. The investigated 1T1R arrays show stable switching with two distinct memory states up to fluences of 5×10^{10} ions/cm². At higher fluences, the access transistor is affected by the heavy ions. After an exposure to 1×10^{12} ions/cm², a reduced switching performance is overall found, however, the functionality of 1R memory cells is still preserved. At this fluence, already about 50 % of the device area can be impacted by defective tracks. The induced defects seem to be not yet detrimental for the memory cell functionality, however, the defect-induced phase transition in HfO_2 becomes more probable with increasing fluence. Thus, more unfavorable effects, like the formation of a conductive oxide layer can be expected for larger fluences.
- In Zr- and Si-doped ferroelectric stacks, an irradiation-induced phase transition at fluences above 1×10^{12} ions/cm² from the polar orthorhombic to likely a non-polar cubic or

tetragonal phase is found, which was determined based on a combination of an XRD study with electrical measurements. The transition to an electrically conducting rhombohedral phase is not likely, as ferroelectric properties could be measured after irradiation, which is only possible for insulators. While the remanent polarization of ferroelectric capacitors was found to be decreasing with increased fluences, a partial recovery was achieved through post-cycling of the devices after irradiation. This could be explained by an electric field-induced transformation of the non-polar phase back to the polar phase. The irradiation-induced phase transition in pure HfO_2 was found to be accompanied by grain fragmentation, which is probably similar for doped HfO_2 films. As this fragmentation is not reversible during cycling, the remanent polarization of ferroelectric devices exposed to high fluences could not be fully-recovered. However, the tested devices were found to be functional even after the exposure to 2.4×10^{12} ions/cm^2, revealing an excellent radiation-hardness of ferroelectric capacitors in the electronic energy loss regime.

- For Ge-Sb-Te-based phase-change materials, phase changes obtained from XRD investigations on GST- and Ge-rich GST-based layers could be explained by the effects of bond-breaking and bond-formation occurring due to local temperature spikes, where the dominating effect determines the resulting crystallinity of the active layers after irradiation. The dominating effect was found to be strongly depend on the initial crystallinity and composition of the layers. While in amorphous GST films, bond-formation was found to be dominant, which leads to a crystallization of the layer, the amorphous state in GGST films was found to be extremely stable. In contrast, bond-breaking was dominant in crystalline GGST films, while GST films were revealed to be less affected. These effects could be directly related to the physical properties such as thermal conductivity of the phase-change materials, where especially the high-stability of the amorphous phase of GGST is outstanding. The beam-induced phase transitions were again directly connected to the stability of the resistive memory devices. Obtained PCRAM devices were overall found to be radiation-hard, withstanding the exposure to at least 5×10^{10} ions/cm^2. However, GGST-based PCRAM devices were found to be more stable than GST-based devices, which could be directly related to a starting phase transition from the amorphous to the crystalline phase in GST. The reduced switching performance of the 1T1R arrays at higher fluences was attributed to the affected access transistors, which is similar to tested OxRAM arrays.

Overall, from the obtained ion-irradiation induced phase transitions occurring in the electronic energy loss regime, an improved understanding of the basic mechanisms could be reached. This was achieved by combining different characterization methods such as XRD, XRR, XPS and electrical characterizations as well as different STEM methods. All three tested emerging memory types were found to be extremely radiation-hard, withstanding the impact of at least 5×10^{10} Au ions/cm^2 with an energy of 1.635 GeV. The identified high radiation-resilience of the tested emerging memories enables a use in radiation-intensive environments.

Moreover, combining the resources of different research groups has led to a fruitful cooperation with the partners from CEA-Leti, LTM CNRS, Fraunhofer IPMS CNT and the Advanced Electron Microscopy group of Prof. Leopoldo Molina-Luna at TU Darmstadt, where several joint scientific works could be published.[63, 64, 131, 281, 293, 326, 354] A full list of publications and conference contributions is given at the end of this work (dissemination).

7.2 Future studies

Resistive switching in oxide-based devices: In general, memristors based on hafnium oxide are promising candidates for future memory applications replacing or supplementing existing memory technologies. However, further investigations of the switching properties are required to better understand the memory functionality and to improve the resistive switching characteristics. This is of particular interest for ECM devices showing a non-volatile switching behavior usable for memory applications but also potentially a volatile behavior (threshold switching) that can be used to create working selectors, which can replace transistors in arrays. This becomes relevant in particular for integrated devices in 3D, where sneak path currents have to be avoided. As the true nature for the occurrence of TRS in ECM devices is not known yet, additional studies are required.

Investigations on specifically designed model systems such as Cu/HfO_2/Pt but also Ag/HfO_2/Pt single capacitor devices can help to gain a better understanding of the occurring switching processes. Doping of the HfO_2-layers by Cu or Ag, respectively, can help to achieve a better switching uniformity. As TRS seems to be influenced by the presence of oxygen vacancies in the oxide layer[53, 224], it is of particular interest to study the dependence of the switching behavior of the ECM devices on the oxygen content of switching layer. A precise modification of the oxygen content can be achieved via electron beam evaporation of Hf from a metal source and *in situ* oxidation utilizing an oxygen plasma in the reactive molecular beam epitaxy setup used in this work. To prevent oxidation of substoichiometric hafnium oxide films, the stacks have to be *in situ*-capped. For a successful device preparation, ion beam etching can be used, considering the preparation workflows described in this work. For future investigations and to take a step towards real applications, crosspoint structures and further on crossbar structures have to be created. This includes the usage of access transistors or the development of selectors. Furthermore, when moving away from model systems for real applications, e.g., Pt electrodes should be replaced by a CMOS-compatible material such as TiN.

Currently, extensive research activities are found in the field of neuromorphic computing, which can be seen from a rapidly increasing number of publications and conference contributions. In principle, different emerging memory types such as redox-based, ferroelectric and phase-change memories were recently demonstrated to be suitable for such applications. Especially oxide-based resistive switching devices show very promising characteristics such as an analog (gradual)[59, 81] switching, which is potentially useable for multibit operations and neuromorphic applications. Synaptic plasticity as found in the human brain can be emulated in resistive switching devices by applying different voltage pulses. This paves the way towards future artificial intelligence, which represents a huge field of interest.

Heavy ion irradiation experiments: The cooperation with the Advanced Electron Microscopy Group of TU Darmstadt has led to the development of a pattern matching routine usable for SPED datasets of as grown and irradiated HfO_2 films. More information on the workflow of integrating a 4D-STEM SPED data set were published in the open repository TUdatalib, including the raw data.[326] This pattern matching routine was already successfully applied to data obtained from as grown 20 nm thin oxygen-deficient $HfO_{1.7}$ films and can be in principle applied to other datasets. Furthermore, an improvement of the established routine is striven, implementing e.g., the (calculated) structure of the rhombohedral phase found in hafnium oxide.[128]

The results obtained from the various heavy ion irradiation experiments conducted in the frame of the project WAKeMeUP together with the cooperation partners CEA-Leti, LTM CNRS and Fraunhofer IPMS CNT led to the planning of further irradiation experiments. For this, a beam time proposal was written. The granted beam time is part of the currently running project called StorAIge. More information on the projects are given in the dissemination part at the end of this work. The planned new experiments include the irradiation and investigation of more complex ferroelectric circuits than the reported capacitor stacks as well as phase-change memory-based ovonic threshold switches to compare the behavior to the obtained damaged access transistor circuitry of 1T1R arrays in this study. As OTS can potentially be used to replace transistors in circuits, the radiation-resilience of these comparably new material systems has to be tested. More than 200 samples were recently prepared by the project partners and were irradiated at the GSI Helmholtzzentrum für Schwerionenforschung in Darmstadt.

For additional studies, the irradiation of oxygen-deficient amorphous hafnium oxide films with regards to a potentially induced phase transition is of interest, including extensive structural investigations. This is believed to give additional information on the nature of the obtained phase transitions in oxygen-deficient crystalline films. Furthermore, the investigation of stoichiometric m-HfO_2- as well as oxygen-deficient r-HfO_x-containing (*in situ*-capped) devices exposed to high fluences could be interesting to test their memory functionality and to connect the results to the described induced phase transition in HfO_x. Electrical on-line measurements with high-energy single ions of programmed arrays could be an addition.

Appendix

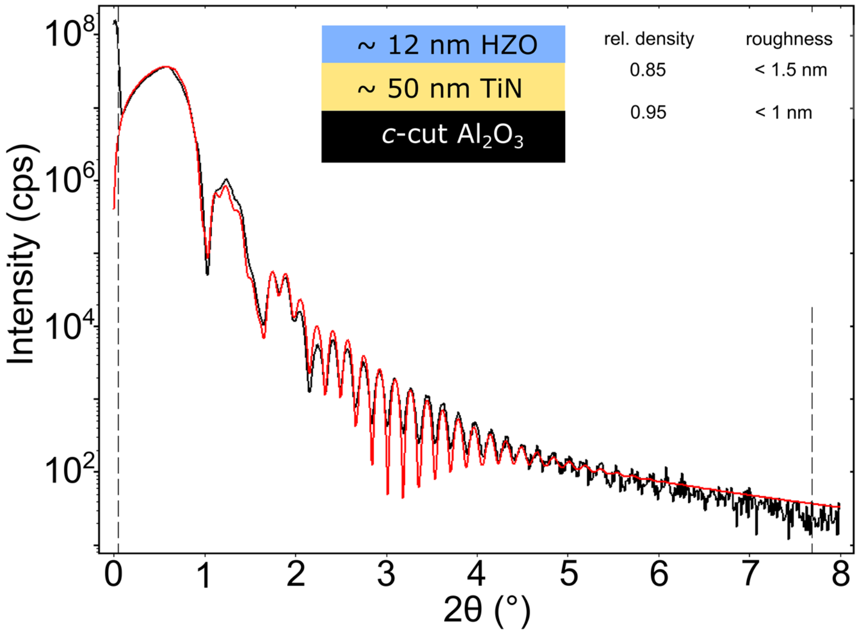

Appendix Figure 1: XRR pattern and corresponding RCRefSim[305] software fit of a HZO/TiN/*c*-cut Sapphire sample. Values of the relative density and roughness of the layers is given additionally. Note that HZO films were found to have a slightly lowered density compared to pure HfO_2 films[125].

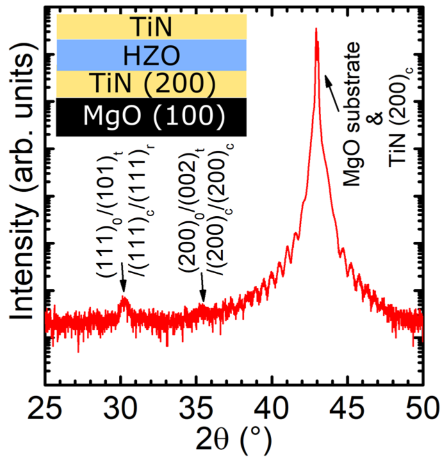

Appendix Figure 2: XRD pattern of a post-annealed TiN/HZO/TiN stack. The HZO film grown on a (002)-oriented MgO substrates plus (200)-TiN bottom electrode with potentially orthorhombic reflections. The good quality of the bottom electrode is indicated by the present Laue oscillations visible around the merged MgO (002) substrate and TiN (002) reflections.

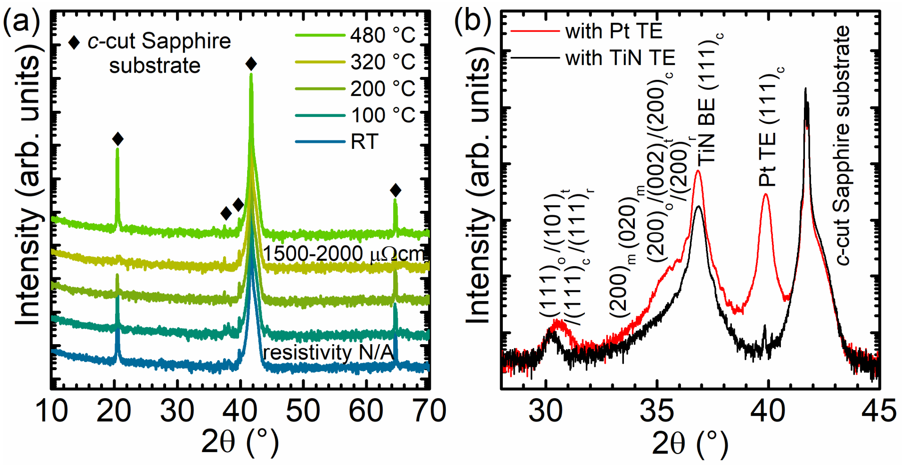

Appendix Figure 3: (a) XRD patterns of sputtered TiN films on c-cut Sapphire substrates with a corresponding resistivity value. N/A labels a non-detectable too high resistivity for the measurement setup. Room temperature resistivity measurements were performed in van der Pauw geometry (eliminating contact resistances). Therefore, Au patches were sputtered through a shadow mask on the corners of the TiN surface (compare[145]). (b) XRD pattern of a post-deposition annealed Pt/HZO/TiN stack in comparison to a pattern obtained from a post-deposition annealed TiN/HZO/TiN stack. For both HZO layers, a characteristic reflection at around $2\theta = 30°$ is visible, still the reflection of the HZO layer in the Pt TE stack is found at slightly larger angles. Additionally, the potential $(200)_o$ reflection is more pronounced.

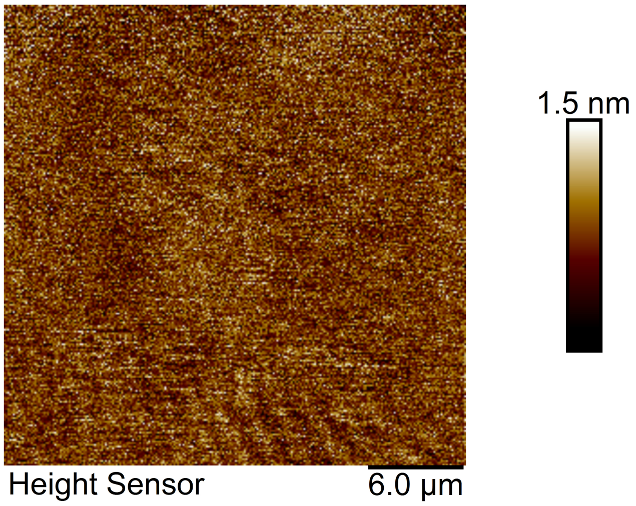

Appendix Figure 4: Exemplary AFM topography image of a Pt film on *c*-cut Sapphire showing a low roughness of the sputtered Pt layer. The image was taken with a Bruker Icon atomic force microscope (Bruker, Billerica, MA, USA) in amplitude modulation (tapping) mode. The setpoint-amplitude to free-amplitude ratio was set between 45 % and 55 % and a cantilever of the type RFESP-75 provided by Bruker was used (nominal force constant: 3 N/m, nominal resonance frequency: 75 kHz).

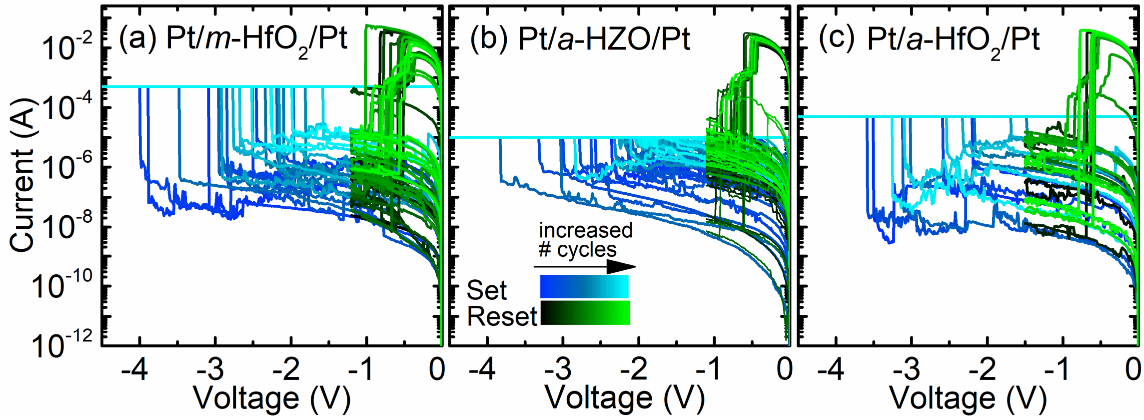

Appendix Figure 5: Current-voltage curves for URS of (a) *m*-HfO_2-, (b) *a*-HZO- and (c) *a*-HfO_2-containing stacks. The color coding from dark to bright (blue/green) indicates the increased number of cycles. Not that in this study, the current compliance used for the set varies. No direct influences on the reset voltages or LRS currents are found.

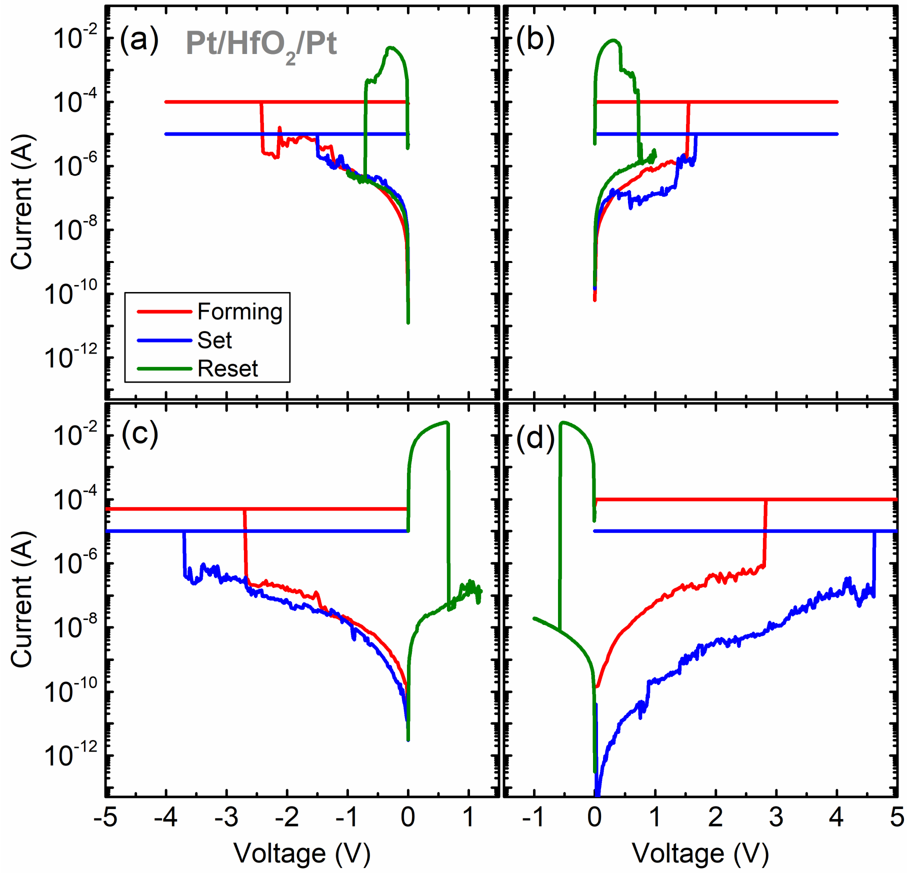

Appendix Figure 6: Exemplary current-voltage curves of Pt/HfO_2/Pt devices revealing possible switching under (a) negative forming/set & negative reset, (b) positive forming/set & positive reset, (c) negative forming/set & positive reset and (d) positive forming/set & negative reset.

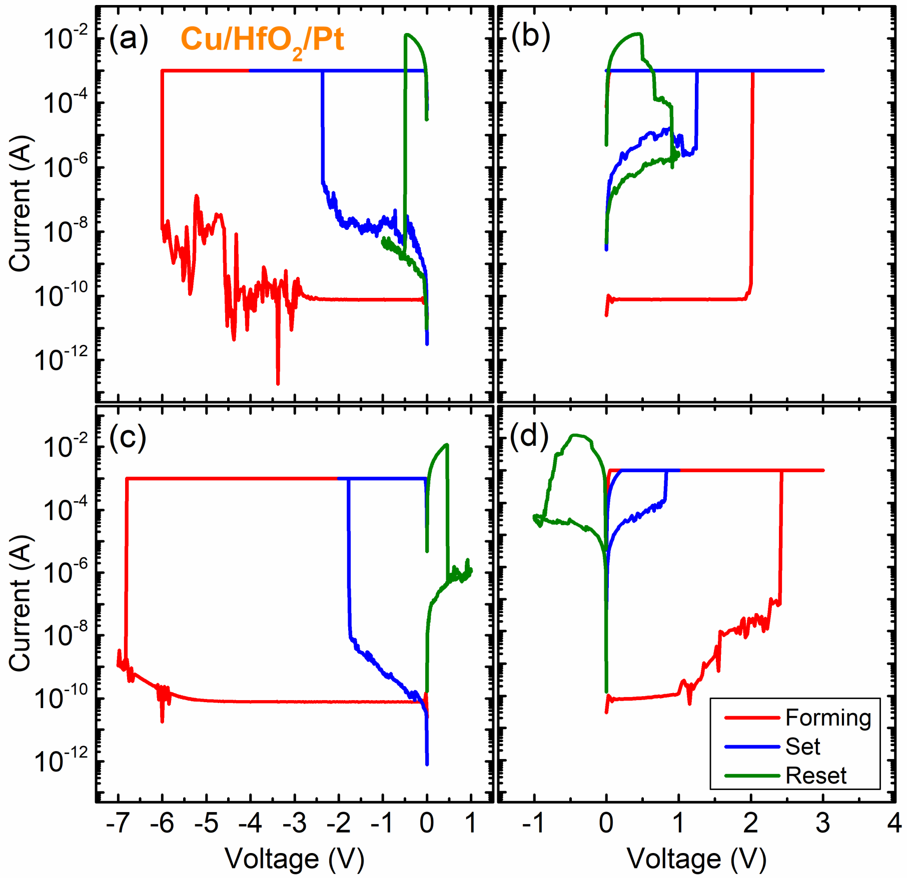

Appendix Figure 7: Exemplary current-voltage curves of Cu/HfO$_2$/Pt devices revealing possible switching under (a) negative forming/set & negative reset, (b) positive forming/set & positive reset, (c) negative forming/set & positive reset and (d) positive forming/set & negative reset.

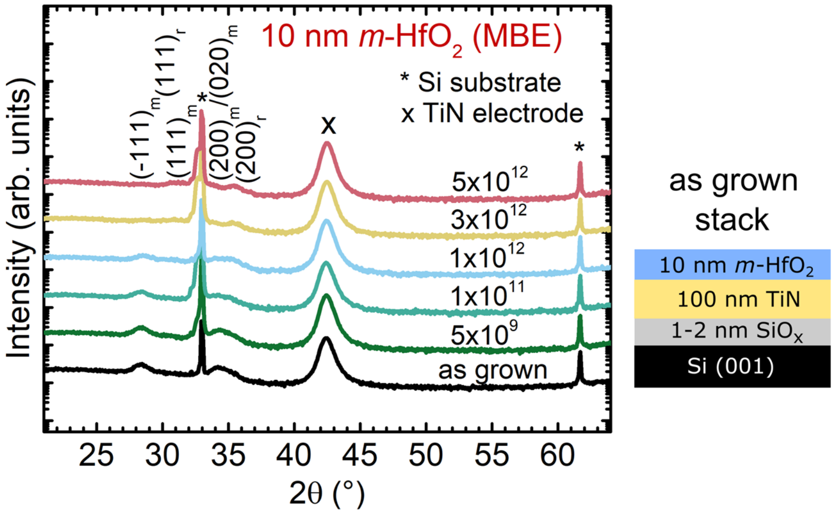

Appendix Figure 8: XRD patterns of as grown and irradiated 10 nm thin m-HfO$_2$ films grown on TiN/SiO$_x$/Si substrates. After irradiation with fluences above 1×10^{12} ions/cm², reflection intensities corresponding to the crystalline HfO$_2$ layer vanish.

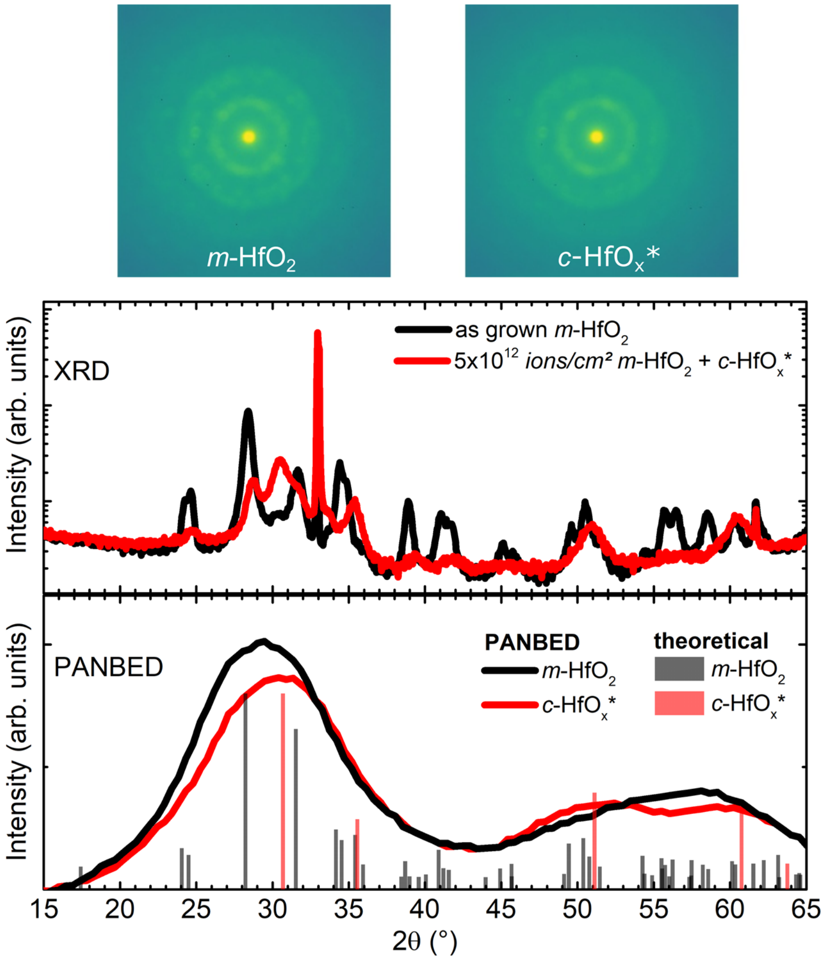

Appendix Figure 9: NBED patterns and XRD patterns of the 200 nm thick hafnium oxide films (as grown versus 5×10^{12} ions/cm²) with rotational averages of the position averaged nanobeam electron diffraction (PANBED) patterns from the m-HfO_2 and LTP c-HfO_x phases of the ACOM datasets. Simulated theoretical peak positions and intensities were deduced from VESTA. Classification of NBED patterns was performed by template matching. The monoclinic and cubic phase can clearly be separated, although the angular resolution is limited (electron probe convergence of 5 mrad). However, cubic or rhombohedral phase cannot be (easily) distinguished. *** Note that the routine was performed using a cubic structure of hafnium oxide (space group: ICDD 04-011-9018, a ≈ 5.06 Å) for the oxygen-deficient phase occurring in HfO_x, which is in accordance with the used pattern matching routine.** Figure partially reproduced with permission from[354], https://doi.org/10.1021/acsnano.2c04841; https://pubs.acs.org/doi/suppl/10.1021/acsnano.2c04841/suppl_file/nn2c04841_si_001.pdf (supporting information). The original publication is licensed under a Creative Commons Attribution 4.0 License (CCBY) and published by AIP Publishing.

List of Figures

Figure 1-1: (a) Schematic representation of the common von Neumann architecture. Blue arrows indicate the bus connections, while the red path shows the immediate data flow. (b) Representation of the von Neumann bottleneck. (c) Schematic of the currently established memory hierarchy. The width of the schematic pyramid indicates the storage capacity of the different memory (on each level). Increasing property trends are represented by arrows. Created using information from [7, 16, 19, 20]. 2

Figure 1-2: Emerging memory classification scheme including ferroelectric (red), magnetic (green) and phase change memories (yellow) as well as redox-based resistive memories (blue) as memory types. While this displays an overview of some important examples, a multiplicity of additional concepts exist which are here summarized as others (grey boxes). Additionally, the operation principle among different memory types can overlap (e.g., ferroelectric tunneling junctions are based on the resistance change but also using a ferroelectric layer). Created using information from [7, 20, 34, 37] 4

Figure 1-3: Schematic representation of switching mechanisms in FeRAM, MRAM, PCRAM and redox-based RRAM. (a) Ferroelectric switching relies of dipole moments (remanent electric polarization) in a ferroelectric material switched by an electric field. (b) In a magnetic tunnel junction (MTJ), the magnetization (direction) of a free layer can be switched by applying a magnetic field, leading to either a parallel or an anti-parallel orientation. (c) In phase-change memories, a chalcogenide material is switched between a crystalline and an amorphous phase by Joule heating induced by a current. (d) In redox-based resistive memories (filamentary) which are based on the movement of ions, a conductive filament composed of oxygen vacancies (oxygen-deficient/metal-rich region) or metal atoms is reversibly (re)formed and ruptured. Redrawn after[38]. * Ferroelectrics are also dielectrics/insulators. 4

Figure 2-1: Schematic representation of device stackings with an oxygen vacancy filament (bright blue) and a Cu filament (orange) and related changes during forming, reset and subsequent set on the example of bipolar resistive switching in a VCM Pt/HfO_2/TiN device. (a) A Pt/HfO_2/TiN stack with oxygen vacancy filament formed when a negative voltage is applied to the top electrode. This process is dominated by a valence change mechanism (for bipolar resistive switching), thus called VCM. (b) A Pt/HfO_2/Pt stack, where oxygen vacancy filament formation and rupturing is dominated by a thermochemical mechanism, thus called TCM. (c) A Cu conductive filament in a Cu/HfO_2/Pt ECM device. The process is dominated by an electrochemical mechanism. (d) Starting from a pristine state of the insulating HfO_2 layer, a forming step is required where an oxygen vacancy filament is stabilized in VCM. This filament can be ruptured in a reset process and (re-)stabilized in a subsequent set. In real devices, the filament in 3D is considered to have a diameter in the tenth of nanometer-range.[77] 13

Figure 2-2: Schematic representation of current-voltage (I-V) curves for (a) unipolar resistive switching – URS, (b) f8-bipolar resistive switching (BRS f8), (c) cf8-bipolar resistive switching (BRS cf8), (d) complementary resistive switching (CRS) and (e) threshold resistive switching (TRS). The set starting from the HRS is given in blue, while the reset starting from the LRS is given in red. cc marks the current compliance. Drawn with information from[75, 107]. 15

Figure 2-3: Exemplary crystal structures of the polymorphous hafnium oxide with Hf ions in gold (larger) and O ions in red (smaller). (a) monoclinic HfO_2, space group $P2_1/c$, (b) tetragonal HfO_2 – $P4_2/nmc$, (c) orthorhombic HfO_2 – *Pbca*, (d) orthorhombic HfO_2 – *Pnma*, (e) orthorhombic HfO_2 – $Pca2_1$ (ferroelectric, mostly doped HfO_2), (f) cubic HfO_2 $Fm3m$, (g) oxygen-deficient rhombohedral $HfO_{1.5}$ – $R3m$. Created using VESTA[129], with information from ICDD PDFs ($P2_1/c$, $P4_2/nmc$, *Pbca*, *Pnma*, Fm-$3m$) and density functional theory (DFT) calculations ($Pca2_1$ [130, 131], $R3m$[128]) 18

Figure 2-4: (a) PZT cell with two distinct polarization states originating from the displacement of the center ion from the unit cell center. (b) Exemplary electric field-dependent electric polarization loop with remanent polarization P_r, saturation polarization P_s and coercive field E_c. Additionally, the achievable distinct remanent polarization states are represented by the minima of the Helmholtz Free Energy F and the moving green ball. (c) Representation of the $Pca2_1$ orthorhombic crystal structure of ferroelectric hafnium oxide. Created with information from[3, 7]. 25

Figure 2-5: A 1T (FeFET) with the ferroelectric capacitor integrated in the gate stack, and a 1T1C memory cell with the ferroelectric capacitor connected to the drain of a FET. Redrawn after[7]. The insulator is a non-ferroelectric dielectric material, like SiO_2. Metal electrodes are presented in yellow. An n-type metal-oxide-semiconductor field-effect transistor (n-type MOSFET or NMOS) is represented in grey and black (n+/p/n+ with a conductive channel). 27

Figure 2-6: (a) Schematic of a mushroom cell, where the programmable region of a phase-change material is changing between the crystalline and amorphous phase, and a schematic time-dependent temperature profile for set, reset and readout operation with corresponding phase changes indicated. T_{melt} = melting temperature, T_{cryst} = crystallization temperature as labeled. Figure reproduced with permission from T. Schenk *et al.*[7], https://doi.org/10.1088/1361-6633/ab8f86; (b) Ternary diagram for Ge-Sb-Te materials for phase-change applications with $Ge_2Sb_2Te_5$ (GST225) and Ge-rich GST (GGST) labeled. Note, that this is an example and not representative for the multitude of different compounds published 29

Figure 2-7: (a) Schematic of a typical 2D array with reading current (blue path) and sneak current (red path). (b) Schematic of a 3D 1S1R array (shared bit line). (a) and (b) reproduced with permission from Seok *et al.*[220], https://doi.org/10.1002/adfm.201303520, © 2014 WILEY-VCH. (c)-(f) 1S-1R device configuration consisting of a $Pd/Ta_2O_5/TaO_x/Pd$ memristor and a $Pd/Ag/HfO_x/Ag/Pd$ selector with corresponding current-voltage characteristics. (c) Scanning electron microscopy image of the selector and memristor (top view, left) and transmission electron microscopy image of the cross section (right). b) Bidirectional threshold switching (cycling) of a $Pd/Ag/HfO_x/Ag/Pd$ selector. c) Repeatable bipolar memristive switching of a $Pd/Ta_2O_5/TaO_x/Pd$ memristor. d) Current-voltage (combined) characteristics of the vertically integrated 1S and 1R cells. Reproduced with permission from Midya *et al.*[112], https://doi.org/10.1002/adma.201604457, © 2017 WILEY-VCH. 31

Figure 3-1: Schematic representation of the nuclear and electronic energy loss in dependence of the specific energy of the projectile in a double log presentation (left). Defect formation at low specific energies is dominated by nuclear energy loss, while at higher energies, the electronic energy loss leads to complex defects and track formation. Redrawn after[231]. . 34

Figure 3-2: Schematic representation of the energy loss dE/dx in dependence of the path length (Bragg curve). Most energy is deposited before the ion stops. The ion range is defined as the integral of the reciprocal energy loss $(dE/dx)^{-1}$ over the full ion energy. Heavy ions with the same specific energy have a similar ion range in the same target material. Redrawn after[241]. 36

Figure 4-1: Schematic of the reactive molecular beam epitaxy setup used in this work with load lock chamber, UHV growth chamber, corresponding pumping systems (backing and turbo pump), manipulator with substrate and shutter, RHEED system, QCM sensors as well as electron guns, crucibles and radical sources). Figure from Buckow *et al.*[283], http://dx.doi.org/10.1088/0953-2048/26/1/015014. © IOP Publishing. Reproduced with permission. All rights reserved. 42

Figure 4-2: Schematic growth and related processes occurring and schematic representation of the Frank-Van der Merwe, Volmer-Weber and Stranski-Krastanov growth modes. Redrawn with information from[288, 289]. 44

Figure 4-3: (a) Schematic representation of different electron scattering geometries and crystalline structures of films (left) with representation of the Ewald sphere construction (middle) and RHEED diffraction patterns (right). Figure taken from Tang *et al.* [290], http://dx.doi.org/10.1088/0022-3727/40/23/R01; © IOP Publishing. Reproduced with permission. All rights reserved. (b)-(e) Exemplary RHEED patterns of (b) a crystalline (cubic) TiN film with a flat surface grown on *c*-cut Sapphire, (c) a crystalline *m*-HfO_2 film on TiN/*c*-cut Sapphire (island growth), (d) an amorphous HZO film (only blurred rings), (e) a *c*-cut Sapphire single crystalline substrate with an atomically flat surface. 44

Figure 4-4: (a) Cu (orange) and Hf (grey) source with a Cu and Hf pellet. Those pellets are molten inside the crucible utilizing the electron beam to create the respective source. (b) Glued one, two and four TiN/SiO_2/Si 5x5 mm^2 pieces as substrates on substrate holders. (c) from left to right: Backside contacts of a gold QCM, clean front side, and front side of a QCM covered with Hf. As a size reference, a 50 Cent coin is shown in images. 45

Figure 4-5: Schematic representation of applied stack preparation possibilities used. The two workflows are named “with IBE” and “without IBE”. Both yield the same stacking with $30\ \mu m \times 30\ \mu m$ patches (device area). Additionally, an exemplary microscopic top view of the sample surface with four devices is shown. 52

Figure 4-6: Schematic representation of the UNILAC at GSI in Darmstadt. Ions from one of the ion sources are pre-accelerated in the high current injector. At the gas stripper, the charge state of the ions is increased and then the ions are further accelerated in a four-tank Alvarez structure. The beam can be delivered to different experimental stations in the UNILAC hall or injected into the heavy ion synchrotron SIS 18. Figure adjusted from GSI website, where additional information can be found.[298] 54

Figure 4-7: (a) Geometric visualization of Bragg’s law with the incident beam being diffracted at the layers of atoms in the angle θ, depending on the distance of the lattice planes d and the wavelength λ. (b) Schematic arrangement of the parallel beam four-axis goniometer setup and the optical path with corresponding variable axis with angles θ, ω, χ (tilting), Φ (sample rotation). 57

Figure 4-8: Exemplary XRD patterns of polycrystalline powders simulated using VESTA[129], with information from ICDD PDF and corresponding crystallographic information files (for $P2_1/c$, $P4_2/nmc$, *Pbca*, *Pnma* and *Fm*3*m*) and DFT calculations (for $Pca2_1$ [130, 131] and *R*3*m*[128]). The lattice parameters and simulated pattern of the *r*-$HfO_{1.5}$ phase is very close to those obtained from experimental data[128]. The most-relevant reflections for the discussions in this work are indexed. 59

Figure 4-9: Four-sample stage with four exemplary 5×5 mm² samples placed at the positions 1-4. This stage is then mounted to the XRD setup. The distance between the samples is necessary to prevent interference from unwanted scattered X-rays from neighbouring samples. 61

Figure 4-10: Exemplary XRR pattern with information like density, film thickness and surface roughness obtained from critical angle, slope and oscillations. Figure drawn from experimental data of a HfO_2 film grown on TiN/*c*-cut Sapphire. Labeled with information from[304]. 62

Figure 4-11: (a) Energy scheme of the emission of a photoelectron (red) with energy relations of sample to spectrometer work function. (b) Exemplary XPS survey of a 14 nm thick $Hf_{0.5}Zr_{0.5}O_2$ film that was grown on *c*-cut Sapphire with most important lines labeled. 63

Figure 4-12: Schematic setup of a TEM (left) and a STEM (right) with electron beam paths. Redrawn using information from literature[313-315]. Note that these are simplified representations (without a two-part objective lens drawn for TEM; without a first crossover drawn). Additionally, a schematic representation of different STEM annular detectors used for image recognition in different modes (BF, ABF and HAADF), dependent on the angular range of the (diffracted) electron beam. 66

Figure 4-13: (a) Keithley measurement setup with a contacted device and a part of the top electrode tip visible on the monitor screen, (b) Schematic setup of a contacted device to RPMs and SMUs (and potentially usable PMUs). The arrows represent contact tips. 70

Figure 5-1: (a) Schematic of the stacks containing $Hf_xZr_{1-x}O_2$ films on *c*-cut Sapphire. (b) Exemplary XPS spectra and fits of the Hf4f and Zr3d lines corresponding to the $Hf_{0.5}Zr_{0.5}O_2$ film. A Shirley-type background was subtracted. (c) XRR patterns of the $Hf_xZr_{1-x}O_2$ films of different composition grown on *c*-cut Sapphire. Note that the given compositions are the measured (XPS) compositions, while HfO_2 and ZrO_2 act as references. (d) XRD patterns of the $Hf_xZr_{1-x}O_2$ polycrystalline films of different composition grown on *c*-cut Sapphire, crystallizing in a monoclinic (indexed in black) and potentially tetragonal structure (indexed in red). Note that an orthorhombic, cubic or rhombohedral structure is also possible. The increased background ("broader bump") between 30° and 38° stems most likely from an interface effect between *c*-cut Sapphire substrate and $Hf_xZr_{1-x}O_2$ film due to for example the possible formation of nano-crystallites. This result is comparable to literature reports on pure HfO_x films grown on c-cut Sapphire.[145] 77

Figure 5-2: Schematic representation of the TiN/HZO/TiN stacks prepared and investigated, (b) XRD patterns of as grown (red) and post-deposition annealed (green; 600 °C for 20 s) TiN/HZO/TiN stacks of polycrystalline nature. 79

Figure 5-3: XRD patterns of exemplary post-deposition annealing attempts (heating rate: 15 – 20 K/s, holding time: 20 – 60 s with an IR laser system in 380 Torr nitrogen atmosphere) of HZO-containing stacks. Annealed HZO layers are (at least partially) crystallized, showing a characteristic reflection at around $2\theta = 30.25°$, which could be assigned to the polar orthorhombic phase of HZO. 80

Figure 5-4: Electric polarization measurement curves for (a) an annealed TiN/HZO/TiN stack showing a leaky behavior and (b) a reference Pt/HfO_2/TiN stack showing dielectric behavior. 81

Figure 5-5: Resistive switching characteristics of post-deposition annealed TiN/HZO/TiN devices with a potentially polar orthorhombic crystalline structure. (a) Achieved forming step and failed first reset (reset try). (b) Partial/step-wise resets seen for negative and positive voltage up to ±20 V applied. 85

Figure 5-6: XRD and XRR patterns of stacks with a) *m*-HZO film grown at 300 °C, b) *a*-HZO film grown at RT, (c) *m*-HfO_2 film grown at 300 °C, (d) *a*-HfO_2 film grown at RT. The (111) reflection of the cubic Pt cubic electrodes and the *c*-cut Sapphire substrates are also visible. 87

Figure 5-7: (a) Schematic representation of the investigated stacks and corresponding BRS I-V curves of (b) *m*-HZO- and (c) *a*-HZO-containing stacks. The color coding from dark to light blue/green indicates the increased number of cycles for set/reset, respectively........ 88

Figure 5-8: Current-voltage curves for URS of *m*-HZO-containing devices under (a) positive bias voltage polarity and (b) negative bias voltage polarity. The color coding from dark to light blue/green indicates the increased number of cycles. 88

Figure 5-9: Cumulative probability plots of (a) forming voltage, (b) reset voltage and (c) set voltage for the four different investigated stacks. Values were obtained from URS with negative set and reset voltages for 30 devices each. Note that in the shown plots absolute values are given........ 89

Figure 5-10: (a) Schematic device stacks with a Cu versus Pt top electrode and (b) cumulative probability plot of the leakage current for the two different stacks. Pt top electrode-based devices have much higher leakage currents than Cu top electrode-based devices. Note that the devices size (top electrode area) is 30×30 μm^2. The dotted line labeled cc marks the value of 1 mA used as the current compliance. (c) Cumulative probability plot of the forming voltage for both stacks for positive and negative polarity with the lowest values obtained for Cu/HfO_2/Pt stacks for positive voltages. 90

Figure 5-11: Representative 50 endurance cycles of Pt/HfO_2/Pt devices of (a) URS (negative set) and (b) BRS (negative set). These results are indicating a non-polar switching behavior with a large operation voltage variance visible. 92

Figure 5-12: Representative cycles of a Cu/HfO_2/Pt devices of (a) BRS (negative set), (b) URS (positive set), (c) URS (negative set) and (d) BRS (positive set), all showing a different behavior strongly dependent on the operation mode. After the last shown reset routine in positive polarity ((a) and (b)), the devices face a hard-breakdown (permanent set to the on state)... 93

Figure 5-13 Schematic representation of the device stacks with different HfO_2 layer-thicknesses (20nm, 15nm, 10 nm, 7 nm, 5 nm, and 3 nm) on Pt bottom electrodes and *c*-cut Sapphire substrates, with Au/Pt/Cu top electrode layers. Additionally, a high-angle annular dark-field image (HAADF) showing the presence of a crystalline 10 nm HfO_2-film sandwiched between the two metal electrodes (Cu - dark; Pt - bright) and a high crystallinity of the 10 nm thick HfO_2 film is given. In the annular bright-field image (ABF), the crystalline nature of the electrodes can be seen. An Average Background Subtraction Filter (ABSF) was applied to the initial STEM images.[346] Figure partially reproduced with permission from[347]. The original publication is licensed under a Creative Commons Attribution 4.0 License (CCBY) and published by AIP Publishing... 96

Figure 5-14: (a) XRD patterns of the *m*-HfO_2 films of different thickness grown on top of cubic Pt bottom electrodes and *c*-cut Sapphire substrates, (b) Representative current-voltage curves obtained from devices of the six different stacks. A change from an abrupt to a more gradual reset with increasing oxide layer thickness is visible. Figure partially reproduced with permission from[347]. The original publication is licensed under a Creative Commons Attribution 4.0 License (CCBY) and published by AIP Publishing.................................. 97

Figure 5-15: (a) Current-voltage curves of the forming process (cc = 1 mA), (b) cumulative probability plot of the forming voltage obtained from devices of all six samples with varied oxide layer thickness (10 devices each). Figure partially reproduced with permission from[347]. The original publication is licensed under a Creative Commons Attribution 4.0 License (CCBY) and published by AIP Publishing... 97

Figure 5-16: (a) Representative current-voltage curves of the reset process for devices of the six different stacks. Additionally, the curve of G_0 is included (red). For the reset, a maximum voltage of -1 V was applied to prevent a hard-breakdown of the devices by oxygen vacancy filament-formation. (b) Cumulative probability of the maximum reset current and (c) cumulative probability of the HRS current after the reset. Blue arrows label the increase of the oxide layer thickness. Figure partially reproduced with permission from[347]. The original publication is licensed under a Creative Commons Attribution 4.0 License (CCBY) and published by AIP Publishing. 98

Figure 5-17: (a) Cumulative probability of the set voltage. The blue arrow marks an increasing oxide layer thickness. (b) HRS current versus set voltage correlation plot for devices containing HfO_2 layers of different thickness. Values of thinner films are marked with a dark blue ellipse, while values of thicker films are marked with a green ellipse. Figure partially reproduced with permission from[347]. The original publication is licensed under a Creative Commons Attribution 4.0 License (CCBY) and published by AIP Publishing..... 99

Figure 5-18: Conductive filament formation and rupturing model (reset process) for Cu/HfO_2/Pt devices containing HfO_2 layers of various thickness (20 – 3 nm). In thick devices, the reset process is dominated by thermal effects, while with decreasing thickness, the thermal assistance in the reset process is getting less dominant. After the reset in 3 nm and 5 nm thick films, the filament is not completely ruptured, but thinned. The electric field influence on the reset process therefore increases. Black arrows indicate the electric field strength in the oxide layer. Figure partially reproduced with permission from[347]. The original publication is licensed under a Creative Commons Attribution 4.0 License (CCBY) and published by AIP Publishing.. 100

Figure 5-19: Representative current-voltage curves of the HRS obtained in the set process of devices containing (a) 20 nm, (b) 10 nm and (c) 3 nm thick HfO_2 layers. By fitting the slope plotted in log-log scale, ohmic (red fit) and trap-limited/trap-free SCLC conduction (blue fit) can be assigned, dependent on the oxide layer thickness and the applied voltage. Additionally, the slope corresponding to the trap-filled SCLC is shown in purple. This mechanism only occurs for a very short time between trap-limited SCLC and trap-free SCLC. 101

Figure 5-20: Schematic representation of the conduction model for $Cu/HfO_2/Pt$ devices containing HfO_2 layers of three thicknesses (20 nm, 10 nm and 3 nm). With increasing oxide layer thickness, the conduction changes from ohmic to ohmic plus additional SCLC. Note that an additional representation for the trap-filled SCLC is not given, as it only occurs for a very short time between trap-limited SCLC and trap-free SCLC. 102

Figure 5-21: (a) Schematic device stack of “with IBE” and “without IBE” samples with corresponding leakage curves. 15 – 3 nm thick HfO_2 samples prepared using IBE (“with IBE” -red) were found to be leaky, while all stacks prepared “without IBE” (black) showed a reasonably low leakage. * Note that this is a simplified representation, as thinner layers were found to show an increased leakage current in average for “without IBE” devices. However, several devices with a leakage current of 10^{-11} A were found for all stacks with different oxide layer thicknesses, as presented in chapter 5.5. (b) Cumulative probability plot with leakage current values of “without IBE” and “with IBE” Cu/20 nm HfO_2/Pt devices. Overall, “without IBE” devices show lower leakage currents with most devices being found in the HRS with leakage currents around 10^{-15} A, which even might be below the detection limit of the measurement system (insulating devices in their pristine state). About 10 of 50 Cu/20 nm HfO_2/Pt devices prepared “with IBE” were found to be stuck in the LRS (green ellipse). 104

Figure 5-22: Phase and orientation maps obtained for $Cu/HfO_2/Pt$ devices prepared “with IBE” and “without IBE”. Lamellae were cut from the middle of 30 μm × 30 μm devices. Phase maps of a Cu (red)/m-HfO_2 (blue)/Pt (green) (a) “with IBE” sample containing 20 nm HfO_2, (b) “without IBE” sample containing 20 nm HfO_2, (c) “with IBE” sample containing 15 nm HfO_2, (d) “without IBE” sample containing 10 nm HfO_2. (e)-(h) show the corresponding orientation maps. Color wheels for the monoclinic (for HfO_2) and cubic structure (for Pt and Cu) are given at the bottom of the figure. The knowledge about these phases originates from XRD investigations (see chapter 5.5, Figure 5-14)................... 105

Figure 5-23: Schematic representation of an IBE process to create devices from a stack (photoresist/Au/Pt/Cu/HfO_2/Pt/substrate) right before the end. Effects (represented by red dots) like a deposition and movement of impurity atoms and ions, redeposition of material, defect-creation or charge-buildup can occur, likely at the edges and in a small volume of the HfO_2 layer (dashed line). Figure/layer thicknesses are not drawn to scale. 107

Figure 6-1: Schematic overview of sample series A (irradiated stoichiometric, monoclinic hafnium oxide), series B (non-irradiated oxygen-engineered hafnium oxide) and series C irradiated (oxygen-deficient hafnium oxide) mainly containing monoclinic and rhombohedral hafnium oxide films grown on *c*-cut Sapphire substrates. Series A, B and C were characterized using XRD, while for series B containing oxygen-engineered films, XPS investigations were performed. Partially reproduced from[293] with permission. The original publication is licensed under a Creative Commons Attribution 4.0 License (CCBY) and published by IEEE. In the original publication, the rhombohedral phase was labeled as a tetragonal phase.. 112

Figure 6-2: (a) XRD patterns of textured *m*-HfO_2 films revealing a phase transition from the monoclinic (m) to most likely the rhombohedral (r) phase of hafnium oxide with increasing fluence. As a comparison, the reflections corresponding to the tetragonal (t) phase of HfO_x are given, as for irradiated HfO_2 powder samples, a phase transition from the monoclinic to the tetragonal phase was reported.[11] (b) XRD patterns of as grown, oxygen-engineered HfO_x films of four different compositions, showing a similar phase transition with decreasing oxidation conditions and a shift of the rhombohedral (111) reflection towards larger diffraction angles. $(002)_h$ marks the diffraction angle of the hexagonal (002) reflection of hexagonal HfO_x close to metallic Hf (ICDD 00-038-1478). (c) XRD patterns of irradiated *r*-HfO_x films, showing a shift of the (111) reflection. Dotted red lines are guides to the eye. Partially reproduced from[293] with permission. The original publication is licensed under a Creative Commons Attribution 4.0 License (CCBY) and published by IEEE. In the original publication, the rhombohedral phase was labeled as tetragonal............ 113

Figure 6-3: (a) XPS spectra with fits of the Hf $4f_{7/2}$ and Hf $4f_{5/2}$ (left) and O 1s (right) lines of the oxygen-engineered films of series B. The purple area corresponds to the Hf^{4+} state, orange to metallic Hf^0 and green is the convolution of Hf^{X+} sub-oxide states. The O 1s fits include contributions from oxygen bound to Hf (grey) and to surface adsorbates (turquoise). (b) Decreasing oxidation conditions during the growth of the oxygen-engineered films result in an increased ratio of the Hf 4f to O 1s area, compared to the initial ratio for stoichiometric HfO_2 (dotted grey line), and obtained varying composition of HfO_x films (HfO_2, $HfO_{1.8}$, $HfO_{1.65}$, $HfO_{1.1}$). (c) Vacuum transfer unit with turbo pump and vacuum chamber as used for the *in vacuo* transfer from MBE to XPS system. (a) and (b) reproduced from[293] with permission. The original publication is licensed under a Creative Commons Attribution 4.0 License (CCBY) and published by IEEE............................... 115

Figure 6-4: Representation of the increasing rhombohedral (red) phase fraction in hafnium oxide films (this work) with sigmoidal fit and comparison to literature values obtained from powder samples (green) showing an increasing tetragonal phase fraction after irradiation. These were calculated from data reported in literature[11, 240] of experiments with 250 MeV I and 2.31 GeV Pb ions. Linear connections between stars are a guide to the eye. Partially reproduced from[293] with permission. The original publication is licensed under a Creative Commons Attribution 4.0 License (CCBY) and published by IEEE................. 117

Figure 6-5: Relative (Rel.) 2θ diffraction angle of the rhombohedral (111) reflection as a function of fluence (red dots). With decreasing oxidation conditions in oxygen-engineered films and corresponding lower oxygen content, the rhombohedral reflection (blue triangles) shows a similar shift. The dotted black line marks the position of the as grown references. Figure partially reproduced from[293] with permission. The original publication is licensed under a Creative Commons Attribution 4.0 License (CCBY) and published by IEEE. In the original publication, the rhombohedral phase was labeled as tetragonal... 118

Figure 6-6: (a) Schematic representation of the two series of samples containing 200 nm thick m-HfO$_2$ and 10 nm thin m-HfO$_2$. (b) Detailed views of the XRD patterns in the region of the $(111)_m$ and $(111)_r$ reflections as marked in (c) & (d) with a black box. Similar changes as discussed in chapter 6.1.1 are visible. Reflections corresponding to the monoclinic and rhombohedral phase are marked with m and r, respectively. Trends occurring with increasing fluence are illustrated with black arrows. The potentially occurring $(111)_r$ reflection position is also labeled. (c) XRD patterns of thick HfO$_2$ films before (1) and after irradiation ((2)-(7)) on SiO$_x$/Si substrates. A phase transition from the monoclinic (orange ticks)[123, 124] to a rhombohedral phase (blue ticks) [128] of hafnium oxide after irradiation is visible. Additionally, due to the similarity of the rhombohedral to the cubic crystal structure, the reference pattern of a cubic phase of hafnium oxide is given (green ticks)[126]. Note that the given rhombohedral reference is created based on theoretical DFT results for r-HfO$_{1.5}$.[128] In real films, diffraction angles in experimental patterns are closer to those seen in the cubic reference pattern. (d) XRD patterns of 10 nm thin HfO$_2$ films on TiN/SiO$_2$/Si. A decrease in intensity is visible with no directly observable crystalline-to-crystalline phase transition. Si substrate reflections are marked with a *. TiN electrode reflections are marked with an x. Figures (a) and (b) are partially reproduced with permission from[354], https://doi.org/10.1021/acsnano.2c04841. The original publication is licensed under a Creative Commons Attribution 4.0 License (CCBY) and published by American Chemical Society. The rhombohedral (111) reflection was initially labeled as cubic (111). A simulated reference pattern of the rhombohedral structure was added. 120

Figure 6-7: (a) BF-STEM image of the as grown HfO$_2$/SiO$_2$/Si stack with a Pt protection layer on top. Columnar grains of the HfO$_2$ films are visible. (b) HAADF-STEM image of the same area. (c) High-resolution HAADF-STEM image of the area marked by a red square in (b), revealing the polycrystalline nature of the HfO$_2$ film, an amorphous SiO$_2$ layer and a single crystalline Si substrate. The dashed line indicates a change in displayed contrast. (d) High-resolution HAADF-STEM image of the area marked by a red square in (c), with lattice spacings. 122

Figure 6-8: (a) HAADF-STEM image of the as grown 200 nm HfO$_2$/SiO$_2$/Si stack with a Pt protection layer on top, revealing columnar grains of the HfO$_2$ films. (b) HAADF-STEM image of the Pt/HfO$_2$/SiO$_2$/Si stack exposed to 5×10^{12} ions/cm^2. (c) ACOM orientation map of the as grown sample each color represents an orientation. A significant grain fragmentation after irradiation is revealed. Color wheels for the cubic and monoclinic structures are included. (d) ACOM orientation map of the sample exposed to 5×10^{12} ions/cm^2. (e) ACOM Phase map of as grown sample with a high fraction of m-HfO$_2$. Misorientation parts (>10°) and phase boundaries are given in grey. (f) ACOM phase map of the sample exposed to 5×10^{12} ions/cm^2, revealing a higher fraction of the cubic phase. *** Note that the pattern matching routine was performed using a cubic structure of hafnium oxide (space group: ICDD 04-011-9018, a ≈ 5.06 Å) as first reported in literature[145] for the oxygen-deficient phase occurring in HfO$_x$. Lattice parameters are close to the recently found rhombohedral phase.[128] Due to this similarity, the cubic and rhombohedral phases can hardly be distinguished in STEM/SPED (ACOM).** Figure reproduced with permission from[354], https://doi.org/10.1021/acsnano.2c04841. The original publication is licensed under a Creative Commons Attribution 4.0 License (CCBY) and published by American Chemical Society. 124

Figure 6-9: (a) HRTEM image of the as grown 10 nm HfO_2/TiN stack with a Pt protection layer on top. One single grain is visible in the given field of view. (b) Representative HRTEM image of the Pt/HfO_2/TiN stack exposed to 5×10^{12} ions/cm². Significantly smaller grains are identified. Grain boundaries in the HfO_2 layer are highlighted by the green lines. (c) ACOM orientation map of an as grown stack. Each color represents a different orientation as seen from the color wheel for the cubic and monoclinic structures. Grey indicates misorientation (>20°) and phase boundaries. (d) ACOM orientation map of a sample exposed to 5×10^{12} ions/cm². Note that the TiN and Pt layer are also included in the map. * **Note that the pattern matching routine was performed using a cubic structure of hafnium oxide (space group: ICDD 04-011-9018, a ≈ 5.06 Å) as first reported in literature[145] for the oxygen-deficient phase occurring in HfO_x. Lattice parameters are close to the recently found rhombohedral phase.[128]** Figure reproduced with permission from[354], https://doi.org/10.1021/acsnano.2c04841. The original publication is licensed under a Creative Commons Attribution 4.0 License (CCBY) and published by American Chemical Society. 126

Figure 6-10: XRD patterns of 200 nm thick *m/r*-HfO_x and m/*r*-HfO_y films grown on SiO_x/Si substrates before and after irradiation with up to 8×10^{12} ions/cm². A shift of the rhombohedral (111) reflection is visible. Note that there were no experiments performed with 5×10^{9} and 5×10^{12} ions/cm² for the HfO_y sample series. 128

Figure 6-11: XRD patterns of as grown and irradiated 10 nm thin oxygen-deficient HfO_x films grown on TiN/SiO_x/Si with a low overall intensity of the hafnium oxide reflections due to the low volume of the layer. The $(111)_r$ reflection shifts towards larger diffraction angles with increased fluence. Note that the highest fluence is 5×10^{12} ions/cm² and no sample was exposed to 8×10^{12} ions/cm². Substrate reflections are marked with a *, while x marks the cubic (200) reflection of the TiN bottom electrode. 129

Figure 6-12: Resistance versus 10^4 cycles for a 1T1R array with HfO_2-based OxRAM devices. A clear memory gap is present between the LRS (grey) and HRS (blue) mean values (as well as quartile 1 and 3) for 3072 devices after irradiation at a fluence of (a) 1×10^{9} ions/cm² and (b) 5×10^{10} ions/cm². Data presented at RADECS conference with similar figure printed in the conference proceedings[63]. Partially reproduced with permission from[354], https://doi.org/10.1021/acsnano.2c04841. The original publication is licensed under a Creative Commons Attribution 4.0 License (CCBY) and published by American Chemical Society. 131

Figure 6-13: Drain current-drain voltage curves of single NMOS transistors with a gate width of 660 nm after irradiation (at a gate voltage of 1.3V). The curve obtained for 1×10^{9} ions/cm² also represents a curve typically observed for a non-irradiated transistor (not shown). With increasing fluence, lower currents are measured overall. Data presented at RADECS conference with similar figure printed in the conference proceedings[63]. Partially reproduced with permission from[354], https://doi.org/10.1021/acsnano.2c04841. The original publication is licensed under a Creative Commons Attribution 4.0 License (CCBY) and published by American Chemical Society. 131

Figure 6-14: Resistance versus 10^4 cycles of a 1R HfO_2-based OxRAM cell irradiated at a fluence of 1×10^{12} ions/cm^2 and accessed by utilizing a 6700 nm gate width transistor. Data presented at RADECS 2020 conference. Data presented at RADECS conference with figure printed in the conference proceedings[63]. Partially reproduced with permission from[354], https://doi.org/10.1021/acsnano.2c04841. The original publication is licensed under a Creative Commons Attribution 4.0 License (CCBY) and published by American Chemical Society. 132

Figure 6-15: Current-voltage characteristics of a Pt/10 nm HfO_2/TiN device (a) before (as grown Reference) and (b) after being exposed to 5×10^{12} ions/cm^2. Resistive switching is achieved in both devices. 133

Figure 6-16: Schematic drawings showing the irradiated ferroelectric stacks containing 20 nm HSO (Si-doped HfO_2), 20 nm HZO or 10 nm HZO (Zr-doped HfO_2) layers sandwiched between two TiN electrodes on top of a SiO_x/Si substrates. 135

Figure 6-17: XRD patterns of doped ferroelectric hafnium oxide films before and after irradiation, containing (a) 20 nm HSO, (b) 20 nm HZO and (c) 10 nm HZO. With increasing ion fluence, a shift of the initially $(111)_o$ reflection towards larger diffraction angles occurs. Monoclinic reflections vanish at fluences above 5x10^{11} ions/cm^2. (d) Theoretical powder reference patterns of the monoclinic, polar orthorhombic, tetragonal and cubic phase of HfO_2, created based on previously reported structures.[123, 124, 126, 130, 356] The $(111)_c$ reflection of the TiN electrode is marked by x. The Si-substrate reflections located between $2\theta = 32.5° - 34°$ are assigned to the Si (200) reflection due to Umweganregung[353] and is not related to the ferroelectric layer. Partially reproduced with permission from[131]. The original publication is licensed under a Creative Commons Attribution 4.0 License (CCBY) and published by AIP Publishing. 136

Figure 6-18: Field-dependent electric polarization curves before (grey – Ref.) and after exposure to different fluences (top) and after 10000 post-cycles (bottom). The induced pinching of the polarization hysteresis loops is reversed after cycling and the loops are re-opened, showing ferroelectric behavior. Additionally, the loop of a non-irradiated, but cycled reference sample (grey) is shown. Partially reproduced with permission from[131]. The original publication is licensed under a Creative Commons Attribution 4.0 License (CCBY) and published by AIP Publishing 137

Figure 6-19: Values of the remanent polarization after irradiation and 10000 post-cycles for 6 to 10 devices per fluence. A clear trend to lower values with increased fluences is visible. Partially reproduced with permission from[131]. The original publication is licensed under a Creative Commons Attribution 4.0 License (CCBY) and published by AIP Publishing... 139

Figure 6-20: Evolution of the saturation polarization P_S in dependence of up to 10000 field-cycles (post-cycling) using an amplitude of 3 MV/cm. A significant increase after cycling is observed with a saturation reached after about 1000 cycles. For the largest fluence of 2.4×10^{12} ions/cm^2, P_S is even after cycling lower compared to samples exposed to lower fluences for all stack types. Partially reproduced with permission from[131]. The original publication is licensed under a Creative Commons Attribution 4.0 License (CCBY) and published by AIP Publishing. 142

Figure 6-21: Field-dependent electric polarization hysteresis of capacitors poled prior to Au irradiation. A shift of the coercive fields to more positive or negative values are visible for samples poled negatively (top) or positively (bottom), respectively. Trends obtained for increasing fluences are similar to non-poled samples. Partially reproduced with permission from[131]. The original publication is licensed under a Creative Commons Attribution 4.0 License (CCBY) and published by AIP Publishing. 143

Figure 6-22: Schematic of the changes induced by heavy ion irradiation and post-cycling in ferroelectric hafnium oxide-containing stacks. A beam-induced phase transition of the monoclinic (red) and polar orthorhombic (blue) phase to non-polar a cubic or tetragonal (green) phase occurs, accompanied by grain fragmentation at high fluences. The non-polar phase can be (re)transformed to the polar orthorhombic phase upon field-cycling. In contrast, the induced grain fragmentation appears to be irreversible. Partially reproduced with permission from[131]. The original publication is licensed under a Creative Commons Attribution 4.0 License (CCBY) and published by AIP Publishing. 144

Figure 6-23: Schematic representations showing the irradiated phase-change memory stacks containing 100 nm *a*-GST, *cry*-GST, *a*-GGST and *cry*-GGST (full-sheet) layers with a 10 nm SiN encapsulation layer grown on top of a SiO_x/Si substrates. 145

Figure 6-24: XRD patterns of as grown and irradiated GST-based samples consisting of amorphous $Ge_2Sb_2Te_5$ (*a*-GST, Series A) and crystalline $Ge_2Sb_2Te_5$ (*cry*-GST, Series B) with changes occurring at increasing fluence. Si substrate reflections are marked with a *. Partially reproduced with permission from[354], https://doi.org/10.1021/acsnano.2c04841. The original publication is licensed under a Creative Commons Attribution 4.0 License (CCBY) and published by American Chemical Society. 145

Figure 6-25: XRD patterns of as grown and irradiated amorphous $Ge_2Sb_2Te_5$ (*a*-GST) films of Series C, with different fluence steps compared to Series A. Starting at fluences of 3×10^{11} ions/cm² and above, *a*-GST films crystallize in the cubic phase. Partially reproduced with permission from[354], https://doi.org/10.1021/acsnano.2c04841, https://pubs.acs.org/doi/suppl/10.1021/acsnano.2c04841/suppl_file/nn2c04841_si_001.pdf (supporting information). The original publication is licensed under a Creative Commons Attribution 4.0 License (CCBY) and published by AIP Publishing. 146

Figure 6-26: XRD patterns of as grown and irradiated GGST-based samples consisting of amorphous Ge-rich GST (*a*-GGST, Series D) and crystalline Ge-rich GST (*cry*-GGST, Series E) with changes occurring at increasing fluence in *cry*-GGST films only. Si substrate reflections are marked with a *. Partially reproduced with permission from[354], https://doi.org/10.1021/acsnano.2c04841. The original publication is licensed under a Creative Commons Attribution 4.0 License (CCBY) and published by American Chemical Society. 146

Figure 6-27: EDX and HAADF-STEM images with nano-diffraction patterns of (a) as grown amorphous $Ge_2Sb_2Te_5$ (*a*-GST) exposed to 1×10^{13} ions/cm² showing a crystalline structure with large grains and of (b) crystalline Ge-rich GST (*cry*-GGST) exposed to 7×10^{12} ions/cm² with nm-sized crystallites (visible from few and low intensity NBED patterns). EDX maps reveal a uniform distribution of elements for (a) *a*-GST and (b) *a*-Ge/GST segregation in *cry*-GGST.

Reproduced with permission from[354], https://doi.org/10.1021/acsnano.2c04841. The original publication is licensed under a Creative Commons Attribution 4.0 License (CCBY) and published by American Chemical Society. 148

Figure 6-28: Median device resistance values including ±1σ values of (a) GST- and (b) GGST 4kb (1T1R) arrays for the LRS (after set) and HRS (after reset) as a function of fluence (250 devices each). The resistance values of GST-based devices decrease with increasing fluence, while for GGST-based devices, the resistance values increase. Reproduced with permission from[354], https://doi.org/10.1021/acsnano.2c04841. The original publication is licensed under a Creative Commons Attribution 4.0 License (CCBY) and published by American Chemical Society. 150

Figure 6-29: Schematic overview of HfO_2-, HfO_x-, Zr-doped HfO_2 (HZO)-, Si-doped HfO_2 (HSO)-, $Ge_2Sb_2Te_5$ (GST)-based and Ge-rich GST-based sample series. Representative XRD patterns of samples exposed to heavy ions are given, showing different structural changes. Note that these are only a few examples. 153

List of Tables

Table 1-1: Characteristic parameters of SRAM, DRAM, Flash, FeRAM & FeFET, MRAM, PCRAM and redox-based RRAM, given as examples. Information from [4, 7, 20, 41-46]. * ferroelectric memory including perovskite- and hafnium oxide-based memories; ** DRAM in ms-range; *** redox-based resistive random-access memory, with best properties mainly from VCM; **** more potential applications are discussed in the text. F is the feature size of the technology node. 6

Table 2-1: Space group and lattice parameters of relevant structures. Information from Powder Diffraction Files (PDF) from the International Center for Diffraction Data (ICDD) database ($P2_1/c$, $P4_2/nmc$, $Pbca$, $Pnma$, $Fm3m$) and density functional theory (DFT) calculations ($Pca2_1$[130, 131], R3m (r-$HfO_{1.5}$)[128]). Additionally, experimental (exp.) values for r-$HfO_{1.7}$ are given. [128] 19

Table 2-2: Comparison of exemplary parameters of PZT and HfO_2-based ferroelectrics. Values taken from[130, 171, 173]. 25

Table 4-1: Deposition parameters for $Hf_xZr_{x-1}O_2$ films grown on c-cut Sapphire substrates. Additionally, calculated and controlled compositions (QCM thickness ratios) are given. T_{set} is the set temperature of the heat control unit, while T_{pyro} is the temperature at the sample surface prior to deposition measured with a pyrometer, which corresponds to the thermocouple-calibrated temperature. The (system internal) deposition height control was always set to 36.6 and the overall controlled thickness (sum of oxidized Hf and Zr deposited from respective QCMs) was 100 Å. 46

Table 5-1: Calculated, growth-controlled and XPS compositions as well as obtained film thicknesses derived from XRR measurements of the $Hf_xZr_{1-x}O_2$ films grown on c-cut Sapphire substrates. 76

Table 6-1: Remanent polarization (P_r) and saturation polarization (P_S) values obtained for the three stacks before irradiation (Ref.) and at various fluences. 138

Table 6-2: Remanent polarization (P_r) and saturation polarization (P_S) values obtained for the three stacks after 10000 post-cycles after irradiation at various fluences. Additionally, values of a non-irradiated, but cycled reference sample (Ref.) are shown. 138

Table 6-3: HRS and LRS resistances of as grown and irradiated PCRAM devices based on 100 nm thick GST and GGST films. 150

References

1. Chua, L., Memristor-the missing circuit element. *IEEE Transactions on Circuit Theory* **18**, 507-519 (1971).
2. Strukov, D. B., Snider, G. S., Stewart, D. R. & Williams, R. S., The missing memristor found. *Nature* **453**, 80-83 (2008).
3. Schroeder, U., Park, M. H., Mikolajick, T. & Hwang, C. S., The fundamentals and applications of ferroelectric HfO_2. *Nature Reviews Materials* **7**, 653-669 (2022).
4. Lanza, M., Sebastian, A., Lu, W. D., Le Gallo, M., Chang, M. F., Akinwande, D., Puglisi, F. M., Alshareef, H. N., Liu, M. & Roldan, J. B., Memristive technologies for data storage, computation, encryption, and radio-frequency communication. *Science* **376**, eabj9979 (2022).
5. Dittmann, R., Menzel, S. & Waser, R., Nanoionic memristive phenomena in metal oxides: the valence change mechanism. *Advances in Physics* **70**, 155-349 (2021).
6. Zahoor, F., Azni Zulkifli, T. Z. & Khanday, F. A., Resistive Random Access Memory (RRAM): an Overview of Materials, Switching Mechanism, Performance, Multilevel Cell (mlc) Storage, Modeling, and Applications. *Nanoscale Research Letters* **15**, 90 (2020).
7. Schenk, T., Pesic, M., Slesazeck, S., Schroeder, U. & Mikolajick, T., Memory Technology - A Primer for Material Scientists. *Reports on Progress in Physics* **83**, 086501 (2020).
8. Fantini, P., Phase change memory applications: the history, the present and the future. *Journal of Physics D: Applied Physics* **53**, 283002 (2020).
9. Fleetwood, D. M., Radiation Effects in a Post-Moore World. *IEEE Transactions on Nuclear Science* **68**, 509-545 (2021).
10. Schwank, J. R., Shaneyfelt, M. R., Fleetwood, D. M., Felix, J. A., Dodd, P. E., Paillet, P. & Ferlet-Cavrois, V., Radiation Effects in MOS Oxides. *IEEE Transactions on Nuclear Science* **55**, 1833-1853 (2008).
11. Benyagoub, A., Mechanism of the monoclinic-to-tetragonal phase transition induced in zirconia and hafnia by swift heavy ions. *Physical Review B* **72**, 094114 (2005).
12. 'Tsunami of data' could consume one fifth of global electricity by 2025. https://www.theguardian.com/environment/2017/dec/11/tsunami-of-data-could-consume-fifth-global-electricity-by-2025 (accessed 20 Oct 2022).
13. Jones, N., The information factories. *Nature* **561**, 163-166 (2018).
14. Sebastian, A., Le Gallo, M., Khaddam-Aljameh, R. & Eleftheriou, E., Memory devices and applications for in-memory computing. *Nature Nanotechnology* **15**, 529-544 (2020).
15. Gubbi, J., Buyya, R., Marusic, S. & Palaniswami, M., Internet of Things (IoT): A vision, architectural elements, and future directions. *Future Generation Computer Systems* **29**, 1645-1660 (2013).
16. Williams, R. S., What's Next? [The end of Moore's law]. *Computing in Science & Engineering* **19**, 7-13 (2017).
17. Moore, G. E., Cramming more components onto integrated circuits. *Electronics* **38**, 114-117 (1965).
18. Neumann, J. v., First Draft of a Report in the EDVAC. *IEEE Annals of the History of Computing* **15**, 25-75 (1993).
19. Yan, B., Li, B., Qiao, X., Xue, C.-X., Chang, M. F., Chen, Y. & Li, H., Resistive Memory-Based In-Memory Computing: From Device and Large-Scale Integration System Perspectives. *Advanced Intelligent Systems* **1**, 1900068 (2019).
20. Chen, A., A review of emerging non-volatile memory (NVM) technologies and applications. *Solid-State Electronics* **125**, 25-38 (2016).
21. Zidan, M. A., Strachan, J. P. & Lu, W. D., The future of electronics based on memristive systems. *Nature Electronics* **1**, 22-29 (2018).
22. Intel® Optane™ Memory Series https://www.intel.com/content/www/us/en/products/sku/99742/intel-optane-

memory-series-32gb-m-2-80mm-pcie-3-0-20nm-3d-xpoint/specifications.html (accessed 20 Oct 2022).

23. Redaelli, A., Gandolfo, A., Samanni, G., Gomiero, E., Petroni, E., Scotti, L., Lippiello, A., Mattavelli, P., Jasse, J., Codegoni, D., Serafini, A., Ranica, R., Boccaccio, C., Sandrini, J., Berthelon, R., Grenier, J. C., Weber, O., Turgis, D., Valery, A., Del Medico, S., Caubet, V., Reynard, J. P., Dutartre, D., Favennec, L., Conte, A., Disegni, F., De Tomasi, M., Ventre, A., Baldo, M., Ielmini, D., Maurelli, A., Ferreira, P., Arnaud, F., Piazza, F., Cappelletti, P., Annunziata, R. & Gonella, R., BEOL process effects on ePCM reliability. *IEEE Journal of the Electron Devices Society* **10**, 563-568 (2022).
24. Phase-Change Memory (PCM). https://www.st.com/content/st_com/en/about/innovation---technology/PCM.html (accessed 20 Oct 2022).
25. Natsui, M., Suzuki, D., Tamakoshi, A., Watanabe, T., Honjo, H., Koike, H., Nasuno, T., Ma, Y., Tanigawa, T. & Noguchi, Y., A 47.14-μW 200-MHz MOS/MTJ-Hybrid Nonvolatile Microcontroller Unit Embedding STT-MRAM and FPGA for IoT Applications. *IEEE Journal of Solid-State Circuits* **54**, 2991-3004 (2019).
26. Mc Kearney, B., Fujitsu Fram–Non-Volatile Memory of The Future. (2014).
27. FRAM – New Generation of Non-Volatile Memory. https://www.ti.com/lit/ml/szzt014a/szzt014a.pdf (accessed 20 Oct 2022).
28. EXCELON™ F-RAM. https://www.infineon.com/cms/en/product/memories/f-ram-ferroelectric-ram/excelon-f-ram/ (accessed 20 Oct 2022).
29. Cypress Semiconductor Nichtflüchtiger serieller F-RAM Speicher. https://www.mouser.de/cypress-serial-fram/ (accessed 20 Oct 2022).
30. Panasonic Starts World's First Mass Production of ReRAM Mounted Microcomputers. https://news.panasonic.com/global/press/en130730-2 (accessed 20 Oct 2022).
31. Weebit Nano Silicon Oxide ReRAM Technology. https://www.cea.fr/cea-tech/leti/Documents/%C3%A9v%C3%A9nements/Prez%20workshop%20memory%202017/3.2.pdf (accessed 20 Oct 2022).
32. Meet the Weebit ReRAM Bitcell. https://www.weebit-nano.com/technology/reram-bitcell/ (accessed 20 Oct 2022).
33. Ferroelectric hafnium oxide. https://ferroelectric-memory.com/technology/ferroelectric-hafnium-oxide/ (accessed 20 Oct 2022).
34. Wouters, D. J., Waser, R. & Wuttig, M., Phase-Change and Redox-Based Resistive Switching Memories. *Proceedings of the IEEE* **103**, 1274-1288 (2015).
35. Bhatti, S., Sbiaa, R., Hirohata, A., Ohno, H., Fukami, S. & Piramanayagam, S., Spintronics based random access memory: a review. *Materials Today* **20**, 530-548 (2017).
36. Waser, R. & Aono, M., Nanoionics-based resistive switching memories. *Nature Materials* **6**, 833-840 (2007).
37. Waser, R., Dittmann, R., Staikov, G. & Szot, K., Redox-Based Resistive Switching Memories - Nanoionic Mechanisms, Prospects, and Challenges. *Advanced Materials* **21**, 2632-2663 (2009).
38. Berggren, K., Xia, Q., Likharev, K. K., Strukov, D. B., Jiang, H., Mikolajick, T., Querlioz, D., Salinga, M., Erickson, J. R., Pi, S., Xiong, F., Lin, P., Li, C., Chen, Y., Xiong, S., Hoskins, B. D., Daniels, M. W., Madhavan, A., Liddle, J. A., McClelland, J. J., Yang, Y., Rupp, J., Nonnenmann, S. S., Cheng, K. T., Gong, N., Lastras-Montano, M. A., Talin, A. A., Salleo, A., Shastri, B. J., de Lima, T. F., Prucnal, P., Tait, A. N., Shen, Y., Meng, H., Roques-Carmes, C., Cheng, Z., Bhaskaran, H., Jariwala, D., Wang, H., Shainline, J. M., Segall, K., Yang, J. J., Roy, K., Datta, S. & Raychowdhury, A., Roadmap on emerging hardware and technology for machine learning. *Nanotechnology* **32**, 012002 (2021).
39. Moll, J. & Tarui, Y., A new solid state memory resistor. *IEEE Transactions on Electron Devices* **10**, 338-338 (1963).

40. Böscke, T. S., Müller, J., Bräuhaus, D., Schröder, U. & Böttger, U., Ferroelectricity in hafnium oxide thin films. *Applied Physics Letters* **99**, 102903 (2011).
41. Yu, S. & Chen, P.-Y., Emerging Memory Technologies: Recent Trends and Prospects. *IEEE Solid-State Circuits Magazine* **8**, 43-56 (2016).
42. Alao, O., Joshua, J., Kehinde, D., Ehinlafa, E., Agbaje, M. & Akinsola, J., Emerging Memory Technologies. *The International Journal Of Engineering And Science (IJES)* **5**, 61-68 (2016).
43. Petzold, S., Defect Engineering in Transition Metal Oxide-based Resistive Random Access Memory. Dissertation, TU Darmstadt, Darmstadt, Germany (2020).
44. Müller, J., Böscke, T., Müller, S., Yurchuk, E., Polakowski, P., Paul, J., Martin, D., Schenk, T., Khullar, K. & Kersch, A., Ferroelectric hafnium oxide: A CMOS-compatible and highly scalable approach to future ferroelectric memories. in *2013 IEEE International Electron Devices Meeting* 10.18. 11-10.18. 14 (IEEE, 2013).
45. Kumar, D., Aluguri, R., Chand, U. & Tseng, T.-Y., Metal oxide resistive switching memory: materials, properties and switching mechanisms. *Ceramics International* **43**, S547-S556 (2017).
46. Emerging Non-Volatile Memory 2021. https://www.i-micronews.com/products/emerging-non-volatile-memory-2021/?cn-reloaded=1 (accessed 20 Oct 2022).
47. Wong, H. S. P., Lee, H.-Y., Yu, S., Chen, Y.-S., Wu, Y., Chen, P.-S., Lee, B., Chen, F. T. & Tsai, M.-J., Metal–Oxide RRAM. *Proceedings of the IEEE* **100**, 1951-1970 (2012).
48. Zhang, Z., Wu, Y., Wong, H. S. P. & Wong, S. S., Nanometer-Scale in HfO_x RRAM. *IEEE Electron Device Letters* **34**, 1005-1007 (2013).
49. Das, S., Chen, A. & Marinella, M., Beyond CMOS. in *2021 IEEE International Roadmap for Devices and Systems Outbriefs* 01-129 (IEEE, 2021).
50. Wong, H.-S. P. & Salahuddin, S., Memory leads the way to better computing. *Nature Nanotechnology* **10**, 191-194 (2015).
51. Borghetti, J., Snider, G. S., Kuekes, P. J., Yang, J. J., Stewart, D. R. & Williams, R. S., ‘Memristive’ switches enable ‘stateful’ logic operations via material implication. *Nature* **464**, 873-876 (2010).
52. Åkerman, J., Toward a universal memory. *Science* **308**, 508-510 (2005).
53. Banerjee, W., Kim, S. H., Lee, S., Lee, D. & Hwang, H., An Efficient Approach Based on Tuned Nanoionics to Maximize Memory Characteristics in Ag-Based Devices. *Advanced Electronic Materials* **7**, 2100022 (2021).
54. Kim, M. S., Kim, M. S., Lee, G. J., Sunwoo, S. H., Chang, S., Song, Y. M. & Kim, D. H., Bio-Inspired Artificial Vision and Neuromorphic Image Processing Devices. *Advanced Materials Technologies* **7**, 2100144 (2022).
55. Milano, G., Agliuzza, M., de Leo, N. & Ricciardi, C., Speech recognition through physical reservoir computing with neuromorphic nanowire networks. in *2022 International Joint Conference on Neural Networks (IJCNN)* 1-6 (IEEE, 2022).
56. Chen, G., Cao, H., Conradt, J., Tang, H., Rohrbein, F. & Knoll, A., Event-based neuromorphic vision for autonomous driving: A paradigm shift for bio-inspired visual sensing and perception. *IEEE Signal Processing Magazine* **37**, 34-49 (2020).
57. Volkswagen neural networks. https://www.volkswagenag.com/de/news/stories/2019/06/volkswagen-neural-networks.html# (accessed 21 Oct 2022).
58. Milo, V., Zambelli, C., Olivo, P., Pérez, E., K. Mahadevaiah, M., G. Ossorio, O., Wenger, C. & Ielmini, D., Multilevel HfO_2-based RRAM devices for low-power neuromorphic networks. *APL Materials* **7**, 081120 (2019).
59. Petzold, S., Piros, E., Eilhardt, R., Zintler, A., Vogel, T., Kaiser, N., Radetinac, A., Komissinskiy, P., Jalaguier, E., Nolot, E., Charpin-Nicolle, C., Wenger, C., Molina-Luna, L., Miranda, E. & Alff, L., Tailoring the Switching Dynamics in Yttrium Oxide-Based RRAM

Devices by Oxygen Engineering: From Digital to Multi-Level Quantization toward Analog Switching. *Advanced Electronic Materials* **6**, 2000439 (2020).

60. Wei, Y., Vats, G. & Noheda, B., Synaptic behavior in ferroelectric epitaxial rhombohedral $Hf_{0.5}Zr_{0.5}O_2$ thin films. *Neuromorphic Computing and Engineering* **2**, 044007 (2022).
61. Brückerhoff-Plückelmann, F., Feldmann, J., Wright, C. D., Bhaskaran, H. & Pernice, W. H., Chalcogenide phase-change devices for neuromorphic photonic computing. *Journal of Applied Physics* **129**, 151103 (2021).
62. Fleetwood, D. M., Perspective on radiation effects in nanoscale metal–oxide–semiconductor devices. *Applied Physics Letters* **121**, 070503 (2022).
63. Guillaume, N., Lefevre, G., Charpin-Nicolle, C., Grenouillet, L., Vogel, T., Kaiser, N., Piros, E., Petzold, S., Trautmann, C., Sylvain, D., Vallee, C., Alff, L. & Nowak, E., Heavy Ion Irradiation Hardening Study on 4kb arrays HfO_2-based OxRAM. in *2020 20th European Conference on Radiation and Its Effects on Components and Systems (RADECS)* 1-6 (IEEE, 2020).
64. T. Kämpfe, T. Vogel, R. Olivo, M. Lederer, N. Kaiser, S. Petzold, T. Ali, D. Lehninger, C. Trautmann, L. Alff & Seidel, K., Heavy ion irradiation effects on structural and ferroelectric properties of HfO_2 films. in *2020 Joint Conference of the IEEE International Frequency Control Symposium and International Symposium on Applications of Ferroelectrics (IFCS-ISAF)* 1-3 (IEEE, 2020).
65. Explore Space applications. https://www.st.com/en/applications/space.html (accessed 21 Oct 2022).
66. Balatti, S., Ambrogio, S., Wang, Z. & Ielmini, D., True random number generation by variability of resistive switching in oxide-based devices. *IEEE Journal on Emerging and Selected Topics in Circuits and Systems* **5**, 214-221 (2015).
67. Scott, J. C. & Bozano, L. D., Nonvolatile memory elements based on organic materials. *Advanced materials* **19**, 1452-1463 (2007).
68. You, Z. & Ramanathan, S., Mott Memory and Neuromorphic Devices. *Proceedings of the IEEE* **103**, 1289-1310 (2015).
69. Liauw, Y. Y., Zhang, Z., Kim, W., El Gamal, A. & Wong, S. S., Nonvolatile 3D-FPGA with monolithically stacked RRAM-based configuration memory. in *2012 IEEE International Solid-State Circuits Conference* 406-408 (IEEE, 2012).
70. Nebashi, R., Banno, N., Miyamura, M., Bai, X., Funahashi, K., Okamoto, K., Iguchi, N., Numata, H., Sugibayashi, T., Sakamoto, T. & Tada, M., A 171k-LUT Nonvolatile FPGA using Cu Atom-Switch Technology in 28nm CMOS. in *2020 30th International Conference on Field-Programmable Logic and Applications (FPL)* 323-327 (IEEE, 2020).
71. Sheikh, F., Nagisetty, R., Karnik, T. & Kehlet, D., 2.5 D and 3D heterogeneous integration: emerging applications. *IEEE Solid-State Circuits Magazine* **13**, 77-87 (2021).
72. Sawa, A., Resistive switching in transition metal oxides. *Materials Today* **11**, 28-36 (2008).
73. Wilk, G. D., Wallace, R. M. & Anthony, J. M., High-κ gate dielectrics: Current status and materials properties considerations. *Journal of Applied Physics* **89**, 5243-5275 (2001).
74. Choi, J. H., Mao, Y. & Chang, J. P., Development of hafnium based high-k materials—A review. *Materials Science and Engineering: R: Reports* **72**, 97-136 (2011).
75. Sharath, S. U., Vogel, S., Molina-Luna, L., Hildebrandt, E., Wenger, C., Kurian, J., Duerrschnabel, M., Niermann, T., Niu, G., Calka, P., Lehmann, M., Kleebe, H.-J., Schroeder, T. & Alff, L., Control of Switching Modes and Conductance Quantization in Oxygen Engineered HfO_x based Memristive Devices. *Advanced Functional Materials* **27**, 1700432 (2017).
76. Petzold, S., Zintler, A., Eilhardt, R., Piros, E., Kaiser, N., Sharath, S. U., Vogel, T., Major, M., McKenna, K. P., Molina-Luna, L. & Alff, L., Forming-Free Grain Boundary Engineered Hafnium Oxide Resistive Random Access Memory Devices. *Advanced Electronic Materials* **5**, 1900484 (2019).

77. Kwon, D. H., Kim, K. M., Jang, J. H., Jeon, J. M., Lee, M. H., Kim, G. H., Li, X. S., Park, G. S., Lee, B., Han, S., Kim, M. & Hwang, C. S., Atomic structure of conducting nanofilaments in TiO_2 resistive switching memory. *Nature Nanotechnology* **5**, 148-153 (2010).
78. Rupp, J., Waser, R. & Wouters, D., Threshold switching in amorphous Cr-doped vanadium oxide for new crossbar selector. in *2016 IEEE 8th International Memory Workshop (IMW)* 1-4 (IEEE, 2016).
79. Wei, Z., Kanzawa, Y., Arita, K., Katoh, Y., Kawai, K., Muraoka, S., Mitani, S., Fujii, S., Katayama, K. & Iijima, M., Highly reliable TaO_x ReRAM and direct evidence of redox reaction mechanism. in *2008 IEEE International Electron Devices Meeting* 1-4 (IEEE, 2008).
80. Sharath, S. U., Joseph, M. J., Vogel, S., Hildebrandt, E., Komissinskiy, P., Kurian, J., Schroeder, T. & Alff, L., Impact of oxygen stoichiometry on electroforming and multiple switching modes in $TiN/TaO_x/Pt$ based ReRAM. *Applied Physics Letters* **109**, 173503 (2016).
81. Petzold, S., Piros, E., Sharath, S. U., Zintler, A., Hildebrandt, E., Molina-Luna, L., Wenger, C. & Alff, L., Gradual reset and set characteristics in yttrium oxide based resistive random access memory. *Semiconductor Science and Technology* **34**, 075008 (2019).
82. Lin, C.-Y., Wang, S.-Y., Lee, D.-Y. & Tseng, T.-Y., Electrical Properties and Fatigue Behaviors of ZrO_2 Resistive Switching Thin Films. *Journal of The Electrochemical Society* **155**, H615 (2008).
83. Szot, K., Dittmann, R., Speier, W. & Waser, R., Nanoscale resistive switching in $SrTiO_3$ thin films. *Physica Status Solidi (RRL)–Rapid Research Letters* **1**, R86-R88 (2007).
84. Mehonic, A., Shluger, A. L., Gao, D., Valov, I., Miranda, E., Ielmini, D., Bricalli, A., Ambrosi, E., Li, C., Yang, J. J., Xia, Q. & Kenyon, A. J., Silicon Oxide (SiO_x): A Promising Material for Resistance Switching? *Adv Mater* **30**, e1801187 (2018).
85. Li, D., Li, C., Wang, J., Xu, M., Ma, J., Gu, D., Liu, F., Jiang, Y. & Li, W., Multifunctional Analog Resistance Switching of Si_3N_4-Based Memristors through Migration of Ag^+ Ions and Formation of Si-Dangling Bonds. *The Journal of Physical Chemistry Letters* **13**, 5101-5108 (2022).
86. Talyansky, V., Choopun, S., Downes, M., Sharma, R., Venkatesan, T., Li, Y., Salamanca-Riba, L., Wood, M., Lareau, R. & Jones, K., Pulsed laser deposition of titanium nitride films on sapphire. *Journal of materials research* **14**, 3298-3302 (1999).
87. International Centre for Diffraction Data (PDF-4+-software). https://www.icdd.com/pdf-4/ (accessed 15 Aug 2022).
88. Claflin, B., Binger, M. & Lucovsky, G., Interface studies of tungsten nitride and titanium nitride composite metal gate electrodes with thin dielectric layers. *Journal of Vacuum Science & Technology A: Vacuum, Surfaces, and Films* **16**, 1757-1761 (1998).
89. Goux, L., Wang, X. P., Chen, Y. Y., Pantisano, L., Jossart, N., Govoreanu, B., Kittl, J. A., Jurczak, M., Altimime, L. & Wouters, D. J., Roles and Effects of TiN and Pt Electrodes in Resistive-Switching HfO_2 Systems. *Electrochemical and Solid-State Letters* **14**, H244 (2011).
90. Titannitrid. https://www.chemie.de/lexikon/Titannitrid.html (accessed 10 Nov 2022).
91. Platin. https://www.chemie.de/lexikon/Platin.html (accessed 10 Nov 2022).
92. Siegel, S., Baeumer, C., Gutsche, A., Witzleben, M., Waser, R., Menzel, S. & Dittmann, R., Trade-Off Between Data Retention and Switching Speed in Resistive Switching ReRAM Devices. *Advanced Electronic Materials* **7**, 2000815 (2020).
93. Köllensperger, P., Karl, W., Ahmad, M., Pike, W. & Green, M., Patterning of platinum (Pt) thin films by chemical wet etching in Aqua Regia. *Journal of Micromechanics and Microengineering* **22**, 067001 (2012).
94. Kupfer. https://www.chemie.de/lexikon/Kupfer.html (accessed 10 Nov 2022).
95. Silber. https://www.chemie.de/lexikon/Silber.html (accessed 10 Nov 2022).

96. Haemori, M., Nagata, T. & Chikyow, T., Impact of Cu Electrode on Switching Behavior in a Cu/HfO_2/Pt Structure and Resultant Cu Ion Diffusion. *Applied Physics Express* **2**, 061401 (2009).
97. Yoon, J.-W., Yoon, J. H., Lee, J.-H. & Hwang, C. S., Impedance spectroscopic analysis on effects of partial oxidation of TiN bottom electrode and microstructure of amorphous and crystalline HfO_2 thin films on their bipolar resistive switching. *Nanoscale* **6**, 6668-6678 (2014).
98. Ielmini, D., Resistive switching memories based on metal oxides: mechanisms, reliability and scaling. *Semiconductor Science and Technology* **31**, 063002 (2016).
99. Ielmini, D., Bruchhaus, R. & Waser, R., Thermochemical resistive switching: materials, mechanisms, and scaling projections. *Phase Transitions* **84**, 570-602 (2011).
100. Chen, S. & Valov, I., Design of Materials Configuration for Optimizing Redox-Based Resistive Switching Memories. *Advanced Materials* **34**, e2105022 (2021).
101. Valov, I. & Kozicki, M. N., Cation-based resistance change memory. *Journal of Physics D: Applied Physics* **46**, 074005 (2013).
102. Tappertzhofen, S., Waser, R. & Valov, I., Impact of the Counter-Electrode Material on Redox Processes in Resistive Switching Memories. *ChemElectroChem* **1**, 1287-1292 (2014).
103. Goux, L. & Valov, I., Electrochemical processes and device improvement in conductive bridge RAM cells. *Physica Status Solidi (a)* **213**, 274-288 (2016).
104. Tsuruoka, T., Terabe, K., Hasegawa, T. & Aono, M., Forming and switching mechanisms of a cation-migration-based oxide resistive memory. *Nanotechnology* **21**, 425205 (2010).
105. Zhang, M., Long, S., Li, Y., Liu, Q., Lv, H., Miranda, E., Sune, J. & Liu, M., Analysis on the Filament Structure Evolution in Reset Transition of Cu/HfO_2/Pt RRAM Device. *Nanoscale Research Letters* **11**, 269 (2016).
106. Sassine, G., Nail, C., Blaise, P., Sklenard, B., Bernard, M., Gassilloud, R., Marty, A., Veillerot, M., Vallée, C., Nowak, E. & Molas, G., Hybrid-RRAM toward Next Generation of Nonvolatile Memory: Coupling of Oxygen Vacancies and Metal Ions. *Advanced Electronic Materials* **5**, 1800658 (2019).
107. Lee, J. S., Lee, S. & Noh, T. W., Resistive switching phenomena: A review of statistical physics approaches. *Applied Physics Reviews* **2**, 031303 (2015).
108. Wouters, D. J., Zhang, L., Fantini, A., Degraeve, R., Goux, L., Chen, Y. Y., Govoreanu, B., Kar, G. S., Groeseneken, G. V. & Jurczak, M., Analysis of complementary RRAM switching. *IEEE Electron Device Letters* **33**, 1186-1188 (2012).
109. Linn, E., Rosezin, R., Kugeler, C. & Waser, R., Complementary resistive switches for passive nanocrossbar memories. *Nature Materials* **9**, 403-406 (2010).
110. Lian, X., Miranda, E., Long, S., Perniola, L., Liu, M. & Suñé, J., Three-state resistive switching in HfO_2-based RRAM. *Solid-State Electronics* **98**, 38-44 (2014).
111. Long, S., Lian, X., Ye, T., Cagli, C., Perniola, L., Miranda, E., Liu, M. & Sune, J., Cycle-to-Cycle Intrinsic RESET Statistics in HfO_2-Based Unipolar RRAM Devices. *IEEE Electron Device Letters* **34**, 623-625 (2013).
112. Midya, R., Wang, Z., Zhang, J., Savel'ev, S. E., Li, C., Rao, M., Jang, M. H., Joshi, S., Jiang, H., Lin, P., Norris, K., Ge, N., Wu, Q., Barnell, M., Li, Z., Xin, H. L., Williams, R. S., Xia, Q. & Yang, J. J., Anatomy of Ag/Hafnia-Based Selectors with 10^{10} Nonlinearity. *Advanced Materials* **29**, 1604457 (2017).
113. Wang, Y., Zhou, G., Sun, B., Wang, W., Li, J., Duan, S. & Song, Q., Ag/HfO_x/Pt Unipolar Memristor for High-Efficiency Logic Operation. *The Journal of Physical Chemistry Letters* **13**, 8019-8025 (2022).
114. Lim, E. & Ismail, R., Conduction Mechanism of Valence Change Resistive Switching Memory: A Survey. *Electronics* **4**, 586-613 (2015).

115. Piros, E., Petzold, S., Zintler, A., Kaiser, N., Vogel, T., Eilhardt, R., Wenger, C., Molina-Luna, L. & Alff, L., Enhanced thermal stability of yttrium oxide-based RRAM devices with inhomogeneous Schottky-barrier. *Applied Physics Letters* **117**, 013504 (2020).
116. Yuan, F.-Y., Deng, N., Shih, C.-C., Tseng, Y.-T., Chang, T.-C., Chang, K.-C., Wang, M.-H., Chen, W.-C., Zheng, H.-X. & Wu, H., Conduction mechanism and improved endurance in HfO_2-based RRAM with nitridation treatment. *Nanoscale Research Letters* **12**, 1-6 (2017).
117. Cao, X., Li, X., Gao, X., Zhang, Y. W., Liu, X., Wang, Q. & Chen, L., Effects of the compliance current on the resistive switching behavior of TiO_2 thin films. *Applied Physics A* **97**, 883-887 (2009).
118. Tan, T., Guo, T., Wu, Z. & Liu, Z., Charge transport and bipolar switching mechanism in a Cu/HfO_2/Pt resistive switching cell. *Chinese Physics B* **25**, 117306 (2016).
119. Fu, Y., Xia, F., Jia, Y., Jia, C., Li, J., Dai, X., Fu, G., Zhu, B. & Liu, B., Bipolar resistive switching behavior of $La_{0.5}Sr_{0.5}CoO_{3-\sigma}$ films for nonvolatile memory applications. *Applied Physics Letters* **104**, 223505 (2014).
120. Yu, S., Guan, X. & Wong, H.-S. P., Conduction mechanism of TiN/HfO_x/Pt resistive switching memory: A trap-assisted-tunneling model. *Applied Physics Letters* **99**, 063507 (2011).
121. Kwan, C.-P., Street, M., Mahmood, A., Echtenkamp, W., Randle, M., He, K., Nathawat, J., Arabchigavkani, N., Barut, B. & Yin, S., Space-charge limited conduction in epitaxial chromia films grown on elemental and oxide-based metallic substrates. *AIP Advances* **9**, 055018 (2019).
122. Wang, C., Wu, H., Gao, B., Zhang, T., Yang, Y. & Qian, H., Conduction mechanisms, dynamics and stability in ReRAMs. *Microelectronic Engineering* **187**, 121-133 (2018).
123. Ruh, R. & Corfield, P. W., Crystal structure of monoclinic hafnia and comparison with monoclinic zirconia. *Journal of the American Ceramic Society* **53**, 126-129 (1970).
124. Ruh, R., Garrett, H., Domagala, R. & Tallan, N., The Svstern Zirconia-Hafnia. *Journal of the American Ceramic Society* **51**, 23-28 (1968).
125. Puurunen, R. L., Delabie, A., Van Elshocht, S., Caymax, M., Green, M. L., Brijs, B., Richard, O., Bender, H., Conard, T., Hoflijk, I., Vandervorst, W., Hellin, D., Vanhaeren, D., Zhao, C., De Gendt, S. & Heyns, M., Hafnium oxide films by atomic layer deposition for high-κ gate dielectric applications: Analysis of the density of nanometer-thin films. *Applied Physics Letters* **86**, 073116 (2005).
126. Jaffe, J. E., Bachorz, R. A. & Gutowski, M., Low-temperature polymorphs of ZrO_2 and HfO_2: A density-functional theory study. *Physical Review B* **72**, 14407 (2005).
127. Nukala, P., Wei, Y., de Haas, V., Guo, Q., Antoja-Lleonart, J. & Noheda, B., Guidelines for the stabilization of a polar rhombohedral phase in epitaxial $Hf_{0.5}Zr_{0.5}O_2$ thin films. *Ferroelectrics* **569**, 148-163 (2020).
128. Kaiser, N., Song, Y.-J., Vogel, T., Piros, E., Kim, T., Schreyer, P., Petzold, S., Valentí, R. & Alff, L., Crystal and electronic structure of oxygen vacancy stabilized rhombohedral hafnium oxide. *ACS Applied Electronic Materials* **5**, 754-763 (2023).
129. VESTA. https://jp-minerals.org/vesta/en/download.html (accessed 21 Nov 2022).
130. Lederer, M., Material development of doped hafnium oxide for non-volatile ferroelectric memory application. Dissertation, TU Dresden, Dresden, Germany (2022).
131. Lederer, M., Vogel, T., Kämpfe, T., Kaiser, N., Piros, E., Olivo, R., Ali, T., Petzold, S., Lehninger, D., Trautmann, C., Alff, L. & Seidel, K., Heavy ion irradiation induced phase transitions and their impact on the switching behavior of ferroelectric hafnia. *Journal of Applied Physics* **132**, 064102 (2022).
132. Sharath, S. U., Kurian, J., Komissinskiy, P., Hildebrandt, E., Bertaud, T., Walczyk, C., Calka, P., Schroeder, T. & Alff, L., Thickness independent reduced forming voltage in oxygen engineered HfO_2 based resistive switching memories. *Applied Physics Letters* **105**, 073505 (2014).

133. Valov, I., Interfacial interactions and their impact on redox-based resistive switching memories (ReRAMs). *Semiconductor Science and Technology* **32**, 093006 (2017).

134. Li, F. M., Bayer, B. C., Hofmann, S., Dutson, J. D., Wakeham, S. J., Thwaites, M. J., Milne, W. I. & Flewitt, A. J., High-k (k=30) amorphous hafnium oxide films from high rate room temperature deposition. *Applied Physics Letters* **98**, 252903 (2011).

135. McKenna, K., Shluger, A., Iglesias, V., Porti, M., Nafría, M., Lanza, M. & Bersuker, G., Grain boundary mediated leakage current in polycrystalline HfO_2 films. *Microelectronic Engineering* **88**, 1272-1275 (2011).

136. Bersuker, G., Yum, J., Vandelli, L., Padovani, A., Larcher, L., Iglesias, V., Porti, M., Nafría, M., McKenna, K., Shluger, A., Kirsch, P. & Jammy, R., Grain boundary-driven leakage path formation in HfO_2 dielectrics. *Solid-State Electronics* **65-66**, 146-150 (2011).

137. Winkler, R., Zintler, A., Petzold, S., Piros, E., Kaiser, N., Vogel, T., Nasiou, D., McKenna, K. P., Molina-Luna, L. & Alff, L., Controlling the Formation of Conductive Pathways in Memristive Devices. *Advanced Science* **9**, 2201806 (2022).

138. Sharath, S. U., Bertaud, T., Kurian, J., Hildebrandt, E., Walczyk, C., Calka, P., Zaumseil, P., Sowinska, M., Walczyk, D., Gloskovskii, A., Schroeder, T. & Alff, L., Towards forming-free resistive switching in oxygen engineered HfO_{2-x}. *Applied Physics Letters* **104**, (2014).

139. Hildebrandt, E., Kurian, J., Zimmermann, J., Fleissner, A., von Seggern, H. & Alff, L., Hafnium oxide thin films: Effect of growth parameters on oxygen and hafnium vacancies. *Journal of Vacuum Science & Technology B: Microelectronics and Nanometer Structures* **27**, (2009).

140. Gritsenko, V. A., Perevalov, T. V. & Islamov, D. R., Electronic properties of hafnium oxide: A contribution from defects and traps. *Physics Reports* **613**, 1-20 (2016).

141. Arun, N., Sangani, L. D. V., Vinod Kumar, K., Mangababu, A., Krishna, M. G., Pathak, A. P. & Nageswara Rao, S. V. S., Effects of swift heavy ion irradiation on the performance of HfO_2-based resistive random access memory devices. *Journal of Materials Science: Materials in Electronics* **32**, 2973-2986 (2021).

142. Rushchanskii, K. Z., Blügel, S. & Ležaić, M., Ab initio phase diagrams of Hf–O, Zr–O and Y–O: a comparative study. *Faraday discussions* **213**, 321-337 (2019).

143. McKenna, K., Optimal stoichiometry for nucleation and growth of conductive filaments in HfO_x. *Modelling and Simulation in Materials Science and Engineering* **22**, 025001 (2014).

144. Xue, K.-H., Blaise, P., Fonseca, L. R. & Nishi, Y., Prediction of semimetallic tetragonal Hf_2O_3 and Zr_2O_3 from first principles. *Physical Review Letters* **110**, 065502 (2013).

145. Kaiser, N., Vogel, T., Zintler, A., Petzold, S., Arzumanov, A., Piros, E., Eilhardt, R., Molina-Luna, L. & Alff, L., Defect-Stabilized Substoichiometric Polymorphs of Hafnium Oxide with Semiconducting Properties. *ACS Applied Materials & Interfaces* **14**, 1290-1303 (2021).

146. Zhang, H., Liu, L., Gao, B., Qiu, Y., Liu, X., Lu, J., Han, R., Kang, J. & Yu, B., Gd-doping effect on performance of HfO_2 based resistive switching memory devices using implantation approach. *Applied Physics Letters* **98**, 042105 (2011).

147. Wu, Z., Zhu, J., Zhou, Y. & Liu, X., Bipolar Resistive Switching Properties of $Hf_{0.5}Zr_{0.5}O_2$ Thin Film for Flexible Memory Applications. *physica status solidi (a)* **215**, 1700396 (2018).

148. Wu, Z., Zhu, J. & Liu, X., Resistive switching properties of $Hf_xZr_{1-x}O_2$ thin films for flexible memory applications. *Journal of Materials Science: Materials in Electronics* **28**, 10625-10629 (2017).

149. Wu, Z. & Zhu, J., Enhanced Unipolar Resistive Switching Characteristics of $Hf_{0.5}Zr_{0.5}O_2$ Thin Films with High ON/OFF Ratio. *Materials* **10**, 322 (2017).

150. Ryu, S. W., Cho, S., Park, J., Kwac, J., Kim, H. J. & Nishi, Y., Effects of ZrO_2 doping on HfO_2 resistive switching memory characteristics. *Applied Physics Letters* **105**, 072102 (2014).

151. Lee, C.-K., Cho, E., Lee, H.-S., Hwang, C. S. & Han, S., First-principles study on doping and phase stability of HfO_2. *Physical Review B* **78**, 012102 (2008).
152. Ulhas, S. S., Defect Engineering in HfO_2/TiN-based Resistive Random Access Memory (RRAM) Devices by Reactive Molecular Beam Epitaxy. Dissertation, TU Darmstadt, Darmstadt, Germany (2018).
153. Kim, Y.-M. & Lee, J.-S., Reproducible resistance switching characteristics of hafnium oxide-based nonvolatile memory devices. *Journal of Applied Physics* **104**, 114115 (2008).
154. Jung, Y. C., Seong, S., Lee, T., Kim, S. Y., Park, I.-S. & Ahn, J., Improved resistive switching characteristics of a Pt/HfO_2/Pt resistor by controlling anode interface with forming and switching polarity. *Applied Surface Science* **435**, 117-121 (2018).
155. Nagata, T., Haemori, M., Yamashita, Y., Yoshikawa, H., Iwashita, Y., Kobayashi, K. & Chikyow, T., Oxygen migration at Pt/HfO_2/Pt interface under bias operation. *Applied Physics Letters* **97**, 082902 (2010).
156. Jousseaume, V., Fantini, A., Nodin, J., Guedj, C., Persico, A., Buckley, J., Tirano, S., Lorenzi, P., Vignon, R. & Feldis, H., Comparative study of non-polar switching behaviors of NiO-and HfO_2-based oxide resistive-RAMs. in *2010 IEEE International Memory Workshop* 1-4 (IEEE, 2010).
157. Tutuncuoglu, G. & Mannodi-Kanakkithodi, A., Role of defects in resistive switching dynamics of memristors. *MRS Communications* **12**, 531-542 (2022).
158. Tsuruoka, T., Valov, I., Tappertzhofen, S., van den Hurk, J., Hasegawa, T., Waser, R. & Aono, M., Redox Reactions at Cu,Ag/Ta_2O_5 Interfaces and the Effects of Ta_2O_5 Film Density on the Forming Process in Atomic Switch Structures. *Advanced Functional Materials* **25**, 6374-6381 (2015).
159. Yang, X., Long, S., Zhang, K., Liu, X., Wang, G., Lian, X., Liu, Q., Lv, H., Wang, M., Xie, H., Sun, H., Sun, P., Suñé, J. & Liu, M., Investigation on the RESET switching mechanism of bipolar Cu/HfO_2/Pt RRAM devices with a statistical methodology. *Journal of Physics D: Applied Physics* **46**, 245107 (2013).
160. Saadi, M., Gonon, P., Vallée, C., Mannequin, C., Grampeix, H., Jalaguier, E., Jomni, F. & Bsiesy, A., On the mechanisms of cation injection in conducting bridge memories: The case of HfO_2 in contact with noble metal anodes (Au, Cu, Ag). *Journal of Applied Physics* **119**, 114501 (2016).
161. Saadi, M., Gonon, P., Vallée, C., Jomni, F., Jalaguier, E. & Bsiesy, A., Ag/HfO_2-based conductive bridge memories elaborated by atomic layer deposition: impact of inert electrode and HfO_2 crystallinity on resistive switching mechanisms. *Journal of Materials Science: Materials in Electronics* **31**, 13487-13495 (2020).
162. Wang, M., Lv, H., Liu, Q., Li, Y., Xie, H., Long, S., Zhang, K., Liu, X., Sun, H. & Yang, X., Study of one dimension thickness scaling on Cu/HfO_x/Pt based RRAM device performance. in *2012 4th IEEE International Memory Workshop* 1-3 (IEEE, 2012).
163. Butcher, B., He, X., Huang, M., Wang, Y., Liu, Q., Lv, H., Liu, M. & Wang, W., Proton-based total-dose irradiation effects on Cu/HfO_2:Cu/Pt ReRAM devices. *Nanotechnology* **21**, 475206 (2010).
164. Luo, Q., Xu, X., Liu, H., Lv, H., Gong, T., Long, S., Liu, Q., Sun, H., Banerjee, W. & Li, L., Cu BEOL compatible selector with high selectivity ($>10^7$), extremely low off-current (~pA) and high endurance ($>10^{10}$). in *2015 IEEE International Electron Devices Meeting (IEDM)* 10.14.11-10.14.14 (IEEE, 2015).
165. Wang, Y., Liu, Q., Long, S., Wang, W., Wang, Q., Zhang, M., Zhang, S., Li, Y., Zuo, Q., Yang, J. & Liu, M., Investigation of resistive switching in Cu-doped HfO_2 thin film for multilevel non-volatile memory applications. *Nanotechnology* **21**, 045202 (2010).
166. Valov, I. & Tsuruoka, T., Effects of moisture and redox reactions in VCM and ECM resistive switching memories. *Journal of Physics D: Applied Physics* **51**, 413001 (2018).
167. Wang, Z., Rao, M., Midya, R., Joshi, S., Jiang, H., Lin, P., Song, W., Asapu, S., Zhuo, Y., Li, C., Wu, H., Xia, Q. & Yang, J. J., Threshold Switching of Ag or Cu in Dielectrics:

Materials, Mechanism, and Applications. *Advanced Functional Materials* **28**, 1704862 (2017).

168. Banerjee, W., Kashir, A. & Kamba, S., Hafnium Oxide (HfO_2) – a Multifunctional Oxide: A Review on Prospect and Challenges of Hafnium Oxide in Resistive Switching and Ferroelectric Memories. *Small* **18**, 2107575 (2022).
169. Valasek, J., Piezo-electric and allied phenomena in Rochelle salt. *Physical Review* **17**, 475 (1921).
170. Ali, T., Polakowski, P., Büttner, T., Kämpfe, T., Rudolph, M., Pätzold, B., Hoffmann, R., Czernohorsky, M., Kühnel, K. & Steinke, P., Principles and challenges for binary oxide based ferroelectric memory FeFET. in *2019 IEEE 11th International Memory Workshop (IMW)* 1-4 (IEEE, 2019).
171. Lederer, M., Lehninger, D., Ali, T. & Kämpfe, T., Review on the microstructure of ferroelectric hafnium oxides. *physica status solidi (RRL) – Rapid Research Letters* **16**, 2200168 (2022).
172. Max, B., Pešić, M., Slesazeck, S. & Mikolajick, T., Interplay between ferroelectric and resistive switching in doped crystalline HfO_2. *Journal of Applied Physics* **123**, 134102 (2018).
173. Müller, J., Polakowski, P., Mueller, S. & Mikolajick, T., Ferroelectric Hafnium Oxide Based Materials and Devices: Assessment of Current Status and Future Prospects. *ECS Journal of Solid State Science and Technology* **4**, N30-N35 (2015).
174. Park, M. H., Schenk, T., Fancher, C. M., Grimley, E. D., Zhou, C., Richter, C., LeBeau, J. M., Jones, J. L., Mikolajick, T. & Schroeder, U., A comprehensive study on the structural evolution of HfO_2 thin films doped with various dopants. *Journal of Materials Chemistry C* **5**, 4677-4690 (2017).
175. Park, M. H., Chung, C.-C., Schenk, T., Richter, C., Opsomer, K., Detavernier, C., Adelmann, C., Jones, J. L., Mikolajick, T. & Schroeder, U., Effect of Annealing Ferroelectric HfO_2 Thin Films: In Situ, High Temperature X-Ray Diffraction. *Advanced Electronic Materials* **4**, 1800091 (2018).
176. Schenk, T., Anspoks, A., Jonane, I., Ignatans, R., Johnson, B. S., Jones, J. L., Tallarida, M., Marini, C., Simonelli, L., Hönicke, P., Richter, C., Mikolajick, T. & Schroeder, U., Local structural investigation of hafnia-zirconia polymorphs in powders and thin films by X-ray absorption spectroscopy. *Acta Materialia* **180**, 158-169 (2019).
177. Sang, X., Grimley, E. D., Schenk, T., Schroeder, U. & LeBeau, J. M., On the structural origins of ferroelectricity in HfO_2 thin films. *Applied Physics Letters* **106**, 162905 (2015).
178. Schroeder, U., Mittmann, T., Materano, M., Lomenzo, P. D., Edgington, P., Lee, Y. H., Alotaibi, M., West, A. R., Mikolajick, T., Kersch, A. & Jones, J. L., Temperature-Dependent Phase Transitions in $Hf_xZr_{1-x}O_2$ Mixed Oxides: Indications of a Proper Ferroelectric Material. *Advanced Electronic Materials* **8**, 2200265 (2022).
179. Cheng, Y., Gao, Z., Ye, K. H., Park, H. W., Zheng, Y., Zheng, Y., Gao, J., Park, M. H., Choi, J. H., Xue, K. H., Hwang, C. S. & Lyu, H., Reversible transition between the polar and antipolar phases and its implications for wake-up and fatigue in HfO_2-based ferroelectric thin film. *Nature Communications* **13**, 645 (2022).
180. Huan, T. D., Sharma, V., Rossetti, G. A. & Ramprasad, R., Pathways towards ferroelectricity in hafnia. *Physical Review B* **90**, 064111 (2014).
181. Materlik, R., Künneth, C. & Kersch, A., The origin of ferroelectricity in $Hf_{1-x}Zr_xO_2$: A computational investigation and a surface energy model. *Journal of Applied Physics* **117**, 134109 (2015).
182. Zarubin, S., Suvorova, E., Spiridonov, M., Negrov, D., Chernikova, A., Markeev, A. & Zenkevich, A., Fully ALD-grown $TiN/Hf_{0.5}Zr_{0.5}O_2/TiN$ stacks: Ferroelectric and structural properties. *Applied Physics Letters* **109**, 192903 (2016).

183. Hyuk Park, M., Joon Kim, H., Jin Kim, Y., Moon, T. & Seong Hwang, C., The effects of crystallographic orientation and strain of thin $Hf_{0.5}Zr_{0.5}O_2$ film on its ferroelectricity. *Applied Physics Letters* **104**, 072901 (2014).
184. Materano, M., Lomenzo, P. D., Kersch, A., Park, M. H., Mikolajick, T. & Schroeder, U., Interplay between oxygen defects and dopants: effect on structure and performance of HfO_2-based ferroelectrics. *Inorganic Chemistry Frontiers* **8**, 2650-2672 (2021).
185. Lehninger, D., Ali, T., Olivo, R., Lederer, M., Kämpfe, T., Mertens, K. & Seidel, K., Furnace annealed HfO_2-films for the integration of ferroelectric functionalities into the BEoL. in *2020 Joint Conference of the IEEE International Frequency Control Symposium and International Symposium on Applications of Ferroelectrics (IFCS-ISAF)* 1-3 (IEEE, 2020).
186. Mittmann, T., Materano, M., Chang, S. C., Karpov, I., Mikolajick, T. & Schroeder, U., Impact of Oxygen Vacancy Content in Ferroelectric HZO films on the Device Performance. in *2020 IEEE International Electron Devices Meeting (IEDM)* 18.14.11-18.14.14 (IEEE, 2020).
187. Baumgarten, L., Szyjka, T., Mittmann, T., Materano, M., Matveyev, Y., Schlueter, C., Mikolajick, T., Schroeder, U. & Müller, M., Impact of vacancies and impurities on ferroelectricity in PVD- and ALD-grown HfO_2 films. *Applied Physics Letters* **118**, 032903 (2021).
188. Materano, M., Mittmann, T., Lomenzo, P. D., Zhou, C., Jones, J. L., Falkowski, M., Kersch, A., Mikolajick, T. & Schroeder, U., Influence of Oxygen Content on the Structure and Reliability of Ferroelectric $Hf_xZr_{1-x}O_2$ Layers. *ACS Applied Electronic Materials* **2**, 3618-3626 (2020).
189. Islamov, D. R., Zalyalov, T. M., Orlov, O. M., Gritsenko, V. A. & Krasnikov, G. Y., Impact of oxygen vacancy on the ferroelectric properties of lanthanum-doped hafnium oxide. *Applied Physics Letters* **117**, 162901 (2020).
190. Lee, K., Park, K., Lee, H. J., Song, M. S., Lee, K. C., Namkung, J., Lee, J. H., Park, J. & Chae, S. C., Enhanced ferroelectric switching speed of Si-doped HfO_2 thin film tailored by oxygen deficiency. *Scientific Reports* **11**, 6290 (2021).
191. Mittmann, T., Michailow, M., Lomenzo, P. D., Gartner, J., Falkowski, M., Kersch, A., Mikolajick, T. & Schroeder, U., Stabilizing the ferroelectric phase in HfO_2-based films sputtered from ceramic targets under ambient oxygen. *Nanoscale* **13**, 912-921 (2021).
192. Mittmann, T., Materano, M., Lomenzo, P. D., Park, M. H., Stolichnov, I., Cavalieri, M., Zhou, C., Chung, C. C., Jones, J. L., Szyjka, T., Müller, M., Kersch, A., Mikolajick, T. & Schroeder, U., Origin of Ferroelectric Phase in Undoped HfO_2 Films Deposited by Sputtering. *Advanced Materials Interfaces* **6**, 1900042 (2019).
193. Gronenberg, O., Marquardt, R., Lamprecht, R., Ekici, Y., Schürmann, U., Kohlstedt, H. & Kienle, L., The impact of rapid thermal annealing for the ferroelectricity of undoped sputtered HfO_2 and its wake-up effect. *Journal of Applied Physics* **132**, 094101 (2022).
194. Xu, X., Huang, F. T., Qi, Y., Singh, S., Rabe, K. M., Obeysekera, D., Yang, J., Chu, M. W. & Cheong, S. W., Kinetically stabilized ferroelectricity in bulk single-crystalline HfO_2:Y. *Nature Materials* **20**, 826-832 (2021).
195. Lomenzo, P. D., Materano, M., Mittmann, T., Buragohain, P., Gruverman, A., Kiguchi, T., Mikolajick, T. & Schroeder, U., Harnessing Phase Transitions in Antiferroelectric ZrO_2 Using the Size Effect. *Advanced Electronic Materials* **8**, 2100556 (2021).
196. Wei, Y., Nukala, P., Salverda, M., Matzen, S., Zhao, H. J., Momand, J., Everhardt, A. S., Agnus, G., Blake, G. R. & Lecoeur, P., A rhombohedral ferroelectric phase in epitaxially strained $Hf_{0.5}Zr_{0.5}O_2$ thin films. *Nature materials* **17**, 1095-1100 (2018).
197. Bégon-Lours, L., Mulder, M., Nukala, P., De Graaf, S., Birkhölzer, Y. A., Kooi, B., Noheda, B., Koster, G. & Rijnders, G., Stabilization of phase-pure rhombohedral $HfZrO_4$ in pulsed laser deposited thin films. *Physical Review Materials* **4**, 043401 (2020).

198. Shimizu, T., Katayama, K., Kiguchi, T., Akama, A., Konno, T. J., Sakata, O. & Funakubo, H., The demonstration of significant ferroelectricity in epitaxial Y-doped HfO_2 film. *Scientific Reports* **6**, 32931 (2016).
199. Hsain, H. A., Lee, Y., Materano, M., Mittmann, T., Payne, A., Mikolajick, T., Schroeder, U., Parsons, G. N. & Jones, J. L., Many routes to ferroelectric HfO_2: A review of current deposition methods. *Journal of Vacuum Science & Technology A* **40**, 010803 (2022).
200. Zacharaki, C., Tsipas, P., Chaitoglou, S., Fragkos, S., Axiotis, M., Lagoyiannis, A., Negrea, R., Pintilie, L. & Dimoulas, A., Very large remanent polarization in ferroelectric $Hf_{1-x}Zr_xO_2$ grown on Ge substrates by plasma assisted atomic oxygen deposition. *Applied Physics Letters* **114**, 112901 (2019).
201. Hyuk Park, M., Joon Kim, H., Jin Kim, Y., Lee, W., Moon, T. & Seong Hwang, C., Evolution of phases and ferroelectric properties of thin $Hf_{0.5}Zr_{0.5}O_2$ films according to the thickness and annealing temperature. *Applied Physics Letters* **102**, 242905 (2013).
202. Lomenzo, P. D., Takmeel, Q., Moghaddam, S. & Nishida, T., Annealing behavior of ferroelectric Si-doped HfO_2 thin films. *Thin Solid Films* **615**, 139-144 (2016).
203. Park, M. H., Lee, Y. H., Mikolajick, T., Schroeder, U. & Hwang, C. S., Thermodynamic and kinetic origins of ferroelectricity in fluorite structure oxides. *Advanced Electronic Materials* **5**, 1800522 (2019).
204. Pešić, M., Fengler, F. P. G., Larcher, L., Padovani, A., Schenk, T., Grimley, E. D., Sang, X., LeBeau, J. M., Slesazeck, S., Schroeder, U. & Mikolajick, T., Physical Mechanisms behind the Field-Cycling Behavior of HfO_2-Based Ferroelectric Capacitors. *Advanced Functional Materials* **26**, 4601-4612 (2016).
205. Higashi, Y., Florent, K., Subirats, A., Kaczer, B., Di Piazza, L., Clima, S., Ronchi, N., McMitchell, S. R., Banerjee, K. & Celano, U., New insights into the imprint effect in FE-HfO_2 and its recovery. in *2019 IEEE International Reliability Physics Symposium (IRPS)* 1-7 (IEEE, 2019).
206. Ferroelectric Memory Company - Partners. https://ferroelectric-memory.com/company/partners/ (accessed 10 Nov 2022).
207. Shedding new light onto the structure of ferroelectric hafnium oxide films https://www.merckgroup.com/en/news-stories/news-in-electronics/electronicsmediaresources/innovation-thoughts/ferroelectric-hafnium-oxide-films.html (accessed 10 Nov 2022).
208. Le Gallo, M. & Sebastian, A., An overview of phase-change memory device physics. *Journal of Physics D: Applied Physics* **53**, 213002 (2020).
209. Noé, P., Vallée, C., Hippert, F., Fillot, F. & Raty, J.-Y., Phase-change materials for non-volatile memory devices: from technological challenges to materials science issues. *Semiconductor Science and Technology* **33**, 013002 (2017).
210. Shportko, K., Kremers, S., Woda, M., Lencer, D., Robertson, J. & Wuttig, M., Resonant bonding in crystalline phase-change materials. *Nature Materials* **7**, 653-658 (2008).
211. Prazakova, L., Nolot, E., Martinez, E., Fillot, F., Rouchon, D., Rochat, N., Bernard, M., Sabbione, C., Morel, D. & Bernier, N., Temperature driven structural evolution of Ge-rich GeSbTe alloys and role of N-doping. *Journal of Applied Physics* **128**, 215102 (2020).
212. Cecchi, S., Lopez Garcia, I., Mio, A. M., Zallo, E., Abou El Kheir, O., Calarco, R., Bernasconi, M., Nicotra, G. & Privitera, S. M. S., Crystallization and Electrical Properties of Ge-Rich GeSbTe Alloys. *Nanomaterials* **12**, 631 (2022).
213. Prazakova, L., Nolot, E., Martinez, E., Rouchon, D., Fillot, F., Bernier, N., Elizalde, R., Bernard, M. & Navarro, G., The effect of Ge content on structural evolution of Ge-rich GeSbTe alloys at increasing temperature. *Materialia* **21**, 101345 (2022).
214. Zuliani, P., Palumbo, E., Borghi, M., Dalla Libera, G. & Annunziata, R., Engineering of chalcogenide materials for embedded applications of Phase Change Memory. *Solid-State Electronics* **111**, 27-31 (2015).

215. V. Sousa, G. Navarro, N. Castellani, M. Coué, O. Cueto, C. Sabbione, P. Noé, L. Perniola, S. Blonkowski, P. Zuliani & Annunziata, R., Operation Fundamentals in 12Mb Phase Change Memory Based on Innovative Ge-rich GST Materials Featuring High Reliability Performance. in *2015 Symposium on VLSI Technology Digest of Technical Papers (VLSI Technology)* T98-T99 2015).
216. Ovshinsky, S. R., Reversible Electrical Switching Phenomena in Disordered Structures. *Physical Review Letters* **21**, 1450-1453 (1968).
217. Servalli, G., A 45nm generation phase change memory technology. in *2009 IEEE International Electron Devices Meeting (IEDM)* 1-4 (IEEE, 2009).
218. Choi, Y., Song, I., Park, M.-H., Chung, H., Chang, S., Cho, B., Kim, J., Oh, Y., Kwon, D. & Sunwoo, J., A 20nm 1.8V 8Gb PRAM with 40MB/s program bandwidth. in *2012 IEEE International Solid-State Circuits Conference* 46-48 (IEEE, 2012).
219. Navarro, G., Bourgeois, G., Kluge, J., Serra, A. L., Verdy, A., Garrione, J., Cyrille, M. C., Bernier, N., Jannaud, A., Sabbione, C., Bernard, M., Nolot, E., Fillot, F., Noé, P., Fellouh, L., Rodriguez, G., Beugin, V., Cueto, O., Castellani, N., Coignus, J., Delaye, V., Socquet-Clerc, C., Magis, T., Boixaderas, C., Barnola, S. & Nowak, E., Phase-Change Memory: Performance, Roles and Challenges. in *IEEE International Memory Workshop (IMW)* 1-4 2018).
220. Seok, J. Y., Song, S. J., Yoon, J. H., Yoon, K. J., Park, T. H., Kwon, D. E., Lim, H., Kim, G. H., Jeong, D. S. & Hwang, C. S., A Review of Three-Dimensional Resistive Switching Cross-Bar Array Memories from the Integration and Materials Property Points of View. *Advanced Functional Materials* **24**, 5316-5339 (2014).
221. Minguet Lopez, J., Rafhay, Q., Dampfhoffer, M., Reganaz, L., Castellani, N., Meli, V., Martin, S., Grenouillet, L., Navarro, G., Magis, T., Carabasse, C., Hirtzlin, T., Vianello, E., Deleruyelle, D., Portal, J. M., Molas, G. & Andrieu, F., 1S1R Optimization for High-Frequency Inference on Binarized Spiking Neural Networks. *Advanced Electronic Materials* **8**, 2200323 (2022).
222. Zhu, M., Ren, K. & Song, Z., Ovonic threshold switching selectors for three-dimensional stackable phase-change memory. *MRS Bulletin* **44**, 715-720 (2019).
223. Banerjee, W., Kim, S. H., Lee, S., Lee, S., Lee, D. & Hwang, H., Deep Insight into Steep-Slope Threshold Switching with Record Selectivity ($>4\times10^{10}$) Controlled by Metal-Ion Movement through Vacancy-Induced-Percolation Path: Quantum-Level Control of Hybrid-Filament. *Advanced Functional Materials* **31**, 2104054 (2021).
224. Shukla, N., Ghosh, R. K., Grisafe, B. & Datta, S., Fundamental mechanism behind volatile and non-volatile switching in metallic conducting bridge RAM. in *2017 IEEE International Electron Devices Meeting (IEDM)* 4.3. 1-4.3. 4 (IEEE, 2017).
225. Stassinopoulos, E. & Raymond, J. P., The space radiation environment for electronics. *Proceedings of the IEEE* **76**, 1423-1442 (1988).
226. Lang, M., Djurabekova, F., Medvedev, N., Toulemonde, M. & Trautmann, C., *Fundamental phenomena and applications of swift heavy ion irradiations* in *Comprehensive Nuclear Materials,* R. J. M. Konings, R. E. Stoller, Eds. (Elsevier, ebook, 2020), pp. 485-516.
227. Swordy, S. P., The energy spectra and anisotropies of cosmic rays. *Space Science Reviews* **99**, 85-94 (2001).
228. Ziegler, J. F., Terrestrial cosmic ray intensities. *IBM Journal of Research and Development* **42**, 117-140 (1998).
229. Spohr, R., *Ion tracks and microtechnology: principles and applications*. (Vieweg, Braunschweig, ed. 1, 1990), pp. 284.
230. Toulemonde, M., Trautmann, C., Balanzat, E., Hjort, K. & Weidinger, A., Track formation and fabrication of nanostructures with MeV-ion beams. *Nuclear Instruments and Methods in Physics Research Section B: Beam Interactions with Materials and Atoms* **216**, 1-8 (2004).
231. Trautmann, C., *Micro-and nanoengineering with ion tracks* in *Ion Beams in Nanoscience and Technology*. (Springer, Berlin, Heidelberg, 2009), pp. 369-387.

232. Sigmund, P., *Stopping of heavy ions: a theoretical approach*. (Springer, Berlin, Heidelberg, 2004), pp. 178.
233. Fleischer, R. L., Price, P. B. & Walker, R. M., *Nuclear tracks in solids: principles and applications*. (University of California Press, Berkeley, ed. 1, reprint, 2022), pp. 632.
234. Gervais, B. & Bouffard, S., Simulation of the primary stage of the interaction of swift heavy ions with condensed matter. *Nuclear Instruments and Methods in Physics Research Section B: Beam Interactions with Materials and Atoms* **88**, 355-364 (1994).
235. Ziegler, J. F., Ziegler, M. D. & Biersack, J. P., SRIM – The stopping and range of ions in matter (2010). *Nuclear Instruments and Methods in Physics Research Section B: Beam Interactions with Materials and Atoms* **268**, 1818-1823 (2010).
236. Silk, E. & Barnes, R., Examination of fission fragment tracks with an electron microscope. *Philosophical Magazine* **4**, 970-972 (1959).
237. Balamurugan, B., Mehta, B., Avasthi, D., Singh, F., Arora, A. K., Rajalakshmi, M., Raghavan, G., Tyagi, A. & Shivaprasad, S., Modifying the nanocrystalline characteristics—structure, size, and surface states of copper oxide thin films by high-energy heavy-ion irradiation. *Journal of Applied Physics* **92**, 3304-3310 (2002).
238. Benyagoub, A., Swift heavy ion induced crystalline-to-crystalline phase transition in zirconia and hafnia: a comparative study. *Nuclear Instruments and Methods in Physics Research Section B: Beam Interactions with Materials and Atoms* **218**, 451-456 (2004).
239. Benyagoub, A., Evidence of an ion-beam induced crystalline-to-crystalline phase transformation in hafnia. *The European Physical Journal B - Condensed Matter* **34**, 395-398 (2003).
240. Schuster, B., Oxide ceramics under extreme pressure and radiation conditions. Dissertation, TU Darmstadt, Darmstadt, Germany (2011).
241. Trautmann, C., Lecture: Materials research with energetic ion beams - Basic aspects and nanotechnology. (TU Darmstadt, Materials Science, 2021).
242. Fleischer, R., Price, P. & Walker, R., Ion explosion spike mechanism for formation of charged-particle tracks in solids. *Journal of Applied Physics* **36**, 3645-3652 (1965).
243. Toulemonde, M., Paumier, E. & Dufour, C., Thermal spike model in the electronic stopping power regime. *Radiation Effects and Defects in Solids* **126**, 201-206 (2006).
244. Toulemonde, M., Transient thermal processes in heavy ion irradiation of crystalline inorganic insulators. *Nuclear Instruments and Methods in Physics Research B* **166**, 903-912 (2000).
245. Toulemonde, M., Dufour, C. & Paumier, E., Transient thermal process after a high-energy heavy-ion irradiation of amorphous metals and semiconductors. *Physical Review B* **46**, 14362-14369 (1992).
246. Benyagoub, A., Levesque, F., Couvreur, F., Gibert-Mougel, C., Dufour, C. & Paumier, E., Evidence of a phase transition induced in zirconia by high energy heavy ions. *Applied Physics Letters* **77**, 3197-3199 (2000).
247. Garvie, R. C. & Nicholson, P. S., Phase analysis in zirconia systems. *Journal of the American Ceramic Society* **55**, 303-305 (1972).
248. Gibbons, J. F., Ion implantation in semiconductors—Part II: Damage production and annealing. *Proceedings of the IEEE* **60**, 1062-1096 (1972).
249. Dhanunjaya, M., Avasthi, D. K., Pathak, A. P., Khan, S. A. & Nageswara Rao, S. V. S., Grain fragmentation and phase transformations in hafnium oxide induced by swift heavy ion irradiation. *Applied Physics A* **124**, 1-10 (2018).
250. Dhanunjaya, M., Khan, S. A., Pathak, A. P., Avasthi, D. K. & Nageswara Rao, S. V. S., Ion induced crystallization and grain growth of hafnium oxide nano-particles in thin-films deposited by radio frequency magnetron sputtering. *Journal of Physics D: Applied Physics* **50**, 505301 (2017).
251. Li, Z., Zeng, J., Sun, Y., Liu, J., Zhai, P., Liu, T., Bi, J., Zhang, Z., Zhang, S., Hu, P. & Xu, L., Latent Reliability Degradation of Ultrathin Amorphous HfO_2 Dielectric After Heavy Ion

Irradiation: The Impact of Nano-Crystallization. *IEEE Electron Device Letters* **40**, 1634-1637 (2019).

252. Suvorova, E. I., Uvarov, O. V., Arkharova, N. A., Ibrayeva, A. D., Skuratov, V. A. & Buffat, P. A., Structure evolution, bandgap, and dielectric function in La-doped hafnium oxide thin layer subjected to swift Xe ion irradiation. *Journal of Applied Physics* **128**, (2020).
253. Yang, X., Bi, J., Xu, Y., Xi, K. & Ji, L., The effects of proton radiation on aluminum oxide/zirconium-doped hafnium oxide stacked ferroelectric tunneling junctions. *Applied Physics Express* **14**, 061001 (2021).
254. Wang, Y., Huang, F., Hu, Y., Cao, R., Shi, T., Liu, Q., Bi, L. & Liu, M., Proton Radiation Effects on Y-Doped HfO_2-Based Ferroelectric Memory. *IEEE Electron Device Letters* **39**, 823-826 (2018).
255. Vinod Kumar, K., Arun, N., Mangababu, A., Ojha, S., Nageswara Rao, S. V. S. & Pathak, A. P., 120 MeV Ag ion irradiation induced intermixing, grain fragmentation in HfO_2/GaO_x thin films and consequent effects on the electrical properties of HfO_2/GaO_x/Si-based MOS capacitors. *Radiation Effects and Defects in Solids* **175**, 150-159 (2020).
256. De Bastiani, R., Piro, A. M., Grimaldi, M. G. & Rimini, E., Amorphization kinetics of $Ge_2Sb_2Te_5$ thin film induced by ion implantation. *Nuclear Instruments and Methods in Physics Research Section B: Beam Interactions with Materials and Atoms* **257**, 572-576 (2007).
257. De Bastiani, R., Piro, A. M., Crupi, I., Grimaldi, M. G. & Rimini, E., Effect of ion irradiation on the stability of amorphous $Ge_2Sb_2Te_5$ thin films. *Nuclear Instruments and Methods in Physics Research Section B: Beam Interactions with Materials and Atoms* **266**, 2511-2514 (2008).
258. Kanda, N., Thakur, A., Singh, F. & Singh, A. P., Effect of ion irradiation on the optical properties of Ag-doped $Ge_2Sb_2Te_5$ (GST) thin films. *Nuclear Instruments and Methods in Physics Research Section B: Beam Interactions with Materials and Atoms* **467**, 40-43 (2020).
259. Gerardin, S., Bagatin, M., Paccagnella, A., Grurmann, K., Gliem, F., Oldham, T. R., Irom, F. & Nguyen, D. N., Radiation Effects in Flash Memories. *IEEE Transactions on Nuclear Science* **60**, 1953-1969 (2013).
260. He, X., Wang, W., Butcher, B., Tanachutiwat, S. & Geer, R. E., Superior TID Hardness in TiN/HfO_2/TiN ReRAMs After Proton Radiation. *IEEE Transactions on Nuclear Science* **59**, 2550-2555 (2012).
261. Gerardin, S. & Paccagnella, A., Present and Future Non-Volatile Memories for Space. *IEEE Transactions on Nuclear Science* **57**, 3016-3039 (2010).
262. Dodd, P. E., Shaneyfelt, M. R., Schwank, J. R. & Felix, J. A., Current and Future Challenges in Radiation Effects on CMOS Electronics. *IEEE Transactions on Nuclear Science* **57**, 1747-1763 (2010).
263. Marinella, M. J., Radiation Effects in Advanced and Emerging Nonvolatile Memories. *IEEE Transactions on Nuclear Science* **68**, 546-572 (2021).
264. Bi, J. S., Han, Z. S., Zhang, E. X., McCurdy, M. W., Reed, R. A., Schrimpf, R. D., Fleetwood, D. M., Alles, M. L., Weller, R. A., Linten, D., Jurczak, M. & Fantini, A., The Impact of X-Ray and Proton Irradiation on HfO_2/Hf-Based Bipolar Resistive Memories. *IEEE Transactions on Nuclear Science* **60**, 4540-4546 (2013).
265. Weeden-Wright, S. L., Bennett, W. G., Hooten, N. C., Zhang, E. X., McCurdy, M. W., King, M. P., Weller, R. A., Mendenhall, M. H., Alles, M. L., Linten, D., Jurczak, M., Degraeve, R., Fantini, A., Reed, R. A., Fleetwood, D. M. & Schrimpf, R. D., TID and Displacement Damage Resilience of 1T1R HfO_2/Hf Resistive Memories. *IEEE Transactions on Nuclear Science* **61**, 2972-2978 (2014).
266. Fang, R., Gonzalez Velo, Y., Chen, W., Holbert, K. E., Kozicki, M. N., Barnaby, H. & Yu, S., Total ionizing dose effect of γ-ray radiation on the switching characteristics and filament stability of HfO_x resistive random access memory. *Applied Physics Letters* **104**, 183507 (2014).

267. Hu, S., Liu, Y., Chen, T., Guo, Q., Li, Y.-D., Zhang, X.-Y., Deng, L., Yu, Q., Yin, Y. & Hosaka, S., γ-Ray Radiation Effects on an HfO_2-Based Resistive Memory Device. *IEEE Transactions on Nanotechnology* **17**, 61-64 (2017).
268. Alayan, M., Bagatin, M., Gerardin, S., Paccagnella, A., Larcher, L., Vianello, E., Nowak, E., De Salvo, B. & Perniola, L., Experimental and Simulation Study of the Effects of Heavy-ion Irradiation on HfO_2-based RRAM Cells. *IEEE Transactions on Nuclear Science* **64**, 2038-2045 (2017).
269. Petzold, S., Sharath, S. U., Lemke, J., Hildebrandt, E., Trautmann, C. & Alff, L., Heavy Ion Radiation Effects on Hafnium Oxide-Based Resistive Random Access Memory. *IEEE Transactions on Nuclear Science* **66**, 1715-1718 (2019).
270. He, X. & Geer, R. E., Heavy Ion Radiation Effects on TiN/HfO_2/W RRAM. in *2013 IEEE Aerospace Conference* 1-7 (IEEE, 2013).
271. Nimmala, A., Pathak, A. P., Ghanashyam Krishna, M., Motapothula, M. & Sunkaranam, V. S. N. R., Radiation Response of HfO_x-Based Resistive Random Access Memory (RRAM) Devices. *ACS Applied Electronic Materials* **4**, 5594-5601 (2022).
272. Bennett, W. G., Hooten, N. C., Schrimpf, R. D., Reed, R. A., Mendenhall, M. H., Alles, M. L., Bi, J., Zhang, E. X., Linten, D. & Jurzak, M., Single-and Multiple-Event Induced Upsets in HfO_2/Hf 1T1R RRAM. *IEEE Transactions on Nuclear Science* **61**, 1717-1725 (2014).
273. Yao, K., Yue, S., Zhang, Y., Wang, L., Li, J., Han, X. & Zha, Q., Single-Event Effects Induced by Heavy Ions in 40nm Resistive Random Access Memory. in *2022 IEEE 6th Advanced Information Technology, Electronic and Automation Control Conference (IAEAC)* 1437-1441 (IEEE, 2022).
274. Li, Z., Jiao, Y., Li, J., Cai, C., Liu, Y., Zhao, S., Fan, X. & Liu, J., The reliabilities of HfO_2-based ferroelectric devices under swift heavy ion irradiation. *Japanese Journal of Applied Physics* **61**, 070911 (2022).
275. Rodgers, J., Rockett, L., Maimon, J., Storey, T. & Nixon, P., Characterization and Qualification of Radiation Hardened Nonvolatile Phase Change Memory Technology. in *2010 IEEE Aerospace Conference* 1-8 (IEEE, 2010).
276. Rodgers, J., Maimon, J., Storey, T., Lee, D., Graziano, M., Rockett, L. & Hunt, K., A 4-Mb Non-Volatile Chalcogenide Random Access Memory Designed for Space Applications: Project Status Update. in *2008 9th Annual Non-Volatile Memory Technology Symposium (NVMTS)* 1-6 (IEEE, 2008).
277. Gasperin, A., Paccagnella, A., Schwank, J. R., Vizkelethy, G., Ottogalli, F. & Pellizzer, F., Analysis of Proton and Heavy-Ion Irradiation Effects on Phase Change Memories With MOSFET and BJT Selectors. *IEEE Transactions on Nuclear Science* **55**, 3189-3196 (2008).
278. Gerardin, S., Bagatin, M., Paccagnella, A., Visconti, A., Bonanomi, M., Beltrami, S. & Ferlet-Cavrois, V., Upsets in Phase Change Memories Due to High-LET Heavy Ions Impinging at an Angle. *IEEE Transactions on Nuclear Science* **61**, 3491-3496 (2014).
279. Gerardin, S., Bagatin, M., Paccagnella, A., Visconti, A., Bonanomi, M., Pellizzer, F., Vela, M. & Ferlet-Cavrois, V., Single Event Effects in 90-nm Phase Change Memories. *IEEE Transactions on Nuclear Science* **58**, 2755-2760 (2011).
280. Proton Irradiation of the 16GB Intel Optane SSD. https://ntrs.nasa.gov/api/citations/20180000932/downloads/20180000932.pdf (accessed 20 Aug 2022).
281. Serra, A. L., Vogel, T., Lefevre, G., Petzold, S., Kaiser, N., Bourgeois, G., Cyrille, M. C., Alff, L., Trautmann, C., Vallee, C., Sylvain, D., Charpin-Nicolle, C., Navarro, G. & Nowak, E., Heavy Ions Radiation Effects on 4kb Phase-Change Memory. in *2020 20th European Conference on Radiation and Its Effects on Components and Systems (RADECS)* 1-4 (IEEE, 2020).
282. Cho, A. Y. & Arthur, J., Molecular beam epitaxy. *Progress in Solid State Chemistry* **10**, 157-191 (1975).

283. Buckow, A., Retzlaff, R., Kurian, J. & Alff, L., Growth of superconducting epitaxial $LaNi_xBi_2$ pnictide thin films with a Bi square net layer by reactive molecular beam epitaxy. *Superconductor Science and Technology* **26**, 015014 (2013).
284. Alff, L., Klein, A., Komissinskiy, P. & Kurian, J., Vapor-Phase Deposition of Oxides. *Ceramics Science and Technology*, 267-290 (2013).
285. Schlom, D. G., Perspective: Oxide molecular-beam epitaxy rocks! *APL Materials* **3**, 062403 (2015).
286. Lu, C. & Czanderna, A. W., *Applications of piezoelectric quartz crystal microbalances*. (Elsevier, Amsterdam, ed. 1, reprint, 2012), pp. 393.
287. Ichimiya, A. & Cohen, P. I., *Reflection high-energy electron diffraction*. (Cambridge University Press, Cambridge, ed. 1, 2004).
288. Rockett, A., *The materials science of semiconductors*. (Springer, New York, ed. 1, 2007).
289. Ohring, M., Substrate surfaces and thin-film nucleation. *Materials Science of Thin Films: Deposition & Structure* **2**, 357-415 (2002).
290. Tang, F., Parker, T., Wang, G. & Lu, T., Surface texture evolution of polycrystalline and nanostructured films: RHEED surface pole figure analysis. *Journal of Physics D: Applied Physics* **40**, R427 (2007).
291. Chen, W.-C., Lin, Y.-R., Guo, X.-J. & Wu, S.-T., Heteroepitaxial TiN of Very Low Mosaic Spread on Al_2O_3. *Japanese Journal of Applied Physics* **42**, 208-212 (2003).
292. Shin, C.-S., Rudenja, S., Gall, D., Hellgren, N., Lee, T.-Y., Petrov, I. & Greene, J., Growth, surface morphology, and electrical resistivity of fully strained substoichiometric epitaxial TiN_x ($0.67\leqslant x< 1.0$) layers on MgO (001). *Journal of Applied Physics* **95**, 356-362 (2004).
293. Vogel, T., Kaiser, N., Petzold, S., Piros, E., Guillaume, N., Lefevre, G., Charpin-Nicolle, C., David, S., Vallee, C., Nowak, E., Trautmann, C. & Alff, L., Defect-induced phase transition in hafnium oxide thin films: comparing heavy ion irradiation and oxygen engineering effects. *IEEE Transactions on Nuclear Science* **68**, 1542-1547 (2021).
294. Behera, A., Aich, S. & Theivasanthi, T., *Magnetron sputtering for development of nanostructured materials* in *Design, Fabrication, and Characterization of Multifunctional Nanomaterials,* N. K. S. Thomas, A. R. Abraham, Ed. (Elsevier, Amsterdam, 2022), pp. 177-199.
295. Vossen, J., Control of film properties by rf-sputtering techniques. *Journal of Vacuum Science and Technology* **8**, S12-S30 (1971).
296. Ohring, M., *Plasma and ion beam processing of thin films* in *Materials Science of Thin Films*. (Elsevier, Amsterdam, 2002), pp. 203-275.
297. Fonash, S. J., An overview of dry etching damage and contamination effects. *Journal of The Electrochemical Society* **137**, 3885 (1990).
298. Schematic of the UNILAC at GSI. http://www-bd.gsi.de/dokuwiki/lib/exe/fetch.php?media=projects:bif-monitor:unilac_bif_new_3.png (accessed 14 Nov 2022).
299. UNILAC overview. https://www.gsi.de/en/work/beschleunigerbetrieb/beschleuniger/unilac/unilac (accessed 14 Nov 2022).
300. linear accelerator. https://www.gsi.de/en/researchaccelerators/accelerator_facility/linear_accelerator (accessed 14 Nov 2022).
301. accelorator facility. https://www.gsi.de/en/researchaccelerators/accelerator_facility (accessed 14 Nov 2022).
302. Stoller, R. E., Toloczko, M. B., Was, G. S., Certain, A. G., Dwaraknath, S. & Garner, F. A., On the use of SRIM for computing radiation damage exposure. *Nuclear Instruments and Methods in Physics Research Section B: Beam Interactions with Materials and Atoms* **310**, 75-80 (2013).

303. Harrington, G. F. & Santiso, J., Back-to-Basics tutorial: X-ray diffraction of thin films. *Journal of Electroceramics* **47**, 141-163 (2021).
304. Yasaka, M., X-ray thin-film measurement techniques. *The Rigaku Journal* **26**, 1-9 (2010).
305. Zaumseil, P., RCRefSim (Rocking curve and reflectivity simulation) software. (IHP Frankfurt Oder, Innovations for High Performance Microelectronics, 2005).
306. Watts, J. F. & Wolstenholme, J., *An introduction to surface analysis by XPS and AES*. (John Wiley & Sons, Hoboken, ed. 2, 2019), pp. 288.
307. Van der Heide, P., *X-ray photoelectron spectroscopy: an introduction to principles and practices*. (John Wiley & Sons, Hoboken, ed. 1, 2011), pp. 264.
308. Seah, M., The quantitative analysis of surfaces by XPS: a review. *Surface and Interface Analysis* **2**, 222-239 (1980).
309. Barr, T. L. & Seal, S., Nature of the use of adventitious carbon as a binding energy standard. *Journal of Vacuum Science & Technology A: Vacuum, Surfaces, and Films* **13**, 1239-1246 (1995).
310. CASA XPS manual, CASA XPS software Ltd (2009). http://www.casaxps.com/ebooks/XPS%20AES%20Book%20new%20margins%20rev%201.2%20for%20web.pdf (accessed 10 Aug 2022).
311. Morant, C., Galan, L. & Sanz, J., An XPS study of the initial stages of oxidation of hafnium. *Surface and Interface Analysis* **16**, 304-308 (1990).
312. Moulder, J. F., Stickle, W. F., Sobol, P. E. & Bomben, K. D., *Handbook of X-ray photoelectron spectroscopy*. (Perkin-Elmer Corporation, Eden Prairie, Minnesota, ed. 1, 1992), pp. 260.
313. Fultz, B. & Howe, J. M., *Transmission electron microscopy and diffractometry of materials*. (Springer, Berlin, Heidelberg, ed. 4, 2012), pp. 748.
314. Carter, C. B. & Williams, D. B., *Transmission electron microscopy: Diffraction, imaging, and spectrometry*. (Springer, Basel, ed. 1, 2016), pp. 518.
315. Molina-Luna, L., Lecture: Scanning Transmission Electron Microscopy (STEM) for Materials Science. (TU Darmstadt, Materials Science, 2020).
316. Pennycook, S. J., *Structure determination through Z-contrast microscopy* in *Advances in imaging and electron physics,* P. W. Hawkes, P. G. Merli, M. Calestani, M. Vittori-Antisari, Eds. (Elsevier, Amsterdam, 2002), pp. 173-206.
317. Viladot, D., Veron, M., Gemmi, M., Peiro, F., Portillo, J., Estrade, S., Mendoza, J., Llorca-Isern, N. & Nicolopoulos, S., Orientation and phase mapping in the transmission electron microscope using precession-assisted diffraction spot recognition: state-of-the-art results. *Journal of Microscopy* **252**, 23-34 (2013).
318. Cautaerts, N., Crout, P., Ånes, H. W., Prestat, E., Jeong, J., Dehm, G. & Liebscher, C. H., Free, flexible and fast: Orientation mapping using the multi-core and GPU-accelerated template matching capabilities in the python-based open source 4D-STEM analysis toolbox Pyxem. *Ultramicroscopy* **237**, 113517 (2022).
319. Ophus, C., Four-dimensional scanning transmission electron microscopy (4D-STEM): From scanning nanodiffraction to ptychography and beyond. *Microscopy and Microanalysis* **25**, 563-582 (2019).
320. Spurgeon, S. R., Ophus, C., Jones, L., Petford-Long, A., Kalinin, S. V., Olszta, M. J., Dunin-Borkowski, R. E., Salmon, N., Hattar, K. & Yang, W.-C. D., Towards data-driven next-generation transmission electron microscopy. *Nature Materials* **20**, 274-279 (2021).
321. Zintler, A., Investigating the influence of microstructure and grain boundaries on electric properties in thin film oxide RRAM devices–A component specific approach. Dissertation, TU Darmstadt, Darmstadt, Germany (2022).
322. Zintler, A., Eilhardt, R., Wang, S., Krajnak, M., Schramowski, P., Stammer, W., Petzold, S., Kaiser, N., Kersting, K., Alff, L. & Molina-Luna, L., Machine Learning Assisted Pattern Matching: Insight into Oxide Electronic Device Performance by Phase Determination in 4D-STEM Datasets. *Microscopy and Microanalysis* **26**, 1908-1909 (2020).

323. Krajnak, M., Blazit, J.-D., Zintler, A., Eilhardt, R., Weiss, J., Cosart, D., Molina-Luna, L., Tencé, M., Gloter, A., Allen, C. & McGrouther, D., Transforming Transmission Electron Microscopy with MerlinEM Electron Counting Detector. *Microscopy and Microanalysis* **26**, 1944-1945 (2020).
324. HyperSpy. https://zenodo.org/record/4923970#.YgP0E_gxkUF (accessed 28 Feb 2022).
325. OpenCV. https://opencv.org/ (accessed 28 Feb 2022).
326. Vogel, T., Zintler, A., Kaiser, N., Guillaume, N., Lefèvre, G., Lederer, M., Serra, A. L., Piros, E., Kim, T., Schreyer, P., Eilhardt, R., Nasiou, D., Olivio, R., Ali, T., Lehninger, D., Arzumanov, A., Charpin-Nicolle, C., Bourgeois, G., Grenouillet, L., Cyrille, M.-C., Navarro, G., Seidel, K., Kämpfe, T., Petzold, S., Trautmann, C., Molina-Luna, L. & Alff, L., Integration of labeled 4D-STEM SPED data for confirmation of phase identification. *TU datalib*, DOI 10.48328/tudatalib-48896 (2022).
327. Zintler, A., Eilhardt, R., Petzold, S., Kaiser, N., Ulhas, S., Alff, L. & Molina-Luna, L., Correlation of Structural Modifications by Multiscale Phase Mapping in Filamentary Type HfO_2-based RRAM: Towards a Component Specific in situ TEM Investigation. *Microscopy and Microanalysis* **25**, 1842-1843 (2019).
328. Prume, K., Schmitz, T. & Tiedke, S., *Electrical characterization of ferroelectrics* in *Polar Oxides*. (Wiley, online, 2005), pp. 53-75.
329. Schenk, T., Yurchuk, E., Mueller, S., Schroeder, U., Starschich, S., Böttger, U. & Mikolajick, T., About the deformation of ferroelectric hystereses. *Applied Physics Reviews* **1**, 041103 (2014).
330. Tiedke, S. & Schmitz, T., *Electrical characterization of nanoscale ferroelectric structures* in *Nanoscale Characterisation of Ferroelectric Materials,* M. Alexe, A. Gruverman, Eds. (Springer, Berlin, Heidelberg, 2004), pp. 87-114.
331. Cardoletti, J., Deposition and modelling of lead zirconate titanate thin films on stainless steel for MEMS applications. Dissertation, TU Darmstadt, Darmstadt, Germany (2021).
332. Keithley 4200-SCS user manual. https://www.cedesa.com.mx/pdf/keithley/keithley_4200-SCS_user_manual.pdf (accessed 15 Nov 2022).
333. George, S. M., Atomic layer deposition: an overview. *Chemical Reviews* **110**, 111-131 (2010).
334. Lebedinskii, Y. & Zenkevich, A., Silicide formation at HfO_2–Si and ZrO_2–Si interfaces induced by Ar^+ ion bombardment. *Journal of Vacuum Science & Technology A: Vacuum, Surfaces, and Films* **22**, 2261-2264 (2004).
335. Perevalov, T. V., Prosvirin, I. P., Suprun, E. A., Mehmood, F., Mikolajick, T., Schroeder, U. & Gritsenko, V. A., The atomic and electronic structure of $Hf_{0.5}Zr_{0.5}O_2$ and $Hf_{0.5}Zr_{0.5}O_2$:La films. *Journal of Science: Advanced Materials and Devices* **6**, 595-600 (2021).
336. Triyoso, D. H., Hegde, R. I., Schaeffer, J. K., Roan, D., Tobin, P. J., Samavedam, S. B., White, B. E., Gregory, R. & Wang, X. D., Impact of Zr addition on properties of atomic layer deposited HfO_2. *Applied Physics Letters* **88**, 222901 (2006).
337. Böscke, T. S., Hung, P. Y., Kirsch, P. D., Quevedo-Lopez, M. A. & Ramírez-Bon, R., Increasing permittivity in HfZrO thin films by surface manipulation. *Applied Physics Letters* **95**, 052904 (2009).
338. Müller, J., Böscke, T. S., Schröder, U., Mueller, S., Bräuhaus, D., Böttger, U., Frey, L. & Mikolajick, T., Ferroelectricity in Simple Binary ZrO_2 and HfO_2. *Nano Letters* **12**, 4318-4323 (2012).
339. Böscke, T. S., Teichert, S., Bräuhaus, D., Müller, J., Schröder, U., Böttger, U. & Mikolajick, T., Phase transitions in ferroelectric silicon doped hafnium oxide. *Applied Physics Letters* **99**, 112904 (2011).
340. Sigov, A., Podgorny, Y., Vorotilov, K. & Vishnevskiy, A., Leakage currents in ferroelectric thin films. *Phase Transitions* **86**, 1141-1151 (2013).

341. Mehdizadeh, M., *The impact of fields on materials at RF/microwave frequencies* in *Microwave/RF applicators and probes for material heating, sensing, and plasma generation*. (William Andrew Applied Science Publishers, Norwich, NY, 2009), pp. 1-34.
342. Kim, S. J., Mohan, J., Kim, H. S., Hwang, S. M., Kim, N., Jung, Y. C., Sahota, A., Kim, K., Yu, H. Y., Cha, P. R., Young, C. D., Choi, R., Ahn, J. & Kim, J., A Comprehensive Study on the Effect of TiN Top and Bottom Electrodes on Atomic Layer Deposited Ferroelectric $Hf_{0.5}Zr_{0.5}O_2$ Thin Films. *Materials* **13**, 2968 (2020).
343. Fengler, F. P. G., Nigon, R., Muralt, P., Grimley, E. D., Sang, X., Sessi, V., Hentschel, R., LeBeau, J. M., Mikolajick, T. & Schroeder, U., Analysis of Performance Instabilities of Hafnia-Based Ferroelectrics Using Modulus Spectroscopy and Thermally Stimulated Depolarization Currents. *Advanced Electronic Materials* **4**, 1700547 (2018).
344. Liu, T., Verma, M., Kang, Y. & Orlowski, M. K., Coexistence of bipolar and unipolar switching of Cu and oxygen vacancy nanofilaments in Cu/TaO_x/Pt resistive devices. *ECS Solid State Letters* **1**, Q11-Q13 (2012).
345. Li, Y., Long, S., Liu, Y., Hu, C., Teng, J., Liu, Q., Lv, H., Sune, J. & Liu, M., Conductance Quantization in Resistive Random Access Memory. *Nanoscale Research Letters* **10**, 420 (2015).
346. Kilaas, R., Optimal and near-optimal filters in high-resolution electron microscopy. *Journal of Microscopy* **190**, 45-51 (1998).
347. Kim, T., Vogel, T., Piros, E., Nasiou, D., Kaiser, N., Schreyer, P., Winkler, R., Zintler, A., Arzumanov, A. & Petzold, S., Oxide thickness-dependent resistive switching characteristics of Cu/HfO_2/Pt ECM devices. *Applied Physics Letters* **122**, 023502 (2023).
348. Milano, G., Raffone, F., Luebben, M., Boarino, L., Cicero, G., Valov, I. & Ricciardi, C., Water-Mediated Ionic Migration in Memristive Nanowires with a Tunable Resistive Switching Mechanism. *ACS Applied Materials & Interfaces* **12**, 48773-48780 (2020).
349. Clarke, H., Deremo, L., Anderson, J., Ganguli, S. & Shamberger, P. J., Conductive filament shape in HfO_2 electrochemical metallization cells under a range of forming voltages. *Nanotechnology* **31**, 075706 (2020).
350. McBrayer, J. D., Swanson, R. M. & Sigmon, T. W., Diffusion of Metals in Silicon Dioxide. *Journal of The Electrochemical Society* **133**, 1242-1246 (2019).
351. Kotilainen, M., Krumpolec, R., Franta, D., Souček, P., Homola, T., Cameron, D. C. & Vuoristo, P., Hafnium oxide thin films as a barrier against copper diffusion in solar absorbers. *Solar Energy Materials and Solar Cells* **166**, 140-146 (2017).
352. Abe, T., Sundman, B. & Onodera, H., Thermodynamic assessment of the Cu−Pt system. *Journal of Phase Equilibria and Diffusion* **27**, 5-13 (2006).
353. Zaumseil, P., High-resolution characterization of the forbidden Si 200 and Si 222 reflections. *Journal of Applied Crystallography* **48**, 528-532 (2015).
354. Vogel, T., Zintler, A., Kaiser, N., Guillaume, N., Lefèvre, G., Lederer, M., Serra, A. L., Piros, E., Kim, T., Schreyer, P., Winkler, R., Nasiou, D., Olivo, R. R., Ali, T., Lehninger, D., Arzumanov, A., Charpin-Nicolle, C., Bourgeois, G., Grenouillet, L., Cyrille, M.-C., Navarro, G., Seidel, K., Kämpfe, T., Petzold, S., Trautmann, C., Molina-Luna, L. & Alff, L., Structural and Electrical Response of Emerging Memories Exposed to Heavy Ion Radiation. *ACS Nano* **16**, 14463-14478 (2022).
355. Lanza, M., Waser, R., Ielmini, D., Yang, J. J., Goux, L., Sune, J., Kenyon, A. J., Mehonic, A., Spiga, S., Rana, V., Wiefels, S., Menzel, S., Valov, I., Villena, M. A., Miranda, E., Jing, X., Campabadal, F., Gonzalez, M. B., Aguirre, F., Palumbo, F., Zhu, K., Roldan, J. B., Puglisi, F. M., Larcher, L., Hou, T. H., Prodromakis, T., Yang, Y., Huang, P., Wan, T., Chai, Y., Pey, K. L., Raghavan, N., Duenas, S., Wang, T., Xia, Q. & Pazos, S., Standards for the Characterization of Endurance in Resistive Switching Devices. *ACS Nano* **15**, 17214−17231 (2021).
356. Perevalov, T. V., Gritsenko, V. A., Erenburg, S. B., Badalyan, A. M., Wong, H. & Kim, C. W., Atomic and electronic structure of amorphous and crystalline hafnium oxide: X-ray

photoelectron spectroscopy and density functional calculations. *Journal of Applied Physics* **101**, 053704 (2007).

357. Mart, C., Kämpfe, T., Kühnel, K., Czernohorsky, M., Kolodinski, S., Wiatr, M., Weinreich, W. & Eng, L. M., Enhanced pyroelectric response at morphotropic and field-induced phase transitions in ferroelectric hafnium oxide thin films. *APL Materials* **9**, 051120 (2021).
358. Lederer, M., Abdulazhanov, S., Olivo, R., Lehninger, D., Kämpfe, T., Seidel, K. & Eng, L. M., Electric field-induced crystallization of ferroelectric hafnium zirconium oxide. *Scientific Reports* **11**, 1-7 (2021).
359. Lederer, M., Olivo, R., Lehninger, D., Abdulazhanov, S., Kämpfe, T., Kirbach, S., Mart, C., Seidel, K. & Eng, L. M., On the Origin of Wake-Up and Antiferroelectric-Like Behavior in Ferroelectric Hafnium Oxide. *Physica Status Solidi (RRL)–Rapid Research Letters* **15**, 2100086 (2021).
360. Tashiro, Y., Shimizu, T., Mimura, T. & Funakubo, H., Comprehensive study on the kinetic formation of the orthorhombic ferroelectric phase in epitaxial Y-doped ferroelectric HfO_2 thin films. *ACS Applied Electronic Materials* **3**, 3123-3130 (2021).
361. Shimizu, T., Tashiro, Y., Mimura, T., Kiguchi, T., Shiraishi, T., Konnno, T. J., Sakata, O. & Funakubo, H., Electric-Field-Induced Ferroelectricity in 5% Y-doped $Hf_{0.5}Zr_{0.5}O_2$: Transformation from the Paraelectric Tetragonal Phase to the Ferroelectric Orthorhombic Phase. *Physica Status Solidi (RRL)–Rapid Research Letters* **15**, 2000589 (2021).
362. Cinkaya, H., Ozturk, A., Sirri Atilla Hasekioğlu, A., Evren Kaya, Z., Kalem, S., Charpin-Nicolle, C., Bourgeois, G., Guillaume, N., Claire.Cyrille, M., Garrione, J., Navarro, G. & Nowak, E., Structural properties of Ge-Sb-Te alloys. *Solid-State Electronics* **185**, 108101 (2021).
363. Bastiani, R. D., Piro, A. M., Grimaldi, M. G., Rimini, E., Baratta, G. & Strazzulla, G., Structural Evolution of Amorphous $Ge_2Sb_2Te_5$ Thin Films in the Transition to the Crystalline Phase. *MRS Online Proceedings Library* **1072**, G02-05 (2008).
364. Lyeo, H.-K., Cahill, D. G., Lee, B.-S., Abelson, J. R., Kwon, M.-H., Kim, K.-B., Bishop, S. G. & Cheong, B.-k., Thermal conductivity of phase-change material $Ge_2Sb_2Te_5$. *Applied Physics Letters* **89**, 151904 (2006).
365. Zhou, D., Wu, L., Guo, Q., Peng, C., He, C., Song, Z., Rao, F., Li, Y. & Xi, S., High tolerance of proton irradiation of $Ge_2Sb_2Te_5$ phase change material. *Journal of Alloys and Compounds* **575**, 229-232 (2013).

Acknowledgements

At this point, I would like to thank everyone who directly or indirectly contributed to this work.

First and foremost, I would like to thank Prof. Dr. Lambert Alff for his supervision throughout the years, since I joined his group for my Advanced Research Lab, and for giving me the opportunity to learn new skills on a personal and scientific level and for the always open door for discussions on the way towards this written thesis.

A special thanks goes also to Prof. Dr. Christina Trautmann for everything related to the heavy ion irradiation experiments conducted for this work, her supervision and patience during paper writing and for taking over the role of the second referee.

I would like to thank Prof. Dr. Molina Luna and Prof. Dr. Christian Hochberger for being members of my committee and the fruitful cooperation with the RRAM group in our joint projects. I thank Prof. Dr. Molina-Luna and his AEM group additionally, especially Despina Nasiou and Robert Winkler for the great discussions and the electron microscopy investigations performed as part of our RRAM subgroup family. My sincere thanks goes to Dr. Alexander Zintler for the acquisition of the (S)TEM/SPED datasets, the endless discussions and for teaching me some quite fancy stuff. I would like to thank all members of the entire ATFT group for the great working atmosphere and the amazing time. You have become valued friends.

I would like to also thank the mechanical and electronic workshop of the Materials Science department and especially Michael Weber, making many almost impossible things possible.

A sincere thanks to Jürgen Schreeck, Gabriele Haindl, Heinz Mohren, Stephan Diefenbach and Andreas Hönl for the help with technical matters, everything regarding vacuum systems, deliveries, keys and transponders, computers, etc. A huge thanks also to Marion Bracke, Angela Dreher and Dr. Márton Major for the open doors and the reliable assistance with project issues. I also thank all professors and scientific staff of the Department who have contributed to this work with advice.

A sincere thanks goes to my colleague and friend Nico Kaiser for the comradely cooperation. I would like to also thank Eszter Piros for her help at any time. We were able to solve a bunch of problems together in the last 5 years.

Thank you to Dr. Philipp Kehne und Dr. Stefan Petzold for your supervision, the kind introduction to the group and everything I was taught in the very beginning, when I had to learn a lot from scratch. Thanks also to Dr. Juliette Cardoletti for the fun we had when setting up the ferroelectric measurement equipment.

I like to also thank the students who chose me as a supervisor for trusting me. I hope that I could introduce everyone well to the topic and our group. I am happy that I was lucky enough to meet some good people on a personal and professional level.

Thanks to Dr. Philipp Komissinskiy for various scientific discussions on different topics, to Dr. Gennady Cherkashinin and Dr. Thimo Ferber for the close collaboration at the XPS servicing and to Dr. Alexey Arzumanov for the introduction to the ion beam etching system.

A sincere thanks goes to all project partners for the fruitful cooperation within StorAIge and WAKeMeUP and the joint publications and conference contributions, especially Dr. Christelle Charpin-Nicolle, Dr. Gabriele Navarro, Dr. Anna Lisa Serra, Dr. Gauthier Lefèvre, Dr. Nicolas Guillaume, Dr. Maximilian Lederer, Dr. Thomas Kämpfe, Dr. David Lehninger und Dr. Konrad Seidel. I would also like to thank Dr. Fernando Aguirre and Prof. Dr. Enrique Miranda for the close collaboration with our RRAM group.

A huge thanks goes to Anna Lisa Eichhorn and Dr. Christian Dietz for the AFM investigations and Dr. Enrico Bruder for the help with orientation map analysis. Additionally, a sincere thanks goes to Dr. Stefan Flege, Dr. Ruriko Hatada and Prof. Dr. Wolfgang Ensinger for introducing me to the fascinating world of thin films during my bachelor thesis and for the joint publication.

Additionally, I want to thank all my past and present colleagues, Tom Faske, Marcel Urban, Constantin Wansorra and the whole Sofa crew for inspiring discussions, and anyone I may have unintentionally forgotten. A huge thanks to all proofreaders of this work.

Apart from work, I would also like to thank the football groups, foremost, the “Orheiljer“ and the friends sharing with me a relaxed fast run in the forests located around Darmstadt.

I also thank the funding agencies of the projects WAKeMeUP and StorAIge. These projects received funding from the Electronic Components and Systems for European Leadership Joint Undertaking in collaboration with the European Union’s H2020 Framework Programme (H2020/2014-2020) and National Authorities, under grant agreement no. 783176 and 101007321. Funding by the Federal Ministry of Education and Research (BMBF) under contract 16ESE0298 and 16ESE0298 are gratefully acknowledged.

The heavy ion irradiation experiments are based on the experiment UMAT and were conducted at the X0 beamline of the GSI Helmholtzzentrum für Schwerionenforschung in Darmstadt, Germany, in the frame of FAIR Phase-0.

Last but certainly not least, I would express my deep gratitude to my close friends, my girlfriend and my family for always being around, their never ending support and for all their love making this world a good place to be.

Curriculum Vitae

May 2018 – March 2023	**Research Assistant and PhD Candidate** at Advanced Thin Film Technology Division (Dünne Schichten), Departement of Materials Science, TU Darmstadt
April 2016 – July 2017	**Student Assistant at Department of Materials Science, TU Darmstadt**, as a tutor in Materials Science II (solid state thermodynamics) & Material Science V (solid state physics)
October 2015 – February 2018	**Master of Science program in Materials Science at TU Darmstadt, Germany**; Graduation in February 2018 - **Master of Science (M. Sc.) Materialwissenschaft (Materials Science)** o Master Thesis topic: „PLD growth investigations of Scandium-substituted NASICON solid electrolyte thin films“
August 2014 – October 2014	**Internship at the research and development department of Pirelli Germany GmbH, Breuberg, Germany** o Topic: „Korrelationsanalysen der Parameter eines Rheovulkameters und Bewertung der Vorhersagemöglichkeiten für die Halbzeugverarbeitung von Mischungen“
October 2012 – September 2015	**Bachelor of Science program in Materials Science at TU Darmstadt, Germany**; Graduation in September 2015 - **Bachelor of Science (B.Sc.) Materialwissenschaft (Materials Science)** o Bachelor Thesis topic: „Verbesserung der Adhäsion von DLC-Schichten auf Kupfer“

Dissemination

List of publications as first author:

(* = these authors contributed equally to the specific publication)

T. Vogel, N. Kaiser, S. Petzold, E. Piros, N. Guillaume, G. Lefèvre, C. Charpin-Nicolle, S. David, C. Vallée, E. Nowak, C. Trautmann, and Lambert Alff, "Defect-Induced Phase Transition in Hafnium Oxide Thin Films: Comparing Heavy Ion Irradiation and Oxygen-Engineering Effects," *IEEE Transactions on Nuclear Science* **68**, 8, 1542-1547 (2021). https://doi.org/10.1109/TNS.2021.3085962

M. Lederer*, **T. Vogel***, T. Kämpfe, N. Kaiser, E. Piros, R. Olivo, T. Ali, S. Petzold, D. Lehninger, C. Trautmann, L. Alff, and K. Seidel, "Heavy ion irradiation induced phase transitions and their impact on the switching behavior of ferroelectric hafnia", *Journal of Applied Physics* **132**, 6, 064102 (2022). https://doi.org/10.1063/5.0098953

T. Vogel, A. Zintler, N. Kaiser, N. Guillaume, G. Lefèvre, M. Lederer, A. L. Serra, E. Piros, T. Kim, P. Schreyer, R. Winkler, D. Nasiou, R. Olivo, T. Ali, D. Lehninger, A. Arzumanov, C. Charpin-Nicolle, G. Bourgeois, L. Grenouillet, M.-C. Cyrille, G. Navarro, K. Seidel, T. Kämpfe, S. Petzold, C. Trautmann, L. Molina-Luna, and L. Alff, "Structural and electrical response of emerging memories exposed to heavy ion radiation", *ACS Nano* **16**, 9, 14463-14478 (2022). https://doi.org/10.1021/acsnano.2c04841

T. Kim*, **T. Vogel***, E. Piros, D. Nasiou, N. Kaiser, P. Schreyer, R. Winkler, A. Zintler, A. Arzumanov, S. Petzold, L. Molina-Luna, L. Alff, "Oxide thickness-dependent resistive switching characteristics of Cu/HfO_2/Pt ECM devices", *Applied Physics Letters* **122**, 2, 023502 (2023). https://doi.org/10.1063/5.0124781

List of topic-related peer-reviewed publications as co-author, incl. conference papers:

S. Petzold, E. Miranda, S. U. Sharath, J. Muñoz-Gorriz, **T. Vogel**, E. Piros, N. Kaiser, R. Eilhardt, A. Zintler, L. Molina-Luna, J. Suñé, and L. Alff, "Analysis and simulation of the multiple resistive switching modes occurring in HfO_x-based resistive random access memories using memdiodes," *Journal of Applied Physics* **125**, 23, 234503 (2019). https://doi.org/10.1063/1.5094864

S. Petzold*, A. Zintler*, R. Eilhardt, N. Kaiser, E. Piros, S. U. Sharath, **T. Vogel**, M. Major, L. Molina-Luna, and L. Alff, "Forming-Free Grain Boundary Engineered Hafnium Oxide Resistive Random Access Memory Devices," *Advanced Electronic Materials* **5**, 10, 1900484 (2019). https://doi.org/10.1002/aelm.201900484

T. Kämpfe, **T. Vogel**, R. Olivo, M. Lederer, N. Kaiser, S. Petzold, T. Ali, D. Lehninger, C. Trautmann, L. Alff, and K. Seidel, "Heavy Ion Irradiation Effects on Structural and Ferroelectric Properties of HfO_2 Films," in *2020 Joint Conference of the IEEE International Frequency Control Symposium and International Symposium on Applications of Ferroelectrics (IFCS-ISAF), IEEE,* 1-3 (2020). https://doi.org/10.1109/IFCS-ISAF41089.2020.9234942

E. Piros, S. Petzold, A. Zintler, N. Kaiser, **T. Vogel**, R. Eilhardt, C. Wenger, L. Molina-Luna, and L. Alff, "Enhanced thermal stability of yttrium oxide-based RRAM devices with inhomogeneous Schottky-barrier," *Applied Physics Letters* **117**, 1, 013504 (2020). https://doi.org/10.1063/5.0009645

E. Piros, M. Lonsky, S. Petzold, A. Zintler, S.U. Sharath, **T. Vogel**, N. Kaiser, R. Eilhardt, L. Molina-Luna, C. Wenger, J. Müller, and L. Alff, "Role of Oxygen Defects in Conductive-Filament Formation in Y_2O_3-Based Analog RRAM Devices as Revealed by Fluctuation Spectroscopy," *Physical Review Applied* **14**, 3, 034029 (2020). http://dx.doi.org/10.1103/PhysRevApplied.14.034029

S. Petzold*, E. Piros*, R. Eilhardt, A. Zintler, **T. Vogel**, N. Kaiser, A. Radetinac, P. Komissinskiy, E. Jalaguier, E. Nolot, C. Charpin-Nicolle, C. Wenger, L. Molina-Luna, E. Miranda, and L. Alff, "Tailoring the Switching Dynamics in Yttrium Oxide-Based RRAM Devices by Oxygen Engineering: From Digital to Multi-Level Quantization toward Analog Switching," *Advanced Electronic Materials* **6**, 11, 2000439 (2020). https://doi.org/10.1002/aelm.202000439

N. Guillaume, G. Lefèvre, C. Charpin-Nicolle, L. Grenouillet, **T. Vogel**, N. Kaiser, E. Piros, S. Petzold, C. Trautmann, D. Sylvain, C. Vallee, L. Alff, and E. Nowak, "Heavy Ion Irradiation Hardening Study on 4kb arrays HfO2-based OxRAM", in *2020 20th European Conference on Radiation and Its Effects on Components and Systems (RADECS)*, 1-6 (2020). https://doi.org/10.1109/RADECS50773.2020.9857730

A. L. Serra, **T. Vogel**, G. Lefèvre, S. Petzold, N. Kaiser, G. Bourgeois, M.-C. Cyrille, L. Alff, C. Trautmann, C. Vallée, S. David, C. Charpin-Nicolle, G. Navarro, E. Nowak, Heavy Ions Radiation Effects on 4kb Phase-Change Memory, in *2020 20th European Conference on Radiation and Its Effects on Components and Systems (RADECS)*, 1-4 (2020). https://doi.org/10.1109/RADECS50773.2020.9857688

N. Kaiser, **T. Vogel**, A. Zintler, S. Petzold, A. Arzumanov, E. Piros, R. Eilhardt, L. Molina-Luna, and L. Alff, "Defect-Stabilized Substoichiometric Polymorphs of Hafnium Oxide with Semiconducting Properties," *ACS Applied Materials & Interfaces* **14**, 1, 1290–1303 (2022). https://doi.org/10.1021/acsami.1c09451

F. L. Aguirre, E. Piros, L. Alff, C. Hochberger, J. Gehrunger, S. Petzold, N. Kaiser, E. Jalaguir, E. Nolot, C. Charpin-Nicolle, **T. Vogel**, L. Molina-Luna, J. Suñé, and E. Miranda, "Compact Model for Oxygen Engineered Yttrium Oxide-Based Resistive Switching Devices," in *2022 IEEE 22nd International Conference on Nanotechnology (NANO)*, 275-278 (2022). https://doi.org/10.1109/NANO54668.2022.9928654

R. Winkler, A. Zintler, S. Petzold, E. Piros, N. Kaiser, **T. Vogel**, D. Nasiou, K. P. McKenna, L. Molina-Luna, and L. Alff, "Controlling the formation of conductive pathways in memristive devices", Adv. Sci. **9**, 33, 2201806 (2022). https://doi.org/10.1002/advs.202201806

F. L. Aguirre, E. Piros, N. Kaiser, **T. Vogel**, S. Petzold, J. Gehrunger, T. Oster, C. Hochberger, J. Suñé, L. Alff, and E. Miranda, "Fast Fitting of the Dynamic Memdiode Model to the Conduction Characteristics of RRAM Devices Using Convolutional Neural Networks", *Micromachines* **13**, 11, 2002 (2022). https://doi.org/10.3390/mi13112002

N. Kaiser*, Y.-J. Song*, **T. Vogel**, E. Piros, T. Kim, P. Schreyer, S. Petzold, R. Valentí, and L. Alff, "Crystal and electronic structure of oxygen vacancy stabilized rhombohedral hafnium oxide", *ACS Applied Electronic Materials* **5**, 2, 754-763 (2023). https://doi.org/10.1021/acsaelm.2c01255

Additional publications:

S. Flege, R. Hatada, **T. Vogel**, E. Bruder, M. Major, W. Ensinger, and K. Baba, "Tightly adhering diamond-like carbon films on copper substrates by oxygen pre-implantation," *Surface and Coatings Technology* **335**, 134-139 (2018). https://doi.org/10.1016/j.surfcoat.2017.12.029

K. Wissel, **T. Vogel**, S. Dasgupta, A.D. Fortes, P.R. Slater, O. Clemens, "Topochemical Fluorination of *n* = 2 Ruddlesden–Popper Type $Sr_3Ti_2O_7$ to $Sr_3Ti_2O_5F_4$ and Its Reductive Defluorination," *Inorganic Chemistry* **59**, 2, 1153-1163 (2019). https://doi.org/10.1021/acs.inorgchem.9b02783

K. Wissel, R. Schoch, **T. Vogel**, M. Donzelli, G. Matveeva, U. Kolb, M. Bauer, "Electrochemical Reduction and Oxidation of Ruddlesden–Popper-Type $La_2NiO_3F_2$ within Fluoride-Ion Batteries," *Chemistry of Materials* **33**, 2, 499-512 (2021). https://doi.org/10.1021/acs.chemmater.0c01762

T. Vogel* and L. Alff*, Abschlussbericht (final report) WAKeMeUP (TU Darmstadt); project term: 01.06.2018-30.04.2021; funding code: 16ESE0298; November 2021. https://www.tib.eu/de/suchen/id/TIBKAT:1786970198/WAKeMeUP-Abschlussbericht-WAKeMeUP-TU-Darmstadt

T. Vogel*, A. Zintler*, N. Kaiser, N. Guillaume, G. Lefèvre, M. Lederer, A. L. Serra, E. Piros, T. Kim, P. Schreyer, R. Winkler, D. Nasiou, R. Olivo, T. Ali, D. Lehninger, A. Arzumanov, C. Charpin-Nicolle, G. Bourgeois, L. Grenouillet, M.-C. Cyrille, G. Navarro, K. Seidel, T. Kämpfe, S. Petzold, C. Trautmann, L. Molina-Luna, and L. Alff, „Integration of labeled 4D-STEM SPED data for confirmation of phase identification," in *TUdatalib*; June 2022; https://doi.org/10.48328/tudatalib-896

Conference contributions as speaker: (contributions as a co-author are not listed)

RADECS 2020 (virtual conference): "Defect-induced phase transition in hafnium oxide thin films by heavy ion irradiation: The role of oxygen defects" – **T. Vogel**, N. Kaiser, S. Petzold, E. Piros, N. Guillaume, G. Lefèvre, C. Charpin-Nicolle, S. David, C. Vallée, E. Nowak, C. Trautmann, L. Alff; oral presentation

EMRS 2021 (virtual conference): "Swift heavy ion irradiation induced effects on HfO_x- and GST-based emerging memories – structural and electrical properties" – **T. Vogel**, T. Kämpfe, N. Guillaume, A. L. Serra, N. Kaiser, G. Lefèvre, M. Lederer, R. Olivo, T. Ali, D. Lehninger, E. Piros, G. Navarro, C. Charpin-Nicolle, S. Petzold, C. Trautmann, L. Alff; oral presentation

Nano 2022 (Sevilla, Spain): "Heavy ion irradiation induced effects on emerging memory materials – crystallinity, microstructure and electrical properties" – **T. Vogel**, A. Zintler, N. Kaiser, T. Kämpfe, M. Lederer, N. Guillaume, A. L. Serra, G. Lefèvre, E. Piros, R. Eilhardt, R. Olivo, T. Ali, D. Lehninger, C. Charpin-Nicolle, G. Navarro, K. Seidel, S. Petzold, L. Molina-Luna, C. Trautmann, L. Alff; oral presentation

CIMTEC 2022 (Perugia, Italy): "Substoichiometric Hafnium Oxide Polymorphs with Semiconducting Properties" – **T. Vogel,** N. Kaiser, A. Zintler, S. Petzold, A. Arzumanov, E. Piros, R. Eilhardt, L. Molina-Luna, L. Alff; oral presentation given on behalf of N. Kaiser

CIMTEC 2022 (Perugia, Italy): "Swift Heavy Ion Irradiation Induced Effects on Emerging Memories - Correlation of Structural and Electrical Properties" – **T. Vogel**, T. Kämpfe,

A. L. Serra, N. Kaiser, M. Lederer, G. Lefèvre, N. Guillaume, R. Olivo, T. Ali, D. Lehninger, E. Piros, G. Navarro, C. Charpin-Nicolle, S. Petzold, C. Trautmann, L. Alff; oral presentation

Additional presentations:

Congress "ECSEL in Deutschland" (ECSEL in Germany), September 2018 (Dresden, Germany): „Presentation of WAKeMeUP" – **T. Vogel** and T. Hummel; poster prepared by T. Vogel, presentation given by T. Hummel

International School of Oxide Electronics ISOE 2019 (Cargèse, France): "Engineering of HfO_{2-x} by MBE for emerging NVMs: RRAM & FeRAM" – **T. Vogel**, S. Petzold, N. Kaiser, E. Piros, M. Major, A. Zintler, R. Eilhardt, L. Molina-Luna, L. Alff; poster presentation

EMRS 2022 (Warsaw, Poland): "Heavy ion irradiation induced defects in emerging memory materials – crystallinity, microstructure and electrical properties" – **T. Vogel***, T. Kämpfe, A. L. Serra, N. Kaiser, M. Lederer, G. Lefèvre, N. Guillaume, R. Olivo, T. Ali, D. Lehninger, E. Piros, G. Navarro, C. Charpin-Nicolle, S. Petzold, C. Trautmann, L. Alff*; *oral presentation given by L. Alff on behalf of T. Vogel

WAKeMeUP (2018 – 2021) and StorAIge (2021 & 2022) international project meetings, German project meetings and EU project reviews (2018-2021), oral presentations and written project reports

Supervision of scientific works:

Y. Badour, "A comparative study of the non-polar switching behavior of $Hf_{0.5}Zr_{0.5}O_2$ and HfO_2-based RRAM devices", Advanced Research Lab (2020)

K. Garcia, "TiN electrode preparation", Research Project (2020)

T. Kim, "Resistive switching in Pt/HfO_2/Pt and Cu/HfO_2/Pt devices", Advanced Research Lab, (2021)

T. Kim, "HfO_2-thickness-dependent switching characteristics of resistive memory devices with a Cu electrode", Master thesis (2022)

J. Uhle, "Resistive switching analysis of RRAM device characteristics containing different top electrode materials", Research Project (2022)

Furthermore, two new PhD candidates, P. Schreyer and T. Kim (start 2022), were introduced to the topic, including the knowledge transfer of different sample preparation and characterization techniques, foremost the reactive molecular beam epitaxy deposition system.

Contributions to projects and proposals:

This work was conducted in the frame of two projects, **WAKeMeUP** and **StorAIge**. The project WAKeMeUP ("Wafers for Automotive and other Key Applications using Memories, embedded in Ulsi Processors", https://www.wakemeup-ecsel.eu/) is a European project running under grant agreement number 783176, which is funded within the Horizon2020 funding program "Electronic Component Systems for European Leadership Joint Undertaking" (ECSEL JU) and on national level (for Germany) by the Bundesministerium für Bildung und Forschung (BMBF) under contract 16ESE0298. Within the project time between May 2018 and December 2021, intra-european consortium partners from industry and academia were working on different emerging memories such as OxRAM, FeRAM and PCRAM. The overall aim for industrial applications was to set-up a pilot line for advanced microcontrollers and to manufacture embedded non-volatile memories for applications required by the market. The results obtained from the irradiation experiments conducted during WAKeMeUP were first published in a written report and submitted in two official project deliverables. Next to scientific tasks, the work within the project included the project administration and management for the partner TU Darmstadt, which was taken over in the last year of the project. This work included the periodic reporting to public financiers and presentations at the general assemblies of the project.

The successful work conducted within WAKeMeUP led to the participation of the project partner TU Darmstadt in the follow-up project StorAIge ("Embedded storage elements on next MCU generation ready for AI on the edge"; grant agreement number 101007321 & BMBF contract number 16MEE0154; https://storaige.eu/)). The StorAIge project started in July 2021 with a probable duration of 36 months. Already during the period of WAKeMeUP, a beam time proposal with the title "Comparative Radiation Hardness Testing of Emerging Non-Volatile Memory Technologies (RRAM & FeRAM) was submitted and got granted in 2020. The experiments of the different project partners are coordinated by the Advanced Thin Film Group of TU Darmstadt and conducted at the Helmholtzzentrum für Schwerionenforschung in Darmstadt. First results will be reported in an official project deliverable in autumn 2023. It is further planned to disseminate the findings at international conferences and publish the results in peer-reviewed journals.

Some additional projects are closely related to this work:

- DFG project (384682067) "In operando investigation of resistive switching in electron transparent lamellae of HfO_x based RRAM devices".
- ERC Starting Grant FOXON (805359) „Functionality of Oxide based devices under Electric-field: Towards Atomic-resolution Operando Nanoscopy" and the ERC PoC STARE (957521) "Machine learning based Software Toolkit for Automated identification in atomic-REsolution operando nanoscopy"
- The project "Energieeffiziente Simulation eines energieeffizienten Speichers/Energy-efficient simulation of an energy-efficient storage" (EES)[2], which is a cooperation of the advanced thin film group of Prof. Lambert Alff and the computer systems group of Prof. Christian Hochberger of TU Darmstadt (Darmstadt, Germany) as well as the group of Prof. Enrique Miranda of the Universitat Autònoma de Barcelona (UAB, Barcelona, Spain) as part of the joint "Sustainability Hub" with Merck KGaA (https://www.merckgroup.com/de/news/sustainability-hub-tu-darmstadt-29-07-2021.html).